

Fundamental Understanding of Removal of Water from a Moist Porous Medium in the Absence and Presence of Ultrasound Mechanism

A Dissertation

Submitted to the Faculty

of the

WORCESTER POLYTECHNIC INSTITUTE

In partial fulfillment of the requirements for the

Degree of Doctor of Philosophy

In

Mechanical Engineering

By

Zahra Noori O'Connor

January 2023

Advisory Committee

Dr. Jamal S. Yagoobi, Major Advisor (WPI)

Dr. Burt S. Tilley, Co-Advisor (WPI)

Dr. Aswin Gnanaskandan, Committee Member (WPI)

Dr. Juan Rodriguez Ramirez, Committee Member (IPN)

Dr. Ken Jewett, Committee Member (Sappi)

Dr. Yuxiang Liu, Graduate Committee Representative (WPI)

© 2023, Zahra Noori O'Connor

Table of Contents

List of Figures	7
List of Tables	16
Nomenclature	18
Acknowledgments.....	23
Abstract of the Dissertation	26
Chapter 1: Introduction.....	29
1.1 Transition Region in Paper Drying Curve.....	31
1.2 Ultrasonic Drying	35
1.3 Ultrasonic Atomization	38
1.4 Motivations and Objectives.....	43
Chapter 2: Fundamental Understanding of Removal of Liquid Thin Film Trapped Between Fibers in Paper Drying Process: Microscopic Approach.....	46
2.1 Theoretical Model	46
2.1.1 Governing Equations and Boundary Conditions.....	46
2.1.2 Numerical Technique	52
2.2 Results and Discussion.....	52
2.2.1 Thin Liquid Film Drying	52
2.2.2 Effect of Fluid Properties on Liquid Film Drying.....	56
2.2.3 Marangoni Effects	59
2.2.4 Effect of Geometrical Parameters on Liquid Film Drying.....	60
2.3 Summary and Conclusions.....	62
Chapter 3: Numerical Study of Removal of Water Trapped Inside a Single Cellulose Fiber	63
3.1 CFD Modeling.....	63
3.1.1 Geometry, Initial and Boundary Conditions	64
3.1.2 Governing Equations	66

3.1.3 Solution Technique.....	70
3.2 Results and Discussion.....	71
3.2.1 Water Removal from a Single Fiber.....	72
3.2.2 Heat Flux at the Water/Vapor Interface	74
3.2.3 Effect of Applied Heat Flux on Increasing the Drying Rate	77
3.2.4 Effect of Surface Tension on Drying Rate and Marangoni Effects.....	78
3.2.5 Effect of Fiber Geometrical Dimensions on Drying Rate	80
3.3 Summary and Conclusions.....	82
Chapter 4: Direct-Contact Ultrasonic Drying of Hand-Sheets	84
4.1 Materials and Experimental Method	84
4.1.1 Design of Experiments	88
4.2 Results and Discussion.....	89
4.2.1 Sample's Weight Measurements	89
4.2.2 Illustration of Ultrasonic Drying	91
4.2.3 Comparing Ultrasonic Drying with Conductive Heat Drying.....	93
4.2.4 Analysis of the Factorial Design of Experiments.....	94
4.2.5 Effect of Controlling Factors on Total Drying Time.....	98
4.2.6 Effect of Different Factors on the Area Under the Drying Curve	101
4.2.7 Colorimeter Measurements	102
4.2.8 Microscopic Measurements.....	104
4.2.9 Profilometry Measurements	107
4.2.10 Tensile Strength Measurements	110
4.2.11 Energy Analysis.....	113
4.3 Summary and Conclusions.....	118
Chapter 5: Airborne Power Ultrasound for Paper Drying: An Experimental Study	120
5.1 Experimental Setup and Methods	120
5.1.1 Experimental Setup	120
5.1.2 Experimental Method.....	126
5.2 Results and Discussion.....	128
5.2.1 Acoustic Characterization of the Transducer Plate in Near Field	128

5.2.2 Effect of Sample Holder	133
5.2.3 Thermal Effect of Airborne Ultrasonic Drying	135
5.2.4 Comparing Airborne Ultrasonic Drying with Conductive Heat Drying	138
5.2.5. Temperature Inside the Sample	139
5.2.6 Analysis of the Factorial Design of Experiments	140
5.2.7 Importance of the Controlling Factors on Total Time of Ultrasonic Drying	143
5.2.8 Importance of the Controlling Factors on Area Under Drying Curve.....	146
5.2.9 Quality measurements	147
5.2.10 Energy Analysis and Drying Rate	156
5.2.11 Comparing Direct-Contact and Non-Contact Ultrasonic Drying	160
5.3 Summary and Conclusions.....	163
Chapter 6: Fundamental Understanding of Ultrasonic Atomization and Resultant Droplet Size: A Numerical Study	164
6.1 Theoretical Model	165
6.1.1 Dimensionless Governing Equations	166
6.1.2 Boundary Conditions and Interface Tracking Strategy	167
6.1.3 Numerical Technique	170
6.1.4. Buckingham Pi Method.....	171
6.2 Experimental Method.....	171
6.3 Results and Discussion.....	172
6.3.1 Effect of Exciting Amplitude on Ultrasonic Atomization.....	173
6.3.2 Effect of Liquid Height on Ultrasonic Atomization.....	177
6.3.3 Effect of Surface Tension on Ultrasonic Atomization	193
6.3.4 Effect of Liquid Viscosity on Ultrasonic Atomization.....	198
6.3.5 Effect of Liquid Density on Ultrasonic Atomization	205
6.3.6 Effect of Exciting Frequency on Ultrasonic Atomization.....	210
6.3.7 Effect of Gravity on Ultrasonic Atomization	213
6.3.8 Non-Dimensional Numbers.....	215
6.3.9 Capillary Wavelength in Ultrasonic Atomization	220
6.3.10 Droplet Size in Ultrasonic Atomization	221

6.3.11 Ultrasonic Atomization of a Water Droplet	230
6.3.12 Airborne Ultrasonic Atomization	232
6.4 Summary and Conclusions	243
Chapter 7: Summary and Recommendations.....	245
7.1 Summary	245
7.2 Recommendations	247
Chapter 8: Impact.....	251
Appendix A: Kinetic Models for Ultrasonic Drying Curves	253
References.....	258

List of Figures

Figure 1. Typical drying kinetics plots: drying curve (left side) and drying rate curve (right side) [14].	32
Figure 2. Utilization of ultrasound according to frequency and power [45].	35
Figure 3. Four effects resulting from ultrasound propagation in a liquid [45].	36
Figure 4. Illustration of the simplified impinging air drying configuration considered in this study.	47
Figure 5. Schematic of the model for an evaporating liquid film between three fibers bounded by a flowing gas layer.	47
Figure 6. Change in liquid volume vs time for the case with operational conditions provided in Table 4.	53
Figure 7. Contours of volume fraction of the liquid layer at different times for the case with operational conditions provided in Table 4.	54
Figure 8. Contours of temperature at different times for the case with operational conditions provided in Table 4.	55
Figure 9. Comparing temperature profiles for the case shown in Figures 4-6 at 5 ms. The profiles are at locations between the first and the second fibers.	56
Figure 10. Change in liquid volume under different inlet velocities.	57
Figure 11. Change in liquid volume under different inlet temperatures.	58
Figure 12. Change in liquid volume under different initial liquid film thicknesses.	59
Figure 13. The effect of Marangoni flows on change in liquid volume vs time. The other properties are fixed according to Table 4.	60
Figure 14. Change in liquid volume vs time for cases with different geometrical parameters: (a) fiber diameter; (b) distance between fibers; and (c) pore height (defined as the inlet for hot dry air in Figure 5). The other properties are fixed according to Table 4.	61
Figure 15. Cross sectional schematic of single-fiber model.	64
Figure 16. Schematic of single fiber model.	65
Figure 17. 2D model for single fiber with set boundary conditions.	65
Figure 18. Change in liquid volume versus time for different mesh cell sizes.	66
Figure 19. Schematic of the cells around the interface between two fluids in VOF method.	67
Figure 20. Comparing softwood and hardwood fibers, schematically.	72

Figure 21. Change in liquid volume and interface position vs time for the case specified with stars in Table 5.....	72
Figure 22. Liquid volume contours at different times for the case specified with stars in Table 5.....	73
Figure 23. Temperature contours (in K) at different times for the case specified with stars in Table 5.....	73
Figure 24. Radial temperature profiles at $x = 500 \mu\text{m}$ (middle of the fiber) at different times for the case specified with stars in Table 5.....	74
Figure 25. Heat flux profiles at $y = 10 \mu\text{m}$ (the inner surface of the fiber) at different times for the case specified with stars in Table 5.....	76
Figure 26. Contours of temperature and volume fraction of water at time = 150 ms. The profiles of temperature and heat flux are plotted at the inner surface of the fiber wall ($y = 10 \mu\text{m}$)...	77
Figure 27. Changes in liquid volume versus time for the cases with different applied heat fluxes. The rest of the properties are specified with stars in Table 5.....	78
Figure 28. Changes in liquid volume versus time for different surface tensions. The rest of the operating parameters are specified with stars in Table 5.....	79
Figure 29. (a) The effect of Marangoni flows on the changes in liquid volume versus time; (b) velocity vectors (m/s) at the interface at time = 50 ms. The length shown here is $15 \mu\text{m}$. The rest of the operating parameters are specified with stars in Table 5.....	79
Figure 30. Changes in liquid volume versus time for the cases with different fiber diameters. The rest of the properties are specified with stars in Table 5.....	80
Figure 31. Changes in liquid volume versus time for the cases with different fiber lengths. The rest of the properties are specified with stars in Table 5.....	81
Figure 32. Changes in liquid volume versus time for the cases with different fiber wall thicknesses. The rest of the properties are specified with stars in Table 5.....	82
Figure 33. The major components of the experimental setup.....	85
Figure 34. (a) Mist generation transducer and (b) paper sample used in the direct-contact ultrasonic drying experiments.....	87
Figure 35. Comparing the weight measurements results using fresh samples and using intermittent method. The number of runs shows the number of repeats of the experiments using the fresh samples.....	90
Figure 36. Comparing the ultrasonic atomization for (a) an over-saturated unrefined softwood hand-sheet with (b) an unrefined softwood hand-sheet with 150% DBMC.....	91
Figure 37. Selected IR image sequences at different times of ultrasonic drying for unrefined hardwood hand-sheet (150% initial DBMC) placed on top of the transducer. The temperatures are in $^{\circ}\text{C}$	92

Figure 38. Temperature changes during direct-contact ultrasonic drying for an unrefined hardwood sample with 150% initial DBMC.....	93
Figure 39. Comparing the drying curves for conductive heating with ultrasonic drying.	94
Figure 40. Ultrasonic drying curves for hardwood samples.	95
Figure 41. Ultrasonic drying curves for softwood samples.	96
Figure 42. Comparing the total time of ultrasonically dried (direct-contact mechanism) hardwood and softwood samples.....	97
Figure 43. Pareto charts of the standardized effects from ANOVA analysis for total time of ultrasonic drying: (a) hardwood and (b) softwood.	99
Figure 44. Pareto charts of the standardized effects from ANOVA analysis for area under the ultrasonic drying curve: (a) hardwood and (b) softwood.....	102
Figure 45. Comparison of whiteness index for ultrasonic drying with heat conductive drying at 80 °C for H-R-150-0.3.	103
Figure 46. Colorimeter measurements ($L^*a^*b^*$) for hardwood and softwood samples dried using ultrasound mechanism.	103
Figure 47. Change in color and whiteness index of ultrasonically dried hand-sheets.....	104
Figure 48. Optical microscopic images for hardwood samples dried with ultrasound mechanism. The initial DBMC for all the samples is 150%. Magnification is 1000X.....	105
Figure 49. Optical microscopic images for softwood samples dried with ultrasound mechanism. The initial DBMC for all the samples is 150%. Magnification is 1000X.....	106
Figure 50. 2D porosity measurands using thresholding of the microscopic images of samples dried with ultrasound mechanism. The initial DBMC for all the samples is 150%.	107
Figure 51. Color view of roughness measurements for hardwood samples. It should be noted that the initial DBMC for all the samples is 150%.	108
Figure 52. Color view of roughness measurements for softwood samples. It should be noted that the initial DBMC for all the samples is 150%.	108
Figure 53. Surface roughness measurements for samples dried with ultrasound mechanism. The initial DBMC for all the samples is 150%.	110
Figure 54. Comparing stress-strain curves for H-R-150-0.3 dried with ultrasonic drying and with conductive heat drying at 80 °C.....	111
Figure 55. Stress-strain curves for different types of pulps with different thicknesses.....	112
Figure 56. Power meter measurements for three stages of input power to the transducer.	113
Figure 57. Changes in load power as a function of drying time for the transducer used in this study. 10 W forward power is applied to the transducer.	114

Figure 58. Comparing the energy factor for hardwood samples.	116
Figure 59. Comparing the energy factor for softwood samples.....	117
Figure 60. Illustration of the effect of high moisture content on DBMC and energy factor for H-R-700-0.3.	118
Figure 61. Left picture: The Solidworks schematic of the experimental testing fixture. Right picture: The assembled experimental fixture in the lab.	121
Figure 62. The experimental setup for non-contact ultrasonic drying.....	122
Figure 63. Airborne power ultrasonic transducer with a rectangular plate radiator [119].	123
Figure 64. Schematic of the airborne ultrasound transducer and the sample holder (left side). Side view of Al plate (right side).	123
Figure 65. Bottom view and side view of Ti plate.....	124
Figure 66. The experimental setup used by Pusonics to measure the acoustic pressure at different distances from the Al plate [120].	128
Figure 67. Sound pressure distribution at a plane parallel to the Al plate at 3 mm from the plate [120].	129
Figure 68. Pressure distribution in a transversal – perpendicular plane of the rectangular Al plate, in free field [120].	129
Figure 69. The average pressure from the Al plate at different distances [120].	130
Figure 70. Pressure distribution along the axis of the Ti plate [121].	130
Figure 71. Contours of pressure at planes parallel to the Ti plate at different distances]: 3.9 mm, 66.8 mm, 164.2 mm, and 178.9 mm [121].	131
Figure 72. Evaluation of average sound pressure with distance from Ti plate [121].	132
Figure 73. Contours of pressure at 12.4 mm plane parallel to the Ti plate [121].	133
Figure 74. Mesh sample holder used in the drying experiments with the Ti plate.	134
Figure 75. Comparing the drying curve for a sample dried using solid holder and a sample dried using mesh holder. Ti plate is used for these experiments and the sample is S-R-150-160.	135
Figure 76. Infrared image of the bottom view of the transducer plate (Ti plate).	136
Figure 77. Infrared image of the side view of the transducer plate (Ti plate).	136
Figure 78. The effect of distance from the plate on temperature (Ti plate).	137
Figure 79. The effect of distance from the plate on drying curves for S-R-150-160 sample dried using Ti plate.....	138
Figure 80. Comparing the drying curves for airborne ultrasonic drying (Ti plate) and conductive heating at 40 °C for S-R-150-160.	139

Figure 81. Temperature measurements inside a sandwich sample during airborne ultrasonic drying for S-R-150-325 (Ti plate).....	140
Figure 82. Airborne ultrasonic drying curves for hardwood samples dried using Al plate.....	142
Figure 83. Airborne ultrasonic drying curves for softwood samples dried using Ti plate.	143
Figure 84. Pareto chart of the standardized effects for total time of ultrasonic drying for hardwood samples (dried using Al plate).	144
Figure 85. Pareto chart of the standardized effects for total time of ultrasonic drying for softwood samples (dried using Ti plate).....	145
Figure 86. Pareto chart of the standardized effects for area under the drying curve for hardwood samples (dried using Al plate).	146
Figure 87. Pareto chart of the standardized effects for area under the drying curve for softwood samples (dried using Ti plate).....	147
Figure 88. L^* , a^* , and b^* for hardwood samples, dried using Al plate.....	148
Figure 89. L^* , a^* , and b^* for softwood samples, dried using Ti plate.	148
Figure 90. Comparison of L^* , a^* , and b^* for S-R-150-160 dried using airborne ultrasonic drying (Ti plate) and a similar sample dried using conductive drying.....	149
Figure 91. Comparing the whiteness indices of an ultrasonically dried sample (Ti plate) with a sample dried using conductive heating at 40 °C. The maximum standard deviation is 0.04.	150
Figure 92. Whiteness index of ultrasonically dried hardwood samples (dried using Al plate)..	151
Figure 93. Whiteness indices of ultrasonically dried softwood samples (dried using Ti plate).	151
Figure 94. Comparing stress-strain curves for an ultrasonically dried sample (Ti plate) with a sample thermally dried sample at 40 °C. The maximum standard deviation is 2.4.....	152
Figure 95. Stress-strain curves for (a) unrefined hardwood samples and (b) refined hardwood samples. The samples are dried using Al plate.	153
Figure 96. Stress-strain curves for (a) unrefined softwood samples and (b) refined softwood samples. The samples are dried using Ti plate.	154
Figure 97. Energy factor and drying rate for different hardwood samples (dried using Al plate). Red curve is for drying rate and blue curve is for energy factor.	157
Figure 98. Energy factor and drying rate for different softwood samples (dried using Ti plate). Red curve is for drying rate and blue curve is for energy factor.	158
Figure 99. Illustration of the effect of high moisture content on drying behavior and energy factor for S-R-700-160 (dried using Ti plate).	160
Figure 100. Comparing the drying rate and energy factor for S-R-150%-160g/m ² , dried by direct-contact (left) and non-contact (right) ultrasonic drying (Ti plate). Red curve is for drying rate and blue curve is for energy factor.	161

Figure 101. 2D schematic of the problem in numerical simulation for direct-contact ultrasonic atomization (not to scale).....	165
Figure 102. Oscillating velocity for 1.7 MHz and 0.55 μm amplitude.....	168
Figure 103. A time sequence of an experimental video for atomization at 1.7 MHz excitation frequency and 10 W power.	172
Figure 104. Volume fraction of water for $0.5A_{th}$ amplitude, 3λ liquid height and 1.7 MHz frequency after 1000τ	173
Figure 105. Volume fraction of water at the interface region for $1A_{th}$ amplitude, 3λ liquid height and 1.7 MHz frequency.....	174
Figure 106. Volume fraction of water at the interface region for $1.1A_{th}$ amplitude, 3λ liquid height and 1.7 MHz frequency.....	175
Figure 107. Droplet formation for $1.1A_{th}$ amplitude, 3λ liquid height and 1.7 MHz frequency at different times: (a) 6.62 μs , (b) 6.73 μs , (c) 6.84 μs , (d) 6.95 μs , (e) 7.06 μs , (f) 7.17 μs , (g) 7.24 μs , and (h) 7.35 μs . The colormap is based on the volume fraction of liquid.....	176
Figure 108. Volume fraction of water at the interface region for $1.2A_{th}$ amplitude, 3λ liquid height and 1.7 MHz frequency.....	177
Figure 109. Volume fraction of water at the interface region for $1A_{th}$ amplitude, 0.5λ liquid height and 1.7 MHz frequency.....	178
Figure 110. Volume fraction of water at the interface region for $1.2A_{th}$ amplitude, 50λ liquid height and 1.7 MHz frequency.....	178
Figure 111. Volume fraction of water at the interface region for $1.8A_{th}$ amplitude, 50λ liquid height and 1.7 MHz frequency.....	179
Figure 112. Volume fraction of water at the interface region for $2A_{th}$ amplitude, 50λ liquid height and 1.7 MHz frequency.....	180
Figure 113. Volume fraction of water at the interface region for $2A_{th}$ amplitude, 50λ liquid height and 1.7 MHz frequency.....	181
Figure 114. Secondary droplets formation and droplets' collisions. $2A_{th}$ amplitude, 50λ liquid height and 1.7 MHz frequency. The colormap is based on volume fraction of liquid.	183
Figure 115. Vertical coordinate of the centerpoint of the interface vs time period.	184
Figure 116. Vertical coordinate of the centerpoint of the interface vs time period. $2A_{th}$ amplitude, 50λ liquid height and 1.7 MHz frequency.	185
Figure 117. Velocity of the centerpoint of the interface vs oscillation period. $2A_{th}$ amplitude, 50λ liquid height and 1.7 MHz frequency.	186
Figure 118. Pressure of the centerpoint of the interface vs time period. $2A_{th}$ amplitude, 50λ liquid height and 1.7 MHz frequency.....	187

Figure 119. Volume fraction of liquid at the interface region for $2.2A_{th}$ amplitude, 50λ liquid height and 1.7 MHz frequency.....	187
Figure 120. Volume fraction of liquid at the interface region for $3A_{th}$ amplitude, 50λ liquid height and 1.7 MHz frequency.....	188
Figure 121. Average velocity of interface for different excitation amplitudes.....	189
Figure 122. Volume fraction of water for $2A_{th}$ amplitude, 30λ liquid height and 1.7 MHz frequency.....	190
Figure 123. Volume fraction of water for $2.05A_{th}$ amplitude, 100λ liquid height and 1.7 MHz frequency.....	190
Figure 124. The effect of liquid height on onset amplitude for atomization at 1.7 MHz frequency.	191
Figure 125. The effect of liquid height on capillary wavelength and droplet size at 1.7 MHz frequency.....	193
Figure 126. The effect of surface tension on onset amplitude for atomization at 1.7 MHz frequency and 50λ liquid height.....	194
Figure 127. Onset atomization amplitude vs Weber number at different surface tension values at 1.7 MHz frequency and 50λ liquid height.	195
Figure 128. Onset atomization amplitude vs Ohnesorge number at different surface tension values at 1.7 MHz frequency and 50λ liquid height.	196
Figure 129. The effect of surface tension on droplet size and capillary wavelength at 1.7MHz frequency and 50λ liquid height.....	197
Figure 130. Comparison of the wavelength and atomization rate for two cases of $0.5\sigma_{base}$ and $4\sigma_{base}$ at 1.7 MHz frequency and 50λ liquid height. The colormap is based on liquid volume fraction.	198
Figure 131. The effect of viscosity on onset amplitude for atomization at 1.7 MHz frequency and 50λ liquid height.	199
Figure 132. Comparison of the interface region for two cases with viscosities $0.5\mu_{base}$ and $4\mu_{base}$ at different time steps. The colormap is based on liquid volume fraction.	200
Figure 133. Capillary wave formation for low and high viscous liquids [86].....	200
Figure 134. Onset atomization amplitude vs Reynolds number at different viscosity values at 1.7 MHz frequency and 50λ liquid height.	202
Figure 135. Onset atomization amplitude vs Ohnesorge number at different viscosity values at 1.7 MHz frequency and 50λ liquid height.	203
Figure 136. The effect of viscosity on droplet size and capillary wavelength at 1.7MHz frequency and 50λ liquid height.....	204

Figure 137. The effect of density on droplet size and capillary wavelength at 1.7MHz frequency and 50λ liquid height.....	206
Figure 138. The effect of density on onset amplitude for atomization at 1.7 MHz frequency and 50λ liquid height.	207
Figure 139. Comparison of the interface region for two cases with densities $0.5\rho_{\text{base}}$ and $2\rho_{\text{base}}$ at different time steps. The colormap is based on liquid volume fraction.....	208
Figure 140. Onset atomization amplitude vs Weber number and Reynolds number at different density values at 1.7 MHz frequency and 50λ liquid height.....	209
Figure 141. Onset atomization amplitude vs Ohnesorge number at different density values at 1.7 MHz frequency and 50λ liquid height.	209
Figure 142. Comparison of the wavelength and atomization rate for two cases of 50 kHz and 2MHz frequencies. The colormap is based on liquid volume fraction.	210
Figure 143. The effect of frequency on droplet size and capillary wavelength at 1.7MHz frequency and 50λ liquid height.....	211
Figure 144. The effect of frequency on onset amplitude for atomization at 50λ liquid height. .	212
Figure 145. The effect of gravity on onset amplitude for atomization at 1.7 MHz frequency and 50λ liquid height.	214
Figure 146. Critical Froude number for atomization as a function of Reynolds number at different Weber numbers. Strouhal number for all cases is 20751.....	217
Figure 147. Critical Froude number for atomization as a function of Reynolds number at different Strouhal numbers. Weber number for all cases is 0.0249.....	217
Figure 148. Critical A/H for atomization as a function of Reynolds number at different Weber numbers. Strouhal number for all cases is 20751.	218
Figure 149. Critical A/H for atomization as a function of Reynolds number at different Strouhal numbers. Weber number for all cases is 0.0249.	218
Figure 150. The estimated non-dimensional numbers for the liquids specified in Table 34.....	220
Figure 151. Peak-to-peak measurements for $\lambda_{\text{measured}}$ from simulations for $2A_{\text{th}}$ amplitude, 50λ liquid height and 1.7 MHz frequency.	220
Figure 152. Measured vs calculated (equation (1-2)) capillary wavelengths.	221
Figure 153. Comparison between the measured droplet size vs the predicted droplet size.....	225
Figure 154. Non-dimensional droplet size as a function of Reynolds number at different Weber numbers. Strouhal number for all cases is 20751.	226
Figure 155. Non-dimensional droplet size as a function of Reynolds number at different Strouhal numbers. Weber number for all cases is 0.0249.	227

Figure 156. Comparing the predictions from equation (6-28) developed from the numerical simulations and the calculated droplet sizes from Lang model.	228
Figure 157. Non-dimensional droplet size as a function of Reynolds number at different Weber numbers. Strouhal number for all cases is 20751.	229
Figure 158. Non-dimensional droplet size as a function of Reynolds number at different Strouhal numbers. Weber number for all cases is 0.0249.	230
Figure 159. 2D schematic of the problem in numerical simulation for direct-contact ultrasonic atomization of a water droplet sitting on a vibrating wall (not to scale).	231
Figure 160. Volume fraction of water at 26.10 μ s.	231
Figure 161. 2D schematic of the problem in numerical simulation for non-contact ultrasonic atomization (not to scale).	233
Figure 162. Contours of absolute pressure (Pa) in the domain at different oscillation periods (for 75 μ m amplitude and 21 kHz frequency).	235
Figure 163. Contours of absolute pressure (Pa) in the domain at different oscillation periods (for 75 μ m amplitude and 21 kHz frequency).	236
Figure 164. Volume fraction of water for the case of 75 μ m amplitude, 3λ liquid height and 21 kHz frequency (airborne).	238
Figure 165. Contours of velocity (m/s) for the case of 75 μ m amplitude, 3λ liquid height and 21 kHz frequency (airborne). At 13.33 ms, the velocity at the upper corners of the domain is higher than 41 m/s.	239
Figure 166. Volume fraction of water for the case of 100 μ m amplitude, 3λ liquid height and 21 kHz frequency (airborne).	240
Figure 167. Contours of velocity (m/s) for the case of 100 μ m amplitude, 3λ liquid height and 21 kHz frequency (airborne).	241
Figure 168. Velocity vectors (m/s) at: (a) 4.75 ms, (b) 5 ms, and (c) 5.25 ms for the case of 100 μ m amplitude, 3λ liquid height and 21 kHz frequency (airborne).	242
Figure 169. Model prediction evaluation under different drying conditions.	257

List of Tables

Table 1. Estimated energy use in common industrial processes [1].	29
Table 2. Estimated energy savings by new technologies [1].	31
Table 3. Summary of the developed correlations in the literature for predicting the droplet sizes in ultrasonic atomization. Except Lang’s model, the other correlations are for atomization from a nozzle.	42
Table 4. Operating conditions for the case shown in Figure 6 and Figure 7.	52
Table 5. Different properties and physical dimensions used in the numerical simulations (* specifies the properties for the base case).	71
Table 6. Comparison between the properties of softwood and hardwood pulps.	86
Table 7. Comparison between the properties of refined and unrefined pulps.	86
Table 8. The derived uncertainty for the experimental tests.	87
Table 9. Upper and lower levels of factors for 2 ³ factorial design of experiments for both hardwood (H) and softwood (S). R defines refined and unR defines unrefined.	89
Table 10. ANOVA for total time of drying for hardwood samples.	98
Table 11. ANOVA for total time of drying for softwood samples.	99
Table 12. Coefficients for equation (4-4) calculated from linear regression analysis.	100
Table 13. ANOVA for area under the drying curve for hardwood samples.	101
Table 14. ANOVA for area under the drying curve for softwood samples.	101
Table 15. Ultimate tensile strain and ultimate tensile stress for different samples.	112
Table 16. The derived uncertainty of the experimental data.	125
Table 17. High and low levels of factors for 2 ³ factorial design of experiments for hardwood (H). R defines refined and unR defines unrefined.	127
Table 18. High and low levels of factors for 2 ³ factorial design of experiments for softwood (S). R defines refined and unR defines unrefined.	127
Table 19. Coefficients for equation (5-3) calculated from linear regression analysis.	145
Table 20. Ultimate tensile strain and ultimate tensile stress for different hardwood samples (dried using Al plate).	154
Table 21. Ultimate tensile strain and ultimate tensile stress for softwood samples (dried using Ti plate).	155

Table 22. Permeability measurements for non-contact ultrasonically dried hardwood samples (Al plate).	155
Table 23. Permeability measurements for non-contact ultrasonically dried softwood samples (Ti plate).	156
Table 24. Correlation for drying rate of different samples (dried using Ti plate) obtained using curve fitting. For simplicity, DBMC is shown as x . R^2 for all the correlations is 0.99.	159
Table 25. Dimensionless parameters for governing equations.	166
Table 26. Properties of liquid and air for the base case study at 1.7 MHz frequency.	170
Table 27. Non-dimensional numbers for different liquid heights.....	192
Table 28. Non-dimensional numbers for different values of surface tension.....	195
Table 29. Non-dimensional numbers for different values of liquid viscosity.	201
Table 30. Non-dimensional numbers for different values of liquid density.	207
Table 31. Non-dimensional numbers for different values of exciting frequency.	212
Table 32. Non-dimensional numbers for different values of gravity.....	214
Table 33. Non-dimensional numbers for different thermophysical properties of liquid and frequencies.	216
Table 34. Non-dimensional numbers for water, cow's milk, and sunflower oil.	219
Table 35. Comparing the measured droplet sizes with Lang model [73] for various parameters.	222
Table 36. Measured droplet sizes and their distributions using ImageJ.	223
Table 37. Geometrical dimension for the base case studied for airborne ultrasonic atomization at 21 kHz frequency.....	234
Table 38. Semi-theoretical and empirical models applied to ultrasonic drying curves from Inyang et al. [140].	253
Table 39. Empirical kinetic models: calculated model parameters.	255
Table 40. Kinetic models prediction evaluation (R^2 , RMSE, and PE).	256

Nomenclature

a	area (m^2)
A	amplitude (m)
b	sample thickness (m)
c	velocity of sound (m/s)
c_p	heat capacity (J/K)
D	droplet size (m)
D_m	mass diffusion coefficient (m^2/s)
E	internal energy (J)
f	frequency (Hz)
f'	surface wave frequency (Hz)
F	force (N)
g	gravity (m/s^2)
h	enthalpy (J)
H	liquid height (m)
h_{fg}	latent heat of evaporation (J/kg)
J	diffusion flux ($\text{kg}/(\text{m}^2.\text{s})$)
k	thermal conductivity ($\text{W}/(\text{m}.\text{K})$)
k_m	mass transfer coefficient ($\text{kg}/(\text{m}^3.\text{s})$)
L	length (m)
m	mass (kg)
\dot{m}	evaporation source term ($\text{kg}/(\text{m}^3.\text{s})$)
n	unit normal
P	pressure (Pa)
q''	heat flux (W/m^2)
Q	volumetric flow rate (m^3/s)
r	radial coordinate (m)

S	source term
S_a	average roughness (μm)
S_q	root mean square roughness (μm)
S_z	maximum height of the areal surface (μm)
t	time
T	temperature (K)
u	velocity in x direction (m/s)
U	velocity field (m/s)
v	velocity in y direction (m/s)
x	horizontal coordinate
y	vertical coordinate
Y	mass fraction

Greek symbols

α	volume fraction
β	constant coefficient
ε	porosity
κ	interface curvature
λ	wavelength (m)
μ	dynamic viscosity (kg/(m.s))
ν	kinematic viscosity (m^2/s)
ρ	density (kg/m^3)
σ	surface tension (N/m)
τ	oscillation period (s)
$\bar{\tau}$	stress tensor (N/m^2)
ω	angular frequency (rad/s)

Subscripts

adj_cell	adjacent cell
-------------	---------------

<i>atm</i>	atmosphere
<i>base</i>	base case study
<i>f</i>	fiber
<i>g</i>	gas
<i>h</i>	heat
<i>in</i>	interface
<i>l</i>	liquid
<i>m</i>	mass
<i>onset</i>	onset threshold
<i>ref</i>	reference
<i>sat</i>	saturation
<i>t</i>	time
<i>th</i>	theoretical
<i>v</i>	vapor

Dimensionless numbers

a^*	red-greenness index
b^*	yellow-blueness index
β	non-dimensional density number
	$\beta = \frac{(\rho_l + \rho_g)}{\rho_g}$
ΔE	color index
Fr	Froude number
	<i>conventional:</i> $\frac{U^2}{gh}$
	<i>modified:</i> $Fr = \frac{A\omega}{\sqrt{gh}}$
L^*	lightness index
N_{In}	$N_{In} = \frac{f^2 A^4}{cQ}$

N_{Oh}		$N_{Oh} = \frac{\mu}{fA^2\rho_l}$
N_{We}		$N_{We} = \frac{fQ\rho_l}{\sigma}$
Oh		Ohnesorge number $Oh = \frac{\sqrt{We}}{Re}$
Re		Reynolds number
	<i>conventional:</i>	$\frac{\rho_l U h}{\mu}$
	<i>modified:</i>	$Re = \frac{\sqrt{gh}h}{v}$
St		Strouhal number $St = \omega \sqrt{\frac{h}{g}}$
We		Weber number
	<i>conventional:</i>	$\frac{\rho_l U^2 h}{\sigma}$
	<i>modified:</i>	$We = \frac{\rho_l (gh)h}{\sigma}$
WI		whiteness index

Abbreviations

Al	aluminum
$ANOVA$	analysis of variance
$CARD$	Center for advanced research in drying
CFD	computational fluid dynamics
$DBMC$	dry basis moisture content
DF	degree of freedom
DOE	Department of energy
EF	energy factor

<i>H</i>	hardwood
<i>LP</i>	load power
<i>MassCEC</i>	Massachusetts clean energy center
<i>MS</i>	mean square
<i>NBHK</i>	northern bleached hardwood kraft
<i>NMR</i>	nuclear magnetic spectroscopy
<i>NBSK</i>	northern bleached softwood kraft
<i>PIV</i>	particle image velocimetry
<i>R</i>	refined
<i>S</i>	softwood
<i>SAW</i>	surface acoustic wave
<i>SD</i>	standard deviation
<i>SS</i>	sum of squares
<i>TAD</i>	through air drying
<i>Ti</i>	titanium
<i>unR</i>	unrefined
<i>UTS</i>	ultimate tensile strength
<i>VOF</i>	volume of fluid

Acknowledgments

First and foremost, I would like to express my sincere gratitude and appreciation to my Ph.D. advisor, Professor Jamal Yagoobi, for his academic guidance and enthusiastic encouragement throughout my research. He trusted me and encouraged me to determine appropriate solution methodologies to organize research findings.

I am extremely grateful to my co-advisor, Professor Burt Tilley, for his continuous guidance and encouragement throughout my Ph.D. program. He has taught me how to look at the problems from a different point of view and I feel fortunate to have had a chance to work with him.

I would like to express my deepest appreciation to Professor Aswin Gnanaskandan, Professor Juan Rodriquez Ramirez, Dr. Ken Jewett, and Professor Yuxiang Liu (Graduate Committee Representative) for taking the time to serve on my Ph.D. committee. Also, Professor Aswin Gnanaskandan, through our collaborative research efforts, taught me how to approach a research problem and I am extraordinarily grateful for his insight, knowledge, and support.

I am forever indebted to my family who has always supported my effort, encouraged me, and believed in me. Without their support in all aspects, I would not be where I am today.

I am immensely grateful for my loving husband, Nathaniel J. O'Connor, whom I met and married to during my Ph.D. program. I am thankful for his unconditional love and unwavering support that has made the path much easier for me.

I would like to also give a special thanks to the O'Connor family who has supported me and welcomed me to their family.

I would like to document my immense gratitude to three of the important people during my Ph.D. program: Patricia Howe, Stuart Howe, and Lawrence Riley. They have always gone above and beyond in supporting me.

I would like to extend my gratitude to all the faculties at WPI especially the ones I worked with closely as teaching assistant including Professor Selcuk Guceri, Professor John Sullivan, and Professor Cosme Furlong.

Special thanks to all my colleges in the Center for Advanced Research in Drying (CARD) and Multi-Scale Heat Transfer (MHT) lab and all my friends at WPI for their encouragement and company.

My appreciation to all the staff at WPI is immeasurable for their support including and not limited to: Dr. Siamak Najafi, Dr. Adriana Hera, Ms. Patricia Howe, Ms. Payton Wilkins, Ms. Statia Canning, Ms. Barbara Edilberti, Ms. Barbara Furhman, Mr. Raymond Ranellone, Mr. Fredrick Brokaw, Mr. Peter Hefti, Mr. James Loisselle, Mr. Ian Anderson, Dr. James Kingsley, Dr. Ermal Toto, Ms. Diane Poirier, Dr. James Eakin, Mr. Lawrence Riley, and Mr. John F. Kennedy.

I would like to thank all the members of the Center for Advanced Research in Drying for their technical feedback on my research, especially Dr. Mark Lippi, Mr. David Turpin, Ms. Lindsey Clifton, Dr. Ken Jewett, and Mr. TJ Green.

At last, but not least, I thank Dr. Fei Xia, my mentor during my internship at Mondelez International, for his advises on how to be a good researcher in industry.

This project is financially supported by the U.S. Department of Energy (DOE), Office of Advanced Manufacturing under Award Number DE-EE0009125, Massachusetts Clean Energy Center (MassCEC), and the Center for Advanced Research in Drying, a U.S. National Science Foundation Industry/University Cooperative Research Center. CARD is located at Worcester Polytechnic Institute and University of Illinois at Urbana-Champaign (co-site). The pulps used in this study were provided by Domtar and I appreciate this.

Zahra Noori O'Connor

Worcester Polytechnic Institute

January 2023

Dedicated to my dad's spirit and my loving mom

Abstract of the Dissertation

Fundamental Understanding of Removal of Water from a Moist Porous Medium in the Absence and Presence of Ultrasound Mechanism

by

Zahra Noori O'Connor

Ph.D. Candidate

Department of Mechanical Engineering

Worcester Polytechnic Institute, 2023

Research Advisor: Dr. Jamal S. Yagoobi

Research Co-Advisor: Dr. Burt S. Tilley

In energy-hungry industry sectors such as papermaking, food processing, chemicals, or pharmaceuticals, the main challenge is to improve the energy efficiency of the process. For example, in the fabrication of paper, a slurry with cellulose fibers and other matter is drained, pressed, and dried. The latter step requires a considerable energy consumption. Therefore, improving the current drying technologies as well as developing novel and more efficient drying technologies is essential in the related industries. In the structure of wet paper, there are two different types of water: free water and associated/bound water. Free water can be easily removed. However, removing bound water consumes a large amount of energy during the process. Bound water is mainly defined as the water inside the nanopores of the product. The intermediate region, i.e., the transition from free water removal to bound water removal, is not studied in the literature. One of the main goals of this dissertation is to improve the energy efficiency of the current drying technologies and understand the dominant mechanisms in paper drying. Study of the bound water removal is out of the scope of this research. The focus is on the intermediate stage of drying, where the remaining free water is either present on the surfaces of the fibers in the form of a liquid film or the water is trapped inside the cellulose fibers. For this purpose, first the physics of removing a thin liquid film trapped between fibers in the paper drying process is explored. In this conjugate

heat transfer problem, the film is assumed to be incompressible, viscous, and subject to evaporation, thermo-capillarity, and surface tension. By using a volume of fluid (VOF) model, the effect of above-mentioned parameters on drying behavior of the thin film is investigated. Second, a single cellulose fiber is considered, heated from its outer surface with the water removed from the two open ends of the fiber. The effect of different parameters on the removal of the trapped water is studied. These parameters encompass applied heat flux, water properties (including surface tension), fiber surface properties, geometry, and the dimensions of a given fiber in micro-scale. The governing transport equations, along with the corresponding boundary conditions are solved numerically using VOF method. Using the temperature measurements, the heat flux in the dynamic three-phase vapor/water/fiber contact line is studied. The effect of impurities and Marangoni flows on evaporation is discussed. The results of this research provide fundamental understanding of water removal at the intermediate stage of paper drying.

To help with innovation and electrification of drying/dehydration processes, another main goal of this dissertation is to develop an innovative drying technology that improves the energy efficiency and product quality, significantly in high energy industry sectors such as papermaking. The current drying technique in the papermaking industry is contact drying, which depends on the conductive and/or convective heat transfer. In this study, for the first time, a systematic study is conducted using an innovative technology for paper drying by applying ultrasound mechanism, both direct-contact and non-contact (airborne). Specially, for airborne ultrasound, there are limited information available in the literature. The advantages of ultrasonic drying include greater energy efficiency, lower time and temperature of drying, improvement of the product quality, and it is considered a green and sustainable technology. Hence, fundamental understanding as well as applied analysis are required to help reduce the energy consumption and carbon footprint. For the direct-contact ultrasonic drying, the effects of initial moisture content, final thickness, and refining condition of the pulp are studied for two different types of pulps (hardwood and softwood) using 2^3 factorial design of experiments. The results of Analysis of Variance (ANOVA) show that in the range of the studied parameters in this research, thickness has the maximum effect on the ultrasonic drying time followed by the initial moisture content. In addition, using a linear regression model, two relationships for the total time of drying and the area under the drying curve as functions of the studied factors are provided. The results confirmed that ultrasonic drying is more efficient at

higher moisture contents and higher thickness of the sample. These results are related to the structural characteristics of the samples such as porosity, pore distribution, and surface roughness. Therefore, microscopic images of the surfaces are studied, and the quality of the ultrasonically dried papers is measured using colorimeter analysis and tensile test measurements. For the airborne ultrasonic drying, three controlling factors are considered in the experiments including the initial moisture content, basis weight, and refining condition. The outcome of the experiments is compared to the results for direct-contact ultrasonic drying of paper. The results confirm that similar to direct-contact, for airborne ultrasonic drying, the basis weight/thickness of the sample is the most important factor in ultrasonic drying and it is followed by the effect of initial moisture content. Using linear regression model, two correlations for predicting the total time of airborne ultrasonic drying and the area under the drying curve are provided. Quality of the dried samples are evaluated, and the permeability measurements confirmed the effect of pore characteristics on ultrasonic drying. The analysis for energy consumption reveals that ultrasonic drying is more efficient at higher moisture contents.

To fundamentally understand the physics behind ultrasonic drying, for the first-time ultrasonic atomization of a liquid layer and the mechanism of droplet formation is numerically studied in great details, both in direct-contact and airborne setups. The effect of different controlling parameters and thermophysical properties of the fluid (including frequency, liquid height, surface tension, viscosity, density, and gravity) on the onset amplitude for direct-contact ultrasonic atomization and mean droplet size are investigated. A correlation for predicting the mean droplet size as a function of non-dimensional numbers (including Reynolds number, Weber number, Froude number or the non-dimensional amplitude, and Strouhal number) is provided. Furthermore, the mechanism of ultrasonic atomization for a direct-contact setup is compared to an airborne setup. This dissertation provides a complete package about the potentials of ultrasonic drying, both direct-contact and non-contact mechanisms and gives insights on the methods of improving the process and reducing carbon footprint. In addition, it sheds light on the physics of ultrasonic atomization and optimizing the design of ultrasonic atomizers in terms of cost and efficiency for different applications.

Chapter 1: Introduction

In this chapter, the background and motivations of this research are discussed. The objectives are defined based on the needs of the related industry and for the purpose of (1) to fundamentally understand removal of water at the final stages of drying to improve the current technology and (2) to develop novel non-thermal drying technologies with the goal of increasing the energy efficiency in drying processes and decreasing the carbon footprint.

Drying, defined as water removal from a moist medium, is one of the most energy intensive processes in industrial applications and it plays an important role in global economy. Drying is an essential operation in industries such as chemical, food, agricultural, pulp and papermaking, polymer, ceramics, wood, and mineral processing. Based on the data in Table 1, industrial drying consumes approximately 12% of the total end-use energy used in manufacturing, corresponding to 1.2 quads annually [1]. The forest products industry sector is among the highest energy consuming industry sectors, mainly after the chemicals.

Table 1. Estimated energy use in common industrial processes [1].

Process heating operation	Description/example applications	Typical temperature range (F)	Estimated (2010) U.S. energy use (TBtu)
Fluid heating, boiling, and distillation	Distillation, reforming, cracking, hydrotreating; chemicals production, food preparation	150–1000°	3,015
Drying	Water and organic compound removal	200–700°	1,178
Metal smelting and melting	Ore smelting, steelmaking, and other metals production	800–3000°	968
Calcining	Lime calcining	1500–2000°	395
Metal heat treating and reheating	Hardening, annealing, tempering	200–2500°	203
Non-metal melting	Glass, ceramics, and inorganics manufacturing	1500–3000°	199
Curing and forming	Polymer production, molding, extrusion	300–2500°	109
Coking	Cokemaking for iron and steel production	700–2000°	88
Other	Preheating; catalysis, thermal oxidation, incineration, softening, and warming	200–3000°	1,049
Total			7,204

In papermaking, cellulose fibers are extracted from fibrous raw materials and then converted to pulp [2]. The fibers are normally a mixture of softwood and hardwood fibers with some other fibers such as straw, bamboo, cotton, and chemical fibers blended in with the wood fibers [3]. Then pulp is mixed with water and is placed on the papermaking machine. In papermaking process, the major sections include forming section, press section, and dryer section. In fact, after the drainage of the water by gravity and the applied suction, additional water is removed by mechanical pressure through a series of presses. Most of the remaining water is then evaporated in the dryer section. Removing the water from the wet web to the final moisture content (6-7%) is a critical step of papermaking process and most of the functional properties of paper are developed in this section [4].

As one of the most important components in papermaking, the dryer section has a great impact on the overall energy consumption. Although only 1% of original water is removed in the dryer section, it is still the most expensive and energy intensive unit in papermaking process [5]. The dryer section costs 40% of total capital cost and consumes more than 60% of total energy used in the paper machine [5]. Thus, any improvement in paper drying process may have a significant impact on the energy consumption at the global level. However, an in-depth understanding of transport phenomena within a paper sheet during drying is needed to improve the current drying processes or to develop new innovative technologies. In this research, to fundamentally understand the current drying technologies and the impact of different conditions on drying time, two numerical simulation models are developed which will be discussed in Chapters 2 and 3.

According to Mujumdar [6], energy consumption in drying ranges from less than 5% for chemical processes industries to 35% for the papermaking operations. The current drying technologies are mostly dependent on conduction and convection thermal heating. As reported by the US Department of Energy [1], 0.5 quads/year of total energy in drying processes (1.2 quad/year) can be saved by applying non-thermal drying technologies (Table 2). This could save the industrial drying about \$16B/year. Therefore, it is crucial to develop sustainable and efficient drying technologies to decrease the industrial energy consumption and carbon footprint. In the last few decades, specific attention has been paid to progression of hybrid drying technologies such as ultrasonic drying [7], microwave drying [8], electrohydrodynamic drying [9 and 10], infrared drying [11], plasma drying [12], and pulsed vacuum drying [13], mostly in combination with

heating. As one of the novel low-temperature drying technologies, ultrasonic drying, is explored in this research and its potentials for energy savings and electrification are studied. Ultrasonic drying will be investigated as two mechanisms: direct-contact and non-contact (airborne). Chapter 4 will discuss direct-contact ultrasonic drying of paper and chapter 5 will be devoted to airborne ultrasonic drying of paper. In addition, to fundamentally understand the physics behind ultrasonic drying and ultrasonic atomization, a sophisticated numerical model will be developed and discussed in great details in chapter 6.

Table 2. Estimated energy savings by new technologies [1].

R&D opportunity	Applications	Estimated annual energy savings opportunity (TBTu/yr)	Estimated annual carbon dioxide (CO ₂) emissions savings opportunity (million metric tonnes [MMT]/yr)
Advanced non-thermal water removal technologies	Drying and concentration	500	35
“Super boilers” (to produce steam with high efficiency, high reliability, and low footprint)	Steam production	350	20
Waste heat recovery systems	Crosscutting	260	25
Hybrid distillation	Distillation	240	20
New catalysts and reaction processes (to improve yields of conversion processes)	Catalysis and conversion	200	15
Lower-energy, high-temperature material processing (e.g., microwave heating)	Crosscutting	150	10
Advanced high-temperature materials for high-temperature processing	Crosscutting	150	10
Net-shape and near-net-shape design and manufacturing	Casting, rolling, forging, additive manufacturing, and powder metallurgy	140	10
Integrated manufacturing control systems	Crosscutting	130	10
Total		2,210	155

In the following sections, an introduction for the chapters in this study is provided.

1.1 Transition Region in Paper Drying Curve

A drying process is characterized by its drying curve, which presents the overall moisture content as a function of time. Typical drying curves reveal three different stages, as shown in Figure 1.

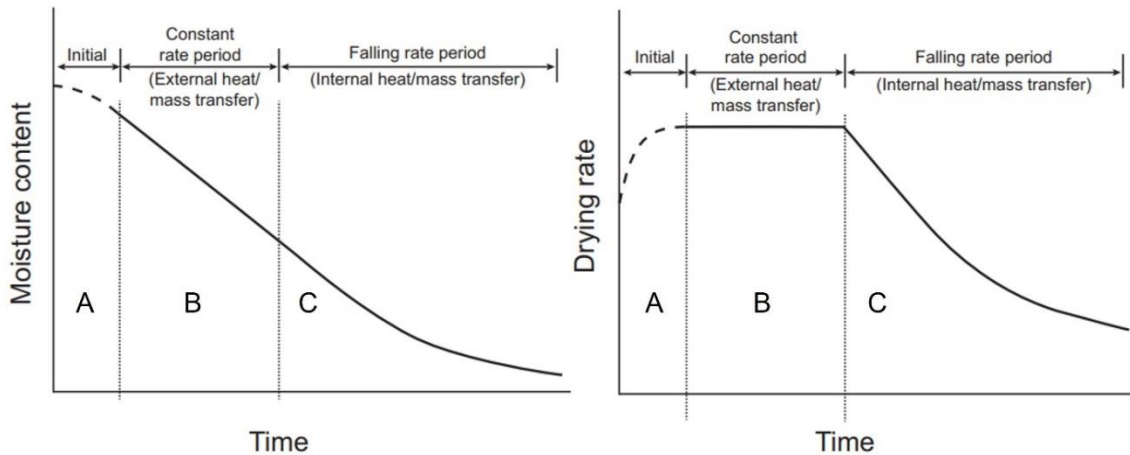


Figure 1. Typical drying kinetics plots: drying curve (left side) and drying rate curve (right side) [14].

The first stage (A) corresponds to a short transient heating. The second stage (B) is marked by a constant drying rate. In the third drying stage (C), the drying rate decreases. The first stage is called “warm-up” period. For paper drying, in the second stage, the majority of the moisture is removed from the paper. While, the third stage displays a significantly lower drying rate, resulting in a longer drying time and larger energy consumption [15]. The moisture within the paper can be classified based on which stage of the drying process the water is removed. In the second stage, *free water* or the water interstitial to the fibers is removed. Removing this water is comparatively easy and most effective. In the third stage, the water removal consists mainly of *associated water* (also known as *bound water*) which includes moisture where capillary forces need to be overcome, along with water that remains bound to the hydrophilic fibers [4, 16]. Removing associated water involves a large amount of energy. The transition between constant rate zone and falling rate zone occurs at a critical moisture content [17]. Topgaard and Soderman in 2002 [18] conducted nuclear magnetic resonance spectroscopy (NMR) experiments on slow drying for hydrated cellulose fiber samples and concluded that the sequence of the water removal for kraft pulp fiber is: (1) bulk water, (2) water in pores in micrometer scale, and (3) water in nanometer size pores. In fact, there is not an agreement about the definition of the bound water [19]. Bound water displays abnormal properties; its vapor pressure is lowered, the dynamic behavior is perturbed and the solution properties are varied [20]. The water bound within the fiber wall has a depressed freezing point compared to that of bulk water due to its location in the small pores within the walls. However,

not all the bound water is able to freeze and a layer of two or three molecules thick in direct contact with the fiber wall does not freeze, even at temperatures well below 0 °C. Therefore, bound water is divided to two types of bound freezing water and bound non-freezing water [21]. According to Park [22], water molecules can interact with cellulose fibers in at least three different ways. First, the water molecules bind to the hydrophilic surfaces through hydrogen bonds. Second, the water is trapped in the cell wall and the small pores. Third, the water molecules that can be absorbed into the fiber walls. Correspondingly, drying the cellulose fibers requires energy both for evaporating the water and also for overcoming the interactions between the cellulose fibers and water. Although there have been many efforts to study bound water transport properties, the chemical states between bound water and the cellulose fiber remains an open question during the drying process. Some of the experimental methods used for this purpose include weighing[23], X-ray computer tomography [24], neutron radiography [25], and NMR images [26-28]. Park et al. [29] categorized different types of water as “easy-to-remove” and “hard-to-remove”. Easy-to-remove water is defined as the true free water whereas hard-to-remove water is the water trapped in the fiber network and all bound water. It was proposed that when the internal diffusion of water to the exposed surface is not fast enough to keep the surface moist, the rate of drying falls. At this point, the drying rate is controlled by the internal diffusion [30]. This transition highly depends on the fiber characteristics including the type, size, and fiber wall thickness.

The predominant method of paper drying is contact drying, which depends on the conductive heat transfer between the moist paper and the surface of heated drums as well as the air that surrounds them. Heat and mass transfer are two mechanisms that are associated in paper drying. The heat transfer aspect of drying is related to the transition of heat through the dryer shell to the wet paper. The removal of the evaporated water vapor from the sheet into the air is related to the mass transfer aspect of paper drying. Therefore, both heat and mass transfer must be considered in the operation of drying section [4].

For drying of tissue paper, a Yankee dryer is the common technology. A Yankee dryer is a pressure vessel with a diameter up to 6 m. In tissue production, only one Yankee dryer is needed. A non-compressive technique for drying tissue is called through air drying (TAD). In TAD, hot air flows through the paper or tissue and evaporates and removes the moisture trapped between the fibers

inside the paper. Determining drying rate curves for TAD, mainly started by Polat et al. [31] in 1992. Chen [32] and Chen and Douglas [33] studied the combination of impingement drying and TAD on the drying rate curve for various grammage, temperatures, and air flow rates. Weineisen [34] studied TAD both experimentally and numerically and concluded that air temperature and pressure drop have significant effects on drying rate curves. Their modeling work showed that the onset of the drying curve depends significantly on the pore size distribution. The effect of fabric structure on TAD is studied by Forughi et al. [35].

The majority of the dry mass in a paper sheet is made of fibers, and, depending on the source, they have different shapes and sizes. Fibers from softwood trees are about 3 mm in length, and the width is in the range of 20-35 μm . While fibers from hardwood trees are typically about 1 mm in length and the width is not as thick. In addition, other factors such as age of the tree, the environment, the season in which the fiber grows, the presence of shade, etc., may have some effects on the properties of the fibers [36]. In papermaking industries, the fibers determine the quality and the properties of the paper [37] such as mechanical strength, opacity, surface smoothness, density, and porosity. Furthermore, different grades of paper have different blends of fiber types. Different fibers with varying properties can show numerous drying behaviors, which can influence the drying process and related energy efficiency. Various experimental methods such as nuclear magnetic resonance pulsed field gradient (NMR PFG) [38] differential scanning calorimetry [30], and high-resolution thermogravimetry [39] have been used to study the drying behavior inside cellulose fibers. However, understanding and exploring the impact of different fiber characteristics on water removal from inside the fibers using experimental methods is very challenging and looking at one single fiber is almost impossible. Although the study of evaporation of water in a single fiber is related to paper drying, the information can be extended to evaporation in a microtube. Microtubes have different applications including in the design of micro-combustors, micro-thrusters, and microturbines. Many studies have been reported the evaporation and heat transfer characteristics in microtubes such as [40-42] and the references in them. The smallest diameter of the tube in these studies is about 0.1 mm and the applied heat flux varies from 400 W/m^2 - 300 kW/m^2 . In most of these studies, the temperature of the liquid at the interface is high enough that boiling occurs. However, in drying of paper fibers, evaporation only occurs at the liquid/gas interface at temperatures lower than boiling point of water.

Stenstrom [43] provided a comprehensive review of research on drying of paper carried out mainly within the past two decades.

1.2 Ultrasonic Drying

As it was mentioned above, one of the most recent developed technologies for drying purposes that has attracted attention in the last few decades is ultrasonic drying. Drying using ultrasound mechanism is not a new idea and to the best of the author’s knowledge, Burger and Sollner [44] were the first to consider removal of water from wet quartz sands using ultrasonic drying, in 1936.

Ultrasound is defined as the acoustic waves with the frequencies higher than the upper limit of the human hearing range, usually around 16 - 20 kHz. These ultrasonic waves can be classified based on their frequency and power. Waves with 20 - 100 kHz frequencies are defined as “low frequency ultrasound” or “power ultrasound”. The power level for these frequencies is usually high and in the range of a few tens of Watts. Ultrasound waves with frequencies higher than 1 MHz are called “low power ultrasound”. The power for this ultrasound is usually less than 10 W. The intermediate range 100 kHz – 1 MHz is “high frequency ultrasound” [45]. Figure 2 shows typical use of ultrasound according to frequency and power.

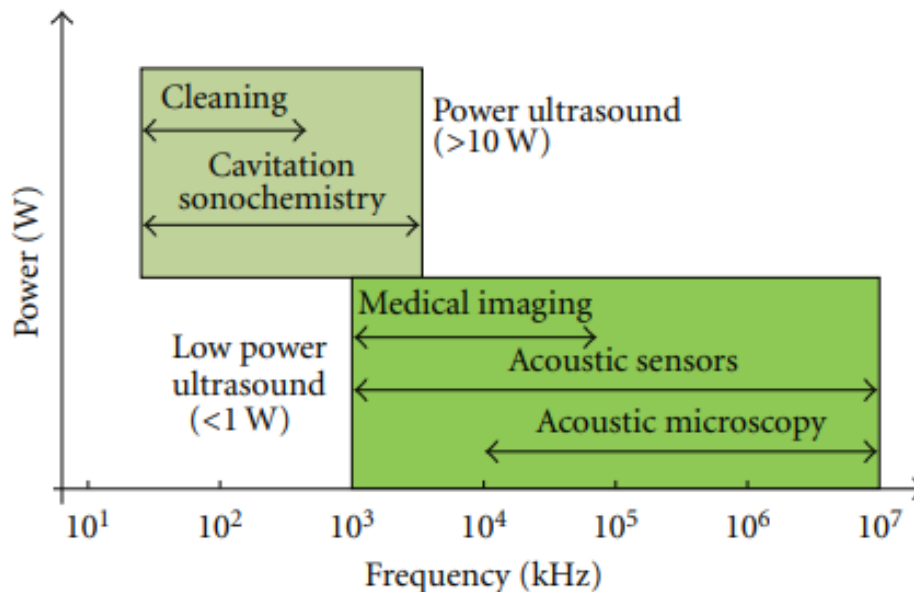


Figure 2. Utilization of ultrasound according to frequency and power [45].

Vibrations in the range of ultrasonic wave frequencies have the excellent characteristic of transporting the energy to a great distance in the liquid phase without great dissipation. Ultrasonic waves have chemical and mechanical effects [46] and experiments have shown that ultrasound vibrations represent the effects such as acoustic streaming, thermal effects, cavitation, and atomization (nebulization), as shown in Figure 3. The effects of ultrasound depend on many factors, including specific drying condition, the nature of the material to be dried and the ultrasonic equipment; and the mechanism may vary significantly [47]. For instance, Peng et al. [48] reported that at high moisture contents, ultrasound induces acoustic nebulization and below a given initial moisture content, ultrasound tends to just generate heat.

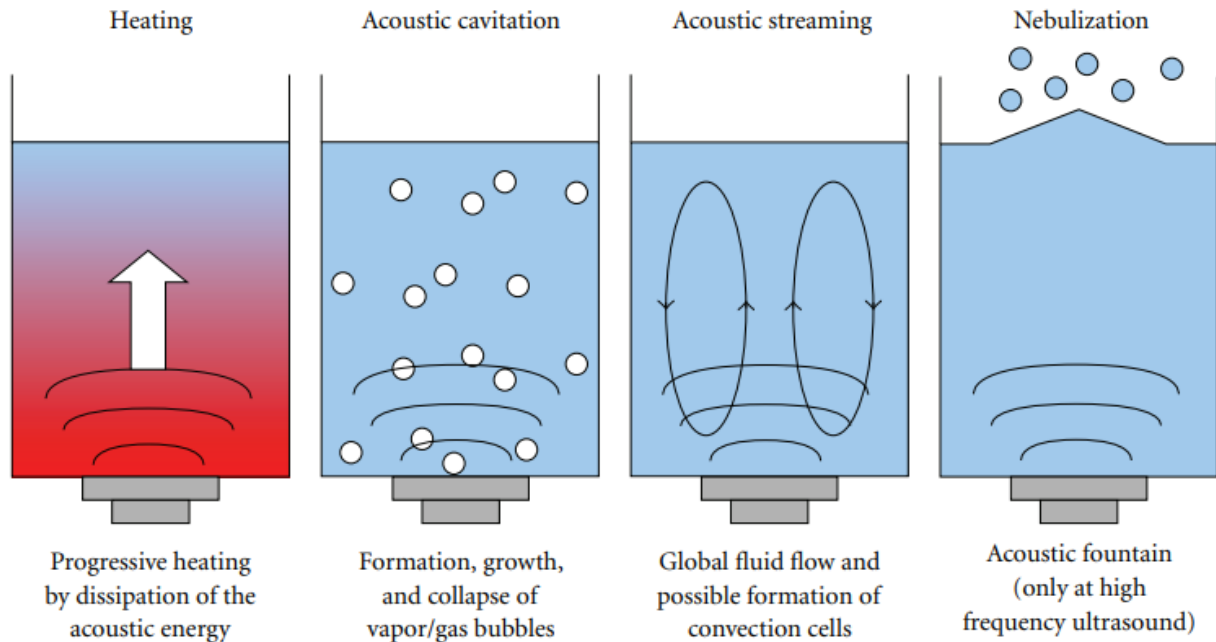


Figure 3. Four effects resulting from ultrasound propagation in a liquid [45].

Many studies have been devoted to the application of ultrasound assisted drying in three different ways: pretreatment, direct-contact, and airborne (non-contact). In ultrasonic pretreatment, the materials get immersed in an ultrasonic bath prior to drying to reduce the drying time [49]. Direct-contact ultrasonic drying requires the material to be in direct contact with the vibrating structure and it uses high-frequency ultrasound waves which can be higher than 1 MHz. According to Gallego-Juarez et al. [50], direct-contact ultrasound efficiently enhances the sound energy transfer

from the transducer to the materials. This technology most recently was used for fabric drying [51] by the researchers at Oak Ridge National lab. For non-contact or airborne ultrasonic drying, the ultrasonic waves travel to the material through air, and it uses high-power waves that are in the range of 20-100 kHz. Ultrasonic drying has different applications including food conservation industries [52-57] and fabric drying [58 and 59]. Ultrasonic drying has widely shown effectiveness on enhancing the drying processes including freeze-drying, hot air drying, vacuum drying, and fluidized bed drying. This mechanism has potentials in decreasing the drying time, enhancing the energy efficiency, and preserving the quality of the dried product [47]. Specifically, in the beginning of the new century, researchers have become more interested in investigating this drying technology [60-62].

The dominant mechanism in ultrasonic drying of porous media is inducing atomization. Atomization helps in mechanically removing of the moisture content in the form of mist, separating water from the porous material without thermal evaporation and thus, largely saving time and decreasing the energy consumption. Momen et al [51] reported significant impacts of the atomization on reducing drying time from hours to seconds and reducing energy consumption of the unit by an order of magnitude. Atomization helps in enabling high energy transfer efficiency from the transducer to the materials. On the other hand, the disadvantages of acoustic atomization are inducing thermal effects and requiring the presence of an important amount of bulk liquid, which limit the application of this drying technology [47]. More information about ultrasonic drying can be found in the review paper by Zhang and Abatzoglou [47].

Fairbanks [63] compared two cases of drying of wet coal particles: (1) in direct contact with the vibrating surface and (2) using non-contact ultrasound. It appeared that the effectiveness of ultrasonic drying was much higher in the direct-contact ultrasonic drying. Another observed difference between these two drying cases was that the effect of heating in direct-contact ultrasonic drying is much higher than non-contact ultrasonic drying. Tao et al. [64] compared airborne ultrasonic drying and contact ultrasonic drying to intensify air drying of blackberries and they reported that in the presence of ultrasound, the drying process was accelerated, the energy consumption was reduced and retention of organic acids in blackberries was enhanced. Zhang and Abatzoglou [47] stated two challenges related to direct-contact ultrasonic drying: First, the heating effect may not be desirable in terms of the quality of the dried products. Second, since the product

must be in direct contact with the transducer, this technology is not easily adaptable to the current convective dryers. Hence, in this regard, non-contact ultrasonic drying is the most ideal in terms of adaptation to the conveyer dryers. However, these technologies have not been employed for paper drying and no systematic research can be found in the literature, studying the effect of different parameters on drying rate and energy efficiency.

1.3 Ultrasonic Atomization

Ultrasonic atomizers use high-frequency vibrations produced by piezoelectric transducers to create fine liquid droplets. As it was mentioned above, the propagation of ultrasonic waves into a liquid results in a series of complex effects including acoustic streaming, heating, acoustic cavitation, and atomization, to name a few. These effects help in enhancement of both external and internal transport phenomena. Among these phenomena, acoustic atomization, also known as nebulization, is the production of fine mist from the liquid surface with a narrow droplet size distribution. This phenomenon was first reported by Wood and Loomis [65] in 1927 for liquids such as benzene, water, and heavy transformer oil. Compared to the conventional nozzles that use a high shear to atomize liquid, ultrasonic atomization has the advantage of producing smaller droplet size (in the range of micrometer to tens of micrometer), narrower size distribution, simplicity of equipment, and controllable atomization rate [66]. Ultrasonic atomization is widely used in many industrial applications such as combustion of fuels [67], porous media drying [68], spray drying [69], spray cooling [70], intensifying the microencapsulation process [71], in humidifiers, and for miniature carriers in pharmaceutical applications [72].

There are two proposed hypotheses for the mechanisms of droplet formation during ultrasonic atomization [48 and 67]: cavitation hypothesis and capillary wave hypothesis. According to capillary wave hypothesis, that was first proposed by Lang [73] in 1962, in a vertically vibrating liquid film, ultrasound generates capillary waves at the liquid-gas interface, and at certain oscillation intensities, the interface becomes unstable, which then atomizes the liquid to form a fine mist. On the other hand, acoustic cavitation hypothesis, that was first suggested by Sollner [74] in 1936, refers to the acoustic bubbles induced by ultrasound, which only occurs in liquid medium. According to this theory, atomization happens through the hydraulic shocks generated by the implosion of cavitation bubbles, especially near the interface of liquid and gas. Perron [75]

reported that large vibrational amplitudes can cause cavitation due to the agglomeration of the bubbles. According to Zhang and Abatzoglou [47], the threshold of sound intensity for appearance of cavitation bubbles is very high and there is no evidence to show the existence of cavitation in ultrasonic dehydration. Therefore, at onset amplitude for atomization, it is unlikely to have cavitation.

Capillary wave theory became of great interest in the middle of 20th century. The capillary surface waves studies are derived from Faraday's instability, which was proposed in 1831 [76]. According to Faraday's instability, the unstable capillary waves are formed at the gas/liquid interface and the collapse of these unstable waves leads to formation of small droplets. Strutt and Rayleigh [77] proposed a correlation between the capillary wavelength, frequency, and liquid/air surface tension. They used this correlation to determine the surface tension of a liquid from the observed surface capillary wavelength. Kelvin derived an equation between the capillary wavelength (λ) and wave frequency (f') and their relationship to the working liquid properties as follows [73]:

$$\lambda = \left(\frac{2\pi\sigma}{\rho_l f'^2}\right)^{1/3} \quad (1-1)$$

where σ is surface tension and ρ is density of liquid. Faraday [76] empirically observed that the capillary surface wave's frequency is half of the exciting frequency (f) for low frequency ranges and argued that the behavior was much like the oscillation of a pendulum. Therefore, capillary wavelength can be calculated as:

$$\lambda = \left(\frac{8\pi\sigma}{\rho_l f^2}\right)^{1/3} \quad (1-2)$$

Qi et al. [78] used scanning laser Doppler vibrometer and high-speed flow visualization to measure the capillary wave frequency and capture the interfacial destabilization process for surface acoustic wave (also known as SAW) atomization at 10-40 MHz frequency. The authors reported that the frequency of the vibrations for the capillary waves at interface is much smaller than half of the exciting frequency and it is in the same order of magnitude as the capillary viscous resonance frequency, which is contrary to the subharmonic half-excitation frequency relationship. This behavior has not been explored in lower range of MHz (1 - 2 MHz) frequencies in the literature.

Benjamin and Ursell in 1954 [79] presented the linear stability of Faraday waves for inviscid fluids and their study was followed for viscous fluids by Kumar and Tuckerman [80]. The non-linear dynamics of Faraday waves have been studied analytically by many researches such as [81 and 82]. Most analytical analysis such as [83] assumed that the droplets are formed periodically from the crests of an orderly pattern of standing capillary waves, with a wavelength that can be related to the frequency by stability analysis. However, after formation of droplets, the orderliness of the capillary wave pattern is lost and the ejection of droplets becomes very random [84]. Several researchers have experimentally investigated the ejection of droplets due to vertical vibrations [84-89] at different range of frequencies. Yule and Suleimani [84] investigated the water droplet formation by using high-speed imaging techniques and a low frequency vibrating film at 300 Hz. The authors claimed that high frequency atomizers can show the same behavior as the low frequency and therefore, their observations can be extended for high frequency vibrations. Recently, Zhang et al. [87] employed laser diffraction and Particle Image Velocimetry (PIV) to investigate the droplet size distribution during ultrasonic atomization for water, glycerol, and sodium dodecyl sulfate at 36 kHz. Tsai et al. [90] studied the atomization from a water droplet at 1 MHz frequency and monitored the brightness of the water droplet during atomization. They related the brightness of the water droplet to the onset threshold for droplet ejection. However, they were not able to see the details of the Faraday waves on the surface of the droplet. Despite the advancements of the technologies, there are practical limitations on camera speed in capturing the details especially at high frequency ultrasonic cases. The most important evidence generated from contemporary photographic study is clear sequences of still photos showing the detachment of droplets from the tips of surface waves [91]. In addition, not only the ejections are fast that high frame rates are required to capture the motion of the droplet, but also due to the motion of the ejected droplet, it can go out of the field of view during atomization [78]. This is especially more challenging at high frequency ultrasonic atomization because even at modest frequencies, the length and time scales are extremely short. Hence, computational fluid dynamics (CFD) has become an essential tool in understanding the phenomena at microscales. Ehrhorn and Semke [91] developed a numerical simulation for modeling the Faraday instabilities on the free surface of water induced by vibrations at 300 Hz. The results of their numerical modeling were qualitatively in agreement with the available experimental results in the literature. Song et al. [92] studied the

capillary surface wave onset amplitude under a vertical sinusoidal oscillation in a horizontal water tank. The frequency was 500 kHz and the vibrational wavelength was 19.3 μm . The liquid height and the tank width were set as six times and thirty times larger than the vibrational wavelength, respectively. In their Finite Element simulation, the tank was filled with water, and they found that the critical vibrational amplitude is 0.38 μm , in which the formation of the Faraday waves was noticeable. However, in their study, they did not consider the instabilities and the motions at the interface of the two-phase problem or neither studied droplet ejection.

Apart from understanding the mechanism of ultrasonic atomization, control of the droplet's size characterization is very crucial in obtaining a product with the desired quality. Lang [73] was the first to claim that the droplet size is directly proportional to capillary wavelength and a correlation for approximating the mean diameter of the ejected droplets (D) was proposed as follows:

$$D = 0.34\lambda = 0.34\left(\frac{8\pi\sigma}{\rho_l f^2}\right)^{1/3} \quad (1-3)$$

The constant in this equation was experimentally obtained via an experiment, in which a molten liquid wax was atomized at 10 - 800 kHz frequencies and the generated droplets were rapidly cooled in air. The size of the solid particles was then measured. Although, this correlation considers the effect of surface tension, density, and frequency on the droplet size, the effect of viscosity is not included in this equation, which is contrary to the experimental observations. Further, Rajan and Pandit [93] by introducing the non-dimensional numbers, proposed a correlation for droplet size and added the amplitude of ultrasonic vibration (A) and viscosity of the liquid (μ). This equation is given as follows:

$$D = \left(\frac{\pi\sigma}{\rho_l f^2}\right)^{1/3} [1 + AN_{We}^{0.22} N_{Oh}^{0.166} N_{In}^{-0.0277}] \quad (1-4)$$

where N_{We} is the Weber number (the ratio of aerodynamic forces to surface tension forces), N_{Oh} is the Ohnesorge number (the ratio of the internal liquid viscosity to surface forces), and N_{In} is the Intensity number (based on ultrasound intensity). These numbers are defined as follow:

$$N_{We} = \frac{fQ\rho_l}{\sigma} \quad (1-5)$$

$$N_{Oh} = \frac{\mu}{fA^2\rho_l} \quad (1-6)$$

$$N_{In} = \frac{f^2 A^4}{cQ} \quad (1-7)$$

Where Q is volumetric flow rate of liquid and c is velocity of sound in liquid.

Other authors [85-88, 94] have applied this use of non-dimensional numbers and developed additional correlations for various ranges of controlling parameters. Table 3 represents a summary of these correlations.

Table 3. Summary of the developed correlations in the literature for predicting the droplet sizes in ultrasonic atomization. Except Lang's model, the other correlations are for atomization from a nozzle.

Reference	Correlation	Range of variables	R ²
Lang, 1962 [73]	$D = 0.34 \left(\frac{8\pi\sigma}{\rho f^2} \right)^{1/3}$	$f = 10 - 800$ kHz synthetic or paraffin wax	
Rajan and Pandit, 2001 [93]	$D = \left(\frac{\pi\sigma}{\rho f^2} \right)^{0.33} [1 + 0.1 N_{We}^{0.22} N_{Oh}^{0.166} N_{In}^{-0.0277}]$	$f = 54$ kHz $A = 2.02-3.78$ μm $Q = 2.16-27.6 \times 10^{-8}$ m^3/s	
Avvaru et al., 2006 [86]	$D = \left(\frac{\pi\sigma}{\rho f^2} \right)^{0.33} + 0.0013 N_{We}^{0.088} N_{Oh}^{-0.14} N_{In}^{0.28}$	$f = 20$ and 40 kHz $Q = 1.04-7.5 \times 10^{-7}$ m^3/s $\mu = 0.01-0.66$ $\text{N.s}/\text{m}^2$	
Barba et al., 2009 [94]	$D = 0.058 \left(\frac{\pi\sigma}{\rho f^2} \right)^{0.33} N_{We}^{0.151} N_{Oh}^{0.192} N_{In}^{-0.02}$	$f = 20$ kHz alinate solution (1, 2 and 3% w/w) $Q = 0.1-0.6$ mm^3/s	0.91
Ramisetty et al., 2013 [85]	$D = 0.00154 \left(\frac{\pi\sigma}{\rho f^2} \right)^{0.33} [1 + N_{We}^{0.154} N_{Oh}^{-0.111} N_{In}^{-0.033}]$	$f = 20-130$ kHz $Q = 0.5-5 \times 10^{-7}$ m^3/s $\rho = 912-1151$ kg/m^3 $\sigma = 0.029-0.073$ N/m $\mu = 0.00089-0.088$ $\text{N.s}/\text{m}^2$ $I = 15907-913752.9$ W/m^2	0.91
Zhang et al., 2021 [87]	$D = \left(\frac{\pi\sigma}{\rho f^2} \right)^{0.33} + 0.0026 N_{We}^{0.0124} N_{Oh}^{-0.0173} N_{In}^{0.1544}$	$f = 36$ kHz $\rho = 900.3-1223$ kg/m^3 $\sigma = 0.011-0.07275$ N/m $\mu = 0.001-0.030$ $\text{N.s}/\text{m}^2$	0.85

These correlations are developed for the case of nozzles that the liquid enters the ultrasonic atomizer at a known flow rate and consequently, they are not valid for droplets generated from a liquid film on top of an ultrasonic vibrator. These correlations are also mostly obtained for a single frequency and therefore, the effect of frequency on ultrasonic atomization has not been well established. In addition, the studied frequencies are in the low ultrasound frequencies range (less than 150 kHz), which may not be applicable at high frequencies. Furthermore, the effect of liquid height is not considered in these studies. CFD simulation as a powerful tool, enables us to

investigate the effect of different parameters on the droplet size as well as capturing details that are impossible or difficult to capture in the experiments. These details include breakup of the generated droplets to form secondary droplets or collision of the droplets. According to Chen and Yang [95], the droplet collisions have four different categories: bouncing, coalescence, separation, and shattering. In the case that the relative velocity of the two droplets is not sufficient to overcome the resistance of the thin gas film between the impact surfaces, bouncing occurs. The reversed motion caused by the recovery of deformed shapes drives the droplets apart. When two droplets contact and permanently merge into a single droplet, coalescence occurs. If the merging is temporary followed by the formation of liquid ligaments, separation happens and as a result the droplet eventually breaks into two or more droplets. In a condition that the two droplets collide at high speed and a thin liquid film is formed by the impact of the droplets, shattering occurs, and small droplets emerge from the sheet boundary. Observing these events in the experiments requires high-speed camera with high resolutions and hence, is not elucidated clearly yet.

1.4 Motivations and Objectives

The United Nation adopted the 17 Sustainable Development Goals (SDGs) by 2030 as a universal call including “industry, innovation, and infrastructure”, as well as “responsible consumption and production” [96]. The motivations for this thesis come from the fact that drying of porous media such as paper consumes a large amount of energy in industrial manufacturing. Improving the current technologies or developing more innovative and energy efficient techniques is very essential to decrease the energy consumption. This research has the goal of contributing to the reduction of energy consumption and greenhouse gas emissions, putting humanity on a path to a more sustainable and green future.

The following main objectives for this project are established to achieve the above goal:

- 1- To fundamentally describe the physics of the drying process in the intermediate stage, from free water toward bound water, where the remaining free water is present on the exterior surfaces of fibers in the form of a liquid film (Chapter 2).
- 2- To investigate the effect of controlling parameters on removal of water trapped inside a single cellulose fiber (Chapter 3).

- 3- To develop direct-contact ultrasonic drying mechanism for porous media including paper drying and investigate the structural characteristics and quality of the ultrasonically dried samples (Chapter 4).
- 4- To conduct experiments for porous medium drying with airborne ultrasound mechanism to reduce the energy consumption in the drying process and to explore the potentials of this technology (Chapter 5).
- 5- To develop a numerical model for simulating ultrasonic atomization and to search the possibilities of improving ultrasonic drying process and optimizing ultrasonic atomizers (Chapter 6).

Regardless of a large volume of theoretical and numerical works conducted in the field (e.g., see [97 and 98]), there is still no clear basic understanding of removal of water at the final stages of drying process, as the transition region from free water removal toward bound water removal. Thus, chapters 2 and 3 of this research are devoted to fundamentally understand the dominant mechanisms and transport phenomena in the transition region in paper drying curve. In Chapter 2, the main objective is to fundamentally describe the physics of water removal, where the remaining free water is present on the exterior surfaces of fibers as a liquid film. For this purpose, a multiphysics numerical model will be developed using VOF method.

Chapter 3 is assigned to study of removal of water trapped inside a single cellulose fiber in micro-scale. Numerical simulation techniques are employed to investigate the effect of different characteristics of fiber on removal of water and provide new insights on this matter. Softwood cells are closed at each end and the radial face of each cell is perforated with many tiny openings (pits). However, hardwood cells are open at the ends and are free of pits on the transverse walls. The study of water removal from pits in nano-scale is out of the scope of this research due to high values of Knudsen number, which implies that continuum does not apply. Thus, this study is considering the drying behavior of water trapped inside hardwood fibers under different conditions.

To the best of the author's knowledge, ultrasonic drying has not been used for paper drying. Chapter 4 provides an in-depth investigation about different aspects of direct-contact ultrasonic drying of paper hand-sheets. Paper samples offer the ability to explore the impacts of porous media

of different characteristics, via wood-type and refinement condition, allowing the work to provide insight into the general applications of ultrasonic drying in porous media. Chapter 5 investigates the potentials of ultrasonic drying in a non-contact ultrasound setup, experimentally. The goal is to understand the effect of airborne ultrasonic drying for porous media such as hand-sheet papers. The outcome of this research is compared with the direct-contact ultrasonic drying of paper in terms of heating effects, drying rate, final product quality, and energy efficiency. Using design of experiments and analysis of variance, the effects of initial moisture content, basis weight/thickness, and refining condition of the pulp for both hardwood and softwood are studied and two correlations for predicting the total time of ultrasonic drying and the area under drying curve are proposed. The most important take aways from these two chapters are the energy efficiency analysis, the drying rates, and the comparison between the two mechanisms in terms of advantages and drawbacks.

In order to explore the mechanism of ultrasonic drying, chapter 6 aims to understand the physics behind ultrasonic atomization and attempts to bridge a knowledge gap in the understanding of ultrasonic oscillatory two-phase flow transport behavior under various operating conditions at a wide range of frequencies (50 kHz – 2 MHz). Since a greater challenge arises from studying high frequency ultrasonic waves due to smaller wavelengths and time scales, CFD simulations are employed, and the results are compared to the available data in the literature. The mechanism of ultrasonic atomization for a thin liquid film, rather than a single liquid droplet, is described in detail, the effect of various controlling parameters and thermophysical properties of liquid on atomization is discussed, and a correlation for predicting the droplet size as a function of non-dimensional numbers is proposed. To the best of the author's knowledge, this is the first time to determine the onset ultrasonic atomization amplitude as a function of controlling parameters including surface tension, viscosity, density, liquid height, and frequency. The differences in the mechanism of ultrasonic atomization for direct-contact and airborne setups are also discussed in detail.

Chapter 2: Fundamental Understanding of Removal of Liquid Thin Film Trapped Between Fibers in Paper Drying Process: Microscopic Approach

The main objective of this chapter is to fundamentally describe the physics of drying process in the intermediate stage, from free water toward bound water, where the remaining free water is present on the exterior surfaces of fibers in the form of a liquid film. To simplify, a configuration is assumed where the drying of the above-mentioned liquid film is achieved with a hot air flowing through the paper/tissue thickness comprised of an array of fibers. The effects of different controlling parameters such as air velocity and temperature, initial height of the liquid film, Marangoni effects, and the fiber dimensions on drying are presented. Numerical simulations have been conducted using VOF model in Ansys FLUENT. The properties of liquid water are considered as functions of temperature, but the properties of the fibers are assumed to be constant.

Keywords: Thin liquid film removal; dominant mechanisms; paper drying; microscale

2.1 Theoretical Model

2.1.1 Governing Equations and Boundary Conditions

A very simple geometry is considered to fundamentally understand the evaporation of liquid film in the vicinity of fibers. Figure 4 illustrates the simplified configuration considered here. The details of the corresponding schematic for the theoretical model presented here are given in Figure 5. Due to the computational expenses, only an array of three fibers is considered.

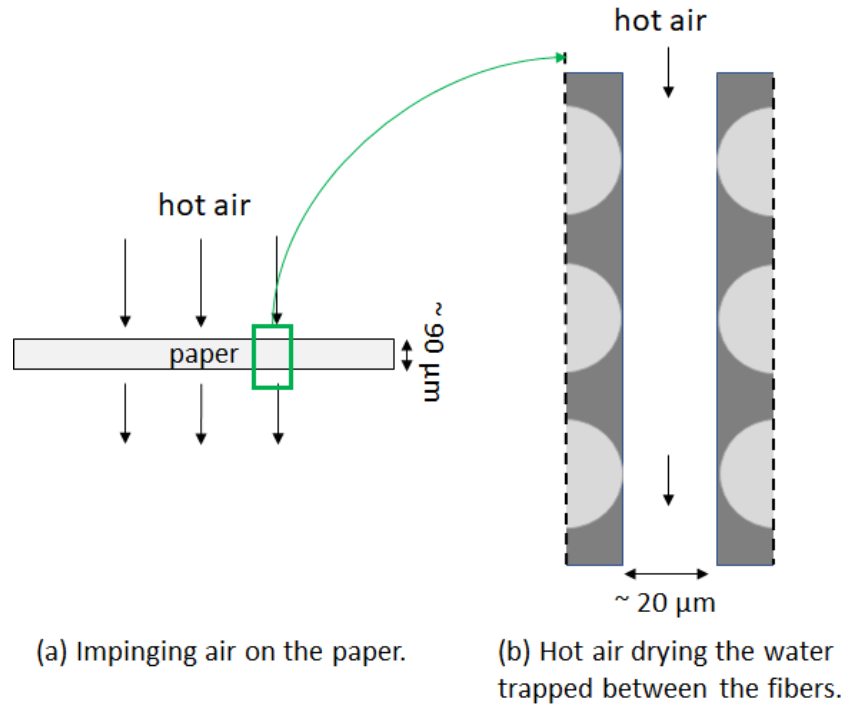


Figure 4. Illustration of the simplified impinging air drying configuration considered in this study.

The evaporating liquid film bounded in between three fibers is confined by an air/vapor layer flowing above it. Due to symmetry conditions, only one half of the geometry is considered. The initial condition is a flat liquid film interface with a flowing dry air above. The liquid thin film is thin enough that gravity effects are negligible, and it is thick enough that continuity applies (see Table 4). In addition, the fluids are immiscible, and the fibers are impermeable

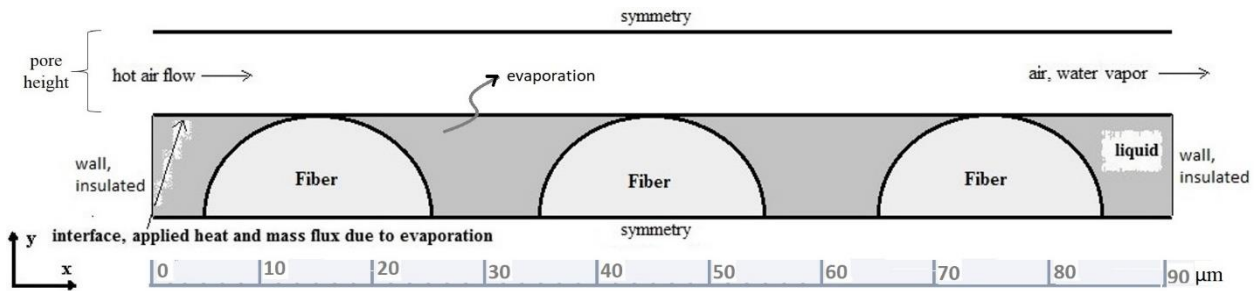


Figure 5. Schematic of the model for an evaporating liquid film between three fibers bounded by a flowing gas layer.

One phase is the gas phase, which is a mixture of air and water vapor, and the other phase is the liquid water. The governing equations for the fluid phase are the conservation of mass (continuity equation), momentum, and energy equations. For a three-dimensional (3D) laminar transient compressible flow, these equations may be written as

$$\frac{\partial \rho}{\partial t} + \nabla \cdot (\rho \vec{v}) = S_m \quad (2-1)$$

$$\frac{\partial}{\partial t} (\rho \vec{v}) + \nabla \cdot (\rho \vec{v} \vec{v}) = -\nabla p + \nabla \cdot (\bar{\tau}) + \rho \vec{g} + \vec{F} \quad (2-2)$$

$$\frac{\partial}{\partial t} (\rho E) + \nabla \cdot (\vec{v}(\rho E + p)) = \nabla \cdot \left(k \nabla T - \sum_j h_j \vec{J}_j \right) + S_h \quad (2-3)$$

where S_m is the mass added to the continuous phase from the dispersed second phase as a result of evaporation here. p is the static pressure and $\bar{\tau}$ is the stress tensor. $\rho \vec{g}$ is the gravitational body force, which is negligible in this problem. \vec{F} is the external body force, which corresponds to capillary forces included in the model. k is the thermal conductivity and \vec{J}_j is the diffusion flux of species j . The first two terms on the right-hand side of equation (2-3) represent energy transfer due to conduction and species diffusion, respectively. S_h includes the heat source due to evaporation (i.e., mass transfer source term multiplied by the heat of evaporation). The values of the air velocities used in this study are in a range that confirm the Reynolds numbers (calculated based on initial height of the interface) are in the laminar regime.

The mass transfer due to evaporation at the liquid-gas interface, S_m , is defined as [99]

$$S_m = k_m \left(\frac{P_v - P_{va}}{P_{atm}} \right) \quad (2-4)$$

where p_v is vapor pressure and p_{va} is vapor pressure in air. The mass transfer coefficient, k_m , is determined from Chilton-Colburn form of the Reynolds's analogy [97 and 100]. Also, h_{fg} is described as a function of temperature by using the equation from Pakowski et al. [101].

In equation (2-3), E is defined as

$$E = h - \frac{P}{\rho} + \frac{v^2}{2} \quad (2-5)$$

where sensible enthalpy h for incompressible flows is described by

$$h = \sum_j Y_j h_j + \frac{P}{\rho} \quad (2-6)$$

and Y_j is the mass fraction of species j .

$$h_j = \int_{T_{ref}}^T c_{p_j} dT \quad (2-7)$$

where T_{ref} is 298.15 K.

Moreover, in order to model the diffusion of water vapor into air, an additional species transport equation is solved. This conservation equation predicts the local mass fraction of water vapor (Y) in the mixture. This equation takes the following form

$$\frac{\partial}{\partial t}(\rho Y) + \nabla \cdot (\rho \vec{v} Y) = -\nabla \cdot \vec{J} \quad (2-8)$$

The mass fraction of the air is determined as one minus the mass fraction of the water vapor in the mixture.

In equation (2-8), \vec{J} is the diffusion flux, which arises due to gradients of concentration. In order to model mass diffusion due to concentration gradients, the diffusion flux can be written as

$$\vec{J} = -\rho D_m \nabla Y \quad (2-9)$$

Here D_m is the mass diffusion coefficient in the mixture.

By using the multiphase flow model in ANSYS Fluent, specifically volume of fluid (VOF), the evaporation of the liquid layer at the interface is modeled in this study. Since there are two phases

in this model, the interface tracking between the phases is accomplished by solving the continuity equation for the volume fraction of water vapor (α) in the following form

$$\frac{1}{\rho} \left[\frac{\partial}{\partial t} (\alpha \rho) + \nabla \cdot (\alpha \rho \vec{v}) \right] = S_m \quad (2-10)$$

where the source term on the right-hand side of equation (2-10) is due to evaporation and is given in equation (2-4). This evaporation source term is describing the mass transfer between the liquid layer and the water vapor species in the mixture. The volume fraction of the mixture is calculated based on the following constraint

$$\alpha_{liquid\ water} + \alpha_{mixture} = 1 \quad (2-11)$$

Moreover, to add the effect of surface tension to the VOF model, a source term (body force) is added to the momentum equation. For two phases, this volume force can be presented as

$$\vec{F} = \sigma \frac{\rho \kappa \nabla \alpha}{\frac{1}{2} (\rho_{liquid\ water} + \rho_{mixture})} \quad (2-12)$$

where ρ is the volume-averaged density and κ is the curvature that is defined in terms of the divergence of the unit normal, \hat{n}

$$\kappa = \nabla \cdot \hat{n} \quad (2-13)$$

It should be mentioned that for two phase flow, $\kappa_{liquid\ water} = -\kappa_{mixture}$ and $\nabla \alpha_{liquid\ water} = -\nabla \alpha_{mixture}$.

In order to include the effect of Marangoni flows or thermocapillary effects into the simulations, the surface tension is considered as a function of temperature as [102]

$$\sigma = 235.8 \left(1 - \frac{T}{647.096} \right)^{1.256} \left[1 - 0.625 \left(1 - \frac{T}{647.096} \right) \right] \text{ mN/m} \quad (2-14)$$

This equation is valid between the triple point (0.01 °C) and 647.096 K.

For the solid phase, only the energy equation is required for conduction through the fiber (conjugate heat transfer problem) as following

$$\frac{\partial}{\partial t}(\rho_f c_{p_f} T) = \nabla \cdot (k_f \nabla T) \quad (2-15)$$

where c_{p_f} is heat capacity of the fiber. ρ_f and k_f are density and thermal conductivity of the fiber material, respectively.

The average properties of the fibers are considered as average properties for porous media chosen from both theoretical and experimental relationships for different porous materials including foods [103]. Furthermore, the properties of air, water vapor, and liquid water are included into the model as functions of temperature, according to [101, 104].

The velocity-inlet and pressure-outlet boundary conditions are applied at the inlet and outlet of the gas domain, respectively. Hot, dry air enters the domain at a constant velocity. For the liquid layer, the lateral boundary conditions are no mass flux and thermally insulated. Symmetry boundary conditions are used for the upper and lower boundaries in Figure 5. On the interface of solid-fluid regions, a no-slip boundary condition is imposed. The initial condition for the simulations is 300 K for temperature and zero velocity everywhere. The range of the values chosen for the diameter of the circular fibers are based on the research of Ververis et al. [105]. This research concluded that the wood fibers have the average diameter about 15-25 μm . In the current research the effect of different fiber diameters and the distance between fibers are studied. To study the effect of each of the parameters, other parameters are held constant. The goal here is that by knowing the effect of different parameters in the current technologies in paper drying industries, the operational conditions can be modified in order to increase the efficiency of the process, decreasing the drying time, and decreasing the energy consumption. The parametric study here includes the effect of inlet velocity and inlet temperature of the flowing dry air, the initial height of the liquid layer (i.e., percentage of the water between the fibers), and Marangoni flows on evaporation (drying) behavior of the thin film are investigated. Additionally, the effect of different geometrical

parameters such as diameter of the fibers, distance between the fibers, and pore height (which is defined as the inlet for the hot air in Figure 5) are studied.

2.1.2 Numerical Technique

The CFD simulations are done by the commercial software ANSYS Fluent 19.1. The pressure-based segregated solver is used, with the SIMPLE algorithm for pressure-velocity coupling. The simulations use second-order upwind discretization. Under-relaxation factors are usually left at Fluent defaults and the convergence criterion is 10^{-6} .

The geometries are meshed with hexahedral cells. A mesh independence study is conducted to determine the minimal number of meshes required to obtain highly accurate results. For laminar flow, the mesh independence of the solution is checked by monitoring the changes in the liquid volume versus time. The results show that an average of approximately 80000 elements is enough for the simulations.

The following sections represent the details of the results for different numerical conditions.

2.2 Results and Discussion

2.2.1 Thin Liquid Film Drying

Figure 6 shows how the liquid volume changes vs time for the case shown in Table 4.

Table 4. Operating conditions for the case shown in Figure 6 and Figure 7.

Properties	Air inlet velocity	Air inlet temperature	Initial height of liquid layer	Surface tension	Diameter of fibers	Distance between fibers	Pore height
Value	5 m/s	400 K	10 μm	Eqn. (2-14)	20 μm	10 μm	10 μm

Figure 6 shows two different stages for drying the thin film between the fibers. It is obvious that in stage 1, the liquid volume is changing almost with a constant slope and then after a critical moisture content, the slope decreases significantly at stage 2 (which means the evaporation rate decreases here). After about 1000 ms the liquid layer is completely dried.

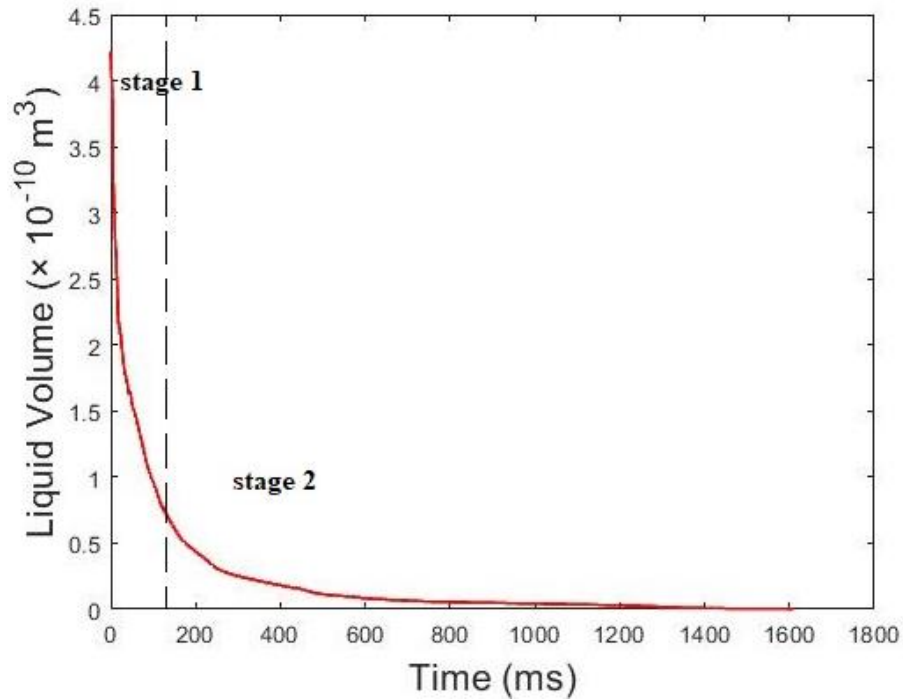


Figure 6. Change in liquid volume vs time for the case with operational conditions provided in Table 4.

In order to interpret the results, Figure 7 shows the contour plots of the volume fraction of the liquid layer as a function of time. In this model, the gas phase is a mixture of air and water vapor. The air enters at the inlet in a dry condition and then the water vapor is added to the dry air as it proceeds toward the outlet. In Figure 7, when the volume fraction of water is 1, it represents the pure liquid water. The volume fraction of water decreases from the fiber/liquid surface toward the liquid/gas interface. Moving from the fiber/liquid surface to the liquid/gas interface, the humidity of air is increasing, by changing the volume fraction of water vapor in the gas phase.

From Figure 7, it is obvious that in the beginning evaporation happens at the interface in a very short time. After that, since the hot air is flowing inside the domain and increases the temperature,

evaporation has high rates (stage 1). Comparing the contours of liquid volume fraction (Figure 7) with the contours of temperature (Figure 8) reveals that at higher temperatures evaporation has higher rates. Contours of temperature in Figure 8 show that after about 30 ms, the temperature in the domain reaches that of the inlet temperature of the inflowing air and it is supposed to be a positive driving force for evaporation. However, as it is obvious from Figure 6, after about 30 ms the evaporation rate decreases. In fact, at this stage of drying there are 3 different phenomena competing with each other. Although, the increase in temperature should increase the drying rate, decreasing the moisture content between the fibers makes the evaporation rate slower. Another effecting parameter here is Marangoni flows (thermocapillary instabilities), which make instabilities in the liquid layer that can change the drying behavior of the thin liquid film.

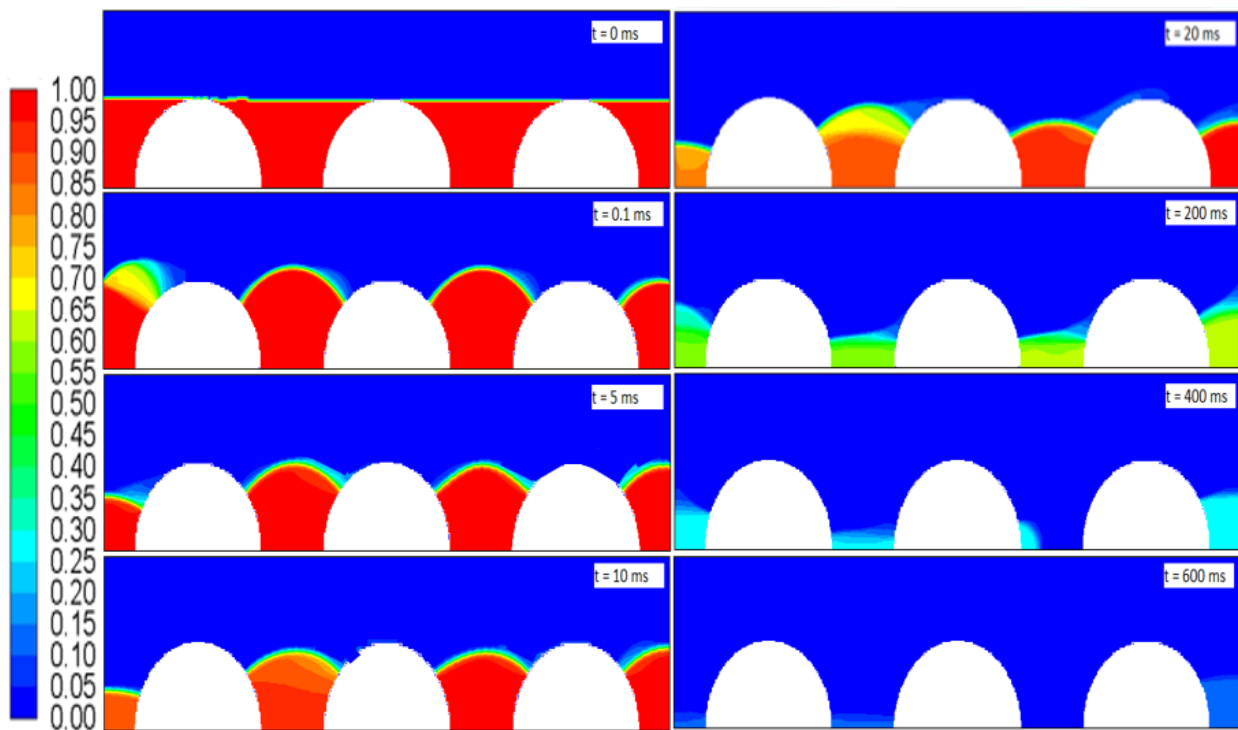


Figure 7. Contours of volume fraction of the liquid layer at different times for the case with operational conditions provided in Table 4.

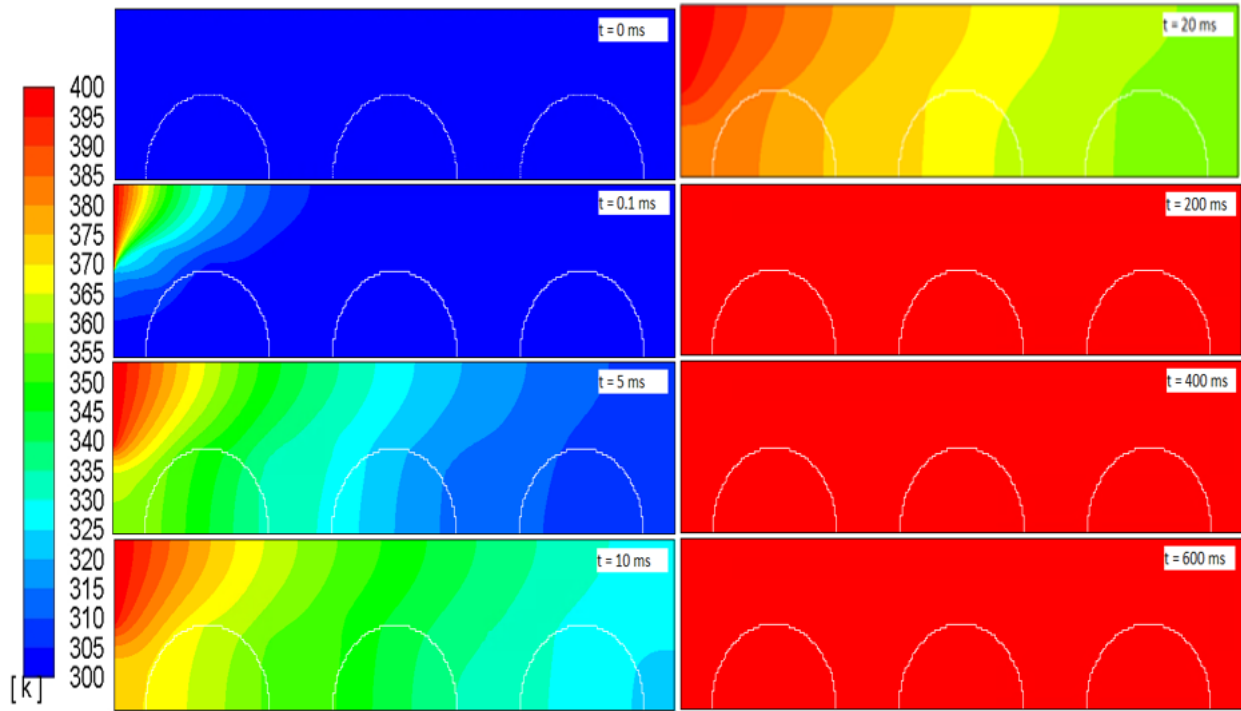


Figure 8. Contours of temperature at different times for the case with operational conditions provided in Table 4.

In the interest of understanding the effect of Marangoni flows on each of the stages of drying, Figure 8 displays the temperature profiles in y-direction along the interface at locations between the first and the second fibers, at 5 ms drying time. Figure 9 reveals that there is a gradient in temperature along the interface. As seen from Figure 8, at the second stage, the temperature is uniform everywhere in the domain. Looking at equation (2-14) for surface tension as a function of temperature shows that with increasing temperature, the surface tension decreases. The gradients in temperature lead to gradients in surface tension and hence, Marangoni flows are stronger. The instabilities induced from Marangoni flows at the interface of liquid/gas makes the evaporation to occur faster. However, at the second stage of drying, the gradients in temperature and thus, the gradients in surface tension decrease. This ends or weakens the impact of instabilities due to Marangoni flows and results in reduction of evaporation rate. For that reason, Marangoni flows help the drying rate at the first stage of drying.

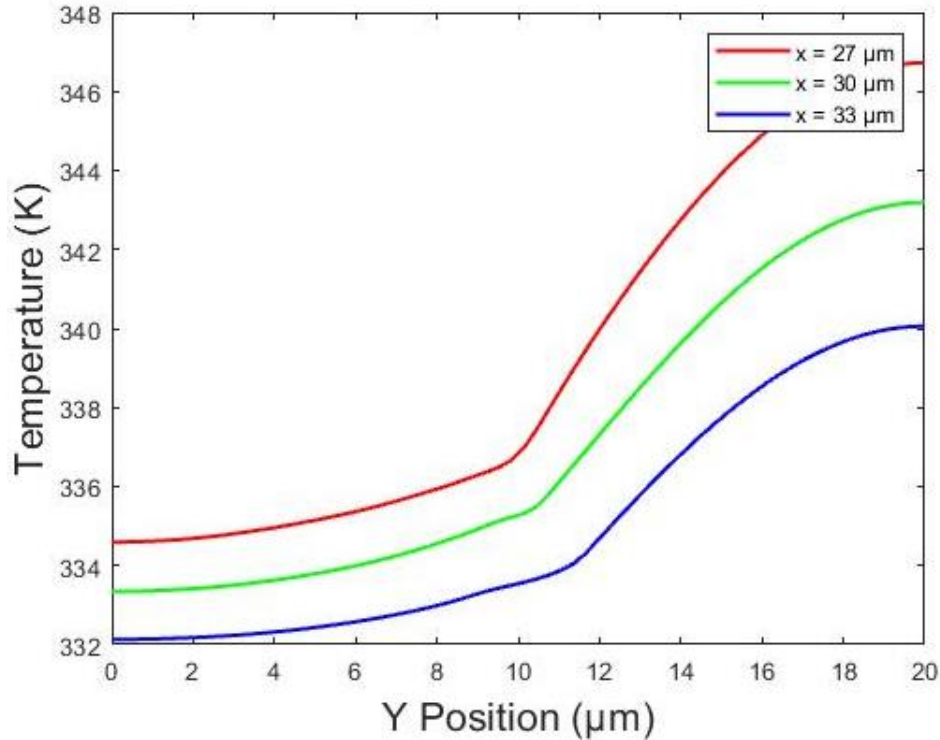


Figure 9. Comparing temperature profiles for the case shown in Figures 4-6 at 5 ms. The profiles are at locations between the first and the second fibers.

2.2.2 Effect of Fluid Properties on Liquid Film Drying

To have a better understanding of the effect of different parameters on liquid film drying, the effect of different parameters on the evaporation rate and the change in height of the interface are also studied in this research, which are presented in Figures 10-13. These parameters include (a) the inlet velocity, (b) the inlet temperature, and (c) the initial height of the liquid layer (i.e., percentage of the liquid between the fibers). It should be noted that in each case, other parameters are constant according to Table 4. Figure 10 shows that increasing the inlet velocity and hence, increasing the convective flow of the gas layer, decreases the drying time. The noteworthy point here is that decreasing the inlet velocity to 1 m/s from 5 m/s leads to a significant change in drying behavior. In the case of 1 m/s, the rate of drying is lower than two other cases since it needs more time for the temperature to increase. Therefore, in this case the heat transfer is the limiting mechanism.

While, for the case with high inlet velocity equal to 10 m/s, the drying rate is very fast, and the overall time of drying is shorter.

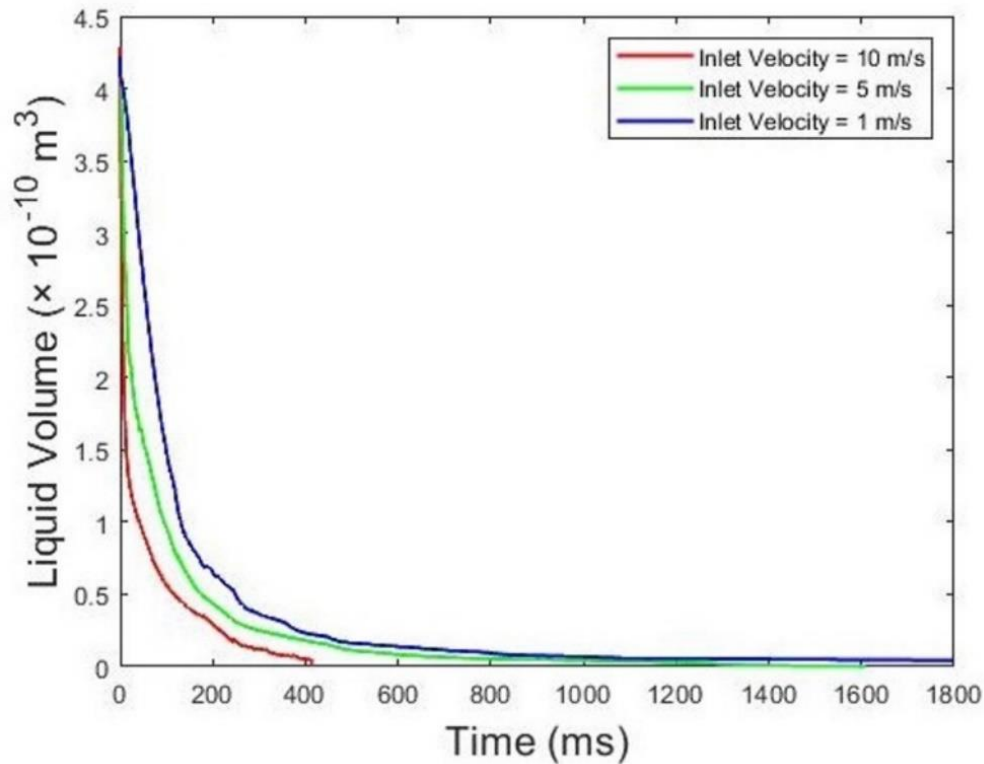


Figure 10. Change in liquid volume under different inlet velocities.

Figure 11 represent the effect of inlet temperature on drying curve. By increasing the inlet temperature, two phenomena are assisting the evaporation rate: (1) at higher temperatures, the vapor pressure is higher and thus, the mass transfer coefficient is higher and (2) at higher inlet temperatures, the gradients of temperature and gradient of surface tension are higher and hence, the effect of Marangoni instabilities on evaporation is higher. This has higher impact on the first stage of drying since the gradients of temperature is higher at this stage.

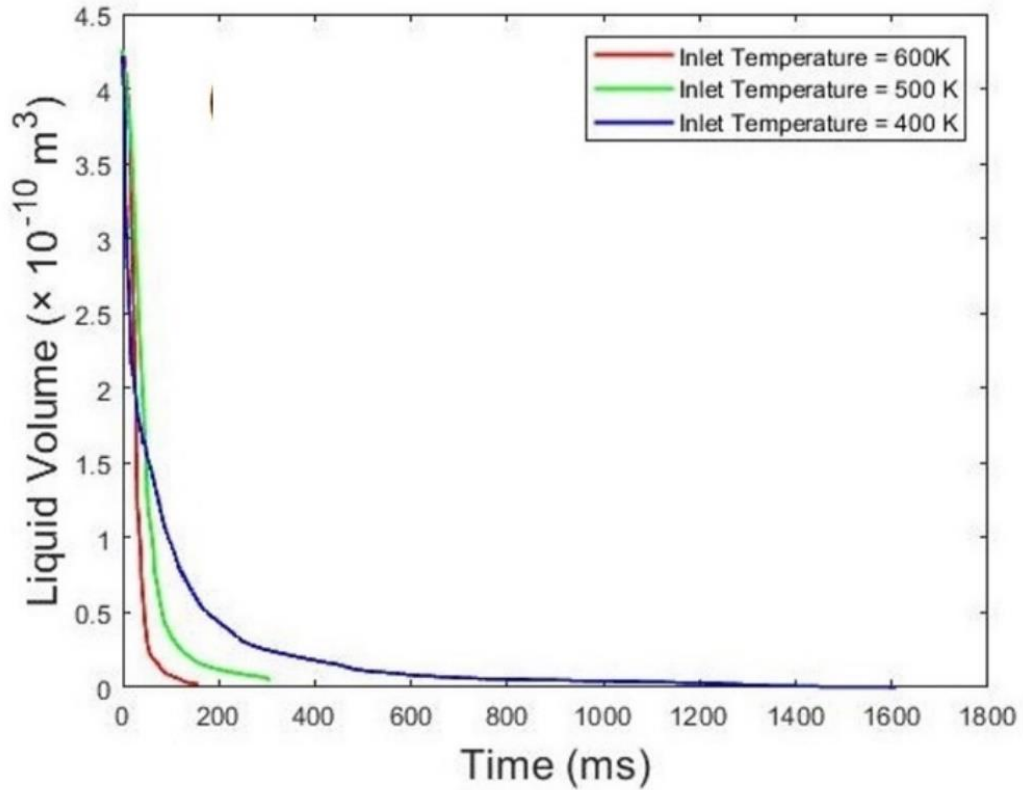


Figure 11. Change in liquid volume under different inlet temperatures.

With increasing the initial height of the liquid layer (Figure 12), the change in the slope of the plot increases and hence, the evaporation happens at a lower rate which results in higher times of drying. At higher liquid heights, the time required for diffusion of temperature inside the liquid is higher and therefore the evaporation rate is lower.

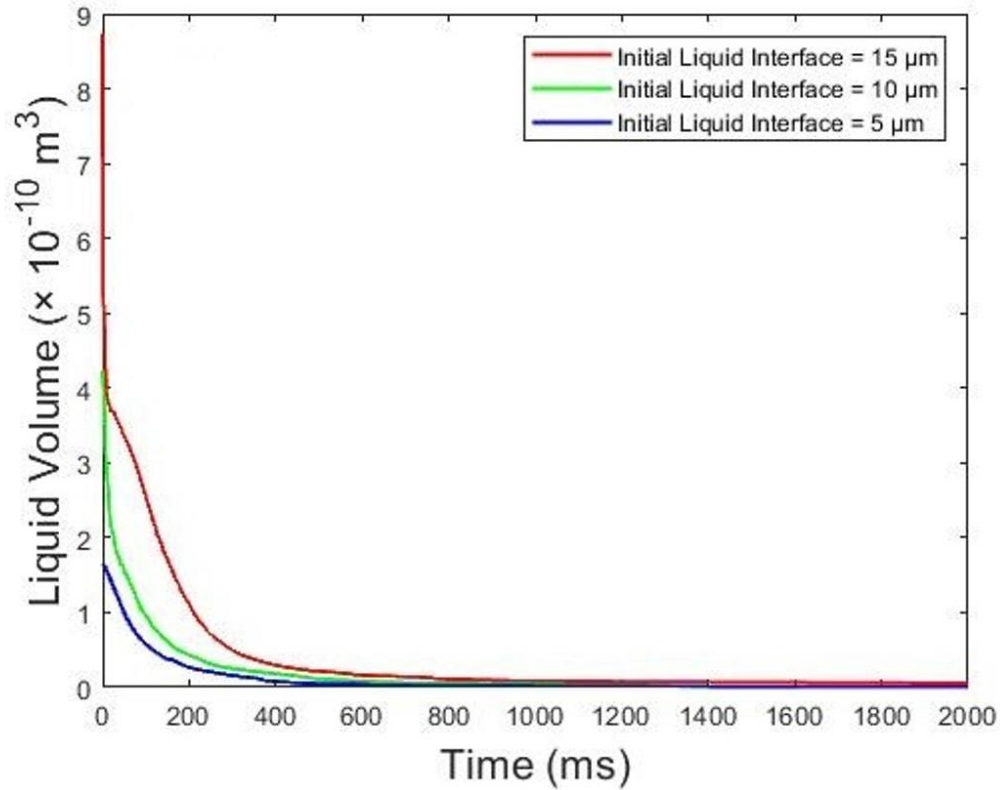


Figure 12. Change in liquid volume under different initial liquid film thicknesses.

2.2.3 Marangoni Effects

To understand the effect of Marangoni flows on drying rate and drying time, two cases with and without including the effect of Marangoni flows (i.e., thermocapillary instabilities) are studied in Figure 13. As it was mentioned before, Marangoni flows are a result of gradient in surface tension along the interface due to gradient in temperature. In agreement with the previous results, Figure 13 shows that the instabilities induced by Marangoni flows result in higher drying rate., thus the evaporation of the liquid layer takes place rapidly. While, as the evaporation proceeds, the effect of Marangoni flows decreases and finally, Marangoni effects cease to exist.

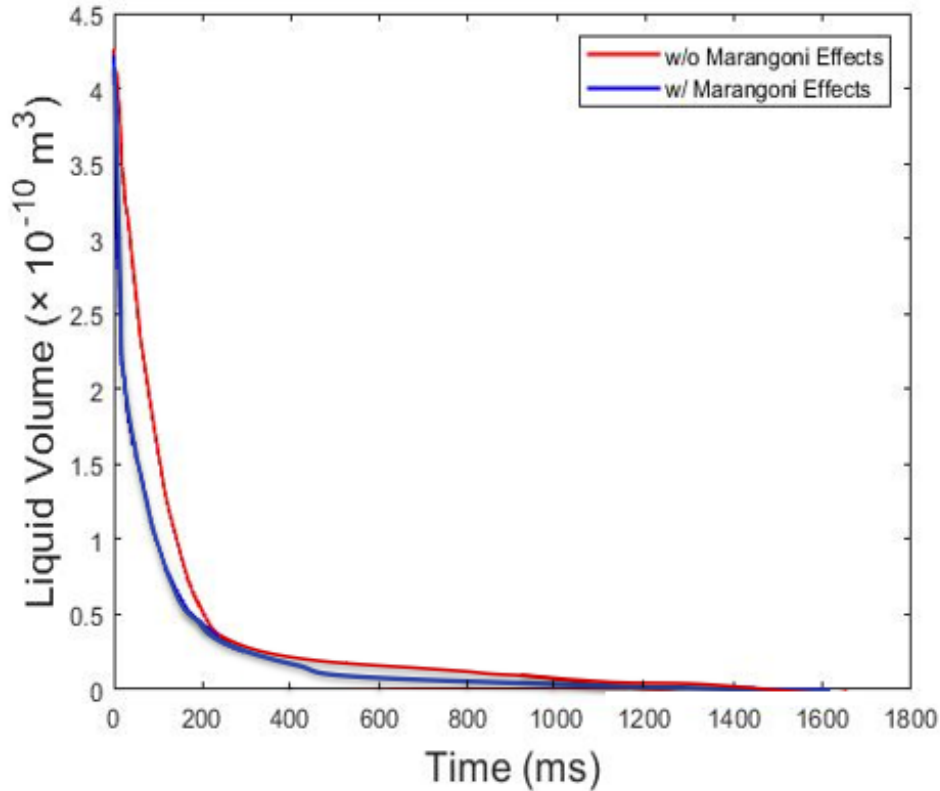


Figure 13. The effect of Marangoni flows on change in liquid volume vs time. The other properties are fixed according to Table 4.

2.2.4 Effect of Geometrical Parameters on Liquid Film Drying

The effect of geometrical parameters such as (a) diameter of fibers, (b) distance between fibers, and (c) pore height (defined as the inlet for hot dry air, Figure 5) are shown in Figure 14. It should be pointed out that in all of these simulations the initial height of the liquid film is the same as the radius of the fiber in a way that liquid film covers the distances between the fibers. Moreover, in all of the simulations, only 3 circular fibers are considered and hence by changing the distance between the fibers and the diameter of the fibers, the length of the domain changes. Figure 14(a) shows that by increasing the fiber diameter, the volume of liquid between fibers increases and leads to increase in drying time and the drying rate also decreases. As illustrated in Figure 14(a), the evaporation rate is rapid roughly in the first 100 ms and after that the evaporation rate starts to decrease significantly. One reason for this drop in the evaporation rate is the decrease in the air

flow velocity in the cavity between the fibers. Increasing distance between fibers has the same effect as shown in Figure 14(b).

For pore height, the inlet for hot dry air, Figure 14(c) shows that increasing the value from 10 μm to 25 μm , decreases the drying time. The reason behind this observation is that by increasing the inlet for hot air, the mass flow rate inside the domain increases and therefore, the drying rate increases.

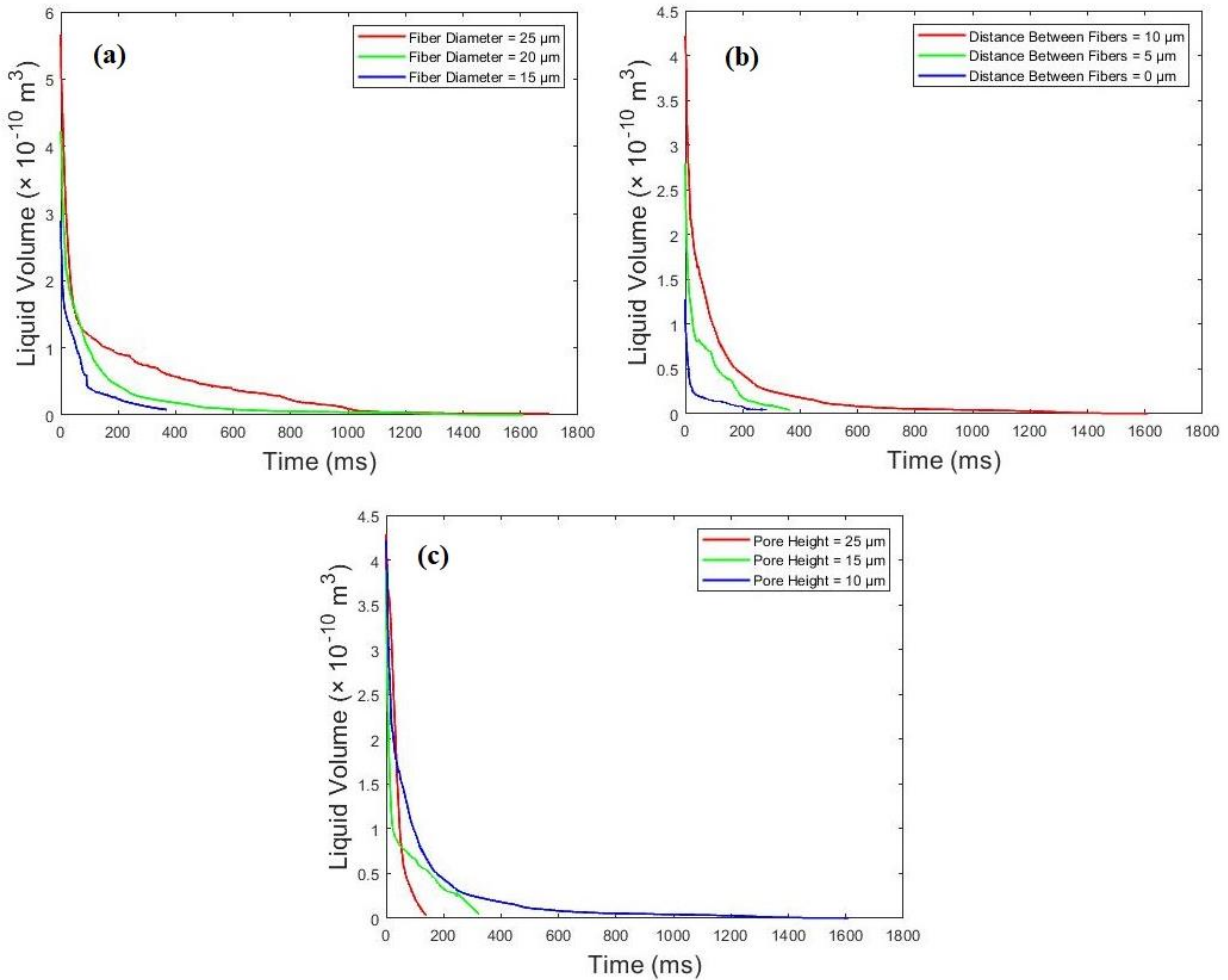


Figure 14. Change in liquid volume vs time for cases with different geometrical parameters: (a) fiber diameter; (b) distance between fibers; and (c) pore height (defined as the inlet for hot dry air in Figure 5). The other properties are fixed according to Table 4.

2.3 Summary and Conclusions

To fundamentally understand the physics of removal of liquid film trapped between paper/tissue fibers during the drying process, a simplified configuration was assumed, and the corresponding theoretical model was developed. The numerical solutions obtained in this study showed the changes in volume fraction of water and temperature during drying the thin liquid film. Since the hot air is entering the domain in the thickness direction, there is a temperature gradient at each cross section of the domain. This temperature gradient results in gradients in surface tension and consequently activates the Marangoni instabilities. The positive effect of the instabilities induced by Marangoni flows increases the drying rate. However, as the temperature becomes uniform in the domain and the gradient of temperature becomes smaller, the effect of Marangoni flows weakens at final state of drying. Additionally, as the moisture content reduces, the drying rate decreases. Therefore, there is two stages for drying the thin film: a high drying rate stage followed by a falling drying rate stage. Higher inlet air velocities and higher inlet air temperatures lead to increasing the drying rate. Nevertheless, increasing the initial liquid height increased the drying time. Furthermore, the effect of geometrical parameters of the fibers on drying rate was studied. Fibers with larger diameters and larger distance between them result in larger volume of trapped liquid and hence, have higher drying times. This work lays the foundation for the upcoming studies to investigate the detail understanding of water removal for a configuration relevant to paper products such as paper tissues.

Chapter 3: Numerical Study of Removal of Water Trapped Inside a Single Cellulose Fiber

In this chapter, as part of the transition region from free water removal toward bound water removal, removal of water trapped inside a single micro-scale fiber is studied. Various hardwood fibers with distinct physical dimensions are considered. The research analyzes the effect of properties of water (e.g., surface tension and Marangoni effects) on drying. In addition, a parametric study has been conducted to understand the effect of heat flux applied to the outer surface of the fiber. Using the temperature measurements, the heat flux in the dynamic three-phase vapor/water/fiber contact line is studied. The results of this chapter provide in-depth information about removal of water from a single cellulose fiber as a microtube. The numerical technique and the results are described in the next sections.

Keywords: final stages of drying curve; hard-to-remove water; cellulose fiber; microtube

3.1 CFD Modeling

Evaporation (condensation) is defined as an endothermic (exothermic) phase transition from liquid to vapor (or from vapor to liquid), which happens at the interface. Understanding the physical concepts and revealing the mechanisms involved in these phenomena, especially at micro and nano scales, requires very high-resolution microscopes, and in some cases, it is impossible to do the experiments. Hence, numerical simulation techniques have been used as a viable replacement for experiments in recent decades. However, numerical simulation of phase change problems is one of the most challenging areas in computational fluid dynamics (CFD). The discontinuities in material properties (e.g., density, viscosity, thermal conductivity, and surface tension) and flow variables, such as pressure at the interface, are some of the challenges in calculating numerical simulation of phase changes. For example, for multiphase flows due to strong surface tension, low viscosity, and a large density ratio, the resolution varies along the interface [106].

To simulate the phase change phenomenon, the Navier-Stokes and energy equations are accompanied by an interface-tracking method. Multiple methods have been developed for

numerical simulation of phase change from liquid to vapor, including volume of fluid (VOF), level-set method (LS), and hybrid methods such as coupled VOF and LS (VOSET), as well as a local front reconstruction method (LFRM). The most used methods for tracking interface are fixed (non-moving) mesh approaches such as VOF and LS. The VOF method has an inherent mass conservation property, and the interface is captured with the heat transfer of the phase change [107]. Considering that the feature of mass conservation for phase change problems is very important, the VOF method is chosen here. The VOF method has been used for numerical studies in a variety of cases such as for volatile liquid droplets, bubbles, film boiling, and inclined channels.

The numerical simulations in this study are conducted using Ansys Fluent 2020 R2. To convert the governing equations to algebraic equations that can be solved numerically, a control volume-based technique is used. Furthermore, the phase change model is added to Ansys Fluent using user-defined-functions (UDFs).

3.1.1 Geometry, Initial and Boundary Conditions

Figure 15 shows a cross-sectional schematic of the single-fiber model. Figure 16 represents the fiber in 3D. Heat flux is applied on the outer surface of the fiber, uniformly, and the inside of the fiber is saturated with liquid water. The water can be removed from the two open ends of the fiber. For simplicity, the tortuosity is considered one in the fiber.

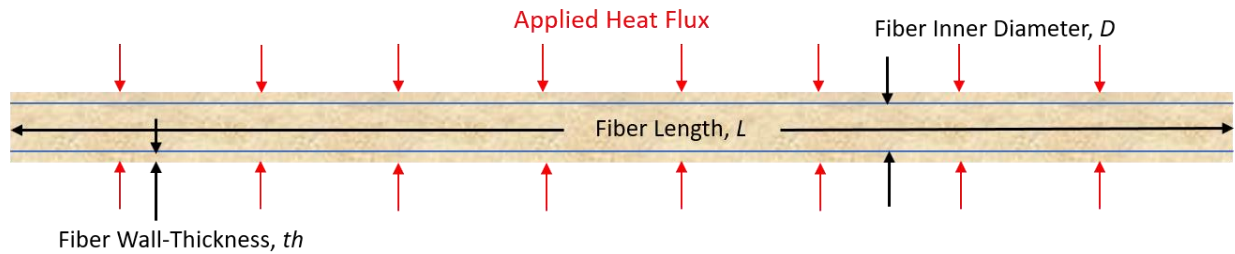


Figure 15. Cross sectional schematic of single-fiber model.

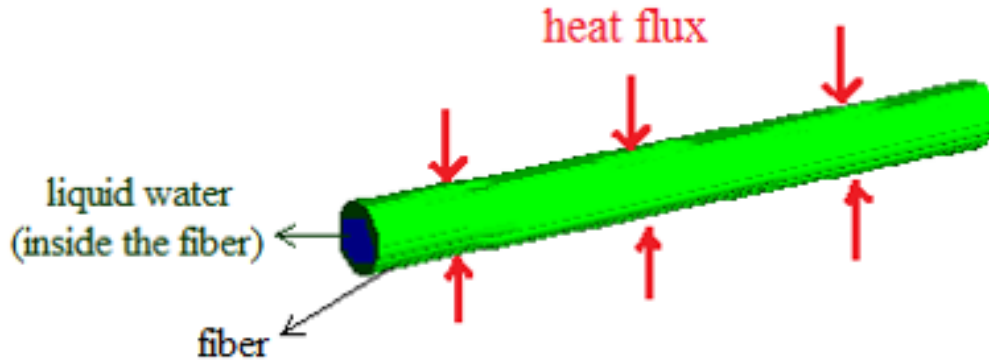


Figure 16. Schematic of single fiber model.

In this study, due to the symmetry of the flow configuration, a 2D axisymmetric geometry is used, as shown in Figure 17. The no-slip, velocity boundary condition is applied on the top wall, i.e., $v_x = v_r = 0$, and the applied wall heat flux to the outer surface of fiber is constant and uniform. The right boundary is set as the symmetry boundary condition, and the left boundary is a pressure outlet with atmospheric pressure and temperature equal to 300 K, initially. As the temperature inside the domain changes during the simulation, the temperature at the pressure outlet boundary is set equal to the adjacent cell temperature ($T_{adj-cell}$). The centerline at the bottom boundary is considered as the centerline axis. The initial value for velocity is zero, and the temperature is initialized as 300 K. It should be noted that since applying the VOF multiphase method requires an interface between liquid and gas phase, the single fiber is not totally filled with liquid water, and a very small length of the fiber (~1%) is filled with water vapor, initially. In the base case, the total length of the fiber is 1 mm and the fiber outer diameter is 14 μm . The initial value for water vapor and the backflow volume fraction of water vapor at the outlet boundary are set to zero.

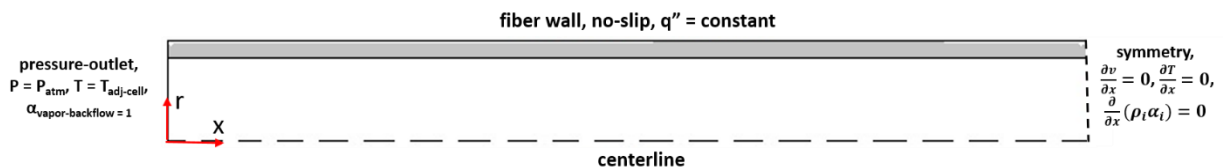


Figure 17. 2D model for single fiber with set boundary conditions.

The results of an independent study of mesh size in Figure 18, revealed that increasing the number of cells beyond 28000 did not alter the numerical results thus, this number of cells was used in the simulations.

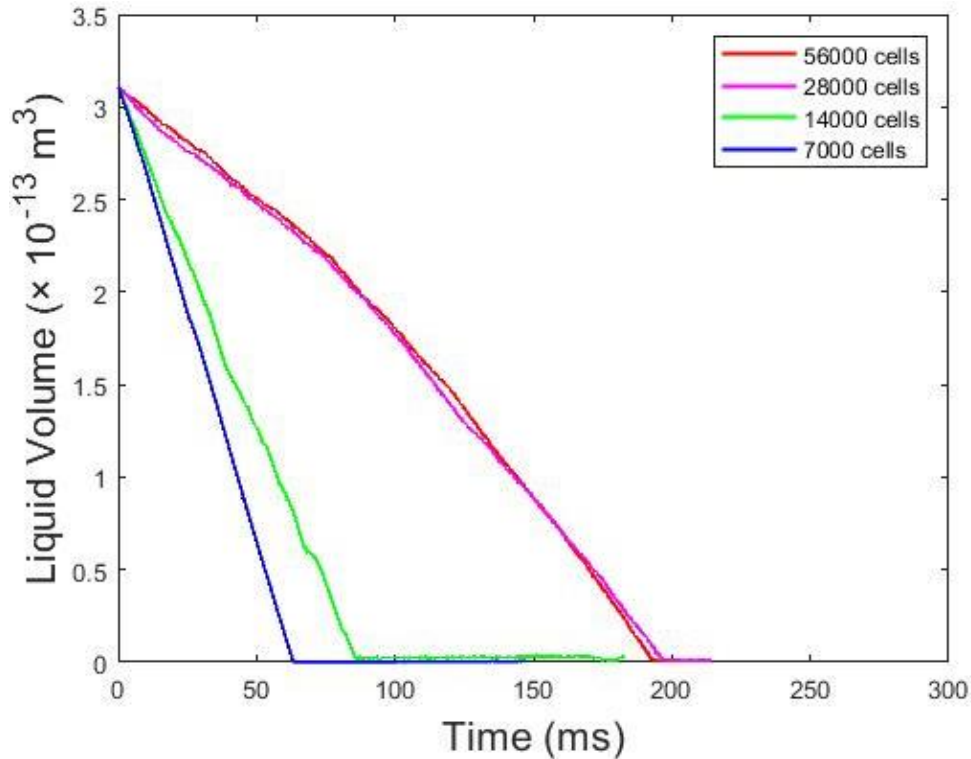


Figure 18. Change in liquid volume versus time for different mesh cell sizes.

3.1.2 Governing Equations

This is a conjugate heat transfer problem that Navier-Stokes equations and conservation of energy are solved for the fluid inside the fiber; for the solid, only the conservation of energy equation is needed. The flow inside the fiber is laminar, and it is solved in transient conditions. To track the interface, the multiphase VOF method is used in this study. The primary phase is set as liquid water, and the secondary phase is water vapor. For simplicity, air is not considered in the simulations.

The VOF method developed by Hirt and Nichols [108] is used here. The VOF method defines a volume fraction α for each of the phases. This model solves a single set of momentum equations for the fluid domain, and the volume fraction of each of the phases in each computational cell is

tracked during the simulation. The value for volume fraction of one phase is zero, if the cell is empty of that phase, and it is 1 if the grid cell is full of that phase. However, if the grid cell is partially filled with the phase, the volume fraction for that phase is between 0 and 1. The sum of volume fractions of all phases equals 1 in each grid cell:

$$\alpha_v + \alpha_w = 1 \quad (3-1)$$

Figure 19 shows the schematic of the cells around the interface region between two fluids. Each of the white and gray regions illustrates one of the phases in the domain and the partially filled cells between the two regions represent the interface.

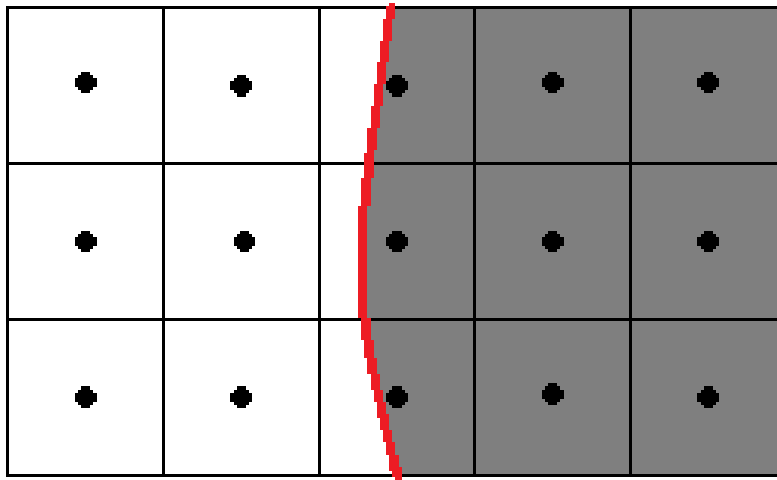


Figure 19. Schematic of the cells around the interface between two fluids in VOF method.

Hence, the interface between the fluids is tracked everywhere in the domain. The governing equations of the volume fraction for the secondary phase in 2D axisymmetric geometry can be written as follows

$$\frac{\partial}{\partial t}(\alpha_v \rho_v) + \frac{\partial}{\partial x}(\alpha_v \rho_v v_x) + \frac{\partial}{\partial r}(\alpha_v \rho_v v_r) + \frac{\alpha_v \rho_v v_r}{r} = \dot{m}_{lv} \quad (3-2)$$

where the subscripts v and l are the two phases, water vapor and liquid water, respectively. ρ is the density, t is the time, and v is the velocity, which has two components in x and r directions. The right-hand side of equation (3-2) shows the production and destruction source terms of the phases, due to mass transfer or a chemical reaction. In this study, the evaporation only happens between

liquid water and water vapor. Therefore, the source term is defined as \dot{m}_{lv} and it can be expressed as follows

$$\dot{m}_{lv} = k_m \left(\frac{P - P_{sat}}{P_{atm}} \right) \quad (3-3)$$

where P_{sat} is a function of temperature [101]. k_m is the mass transfer coefficient (kg/(m³.s)), and it is determined from the Chilton-Colburn form of the Reynolds' analogy, according to Asensio and Yagoobi [109].

The source terms are applied only at the vapor/water interface, and in the rest of the domain the values are zero. In addition, the volume fraction of liquid water is determined as one minus the volume fraction of water vapor.

A single momentum equation is solved throughout the domain, and the resulting velocity field is shared among the phases. The momentum equation for 2D axisymmetric geometries can be expressed as follows

$$\begin{aligned} \frac{\partial}{\partial t}(\rho v_x) + \frac{1}{r} \frac{\partial}{\partial x}(r \rho v_x v_r) + \frac{1}{r} \frac{\partial}{\partial r}(r \rho v_r v_x) \\ = -\frac{\partial P}{\partial x} + \frac{1}{r} \frac{\partial}{\partial x} \left[r \mu \left(2 \frac{\partial v_x}{\partial x} \right) \right] + \frac{1}{r} \frac{\partial}{\partial r} \left[r \mu \left(\frac{\partial v_x}{\partial r} + \frac{\partial v_r}{\partial x} \right) \right] + F_x \end{aligned} \quad (3-4)$$

and

$$\begin{aligned} \frac{\partial}{\partial t}(\rho v_r) + \frac{1}{r} \frac{\partial}{\partial x}(r \rho v_x v_r) + \frac{1}{r} \frac{\partial}{\partial r}(r \rho v_r v_r) \\ = -\frac{\partial P}{\partial r} + \frac{1}{r} \frac{\partial}{\partial x} \left[r \mu \left(\frac{\partial v_r}{\partial x} + \frac{\partial v_x}{\partial r} \right) \right] + \frac{1}{r} \frac{\partial}{\partial r} \left[r \mu \left(2 \frac{\partial v_r}{\partial r} \right) \right] - 2\mu \frac{v_r}{r^2} + F_r \end{aligned} \quad (3-5)$$

where P is the pressure. The properties in the momentum equation are determined from the component phases in each control volume. For example, in a two-phase system, the density, ρ , and the viscosity, μ , are calculated from the volume fractions of all the phases as

$$\rho = \alpha_v \rho_v + (1 - \alpha_v) \rho_l \quad (3-6)$$

$$\mu = \alpha_v \mu_v + (1 - \alpha_v) \mu_l \quad (3-7)$$

Surface tension is a surface force; however, in order to add the effect of surface tension to the source term in the momentum equation, Brackbill [110] converted the surface force into a volume force, F , by the continuum surface force (CFS) model. F has the form

$$F = \sigma \frac{\alpha_v \rho_v \kappa_v \nabla \alpha_v + \alpha_l \rho_l \kappa_l \nabla \alpha_l}{0.5(\rho_v + \rho_l)} \quad (3-8)$$

where the interfacial curvature, κ is obtained from:

$$\kappa_v = -\kappa_l = -\nabla \cdot \left(\frac{\nabla \alpha_v}{|\nabla \alpha_v|} \right) \quad (3-9)$$

The energy equation is also shared between the two phases, and, for 2D axisymmetric geometries, it can be expressed as follows

$$\frac{\partial}{\partial t}(\rho E) + v_r \frac{\partial(\rho E + P)}{\partial r} + v_x \frac{\partial}{\partial x}(\rho E + P) = \left[\frac{1}{r} \frac{\partial}{\partial r} \left(kr \frac{\partial T}{\partial r} \right) + \frac{\partial}{\partial x} \left(k \frac{\partial T}{\partial x} \right) \right] + S_h \quad (3-10)$$

where E is the internal energy and T is the temperature. k is the thermal conductivity determined as follows

$$k = k_l \alpha_l + k_v \alpha_v \quad (3-11)$$

S_h includes any volume heat sources or heat of chemical reaction. In this study, S_h is the heat source due to evaporation and condensation and it is defined as

$$s_h = h_{fg} \dot{m}_{lv} \quad (3-12)$$

where h_{fg} is the latent heat of vaporization, and it is defined as a function of temperature, using the equation by Pakowski [101]. Note that the evaporation source term only is applied at the vapor/water interface.

The remaining terms on the right-hand side of equation (3-10) represent energy transfer due to conduction. Energy and temperature are mass averaged, and they can be defined as

$$E = \frac{\alpha_v \rho_v h_v + \alpha_l \rho_l h_l}{\alpha_v \rho_v + \alpha_l \rho_l} \quad (3-13)$$

$$h_v = \int_{298.15}^T C_{p,v} dT \quad (3-14)$$

$$h_l = \int_{298.15}^T C_{p,l} dT \quad (3-15)$$

where C_p is heat capacity and h is enthalpy. For the conjugate heat transfer problem, an energy equation is solved for the solid phase, which is describing the energy equation for conduction through the fiber. For 2D axisymmetric geometries, this equation can be described as

$$\rho_f C_{p_f} \frac{\partial T}{\partial t} = k_f \left[\frac{1}{r} \frac{\partial}{\partial r} \left(r \frac{\partial T}{\partial r} \right) + \frac{\partial}{\partial x} \left(\frac{\partial T}{\partial x} \right) \right] \quad (3-16)$$

where C_{p_f} is heat capacity of the fiber, ρ_f and k_f are density and thermal conductivity of the fiber material, respectively.

The average thermophysical properties of the fibers are chosen from both theoretical and experimental relationships for cellulose fibers [109] and they are considered constant numbers. Furthermore, the properties of water vapor, and liquid water are included into the model as functions of temperature, according to Pakowski [101].

In order to include the effect of Marangoni flows or thermocapillary effects into the simulations, the surface tension is considered as a function of temperature as

$$\sigma = 235.8 \left(1 - \frac{T}{647.096} \right)^{1.256} \left[1 - 0.625 \left(1 - \frac{T}{647.096} \right) \right] \text{ mN/m} \quad (3-17)$$

This equation is valid between the triple point (0.01 °C) and 647.096 K, according to Petrova et al. [102].

3.1.3 Solution Technique

As the pressure and face mass fluxes are not known, interpolation schemes are employed to compute these values. The second-order upwind scheme is adopted for the inertia terms in the momentum equations (3-4) and (3-5) and convection terms in the energy equation (3-10). The geometric reconstruction scheme is used to determine the face fluxes for the VOF model. This scheme represents the interface between fluids, using a piecewise linear approach. The SIMPLE algorithm is used for pressure-velocity coupling. Numerical simulations are computed in double precision with a segregated solver. Convergence criteria are set as 10^{-5} for continuity and momentum equations and 10^{-7} for energy equation.

3.2 Results and Discussion

Table 5 represents the values of properties and fiber dimensions used in the simulations. In this study, the range of the applied heat flux to the outer surface of the fiber is chosen corresponding to the lower end of actual convective drying of paper products, according to Asensio et al. [109]. The effect of decreasing and increasing surface tension is studied by multiplying equation (3-17) by 0.8 and 1.5, respectively. A constant surface tension equal to 59 mN/m is considered for the cases without Marangoni effect. According to von Bahr et al. [111] it is possible to increase the contact angle between water and fiber to 110°. In this study, the contact angle is constant as 105°. The effect of surface roughness and topology, which may influence the ability of the structure to transport water, as well as the shrinkage of the fiber during drying are not being considered in this research. As it was mentioned above, the fiber geometrical dimensions including inner fiber diameter, fiber length, and fiber wall thickness vary depending on the source and environmental conditions. Softwood fibers are longer and coarser compared to hardwood fibers (see Figure 20). To study the effect of fiber's dimensions on water removal of hardwood fibers, the range of fiber length and fiber diameter are chosen accordingly.

Table 5. Different properties and physical dimensions used in the numerical simulations (* specifies the properties for the base case).

Properties	Applied heat flux to the fiber wall (W/m²)	Surface tension (mN/m)	Inner fiber diameter (μm)	Fiber length (mm)	Fiber wall thickness (μm)
Values	1000	0.8 × eqn. (3-17)	10	0.5	2
	3000*	eqn. (3-17)*	20*	1*	4*
	5000	1.5 × eqn. (3-17)	25	1.5	7
		59			

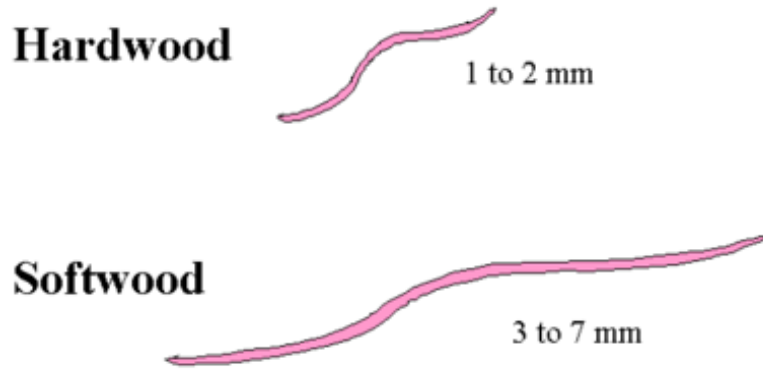


Figure 20. Comparing softwood and hardwood fibers, schematically.

3.2.1 Water Removal from a Single Fiber

For the sake of illustration, the drying curve, which is the liquid volume versus time for one of the cases is shown in Figure 21. The properties for this case are specified with a star in Table 5.

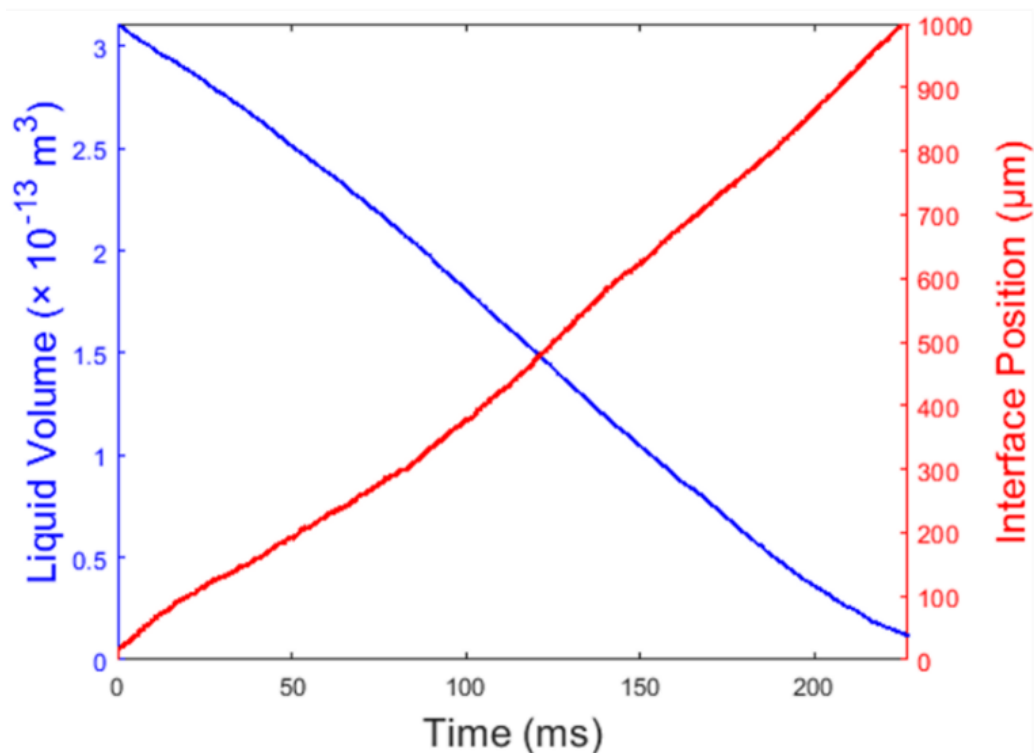


Figure 21. Change in liquid volume and interface position vs time for the case specified with stars in Table 5.

The liquid volume is decreasing over time, and the position of the water/vapor interface is moving toward the center of the fiber (i.e., symmetry boundary). As depicted in Figure 21, for this specific case, the drying time is about 225 ms. This drying curve shows the transition region between free water removal and bound water removal as it is the drying curve for the water trapped inside the fiber. It should be mentioned that in a real scenario, the water also gets removed from the small open pores on the surface of the fiber wall which are not considered in this research.

Figure 22 illustrates the contours of liquid volume at different times. The greater attraction of liquid molecules to each other (due to cohesion) than to the molecules in the vapor (due to adhesion) leads to surface tension at the interface of liquid and vapor, which determines the curvature and shape of the interface. Since surface tension is a function of temperature, the interfacial curvature is changing during the simulation. Another factor determining the shape of the interface is the contact angle between the solid fiber and fluid phases. In this study, the contact angle is assumed to be fixed. Rashid et al. [40] contributed this change in interface shape to the clockwise vortex in liquid and counterclockwise vortex in vapor due to surface tension, vapor recoil, thermos-capillary, viscous force, and geometric constraints.

Figure 23 shows the temperature contours at different drying times. The evaporation only happens at the water/vapor interface. Additionally, the temperature in the vapor phase is higher than the liquid phase, due to the higher thermal diffusivity.

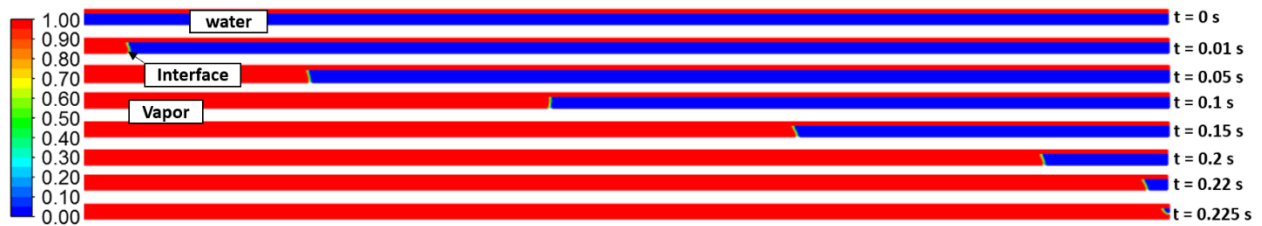


Figure 22. Liquid volume contours at different times for the case specified with stars in Table 5.

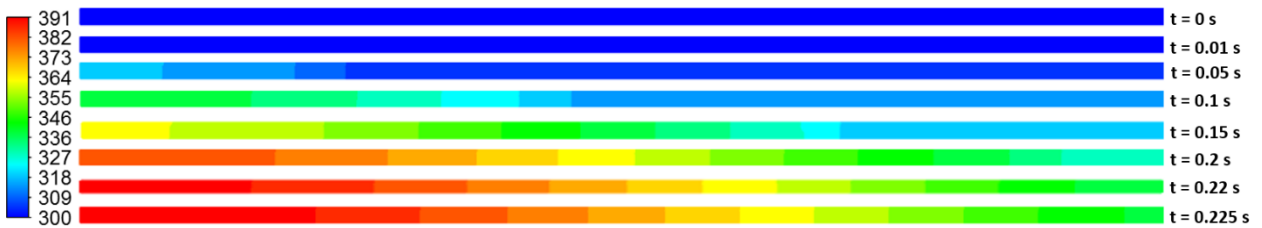


Figure 23. Temperature contours (in K) at different times for the case specified with stars in Table 5.

Comparing the radial temperature profiles at $x = 500 \mu\text{m}$ (Figure 24) with the contours of volume fraction of water (Figure 22) shows that in the liquid region, the slope is higher compared to that in the vapor region. This is due to lower thermal diffusivity of liquid water compared to vapor. In addition, the fiber thermal diffusivity is lower than the fluid thermal diffusivity, therefore, the slope is higher in the fiber wall. Note that the temperature profiles are not corresponding to the water/vapor interface.

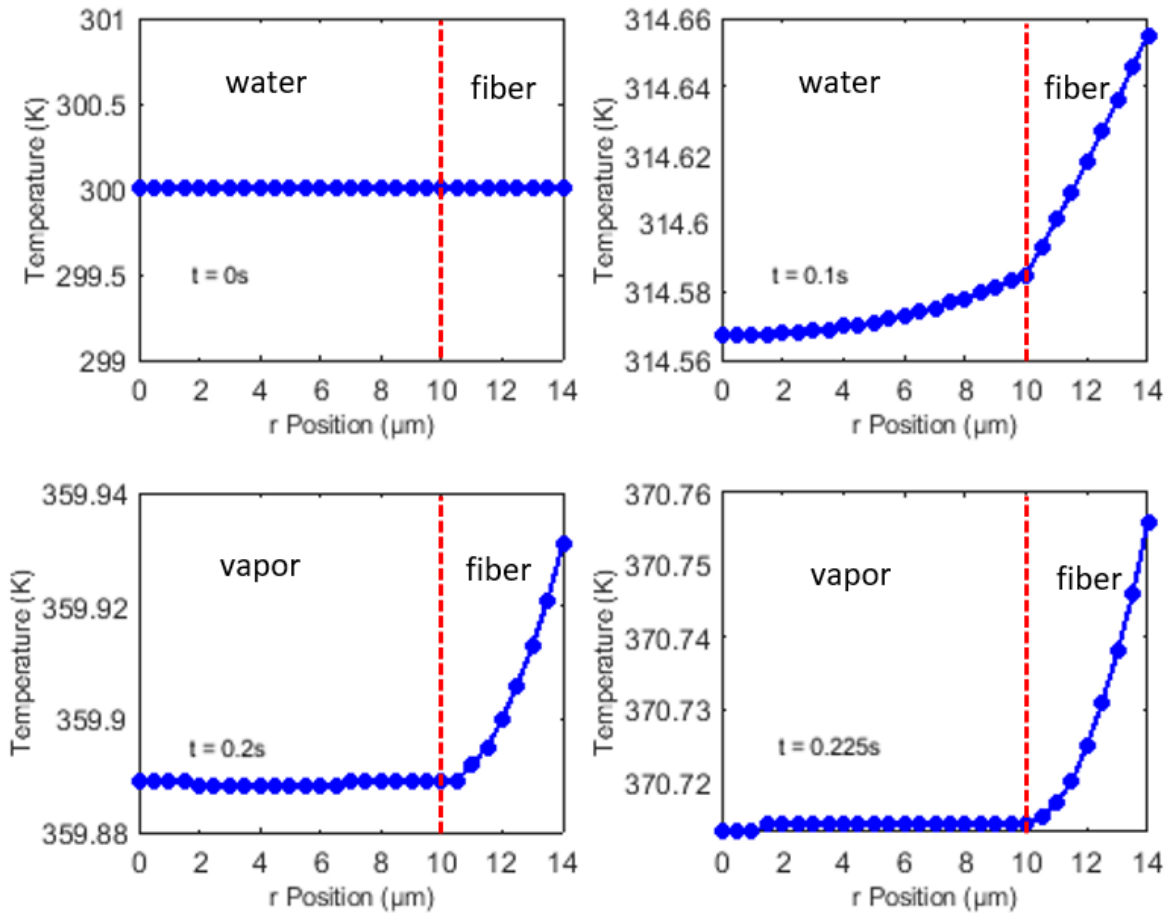


Figure 24. Radial temperature profiles at $x = 500 \mu\text{m}$ (middle of the fiber) at different times for the case specified with stars in Table 5.

3.2.2 Heat Flux at the Water/Vapor Interface

One of the challenges in the dynamic zone of three phase liquid/gas/solid contact line is to understand the heat transfer process in this zone. This phenomenon can contribute to studies of

several physical problems, such as cavitation, boiling, spreading and evaporation of droplets [112 and 113]. In the current paper, the heat flux (q'') along the inner fiber-wall surface, which includes the three-phase contact line of water film with the fiber surface has been calculated using the corresponding temperature profiles as depicted in Figure 25:

$$q'' = \int \lambda \frac{\partial T}{\partial y} \quad (3-18)$$

The heat flux profiles show that the interface position can be tracked by sudden changes in the heat flux. Due to the curvature at the three-phase zone, the evaporation rate is higher at the interface. Therefore, there is a jump in heat flux due to evaporation at the interface. The heat flux at the inner fiber-wall in contact with the liquid phase is slightly less than 3000 W/m^2 , due to the higher thermal conductivity of liquid water compared to that of vapor phase. Furthermore, the symmetry boundary condition at the right boundary of the fiber results in zero heat flux gradient at the right end of the fiber. For the energy balance inside the fiber, the applied heat flux to the outer surface of the fiber should be equal to the sum of the output energy from the inner fiber-wall and the sensible heat of the fiber. As an example, at time = 150 ms, from 3000 W/m^2 heat flux applied to the outer surface of the fiber, 62% consumes for the sensible heat of the fiber.

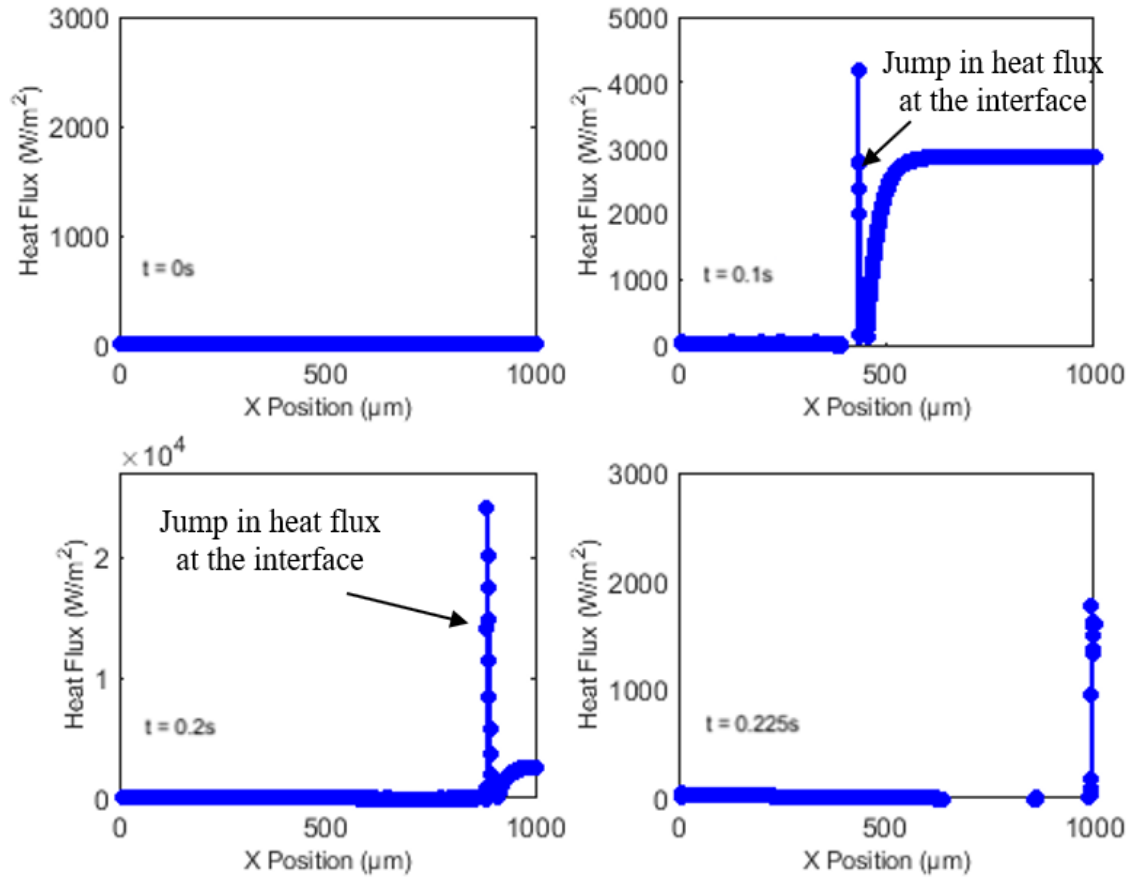


Figure 25. Heat flux profiles at $y = 10 \mu\text{m}$ (the inner surface of the fiber) at different times for the case specified with stars in Table 5.

For illustration purposes, the temperature profile and heat flux profile at inner wall of the fiber at 150 ms are compared in Figure 26. This figure shows that due to higher heat capacity of liquid phase compared to that of vapor phase, the change in the temperature slope for vapor is higher than liquid. The temperature in the vapor phase decreases as it approaches to the interface. There is change in slope of the temperature profile at the interface region due to evaporation. These observations agree with the temperature contours in Figure 26 which show how the vapor temperature changes along the x-direction. In addition, the contours of volume fraction of water specify the position of the interface between liquid water and water vapor. The calculations show that the maximal heat flux occurs in the region of the contact line, and it exceeds the average heat flux on the entire fiber inner wall surface by a factor of 2.5-11. This can be explained by heat inflow from the fiber to the liquid due to the relatively high heat conductivity coefficient of fiber,

and high evaporation rate in the contact line zone. These findings agree with both theoretical and experimental studies that suggest that heat transfer near the contact line can be an order of magnitude higher than the average value [112 and 113]. The current study confirms this behavior.

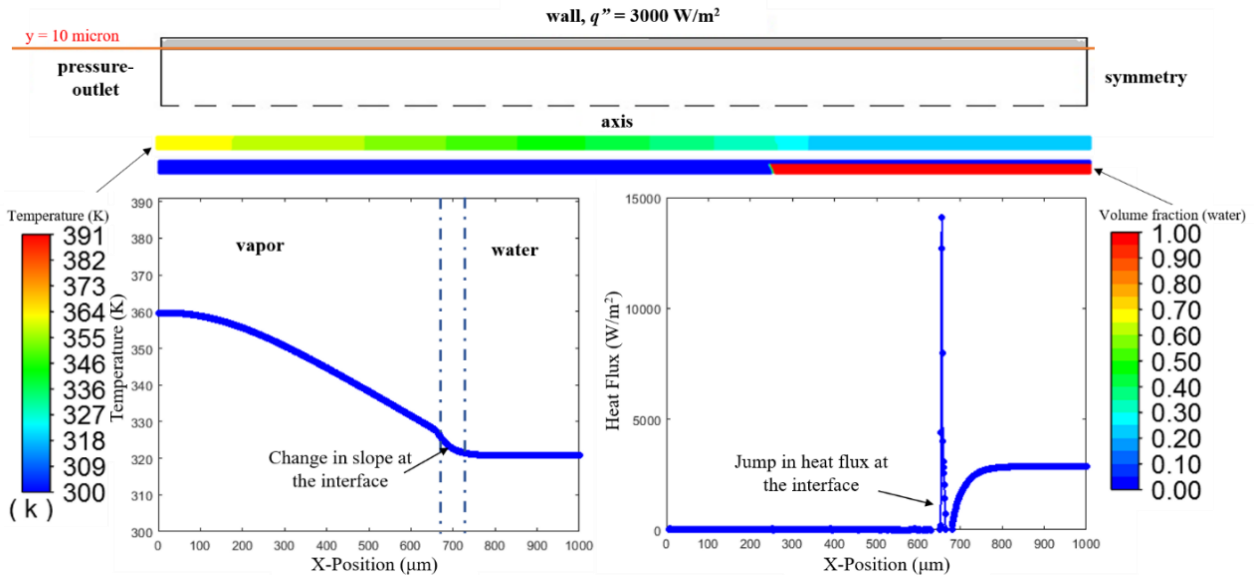


Figure 26. Contours of temperature and volume fraction of water at time = 150 ms. The profiles of temperature and heat flux are plotted at the inner surface of the fiber wall ($y = 10 \text{ micron}$).

3.2.3 Effect of Applied Heat Flux on Increasing the Drying Rate

The effect of applied heat flux to the fiber outer wall on change in the liquid volume is depicted in Figure 27. In the beginning, due to the sensible heat of the fiber, the drying rate is almost the same for different values of applied heat flux (i.e., conjugate heat transfer problem). However, as the fiber warms up, the higher applied heat flux on the outer surface of the fiber wall results in decrease in the drying time. It should be noted that by increasing the applied heat flux by a factor of five, from 1000 W/m^2 to 5000 W/m^2 , the drying time only improves by a factor of 1.5.

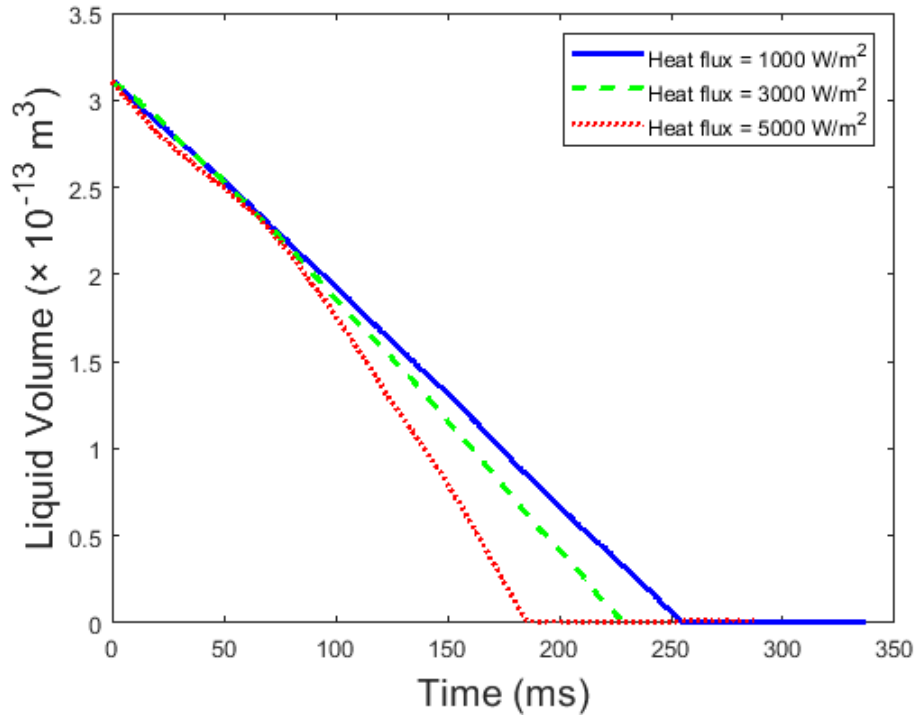


Figure 27. Changes in liquid volume versus time for the cases with different applied heat fluxes. The rest of the properties are specified with stars in Table 5.

3.2.4 Effect of Surface Tension on Drying Rate and Marangoni Effects

The effect of water/air surface tension on liquid volume change with time is shown in Figure 28. Decreasing the surface tension decreases the drying time. Surface tension is the attractive force exerted upon the surface molecules of a liquid by the molecules beneath, which tends to minimize the surface area. Hence, increasing surface tension decreases the interface between liquid and gas phases. Since the evaporation happens only at the interface, decreasing the interface area increases the drying time. It should be noted that the properties considered in this study are for pure water, which is not the case for the paper industry. However, the results show that the presence of impurities enhances the drying rate (i.e., decreases drying time).

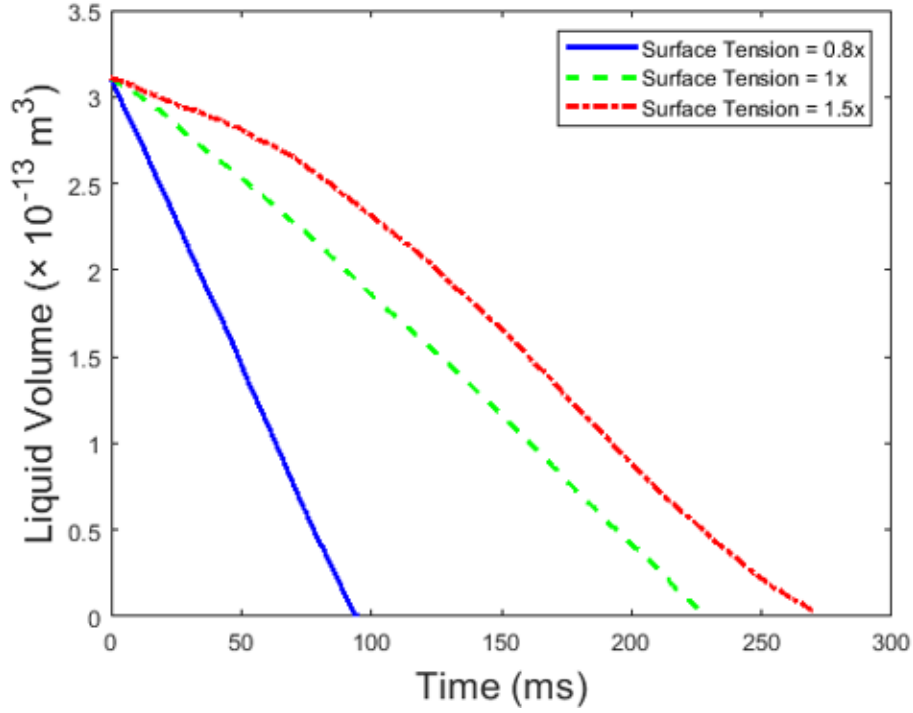


Figure 28. Changes in liquid volume versus time for different surface tensions. The rest of the operating parameters are specified with stars in Table 5.

To explore the effect of Marangoni flows on water removal from a single fiber, the results are compared with a constant surface tension simulation. The plot in Figure 29(a) compares the drying curve for a case without Marangoni effect with a case with Marangoni effect.

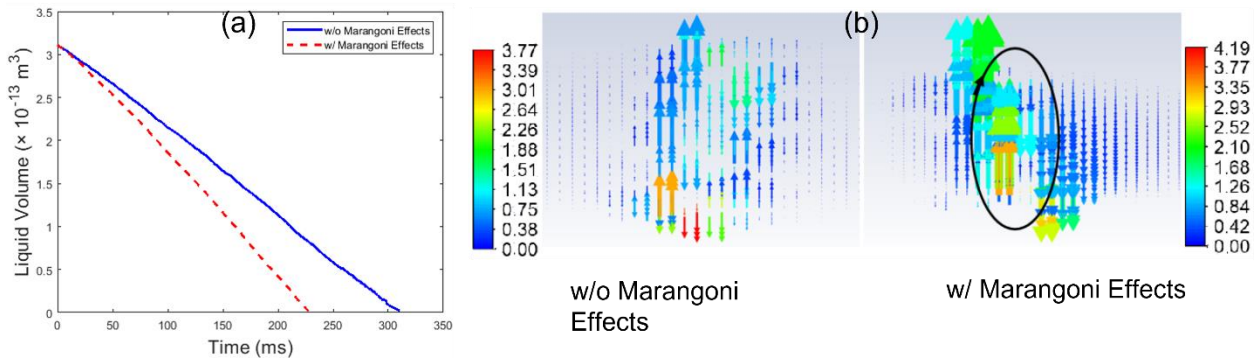


Figure 29. (a) The effect of Marangoni flows on the changes in liquid volume versus time; (b) velocity vectors (m/s) at the interface at time = 50 ms. The length shown here is 15 μm . The rest of the operating parameters are specified with stars in Table 5.

Figure 29(b) compares the velocity vectors at the interface region at time 50 ms, for two cases: without Marangoni effects and with Marangoni effects. The vectors in this figure show that the temperature differences in two sides of the vapor/water interface results in Marangoni instabilities, while in the case of without Marangoni effects (constant surface tension), the vectors are in random directions. The Marangoni flows at the interface result in clockwise flow in the liquid and counter clockwise flow in the vapor, which agrees with the results reported by Rashid et al. [40]. In the presence of Marangoni effects, the instabilities induced at the interface lead to higher drying rate and therefore, reduces the drying time.

3.2.5 Effect of Fiber Geometrical Dimensions on Drying Rate

The physical dimensions of fibers are another effective parameter that can influence the drying behavior of water trapped inside the fiber. In this study, the effect of various fiber diameters, fiber lengths, and the fiber wall thicknesses are considered. Increasing fiber diameter increases the volume of liquid inside the fiber and hence increases the drying time. Figure 30 shows that, under the conditions studied here, by increasing the fiber diameter from 10 μm to 25 μm , the liquid volume inside the fiber increases by a factor of 5, while the drying time increases more than double.

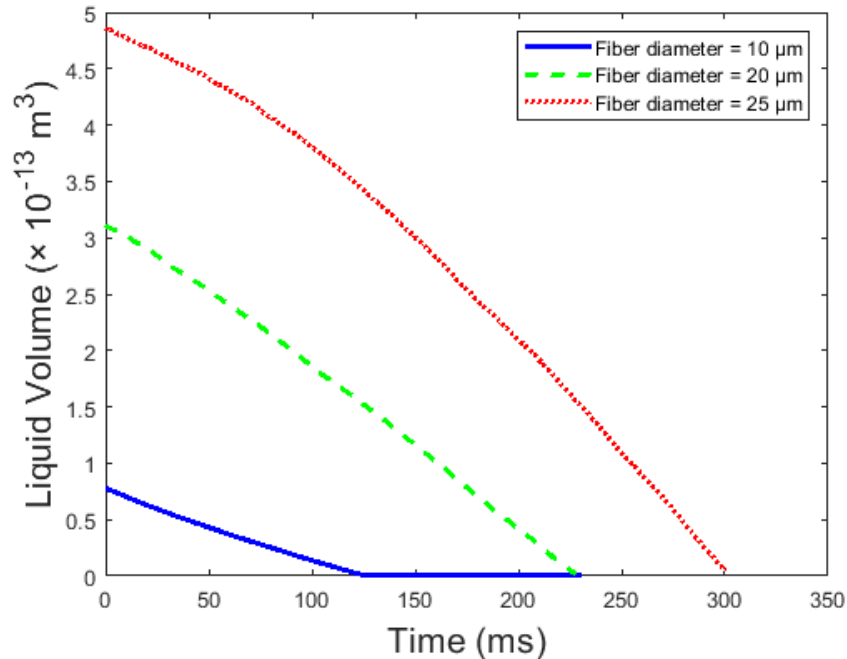


Figure 30. Changes in liquid volume versus time for the cases with different fiber diameters. The rest of the properties are specified with stars in Table 5.

With an identical fiber diameter, the initial liquid volume inside the fiber linearly increases with the fiber length. Figure 31 depicts the liquid volume as a function of drying time for three different fiber lengths. The drying times to reach zero moisture content are almost in sync with the fiber lengths.

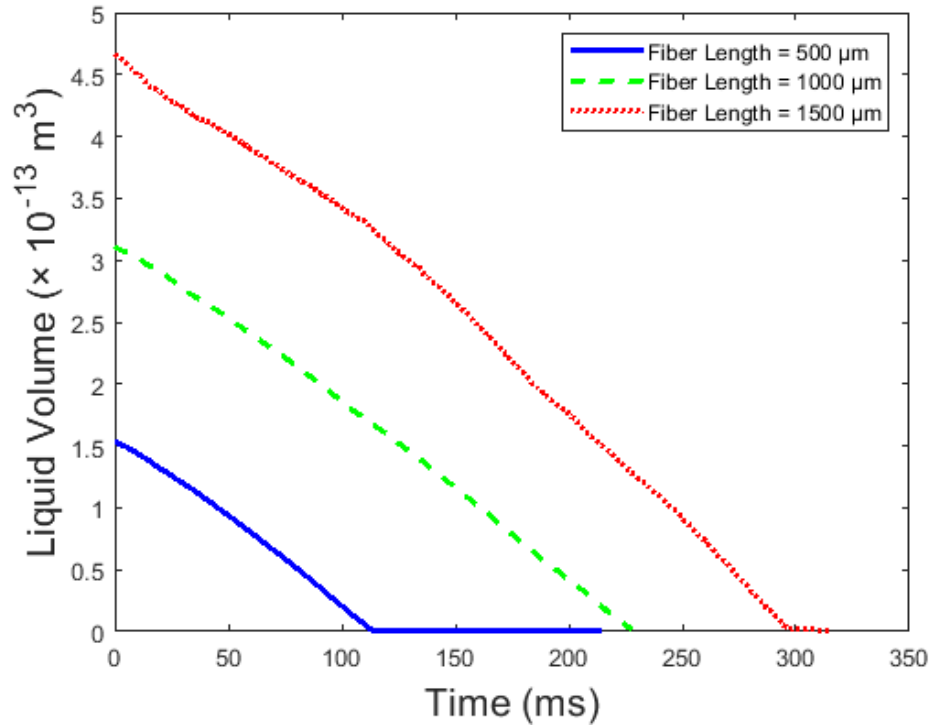


Figure 31. Changes in liquid volume versus time for the cases with different fiber lengths. The rest of the properties are specified with stars in Table 5.

Figure 32 illustrates the effect of fiber wall thickness on the evaporation rate. In the beginning, since the fiber itself is getting heated, the difference in liquid volume change with time in the three cases is not very significant. However, the evaporation rate (i.e., loss of liquid volume with time) becomes higher with the thinner fiber wall. This is simply because the thinner wall has a less resistance to the transfer of heat to the interior of fiber.

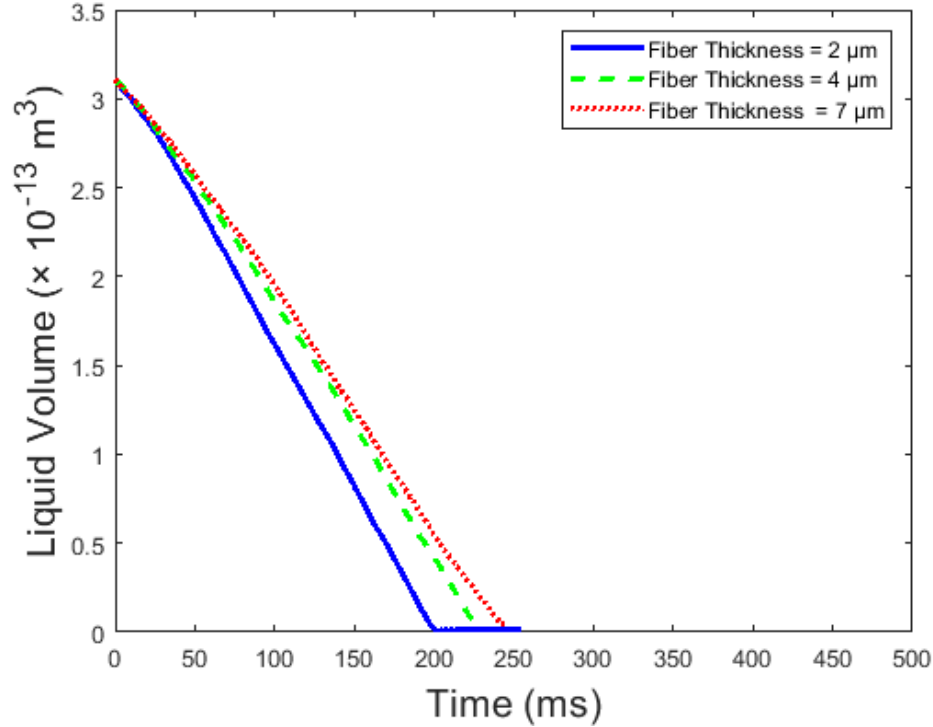


Figure 32. Changes in liquid volume versus time for the cases with different fiber wall thicknesses. The rest of the properties are specified with stars in Table 5.

3.3 Summary and Conclusions

A numerical model was developed for studying a conjugate-heat and mass transfer problem, using the VOF method. The effects of applied heat flux, water properties, fiber surface properties, and physical dimensions of fibers were studied. Moisture removal was studied by monitoring the liquid volume inside the fiber as a function of time. Using the temperature measurements at the contact line of vapor/water/fiber, the heat flux in the dynamic three-phase zone was studied. According to the modeling results, the maximum heat flux occurs in the region of the contact zone, and it exceeds the average heat flux on the entire fiber surface by a factor of 2.5-11. This was explained by heat inflow from the fiber and high evaporation rate in the contact line, due to the interface curvature. Furthermore, the results showed that increasing the applied heat flux and decreasing the surface tension of water/air lead to increasing the rate of water removal from a single cellulose fiber. Applying the instabilities due to Marangoni effects in the simulations, by including the changes of surface tension as a function of temperature, decreases the drying time. Therefore, using

the appropriate surfactants to decrease the surface tension and decrease the drying time is recommended for increasing energy efficiency at the final stages of drying process. Changing the physical dimensions of fibers alters the evaporation behavior for water trapped inside the fiber. Increasing the fiber diameter, fiber length, and fiber wall thickness results in increase in the drying time. This research provided fundamental understanding of the effective factors on removal of water trapped inside a single cellulose fiber in micro scale.

Chapter 4: Direct-Contact Ultrasonic Drying of Hand-Sheets

To the best of the author's knowledge, ultrasonic drying has not been published in the literature for paper drying. Hence, the current chapter is devoted to exploring the potentials and limitations of direct-contact ultrasound for hand-sheet and paper drying. Non-contact ultrasound for paper drying will be addressed in the next chapter. In this chapter, the drying behavior of hand-sheet samples in the presence of ultrasound is compared to the direct contact thermal heating. A series of systematic experiments are conducted to understand the effects of ultrasonic waves on drying behavior of hand-sheet samples. Hand-sheets are Northern bleached hardwood and softwood. The independent variables in the experiments are including the initial dry-basis moisture content (DBMC), final thickness of the sample, and refining condition of the pulp (unrefined vs refined). The utilized research methodology is 2^3 factorial design of experiments to be able to investigate the main and interaction effects between the independent variables on paper drying characteristics. In addition, the quality characteristics of the ultrasonically dried hand-sheets are studied, including color, pore distribution, surface smoothness, and tensile strength. In the following sections, the materials and methods are described and then the results are discussed. The final section presents the conclusion.

Keywords: drying of paper; ultrasonic drying; quality measurements; energy analysis

4.1 Materials and Experimental Method

Figure 33 illustrates the experimental setup for direct-contact ultrasonic drying. The major components in the experimental setup include: a power amplifier (AG 1014, T&C power), an ultrasonic transducer, a microbalance (Sartorius BCE6200, 0.001 g accuracy), an acrylic housing to decrease the noises and fluctuations induced by the surrounding, and a FLIR infrared camera. It should be mentioned that the upper side of the housing was removed to make sure that it does not impact the moisture removal and to record the thermal behavior during the experiments. In addition, type T thermocouples are used to measure the temperature of the sample.

The results of ultrasonic drying are compared to conductive thermal drying experiments using a hot plate (Corning PC-420D). In this case, the samples were simply placed on the top of hot plate maintained at 80 °C.

In preparation of the hand-sheet samples, the procedure of TAPPI T205 standard is followed and the two pressure stages each at 50 psi for 5:30 min and 2:30 min, respectively are applied. The final dry basis moisture content (DBMC) of the sample in this case is 150%. For the samples with 100% DBMC, the samples were dried at ambient until the desired initial moisture content was reached. Four different pulps are used in the experiments: softwood and hardwood, both unrefined and refined. The pulps are Northern Bleached Hardwood Kraft (NBHK) and Northern Bleached Softwood Kraft (NBSK). The refining is performed using Beloit Double Disk refiner. The pulps have consistency of 4% and by adding water, the desired initial weight is obtained. The pulp consistency is defined as the percentage by weight of oven-dry fibers in a stock suspension (slurry).

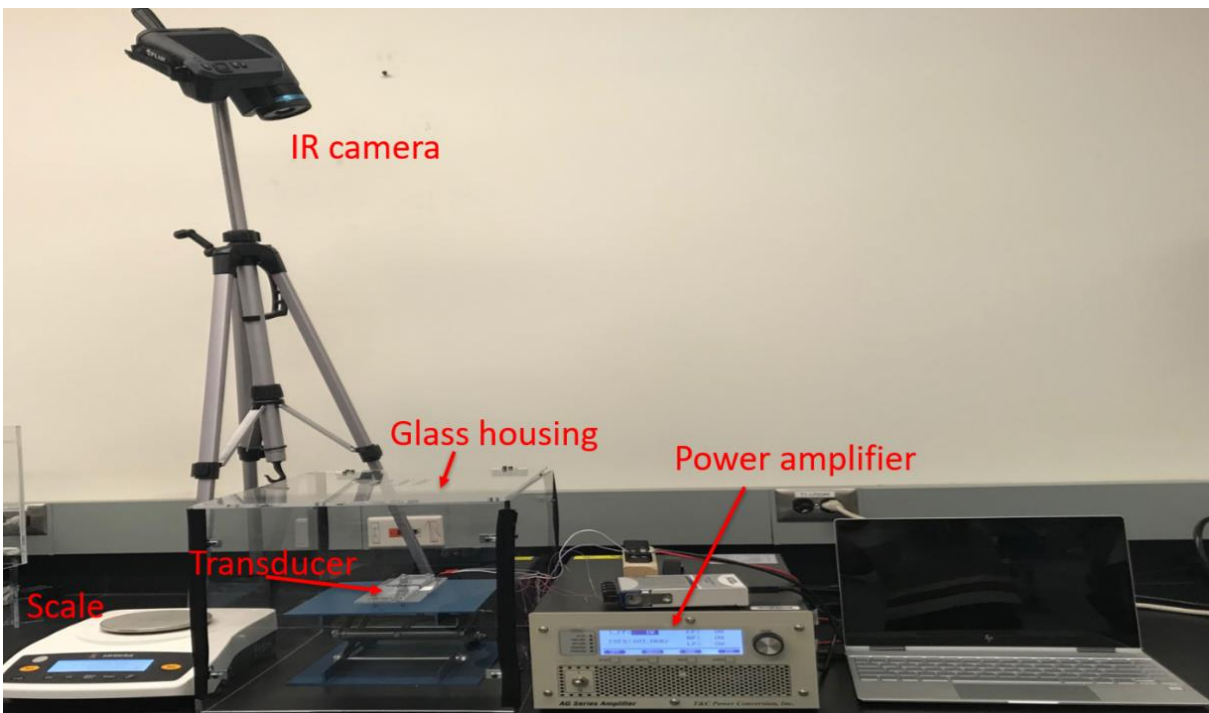


Figure 33. The major components of the experimental setup.

The general qualitative differences between softwood and hardwood and also refined and unrefined are summarized in Table 6 and Table 7, respectively.

Table 6. Comparison between the properties of softwood and hardwood pulps.

Property	Hardwood	Softwood
Pulp Freeness (CSF)		Higher
Water Retention Value (WRV)	Higher	
Surface Roughness	Depends on the species and texture uniformity. In general, softwood is rougher.	
Fiber Length		Higher
Coarseness		Higher
Density	Higher	
Tensile Strength		Higher
Cost	Higher	
Initial Brightness		Higher
Durability	Higher	
Product Porosity		Higher
Resistance to tearing		Higher

Table 7. Comparison between the properties of refined and unrefined pulps.

Property	Refined	Unrefined
Pulp Freeness (CSF)		Higher
Water Retention Value (WRV)	Higher	
Surface Roughness	Depends on the species and texture uniformity	
Fiber Length		Higher
Tensile Strength	Higher	
Density	Higher	
Porosity		Higher

The diameter of the hand-sheet samples was 19.8 mm to precisely match the transducer’s surface size. The mean thickness of the hand-sheets was measured using a digital thickness gauge (accuracy 0.002 mm).

Figure 34(a) shows the piezoelectric transducer used in the experiments. The resonant frequency of the transducer is 1.7 MHz, and its surface area is 314 mm². Since the sample needs to be in direct contact with the transducer, the sample size is the same as the transducer (Figure 34(b)).

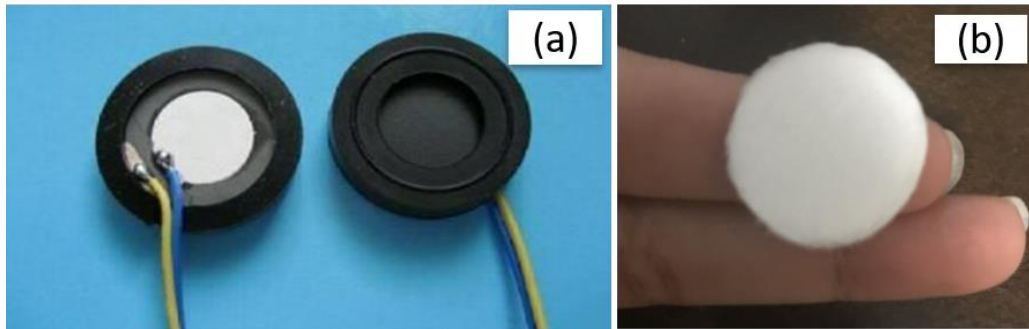


Figure 34. (a) Mist generation transducer and (b) paper sample used in the direct-contact ultrasonic drying experiments.

Dry basis moisture content (DBMC) of the samples is calculated as:

$$DBMC = \frac{\text{Weight of water}}{\text{Weight of dry matter}} = \frac{m_t - m_{bone-dry}}{m_{bone-dry}} \quad (4-1)$$

where m_t is the mass of the sample at time t and bone-dry is the mass of the dried sample, determined by drying it in an oven until its moisture is fully removed.

The uncertainty analysis for the derived quantities is calculated according to Kline and McClintock [114] and are given in Table 8.

Table 8. The derived uncertainty for the experimental tests.

Derived Quantity	Maximum Uncertainty
DBMC	± 8.15%
Whiteness index	± 0.25%
Change in color	± 3.04%
Energy efficiency	± 5.61%

The standard deviation of the reported experimental results for DBMC is 3.8, determined based on repeating each corresponding experiment five times.

Color analysis is done using colorimeter ColorFlex EZ. This device measures the color based on CIELAB color system ($L^*a^*b^*$). The results of colorimeter measurements are used to calculate the change in color index (ΔE) and whiteness index (WI) for hand-sheets dried by ultrasound mechanism.

$$\Delta E = \sqrt{(L_2^* - L_1^*)^2 + (a_2^* - a_1^*)^2 + (b_2^* - b_1^*)^2} \quad (4-2)$$

$$WI = 100 - \sqrt{(100 - L^*)^2 + (a^{*2} + b^{*2})} \quad (4-3)$$

The 2D porosity of the samples are estimated from microscopic images taken with Keyence VHX-7000 4k digital microscope. Thresholding is applied to the microscopic images to measure the pore volume percentage of the hand-sheets in 2D using ImageJ software. Non-contact profilometry measurements are performed using ZYGO 3D profilometer. In addition, Multitest-dV Mecmesin device is used for measuring the tensile strength of the hand-sheets. The samples are chosen as rectangular shapes with about 19.8 mm in length and 5 mm in width. The length between the grips is fixed at 11 mm for all the tests conducted and therefore 9 mm of the length is in the grips' region.

4.1.1 Design of Experiments

Factorial design is a systematic method for designing the experiments to determine the relationship between the factors in an experiment and the response value (outcome). In addition to the effect of individual factors, it also helps to understand the interactive effects of different factors in analyzing the results [115]. In this study, 2^3 factorial design is applied considering three main factors including the initial moisture content, final thickness, and the refining condition of the pulp. Each factor has two levels in this design and the replicate number is 5. Minitab software is used for designing and statistical analyzing of the experimental results by applying analysis of variance (ANOVA). In the analysis, p-values less than 0.05 are considered statistically significant. The relationships between the response values of the experiments; including the total time of drying and the area under the drying curve; and the factors are investigated using a linear regression analysis as follows:

$$Y = f(x) = \beta_0 + \sum_{i=1}^k \beta_i X_i + \sum_{i=1}^k \sum_{j=1}^k \beta_{ij} X_i X_j + \beta_{123} X_1 X_2 X_3 \quad (4-4)$$

where Y is the predicted response as a function of the factors; k is the number of factors, and X_i ($i = 1, 2, 3$) are the controlling factors. β_0 is the constant coefficient, β_{ij} are the coefficients for the interactive effects of the factors, and β_{123} is capturing the interactive effect of all the three factors. Table 9 shows the nine designed experiments along with the upper and lower levels for each factor. In this table, the first 8 experiments are the corners of the cube, and the ninth experiment is center point of the cube. Abbreviations are employed to define each of the experiments and are used in the remaining of the paper.

Table 9. Upper and lower levels of factors for 2^3 factorial design of experiments for both hardwood (H) and softwood (S). R defines refined and unR defines unrefined.

Experiment Number	Factors		
	Refining Condition	Initial Moisture Content – DBMC (%)	Thickness (mm)
H or S-unR-100-0.3	Unrefined	100	0.3
H or S-unR-150-0.3	Unrefined	150	0.3
H or S-unR-100-0.6	Unrefined	100	0.6
H or S-unR-150-0.6	Unrefined	150	0.6
H or S-R-100-0.3	Refined	100	0.3
H or S-R-150-0.3	Refined	150	0.3
H or S-R-100-0.6	Refined	100	0.6
H or S-R-150-0.6	Refined	150	0.6
H or S-Center Point	50%Unrefined & 50%Refined	125	0.45

4.2 Results and Discussion

4.2.1 Sample's Weight Measurements

To determine and verify the accuracy of the method for measuring the sample's weight, similar refined hardwood samples are used and the changes in the weight of the samples are recorded by repeating the experiments. Three different methods are compared: (1) continuous measurements

by placing the scale underneath the transducer and sample during the experiments, (2) intermittent measurements of the weight during the experiments, and (3) using fresh samples to measure the weight at different drying times. The results showed that the ultrasonic vibrations in addition to the noises induced by the connected wires to the setup, changes the weight of the setup artificially and drastically during the experiments. Therefore, continuous measurement of the weight of the sample is not an accurate method for the current setup. The second method is to measure the weight of the sample, intermittently. The third method is to prepare fresh samples and dry it until a specific time and then measure the weight. The latter is the most accurate method for measuring the weight, but also most expensive and time-consuming method among the three. Figure 35 compares the results of the experiments for the intermittent method and the fresh samples method for similar samples. This figure shows that these two methods present very similar results and hence, using intermittent measurements of the weight is an accurate way for the measurements. Therefore, in all the experiments in this chapter, the changes in moisture content are measured by intermittent measurements of the sample's weight at 10 sec intervals.

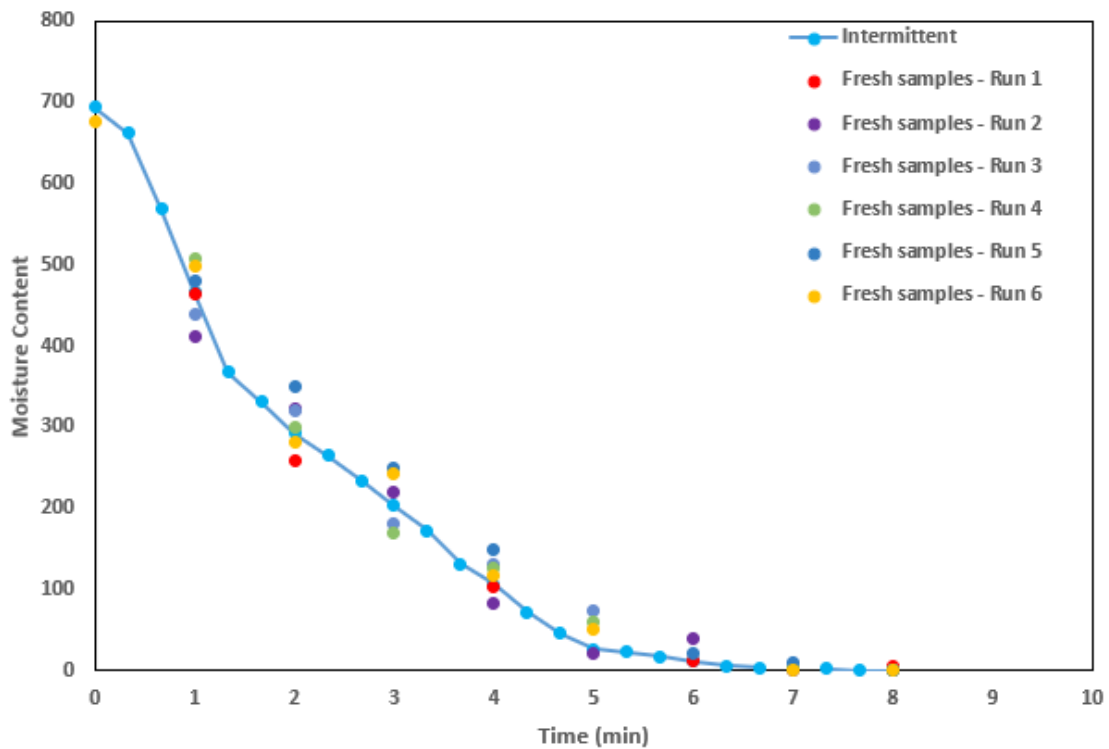


Figure 35. Comparing the weight measurements results using fresh samples and using intermittent method. The number of runs shows the number of repeats of the experiments using the fresh samples.

4.2.2 Illustration of Ultrasonic Drying

As it was mentioned in the introduction, the mechanism of ultrasonic drying is atomization due to the mechanical vibrations. Figure 36 shows the atomization for two hand-sheet samples with two different moisture contents. Figure 36(a) shows the atomization for an over-saturated unrefined softwood hand-sheet and Figure 36(b) shows the atomization for a similar unrefined softwood hand-sheet with moisture content 150% DBMC. For the over-saturated hand-sheet the amount of moisture that is removed by atomization is much higher than the moisture that is removed from the sample with 150% DBMC moisture content. Therefore, ultrasonic atomization rate is higher at higher moisture contents. With the overly saturated samples, the excess moisture resides on the sample surface and thus, readily removeable by the ultrasonic mechanism.

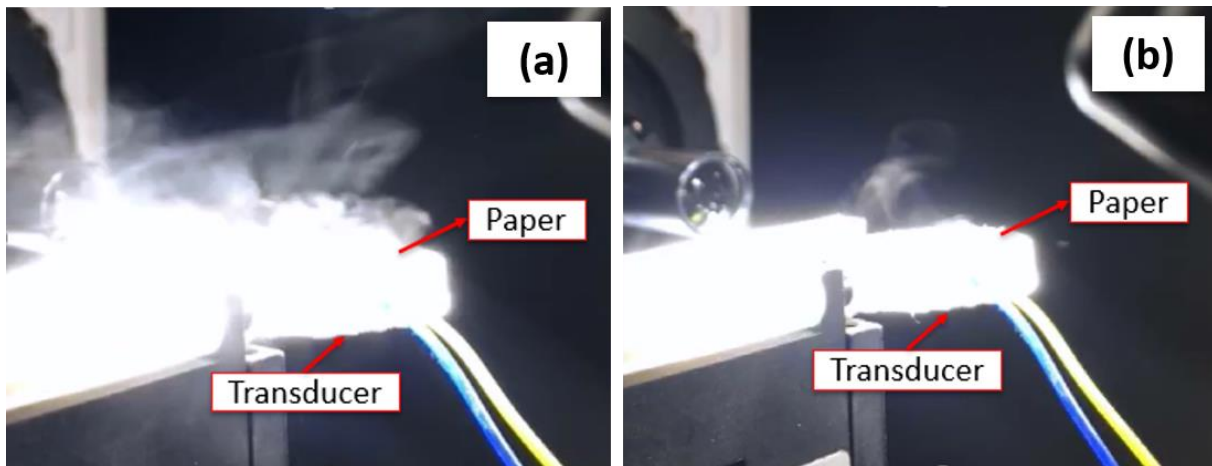


Figure 36. Comparing the ultrasonic atomization for (a) an over-saturated unrefined softwood hand-sheet with (b) an unrefined softwood hand-sheet with 150% DBMC.

Looking at the IR camera images of the unrefined hardwood hand-sheet (150% initial DBMC) placed on the surface of the transducer at selected times (Figure 37) implies that the temperature increases steadily from the center of the transducer toward the outside, which confirms that the center oscillates the most. A similar behavior was also observed in [48] in ultrasonic drying of a fabric sample.

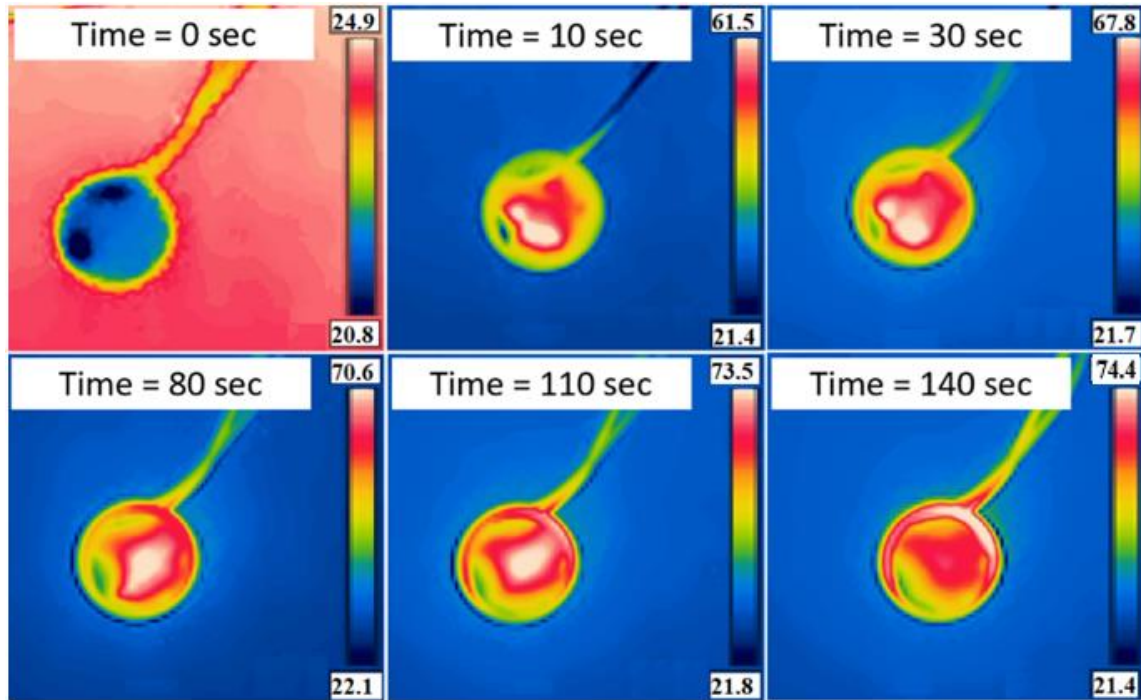


Figure 37. Selected IR image sequences at different times of ultrasonic drying for unrefined hardwood hand-sheet (150% initial DBMC) placed on top of the transducer. The temperatures are in °C.

Temperature measurements during the ultrasonic drying experiments revealed that the temperature of the surface of the sample increases up to about 80 °C before complete drying. Hence, it is concluded that the dominant mechanism for direct-contact ultrasonic drying initially is atomization but at the final stages of drying, heating is also important. In addition, as the hand-sheet dries and moisture content decreases, due to the bulging effect, the temperature of the hand-sheet decreases. It should be mentioned that for a piezoelectric transducer, the temperature must not exceed its curie temperature to function properly. For the piezoelectric used in this study, the curie temperature is 320 °C and since the maximum temperature measured is less than 80 °C, it can be concluded that the working temperature is proper for the employed transducer.

To have a better understanding of the temperature changes during ultrasonic drying, three thermocouples are used to measure the temperature of (1) the transducer's surface (underneath the sample), (2) sample's surface (on top of the sample), and (3) 4 mm above the sample. The thermocouple above the sample, in fact measures the temperature of the mist coming out of the sample. Figure 38 shows the changes in temperature during drying for these three thermocouples.

Initially, all the three thermocouples are at room temperature. After applying ultrasound, the temperature rises. The temperatures of the sample's surface and the transducer's surface continue to increase as the sample gets dried and as more conversion of electrical energy to heating occurs. The temperature of the mist above the sample increases but after some time, the temperature decreases. This decrease in the temperature is due to the decrease in evaporation rate. As the sample gets dried, the amount of moisture in the sample decreases and therefore, the evaporation rate decreases. This results in decrease in mist concentration above the sample and hence, the thermocouple shows a lower temperature. The maximum temperature for the sample's surface and the transducer's surface agrees with the IR images discussed above.

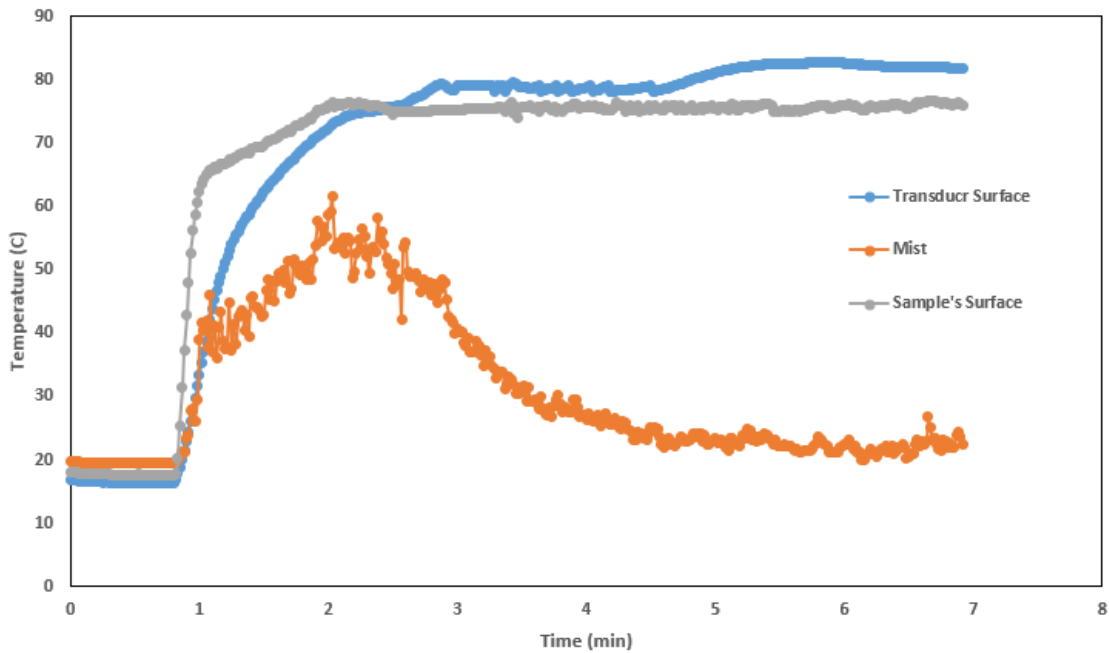


Figure 38. Temperature changes during direct-contact ultrasonic drying for an unrefined hardwood sample with 150% initial DBMC.

4.2.3 Comparing Ultrasonic Drying with Conductive Heat Drying

To have a better illustration of the effect of ultrasound mechanism on drying, thermal drying of hand-sheets is conducted at temperature equal to 80 °C to extract the sole impact of ultrasound.

Figure 39 compares the drying curves for an ultrasonically dried hand-sheet with a hand-sheet dried using conductive heating at 80 °C.

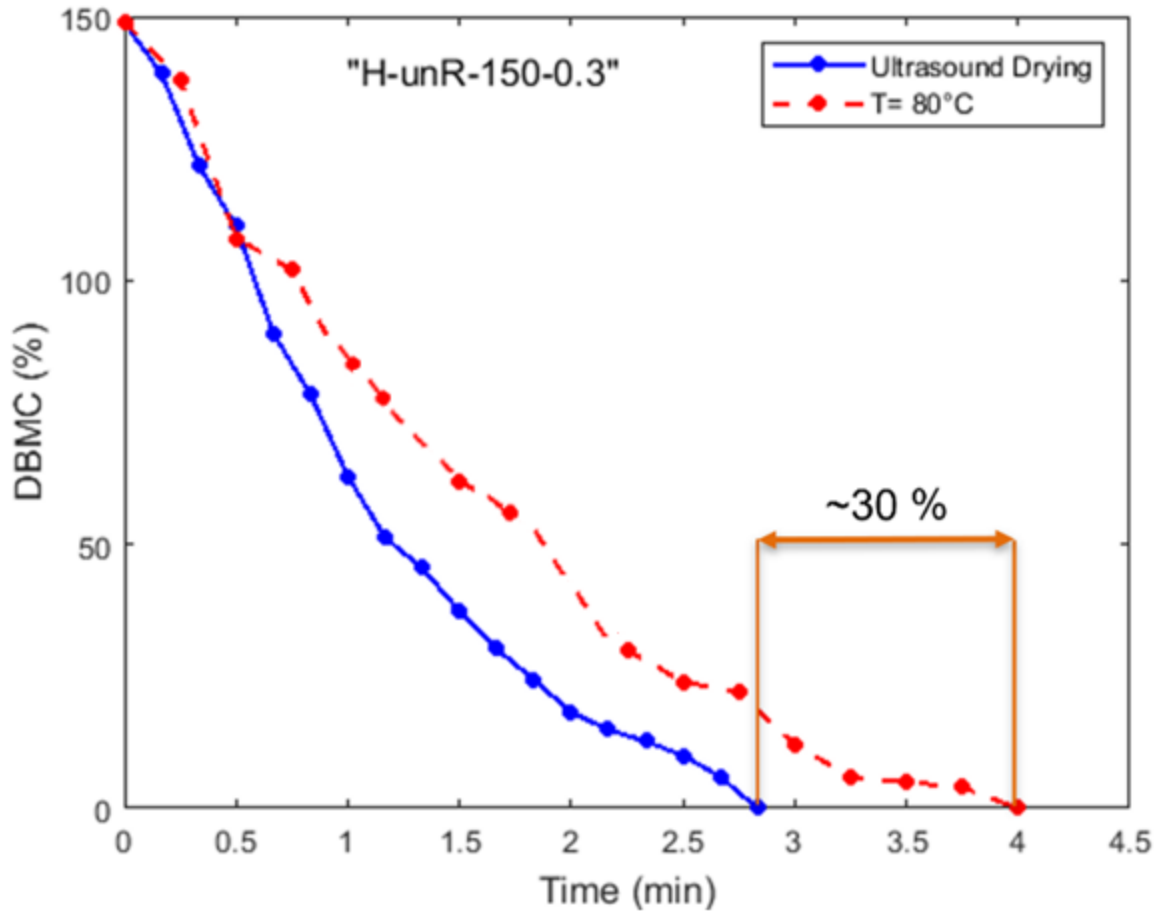


Figure 39. Comparing the drying curves for conductive heating with ultrasonic drying.

This figure shows that in the presence of ultrasound mechanism, the drying time decreases by almost 30% and hence, ultrasonic drying is faster than conductive drying under the operating conditions considered here. This finding confirms the favorable effect of atomization in ultrasonic drying. Many studies (e.g., [45] and [61]) have shown that the ultrasonic atomization enhances the heat and mass transfer coefficients, supporting the results reported in this study.

4.2.4 Analysis of the Factorial Design of Experiments

Figure 40 and Figure 41 are representing the ultrasonic drying curves for hardwood and softwood, respectively. The plots are at different combinations of initial moisture content, thickness, and refining condition of the pulps.

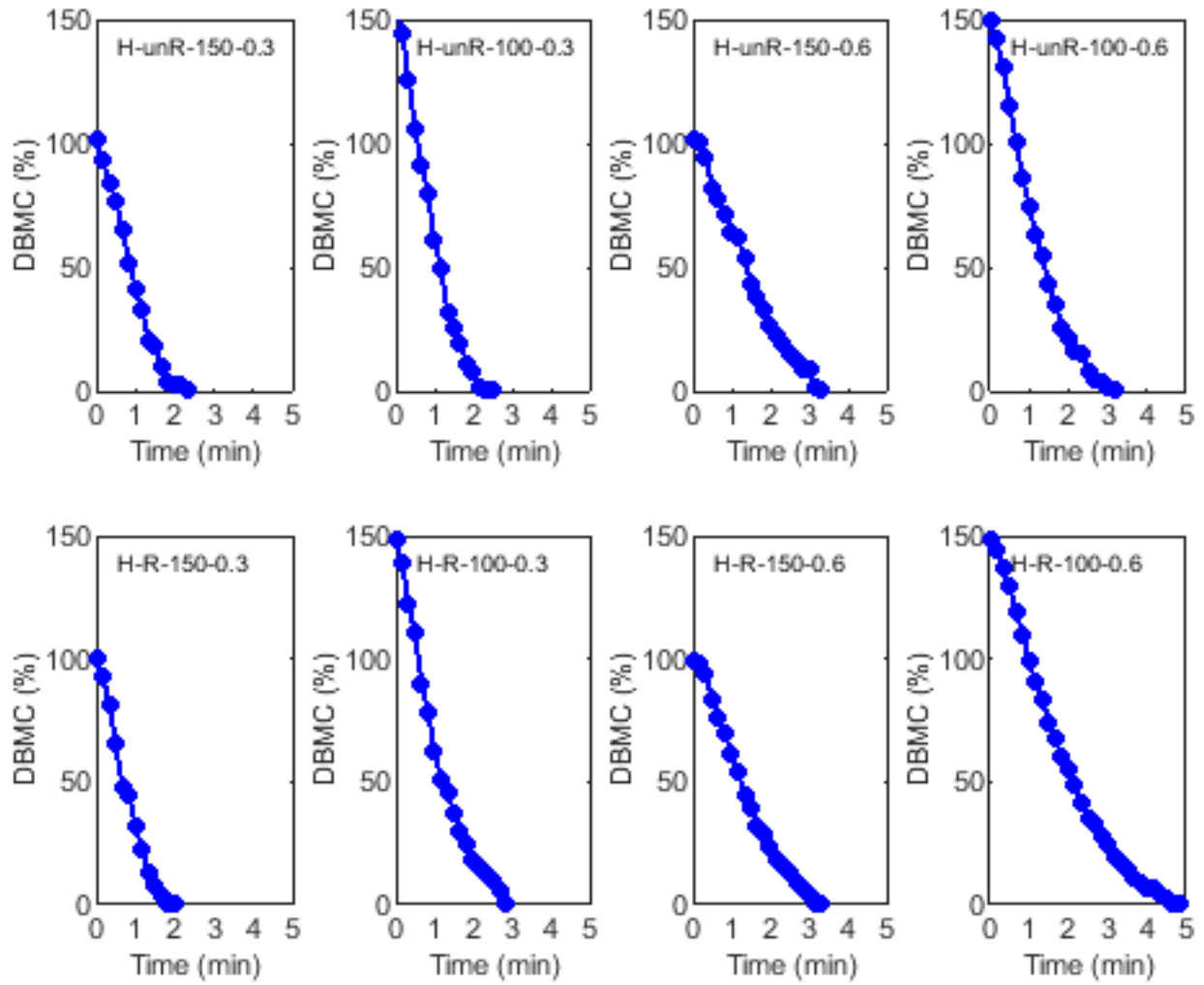


Figure 40. Ultrasonic drying curves for hardwood samples.

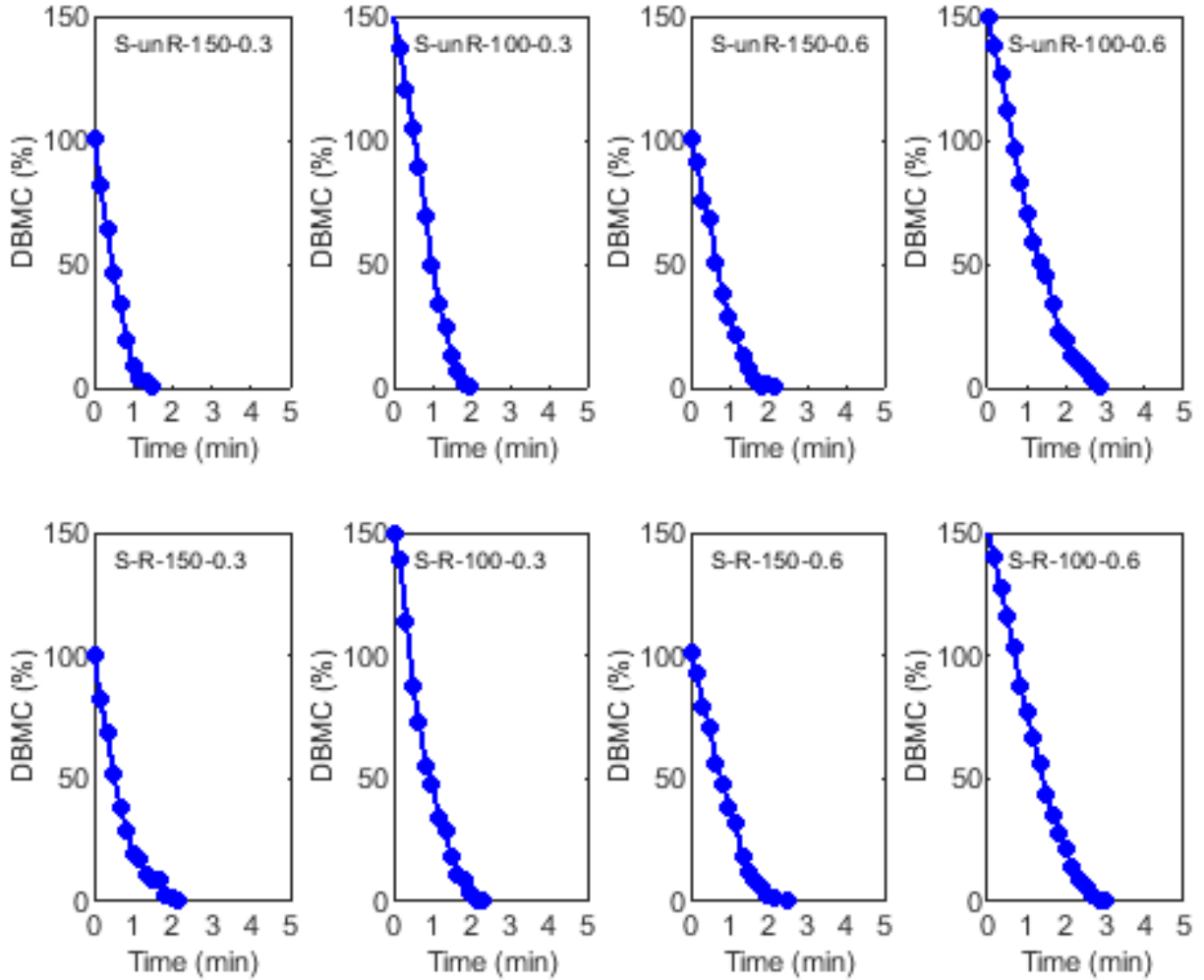


Figure 41. Ultrasonic drying curves for softwood samples.

Ultrasonic drying takes place in two phases: a relatively constant-rate drying period followed by a falling-rate drying period. The constant drying rate period corresponds to the removing of free water within the pores of paper, while the falling drying rate period is governed by the associated (bound) water trapped inside the fibers. This is typical regardless of drying mechanism.

Figure 42 summarizes the results of comparing Figure 40 with Figure 41 in terms of total time of ultrasonic drying. This figure implies that in general, unrefined samples dry faster than refined samples and the drying time for softwood is lower than hardwood. In addition, increasing the thickness and the initial moisture content of the sample increase the drying time. The shortest and longest drying times correspond to S-unR-100-0.3 and H-R-150-0.6, respectively. These

observations are potentially related to the structure and the pore characteristics of the samples. In general, hardwood has lower Canadian Standard Freeness and higher Water Retention Value compared to softwood, which makes it harder to dry. It is important to mention that for refined samples, these results may vary depending on the refining method. Furthermore, hardwood is denser than softwood and therefore its permeability is lower. This will be addressed in more detail in the next sections.

To analyze the results of the 2^3 factorial design of experiments, two response values are considered in this paper, including the total time of drying and the area under the drying curve. These two cases are discussed in the next sections.

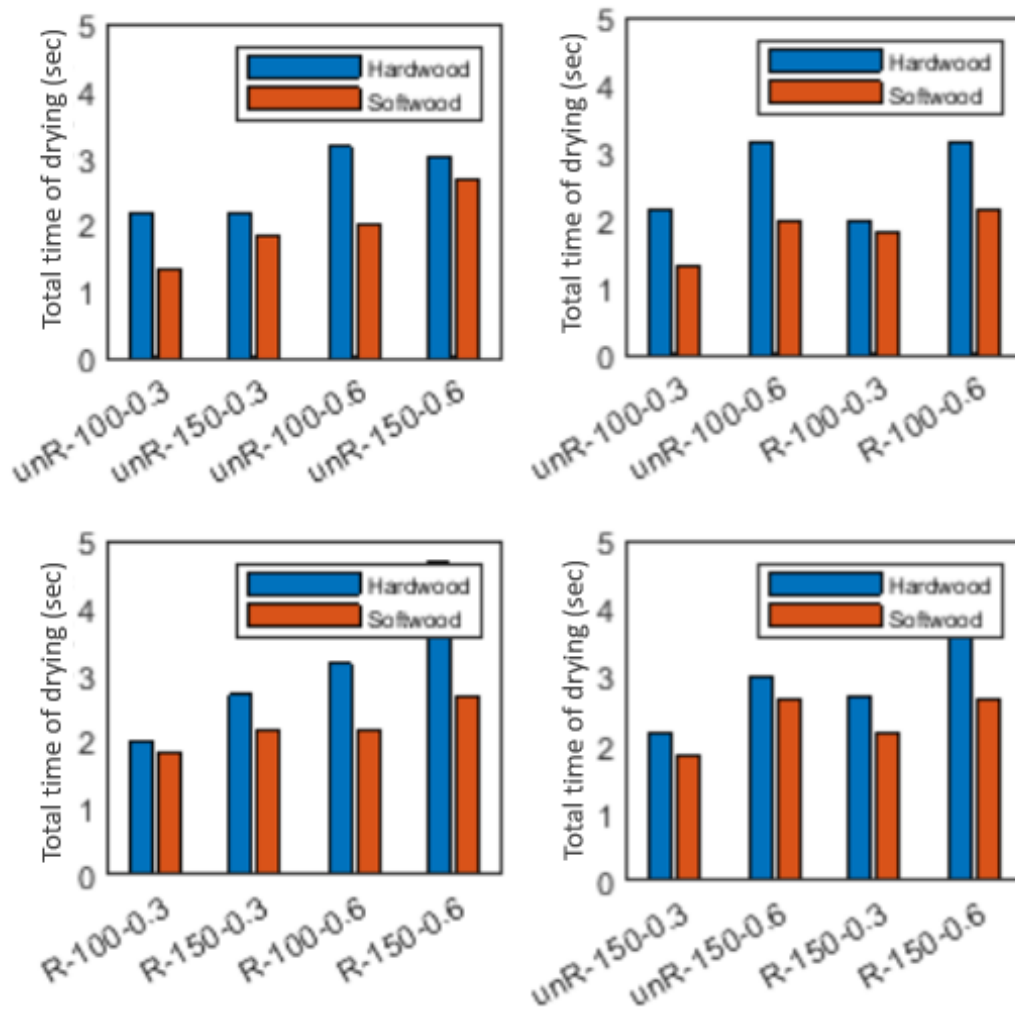


Figure 42. Comparing the total time of ultrasonically dried (direct-contact mechanism) hardwood and softwood samples

4.2.5 Effect of Controlling Factors on Total Drying Time

The analysis of variance (ANOVA) is done for both hardwood and softwood samples and each experiment is repeated 5 times. The results of ANOVA for total time of drying are summarized in Table 10 and Table 11 for hardwood and softwood, respectively.

Table 10. ANOVA for total time of drying for hardwood samples.

Source	Degree of Freedom (DF)	Sum of Squares (SS)	Mean Square (MS)	F	P
Initial DBMC	1	10004.2	10004.2	480.20	0.000
Thickness	1	31537.5	31537.5	1513.80	0.000
Refining Condition	1	9204.2	9204.2	441.80	0.000
Initial DBMC*Thickness	1	704.2	704.2	33.80	0.000
Initial DBMC*Refining Condition	1	2604.2	2604.2	125.00	0.000
Thickness*Refining Condition	1	1504.2	1504.2	72.20	0.000
Initial DBMC*Thickness* Refining Condition	1	2604.2	2604.2	125.00	0.000
Error	16	333.3	20.8		
Total	23	58495.8			

Figure 43 shows the Pareto charts of the standardized effects, which determines the magnitude and the importance of the effects, both for the main factors and their interactive effects. The reference line, the red line on the charts, depends on the significance level, which is defined as 0.05 in this study and the bars that cross this reference line are statistically significant.

Table 11. ANOVA for total time of drying for softwood samples.

Source	DF	SS	MS	F	P
Initial DBMC	1	6666.7	6666.67	106.67	0.000
Thickness	1	8816.7	8816.67	141.07	0.000
Refining Condition	1	3266.7	3266.67	52.27	0.000
Initial DBMC*Thickness	1	600.0	600.0	9.60	0.007
Initial DBMC*Refining Condition	1	416.7	416.67	6.67	0.020
Thickness*Refining Condition	1	266.7	266.67	4.27	0.055
Initial DBMC*Thickness* Refining Condition	1	150.0	150.0	2.40	0.141
Error	16	1000.0	62.50		
Total	23	21183.3			

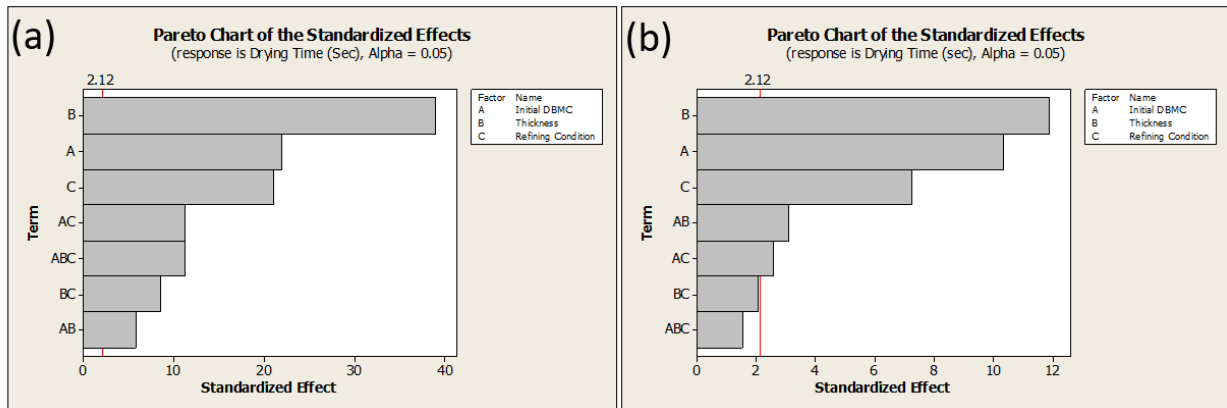


Figure 43. Pareto charts of the standardized effects from ANOVA analysis for total time of ultrasonic drying: (a) hardwood and (b) softwood.

Figure 43 shows that for both hardwood and softwood, of the parameters explored, thickness has the maximum effect on ultrasonic drying time followed by initial DBMC and refining condition of the pulp. The interactive effects of the parameters are less important for predicting the ultrasonic drying time. The results of linear regression analysis for total time of ultrasonic drying are reported in Table 12. The coefficients of determination, R^2 , are 99.43% and 95.28%, meaning that the model

could account for 99.43% and 95.28% variability in data, respectively for hardwood and softwood. According to ANOVA analysis, the models show a significant effect of the studied factors on drying time ($p < 0.01$). These data imply that the predicted correlations by linear regression analysis are adequate in describing drying time.

Table 12. Coefficients for equation (4-4) calculated from linear regression analysis.

		β_0	β_1	β_2	β_3	β_{12}	β_{13}	β_{23}	β_{123}	R^2 (%)
Hardwood	Drying time (sec)	50	0.166667	61.1111	100	1.44444	-0.833333	-294.444	2.77778	99.43
	Area under the Drying Curve (%.min)	-82.479	1.10789	164.350	138.741	0.253337	-1.16480	-433.616	3.84026	97.80
	Whiteness index	74.8997	-0.01433	-4.1305	-1.8087	0.0856239	0.0116954	4.79607	-0.0183577	97.4
Softwood	Drying time (sec)	68.3333	0.066667	-38.888	5.0	1.33333	0.133333	61.1111	-0.666667	95.28
	Area under drying curve (%.min)	-22.699	0.626696	-112.48	57.1106	1.80972	-0.436389	-77.1581	0.647876	99.34
	Whiteness index	55.3066	0.100659	42.1567	-0.2184	-0.273384	0.00405267	0.731954	-0.0079145	96.2

It should be noted that there is a lack of detailed fundamental work on ultrasonic dehydration in the literature and therefore, no in-depth understanding of the phenomena in moist porous material. In chapter 6, the ultrasonic atomization phenomenon, as the main mechanism in ultrasonic drying of a porous medium, in microscale is explored and the impacts of non-dimensional parameters on the process, including Reynolds number, Weber number, Strouhal number, and Froude number, are investigated.

4.2.6 Effect of Different Factors on the Area Under the Drying Curve

In the second case, the response value is the area under the drying curve, which represents the total change in DBMC at the total time of drying. The results of ANOVA for the area under the drying curve are summarized in Table 13 and Table 14, for hardwood and softwood, respectively.

Table 13. ANOVA for area under the drying curve for hardwood samples.

Source	DF	SS	MS	F	P
Initial DBMC	1	22395.1	22395.1	270.62	0.000
Thickness	1	20748.2	20748.2	250.72	0.000
Refining Condition	1	4722.7	4722.7	57.07	0.000
Initial DBMC*Thickness	1	21.7	21.7	0.26	0.616
Initial DBMC*Refining Condition	1	4759.8	4759.8	57.52	0.000
Thickness*Refining Condition	1	1163.4	1163.4	14.06	0.002
Initial DBMC*Thickness* Refining Condition	1	4977.3	4977.3	60.15	0.000
Error	16	1324.1	82.8		
Total	23	60112.2			

Table 14. ANOVA for area under the drying curve for softwood samples.

Source	DF	SS	MS	F	P
Initial DBMC	1	31150.3	31150.3	1855.73	0.000
Thickness	1	6984.9	6984.9	416.12	0.000
Refining Condition	1	440.4	440.4	26.24	0.000
Initial DBMC*Thickness	1	1105.3	1105.3	65.85	0.000
Initial DBMC*Refining Condition	1	314.7	314.7	18.75	0.001
Thickness*Refining Condition	1	7.9	7.9	0.47	0.502
Initial DBMC*Thickness* Refining Condition	1	141.7	141.7	8.44	0.010
Error	16	268.6	16.8		
Total	23	40413.9			

Figure 44 shows the Pareto charts of the standardized effects for this case. This figure represents that for this case, initial DBMC and thickness have the maximum effects. For hardwood, the effect of refining condition of the pulp is after the interactive effect of initial DBMC and thickness (AB) effect. The results of the linear regression for the correlation predicting area under the drying curve are provided in Table 12 both for hardwood and softwood. R^2 values show the high accuracy of the predictions using linear regression in this case.

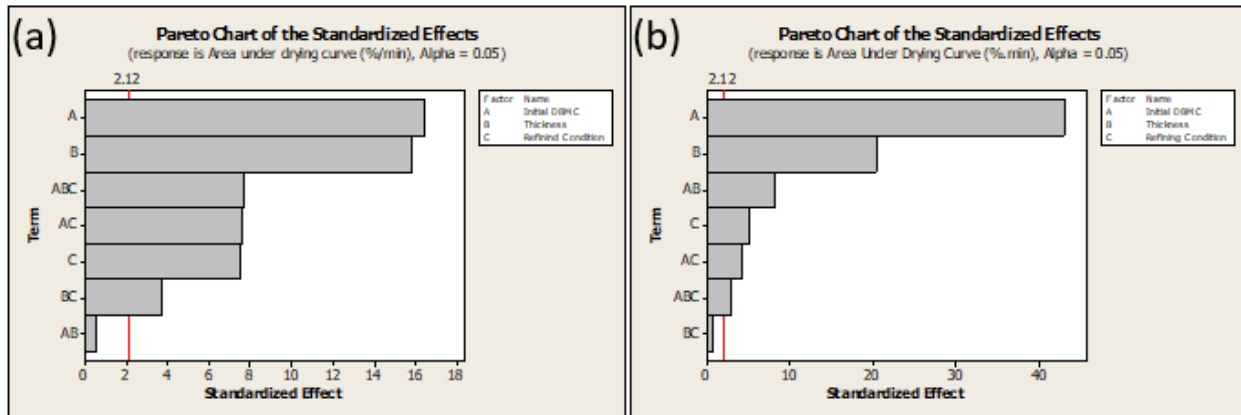


Figure 44. Pareto charts of the standardized effects from ANOVA analysis for area under the ultrasonic drying curve: (a) hardwood and (b) softwood.

The quality of the product is a very important factor in determining the applicability of any drying technology. In the next sections, the measurements related to color, microstructure, surface roughness, and the tensile strength of the hand-sheets dried using ultrasound mechanism are provided.

4.2.7 Colorimeter Measurements

Figure 45 compares the whiteness index for an ultrasonically dried hand-sheet (H-R-150-0.3) with a sample dried using conductive heating at 80 °C. This figure shows that direct-contact ultrasonic drying slightly improves the whiteness index and therefore the product quality.

Figure 46 summarizes the results of color measurements for all samples. The maximum standard deviation for all data is 0.02. In this figure, L^* is the lightness index, a^* is the red-greenness index, and b^* is the yellow-blueness index. Figure 46 shows that the hardwood samples have higher

brightness index compared to softwood samples. The redness in softwood samples is more than hardwood samples, however the yellowness is higher in hardwood samples.

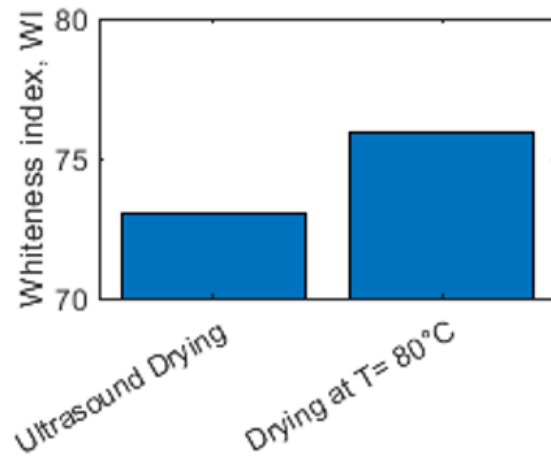


Figure 45. Comparison of whiteness index for ultrasonic drying with heat conductive drying at 80 °C for H-R-150-0.3.

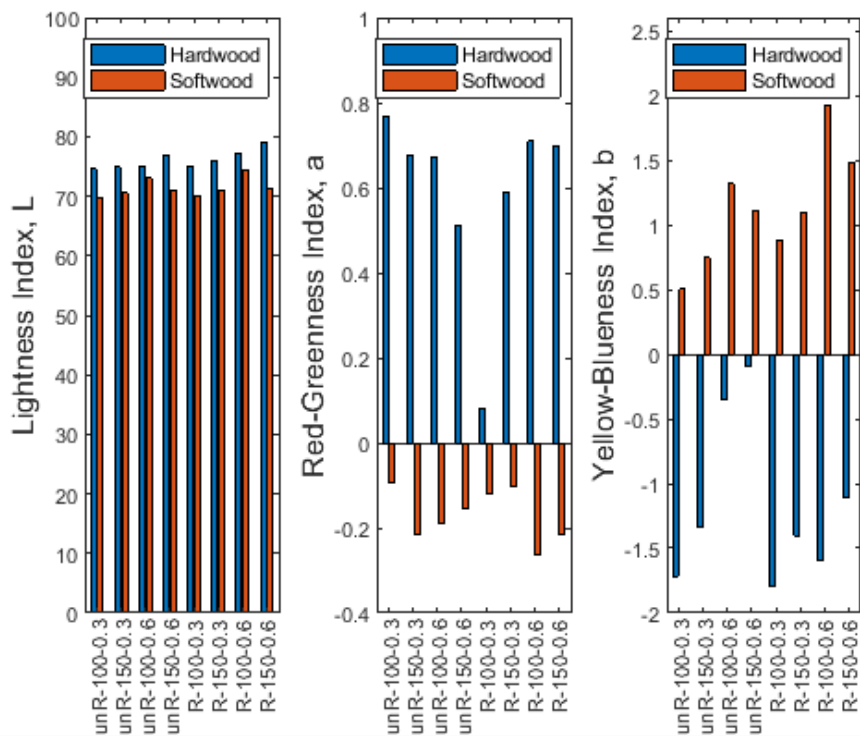


Figure 46. Colorimeter measurements ($L^*a^*b^*$) for hardwood and softwood samples dried using ultrasound mechanism.

The results of colorimeter measurements for the change in color index (ΔE) and whiteness index (WI) for ultrasonically dried hand-sheets are shown in Figure 47.

Change in color after drying is between 1 to 6 and the whiteness index is higher for hardwood samples, as expected from lightness index measurements (Figure 47).

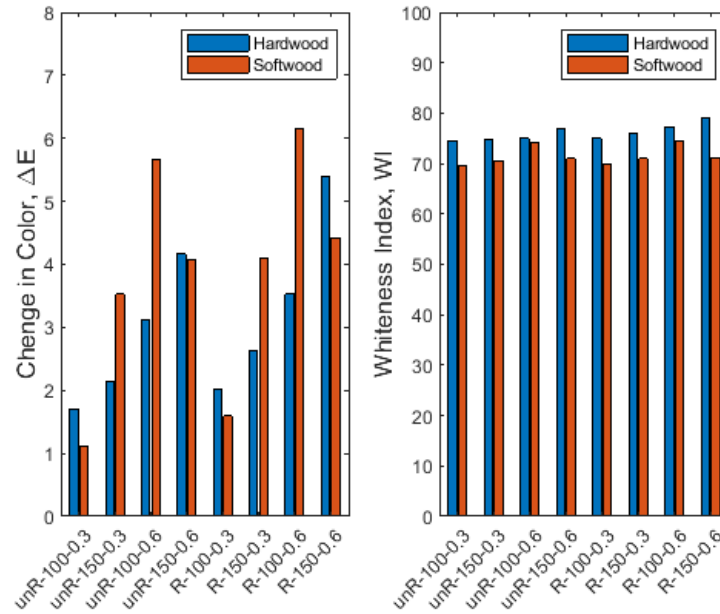


Figure 47. Change in color and whiteness index of ultrasonically dried hand-sheets.

The results represent that overall, the change in color and whiteness index for refined samples are higher than unrefined samples. In addition, increasing the thickness and increasing the initial moisture content, increase WI. Furthermore, increasing the lightness index with increasing the thickness is an implication of increasing the porosity of the samples with increasing the thickness. More details will be addressed in the next section.

ANOVA analysis is done for WI and the results show that thickness has the maximum effect on WI of the hand-sheets dried with ultrasound mechanism. The results of linear regression analysis are reported in Table 12.

4.2.8 Microscopic Measurements

Paper is a porous medium and one of the important parameters in determining its properties is porosity (ϵ). Figure 48 and Figure 49 show the pore distribution in the optical microscopic images

for hardwood and softwood hand-sheets. It should be noted that the initial DBMC for all the samples is 150%.

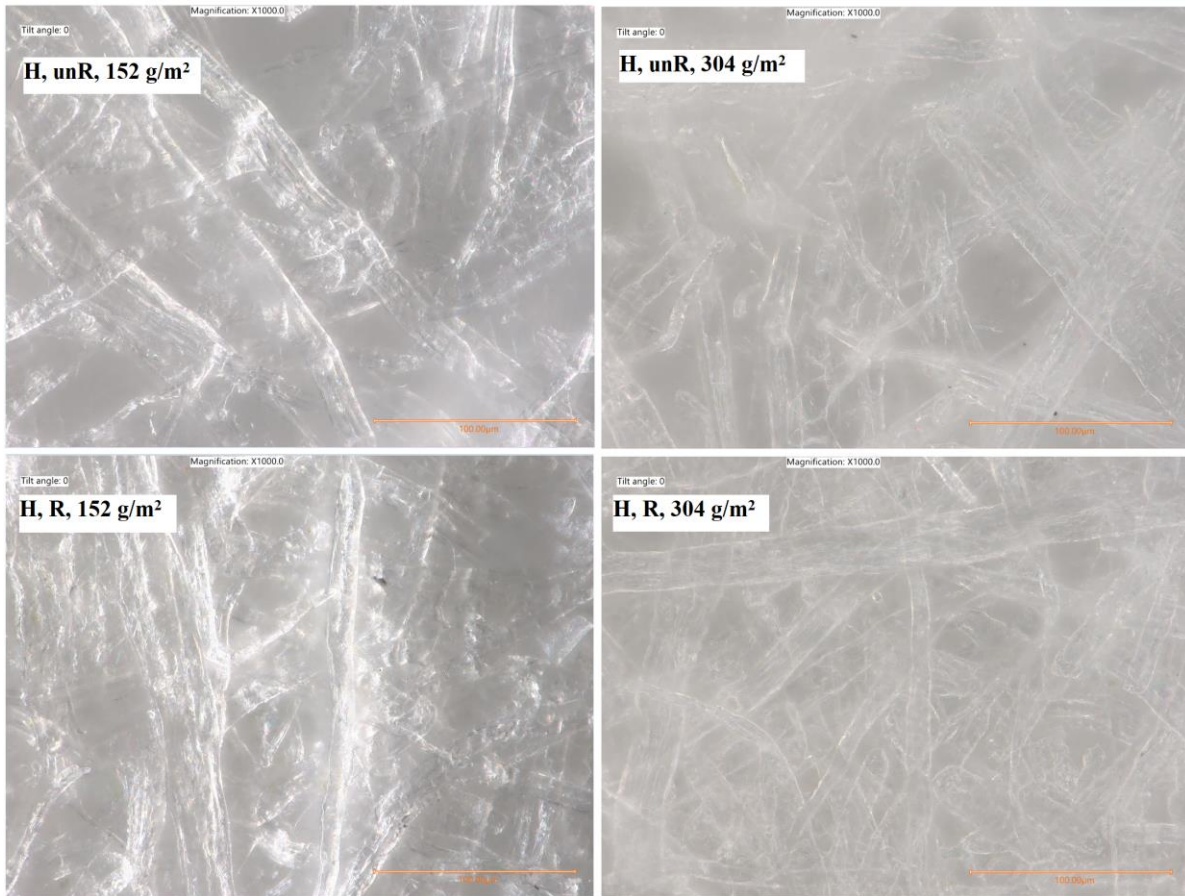


Figure 48. Optical microscopic images for hardwood samples dried with ultrasound mechanism. The initial DBMC for all the samples is 150%. Magnification is 1000X.

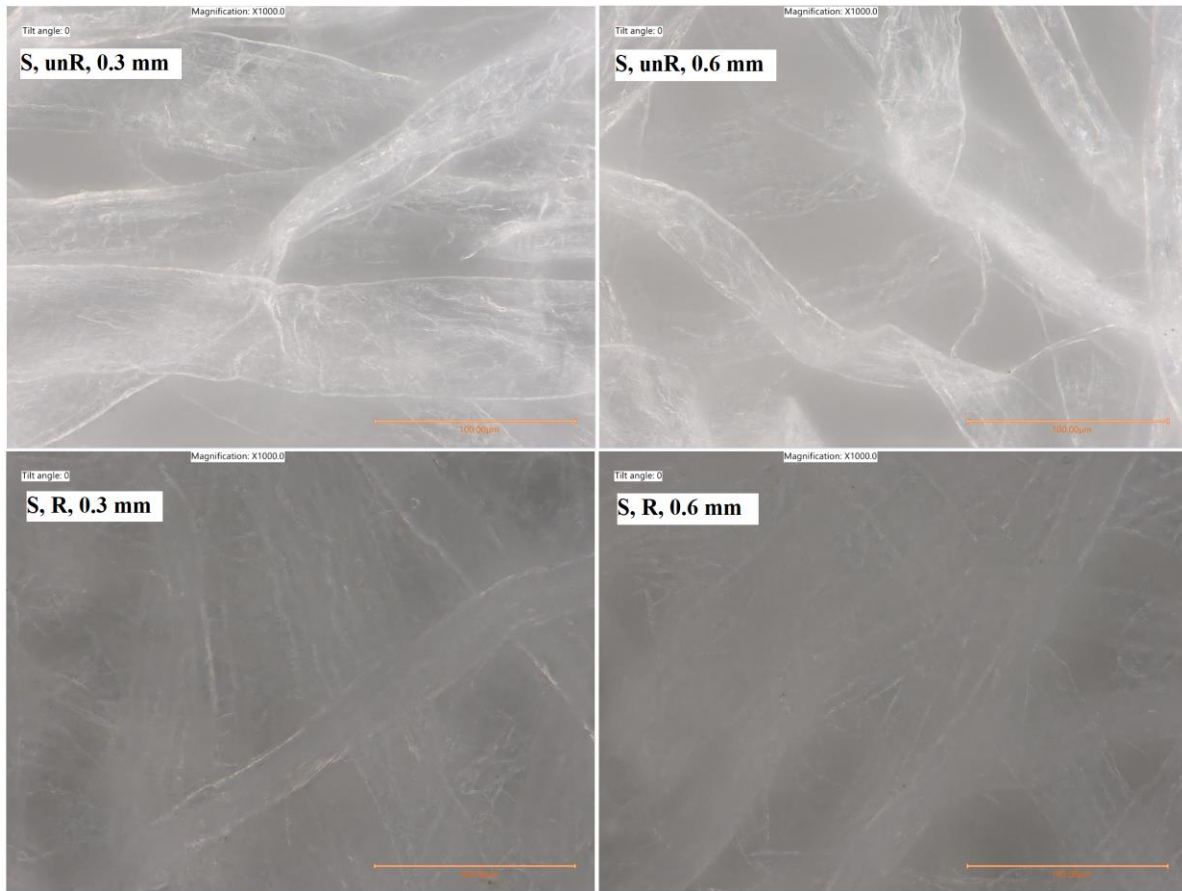


Figure 49. Optical microscopic images for softwood samples dried with ultrasound mechanism. The initial DBMC for all the samples is 150%. Magnification is 1000X.

Comparing the microscopic images for hardwood and softwood reveals the differences in the fiber sizes and pore sizes in different samples. Unrefined samples have larger pores compared to refined samples, while refined fibers are more uniform compared to unrefined fibers. Additionally, the fibers are coarser and longer in unrefined samples. Softwood samples have coarser fibers compared to hardwood samples. Using ImageJ software, thresholding is applied to these microscopic images to measure the pore volume percentage of the hand-sheets in 2D. Figure 50 summarizes the results of these 2D measurements. This figure shows higher pore volume for unrefined samples compared to refined samples. 2D pore volume for softwood samples is higher than hardwood samples. Increasing the thickness, slightly increases the pore volume. These findings are evident that unrefined samples dry faster than refined samples and the drying rate for softwood is higher than that for hardwood.

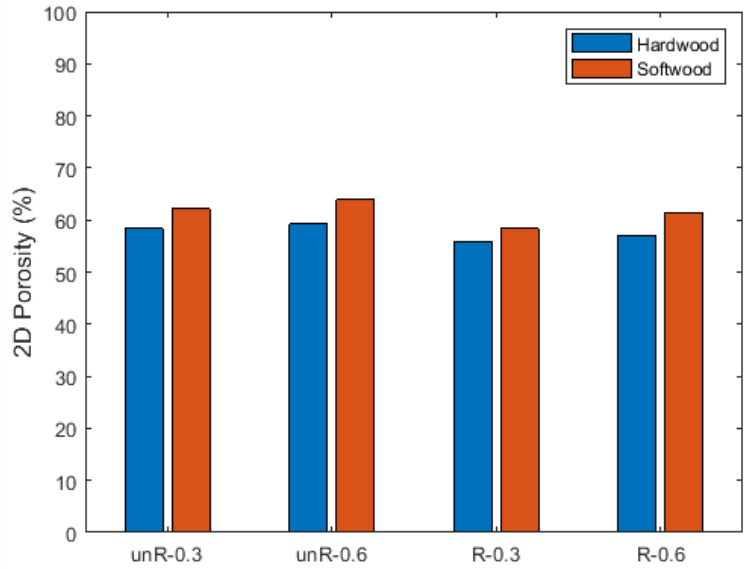


Figure 50. 2D porosity measurands using thresholding of the microscopic images of samples dried with ultrasound mechanism. The initial DBMC for all the samples is 150%.

4.2.9 Profilometry Measurements

Color view of the surface profiles for hardwood and softwood samples are shown in Figure 51 and Figure 52, respectively. It should be noted that the initial DBMC for all the samples is 150%.

The surface roughness depends on the species and texture uniformity. In this study, TAPPI T205 standard is used for preparing the samples, however the bulging effect during the experiments might have influenced the smoothness of the surface and its uniformity.

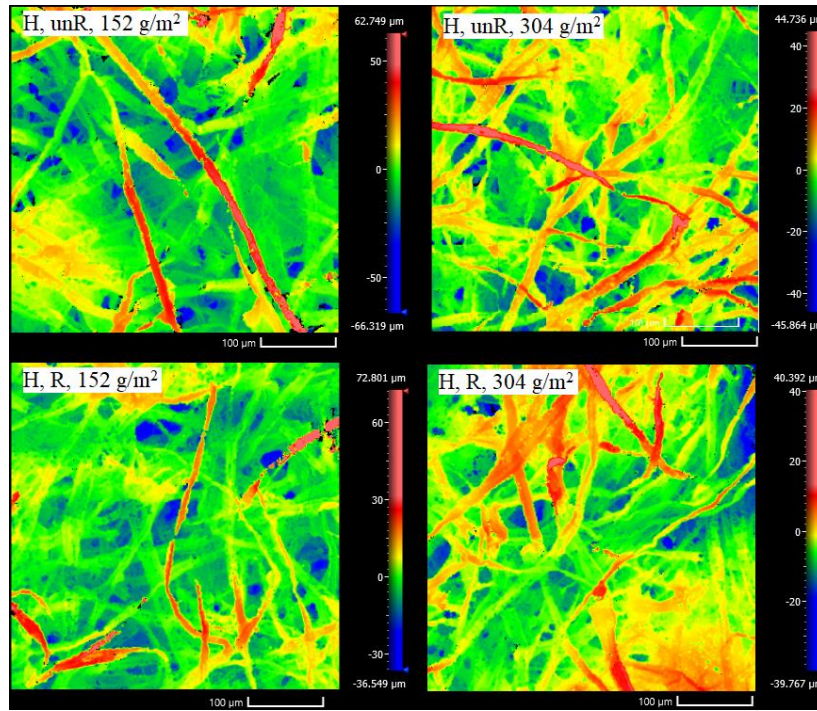


Figure 51. Color view of roughness measurements for hardwood samples. It should be noted that the initial DBMC for all the samples is 150%.

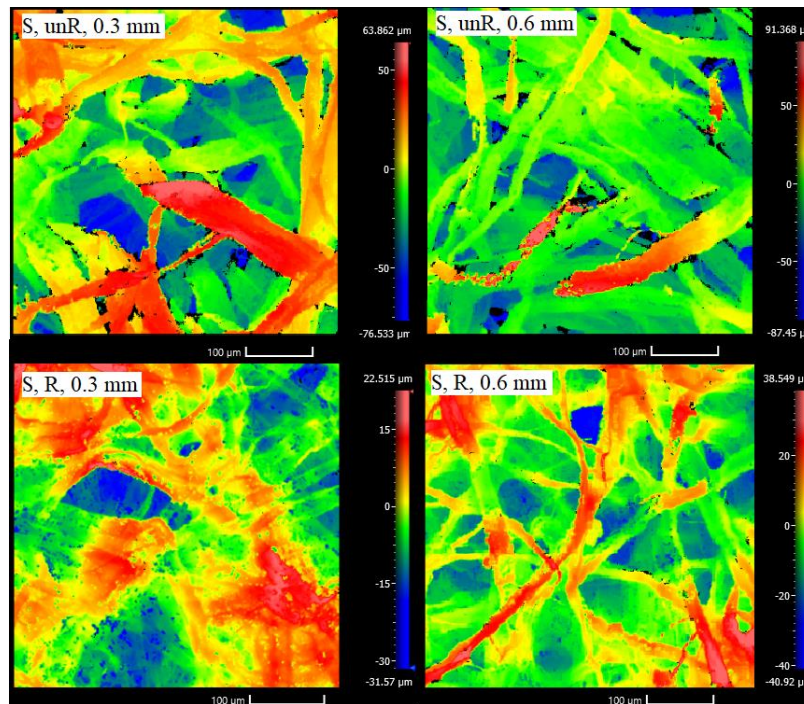


Figure 52. Color view of roughness measurements for softwood samples. It should be noted that the initial DBMC for all the samples is 150%.

Figure 53 shows the results of profilometry measurements. The max standard deviation is 0.05. Sa is the average roughness, Sq is the root mean square roughness evaluated over the complete 3D surface. Sz is the maximum height of the areal surface, which is the peak to valley height.

$$Sa = \frac{1}{A} \iint |Z(x, y)| dx dy \quad (4-5)$$

$$Sq = \sqrt{\frac{1}{A} \iint Z^2(x, y) dx dy} \quad (4-6)$$

$$Sz = \min(Z(x, y)) + \max(Z(x, y)) \quad (4-7)$$

where $Z(x,y)$ are the heights over the surface A in the (x,y) plane.

Figure 53 shows that refined samples have lower roughness compared to unrefined samples. Overall, the roughness indices for softwood samples are higher than hardwood samples. Hardwood samples are more uniform, and they are more suitable for producing smoother surfaces. Qualitatively, the bigger picture here is that ultrasonic drying does not change the behavior of softwood and hardwood after drying.

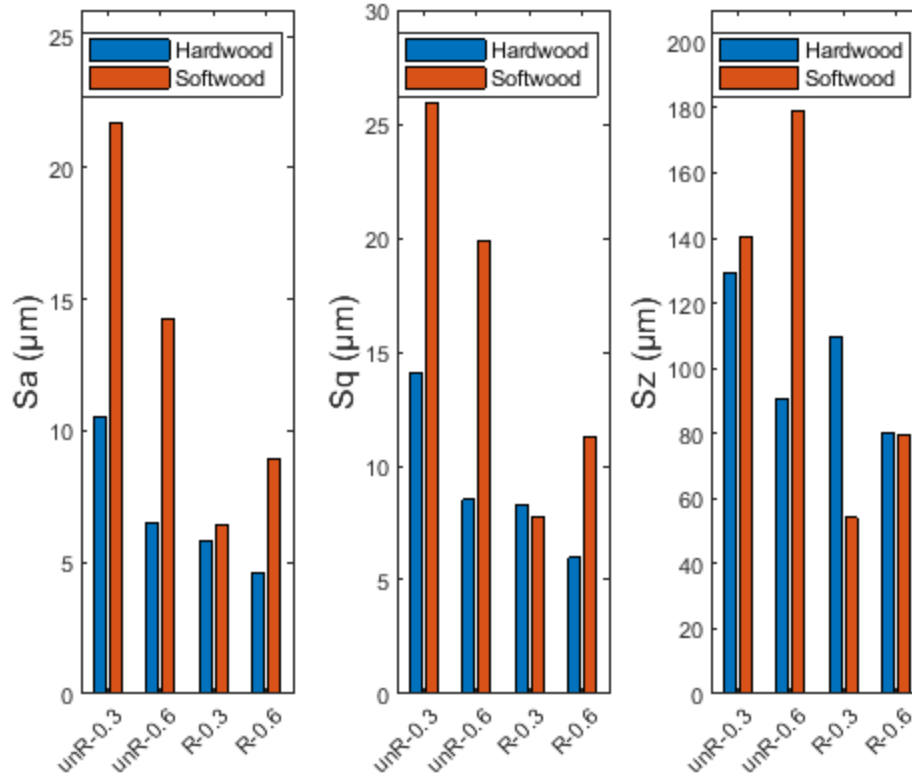


Figure 53. Surface roughness measurements for samples dried with ultrasound mechanism. The initial DBMC for all the samples is 150%.

4.2.10 Tensile Strength Measurements

Tensile strength plays a significant role in various applications of paper products.

Figure 54 compares the tensile strength for H-R-150-0.3 dried using ultrasound mechanism and using conductive heating at 80 °C. The results show that ultrasonic drying does not seem to decrease the tensile strength.

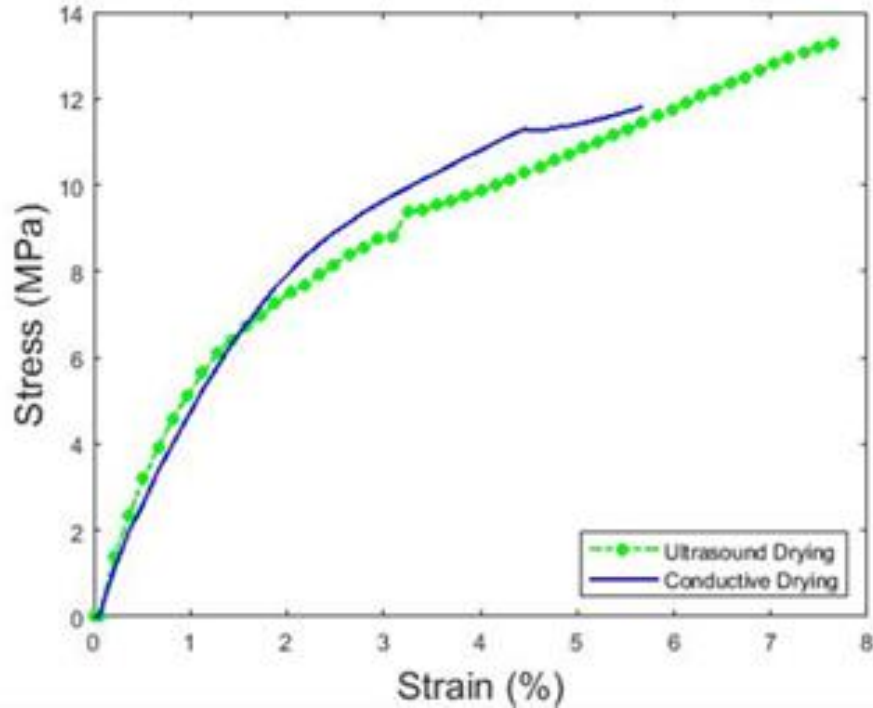


Figure 54. Comparing stress-strain curves for H-R-150-0.3 dried with ultrasonic drying and with conductive heat drying at 80 °C.

The tensile strength measurements revealed that moisture content does not show much influence on the tensile strength of the dried samples within the range of the parameters considered in this study. The stress-strain curves for the samples at 100% DBMC and for the center points are illustrated in Figure 55 and Table 15 summarizes the results. In general, the refined pulps have a higher ultimate tensile strength (UTS) compared to that of unrefined pulps. According to Motamedian et al. [116], refining is a common procedure in paper making industry to improve the mechanical properties of the final product. In addition, the tensile strength is affected by the sample basis weight and thickness. The hand-sheet with a higher thickness has a lower strength because of the stress gradients in the thickness direction. Hagglund et al. [117] proposed a linear elastic 2D finite element analysis to model the stress field under the jaws. The model proposes that the clamping condition during the test results in higher stresses at the surface and lower stresses in the middle of the sheet. Batchelor et al. [118] showed that the level of stress concentration highly depends on the thickness and the grammage of the paper samples. As a result of the stress gradients in the thickness direction, increasing thickness and grammage reduces the strength of the sample.

Furthermore, the tensile strength for the center points is between the tensile strengths for refined and unrefined samples.

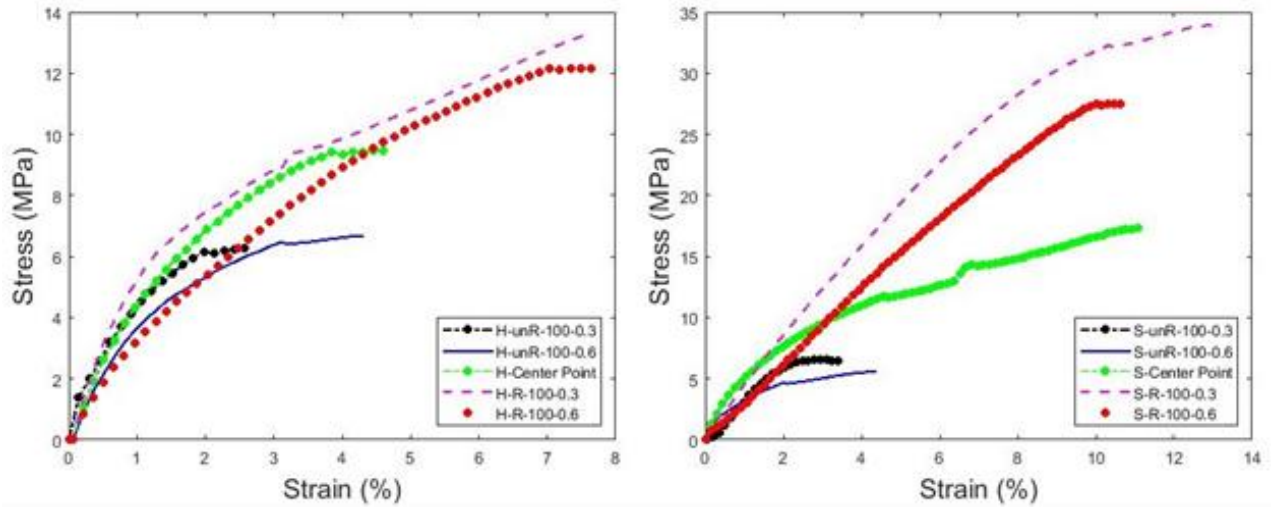


Figure 55. Stress-strain curves for different types of pulps with different thicknesses.

Table 15. Ultimate tensile strain and ultimate tensile stress for different samples.

Sample	Ultimate Tensile Strain (%)	Ultimate Tensile Strength (MPa)
H-unR-100-0.3	2.58	6.28
H-unR-100-0.6	4.31	6.67
H-Center Point	4.6	9.47
H-R-100-0.3	7.64	13.29
H-R-100-0.6	7.63	12.15
S-unR-100-0.3	4.4	5.57
S-unR-100-0.6	3.39	6.6
S-Center Point	11.07	17.29
S-R-100-0.3	13.05	33.93
S-R-100-0.6	10.61	27.49

4.2.11 Energy Analysis

4.2.11-a Energy Consumption of the Power Amplifier

Before discussing the details about the energy efficiency of ultrasonic drying, the energy efficiency of the setup and the power amplifier is studied. A power consumption meter is connected to the power amplifier and the power consumption for three stages including: (1) power amplifier is on but 0 power goes to the transducer, (2) power amplifier is on and inputs 10 W power to the transducer, and (3) power amplifier is on but 0 power goes to the transducer. Figure 56 shows the power consumption at different stages. According to these measurements, inputting 10 W power to the transducer increases the energy consumption by 60 W. In addition, when the input power to the transducer is 0, the power amplifier consumes about 350 W energy just to be turned on. This energy is consumed by the internal components of the power amplifier and gets wasted as heat. A part of that is due to the wide range of frequencies and powers the power amplifier has. Therefore, it is recommended to design and build power amplifiers with a narrower range of frequencies and powers regarding the transducers used in this study in order to increase the energy efficiency of the setup itself.

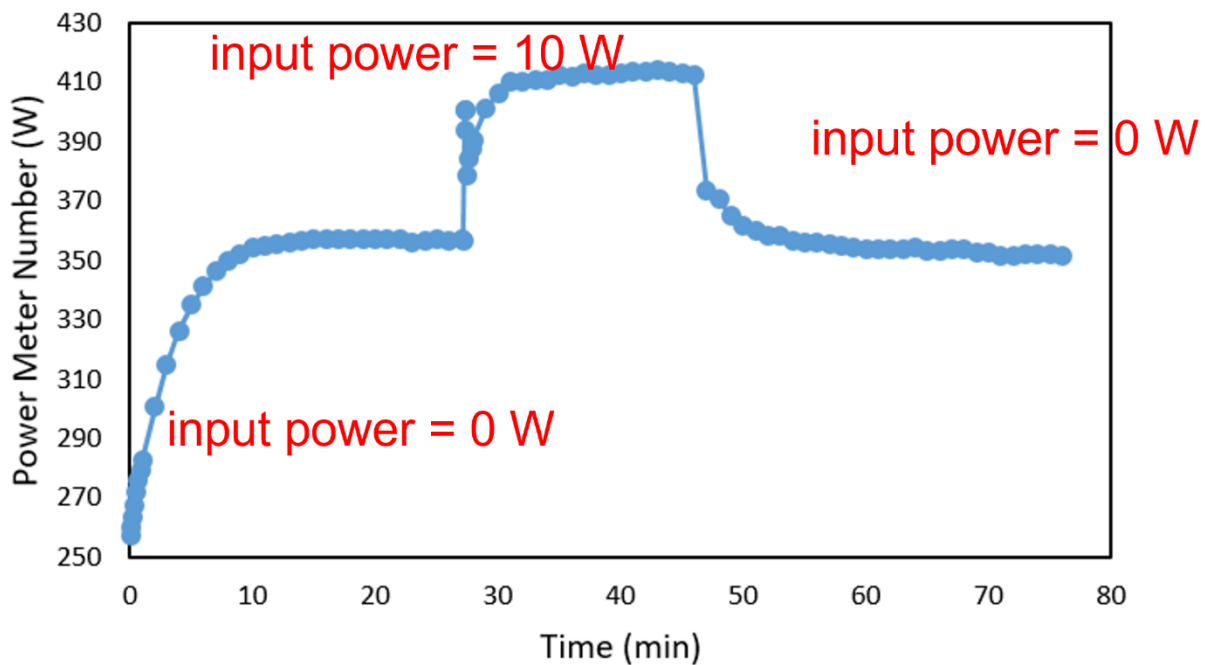


Figure 56. Power meter measurements for three stages of input power to the transducer.

4.2.11-b Energy Efficiency and Drying Rate

It is very important to apply sufficient electrical power to the transducer to induce atomization of water in the moist medium. For the transducer used in this study under the operating frequency of 1.7 MHz, 10 W power is applied to allow for the atomization to take place. As the sample gets dried, due to the changes in impedance, the load power to the transducer changes by drying time. The records show that the changes of load power, for the transducer used in this study, during all the experiments is almost the same and it is represented in Figure 57.

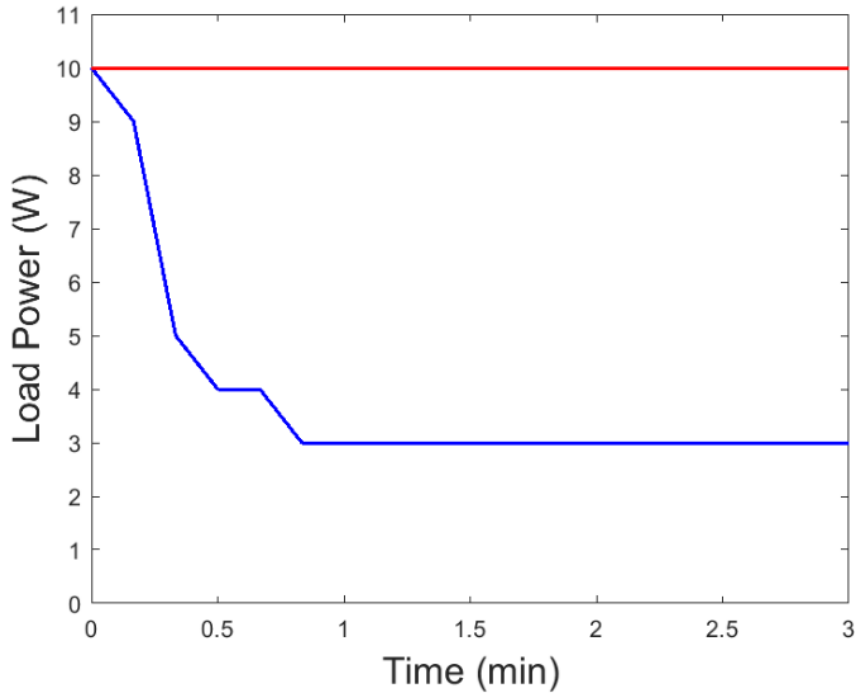


Figure 57. Changes in load power as a function of drying time for the transducer used in this study. 10 W forward power is applied to the transducer.

The following equation is defined to calculate the energy factor (EF), which is defined as the ratio of the energy required for evaporation to the total load power (LP) applied to the transducer:

$$EF = \frac{(m_i - m_t)h_{fg}}{\int LP(t)dt} \quad (4-8)$$

where m_i and m_t are the initial and the instantaneous mass of the sample. h_{fg} is the latent heat of evaporation and it is assumed to be constant at 2500 kJ/kg. t is the time.

Figure 58 and Figure 59 compare the energy factor and drying rates for all the experiments conducted as a function of time. The energy factor (and similarly drying rate) initially increases with the drying time mainly because of the increase in the direct-contact ultrasound transducer surface temperature. However, after reaching its maximum, it decreases simply due to the drop in the available moisture to atomize especially on the sample surface exposed to the ambient air. The overall results confirm that, the unrefined samples have higher energy factors compared to refined samples. This finding agrees with the fact that unrefined samples dry faster than refined samples. It should be mentioned that the load power changes during time is slightly different for different samples which also impacts the results of the calculations for the energy factor. In general, the results show that ultrasonic drying is less energy efficient compared to direct thermal drying for the operating conditions considered in this study. As it was illustrated in section 4.2.2, ultrasonic drying has higher drying rates at higher moisture contents. This can be observed from the energy factor plots in Figure 58 and Figure 59, which energy factor is higher at 150% DBMC compared to that of 100% DBMC. To confirm the effectiveness of ultrasonic drying at high moisture content levels, an additional test was conducted with a paper hand-sheet with initial DBMC of 700% (H-R-700-0.3). As shown in Figure 60, the ultrasound energy factor reaches to about 1.7, illustrating the increase in effectiveness of ultrasonic drying with the increase in moisture content.

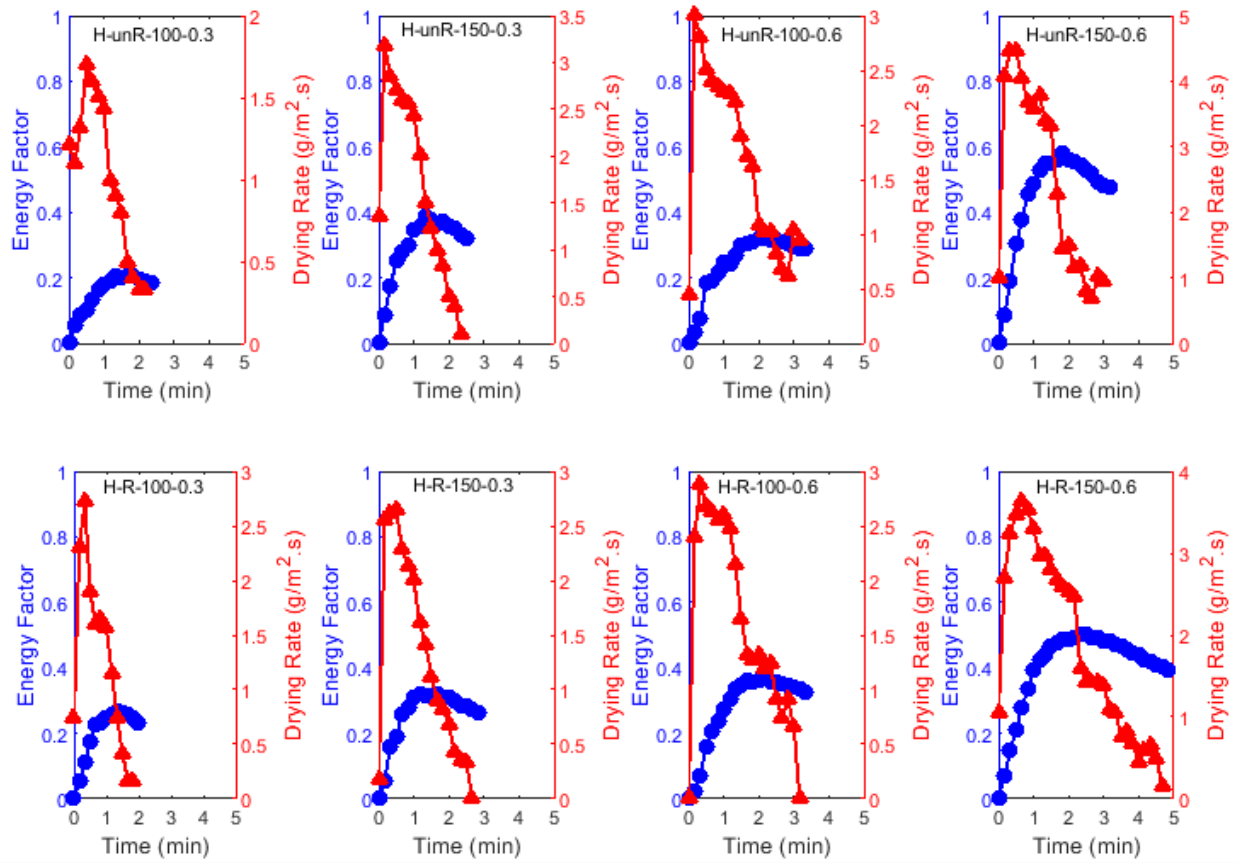


Figure 58. Comparing the energy factor for hardwood samples.

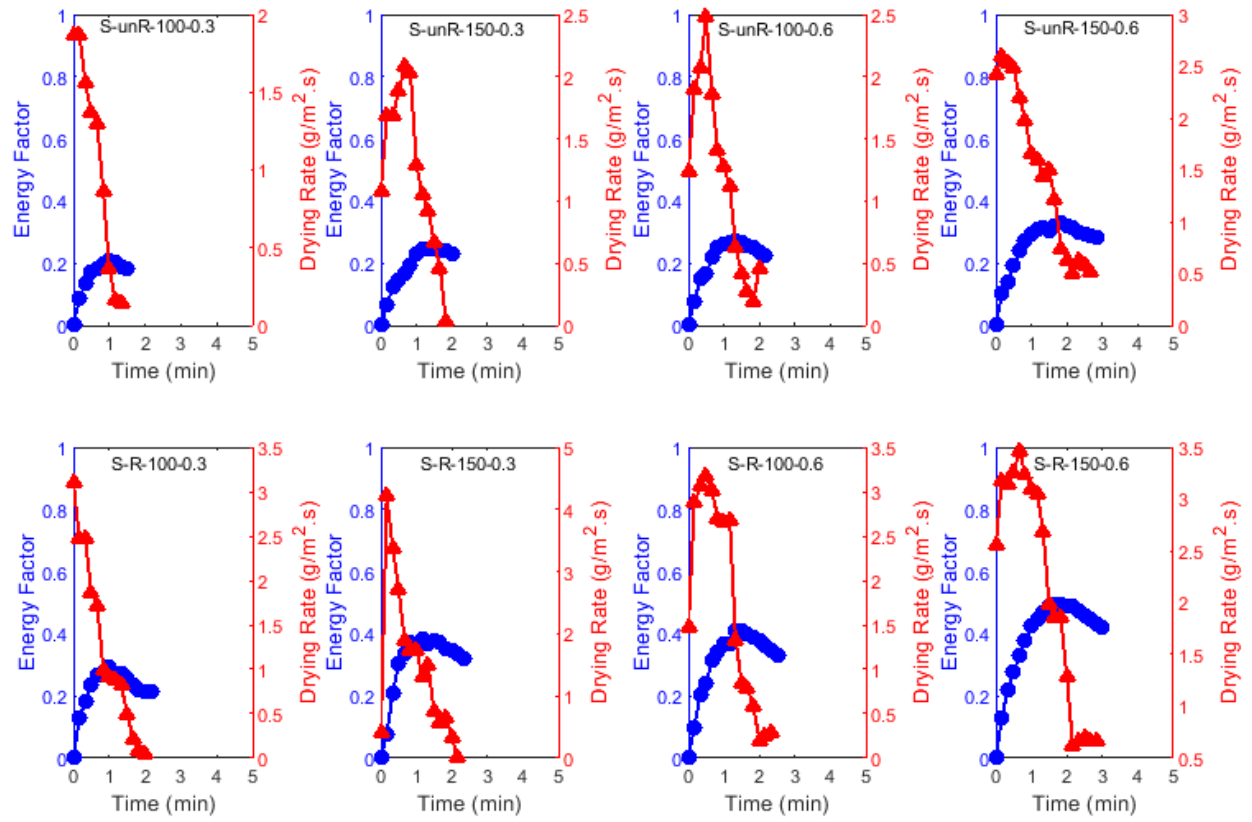


Figure 59. Comparing the energy factor for softwood samples.

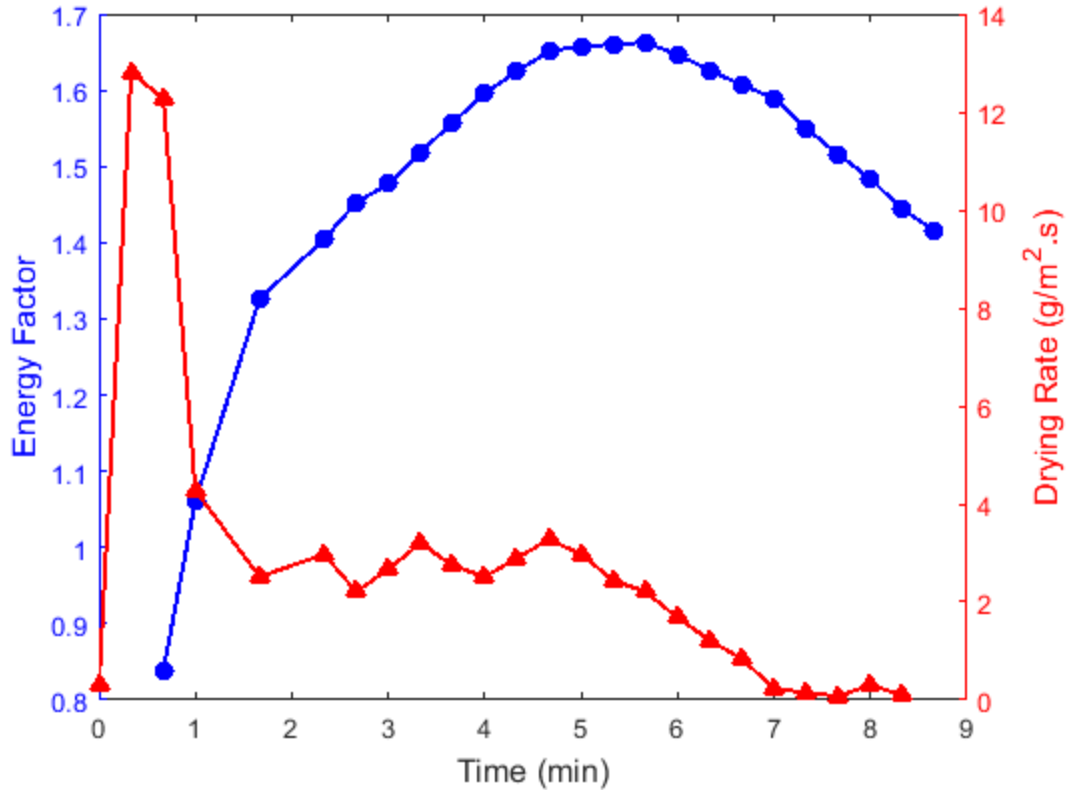


Figure 60. Illustration of the effect of high moisture content on DBMC and energy factor for H-R-700-0.3.

The above analysis assumes that the efficiency of evaporation in a heating process is 100% however, in real cases the efficiency is less than 1 (around 50-60% for a typical drying process). Therefore, in reality, ultrasonic drying has higher energy efficiencies than the numbers calculated in this section.

4.3 Summary and Conclusions

Hardwood and softwood hand-sheet samples are dried using direct-contact ultrasound mechanism. The results confirmed that ultrasonic drying mechanism is more efficient at higher moisture content levels. IR camera images for the temperature on the surface of the transducer revealed that by applying ultrasound, first the temperature in the center increases and then by propagating the oscillations through the surface of the transducer, the temperature increases through the surface. Comparing the drying curve of ultrasound mechanism with the drying curve from thermal drying at 80 °C showed a significant decrease in drying time. ANOVA was done for both hardwood and

softwood. The independent factors in the analysis include initial moisture content, thickness, and refining condition of the pulp and two high and low levels were considered for each factor. The results showed that for the total time of ultrasonic drying, the thickness has the maximum effect and after that initial moisture content is important. These findings for ultrasonic drying behavior of paper samples are related to the structural characteristics of the samples. Therefore, microstructure of the samples was investigated and the surface profilometers were measured. The results showed that softwood fibers are coarser than hardwood fibers. Therefore, the pores in softwood are larger and the porosity is higher compared to hardwood. In addition, unrefined samples have larger pores compared to refined samples and hence, unrefined dries faster. Therefore, as it is expected, the structure of the sample (refined, unrefined, or a mixture) has a significant impact on drying curve. The quality of the ultrasonically dried samples was measured using colorimeter analysis for whiteness index. Using regression analysis, two equations for both hardwood and softwood are provided. These equations describe the total time of drying and whiteness index. To analyze the energy efficiency of the ultrasonically dried samples, energy factor was defined as the ratio of the energy required for evaporation to the energy that generates the ultrasonic vibrations. The higher energy factor means the process is more energy efficient. The results showed that the energy factor for direct-contact ultrasonic drying for the current setup is 0.2-0.6. This implies that better design of transducers is required to increase the efficiency of the process. Furthermore, increasing the initial moisture content to 700% resulted in higher energy efficiency for ultrasonic drying compared to thermal drying. The energy factor for unrefined samples is higher than refined samples, which agrees with the fact that unrefined samples dry faster than refined samples. The refined samples showed higher tensile strength compared to that of unrefined samples. These results confirm the significant impact of ultrasonic drying for reduction of energy consumption and carbon footprint as a green and sustainable energy source. This study provided the foundation for the next studies of fundamental understanding of ultrasound mechanism for porous media drying.

Chapter 5: Airborne Power Ultrasound for Paper Drying: An Experimental Study

As it was shown in the previous chapter, in a direct-contact ultrasonic drying setup, the moist sample must be in direct contact with the vibrating transducer surface. In this chapter, a novel approach for paper drying using airborne ultrasound technology is presented. A unique experimental setup is developed, and a systematic study is applied using 2^3 factorial design of experiments and Analysis of Variance. Three controlling factors are considered in the experiments including the initial moisture content, basis weight, and refining condition. The outcome of the experiments is compared to the results of the previous chapter on direct-contact ultrasonic drying of paper. The results confirm that similar to direct-contact, for airborne ultrasonic drying, the basis weight/thickness of the sample is the most important factor in ultrasonic drying and it is followed by the effect of initial moisture content. Using linear regression model, two correlations for predicting the total time of ultrasonic drying and the area under the drying curve are provided. Quality of the dried samples are evaluated, and the permeability measurements confirmed the effect of pore characteristics on ultrasonic drying. The analysis for energy consumption reveals that airborne ultrasonic drying is more efficient at higher moisture contents.

Keywords: Airborne ultrasonic drying; non-contact ultrasonic drying; paper drying; energy analysis.

5.1 Experimental Setup and Methods

5.1.1 Experimental Setup

An experimental testing fixture has been designed in Solidworks 2021 and assembled as shown in Figure 61. This setup allows to change the distance between the sample and the surface of the transducer and also gives the possibility of using IR camera for monitoring the temperature of the transducer from underneath. Figure 62 shows the experimental setup with the installed ultrasound device. The main components include the transducer part, electric power generator or EPG (power amplifier and dynamic resonance controller) and sample holder. The maximum acoustic intensity

for this airborne transducer in free field is 160 dB, according to the manufacturer. For safety purposes, composite double layers soundproofing foams were used to reduce the sound level around the transducer to less than 80 dB. It should be noted that this is an open system, and the door of the setup was kept open during the experiments. This airborne transducer was purchased from Pusonics S.L., Spain, and according to the manufacturer [119], it is composed of a piezoelectric Langevin-type sandwich, a mechanical amplifier or horn, and an extensive radiator, that provides the required impedance to match with the media. This transducer extends the vibrating surface of the sonotrode to create a larger vibrating surface inside the dryer (Figure 63).

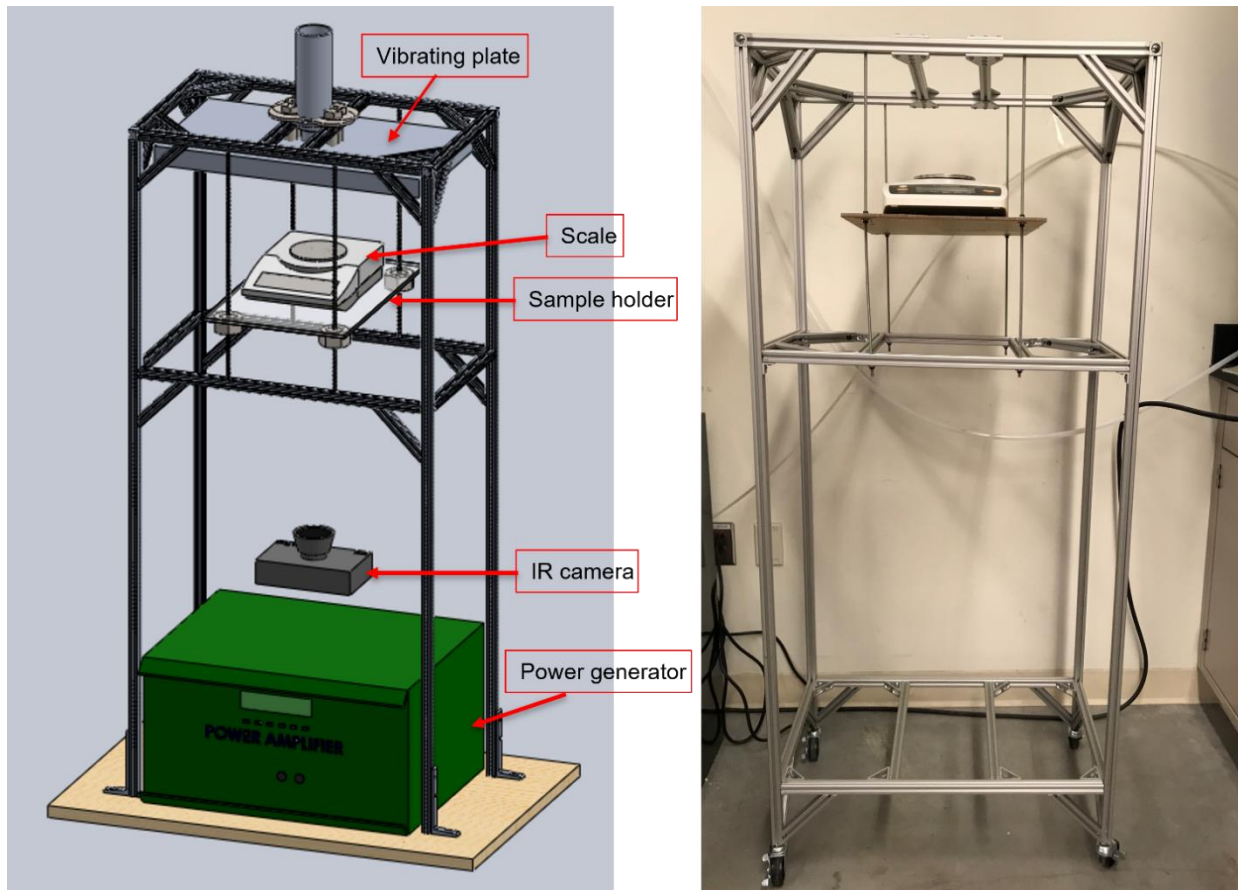


Figure 61. Left picture: The Solidworks schematic of the experimental testing fixture. Right picture: The assembled experimental fixture in the lab.

In this study, two different transducer plates are examined. The first transducer plate is made from aluminum (Al) and its dimensions are 57×30.8×4 cm. The working frequency for this plate is 21

kHz and the maximum ultrasound power (the maximum power recommended by the manufacturer) is 200 W. Unfortunately, this transducer got damaged due to ultrasonic fatigue, after a few weeks of running experiments and therefore, the manufacturer replaced the plate with a titanium (Ti) plate. The dimensions of the titanium plate are 43.3×23.4×3.15 cm. The working frequency for the second plate is also 21 kHz but the maximum applied power is 225 W. A closer look at both transducers and the sample holder are represented in Figure 64 and Figure 65.

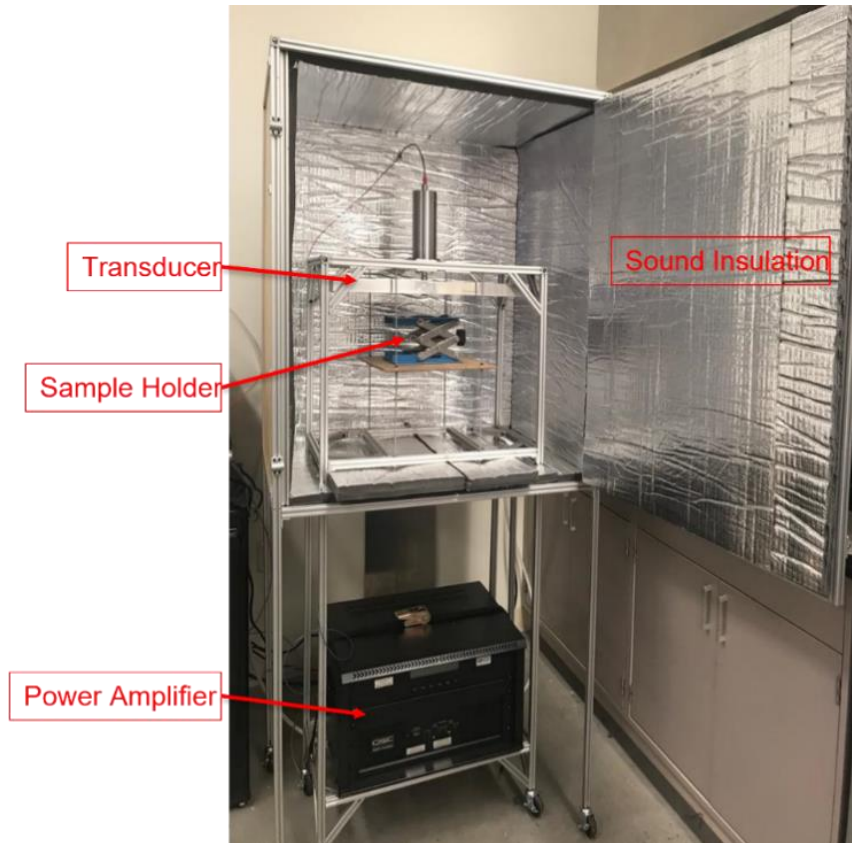


Figure 62. The experimental setup for non-contact ultrasonic drying.



Figure 63. Airborne power ultrasonic transducer with a rectangular plate radiator [119].

The distance between the transducer plate and the sample has a significant role on the drying behavior. The maximum drying efficiency for the Al plate is at 15 mm from the plate and for the Ti plate is at 4 mm from the plate. This will be discussed in detail in the next sections.

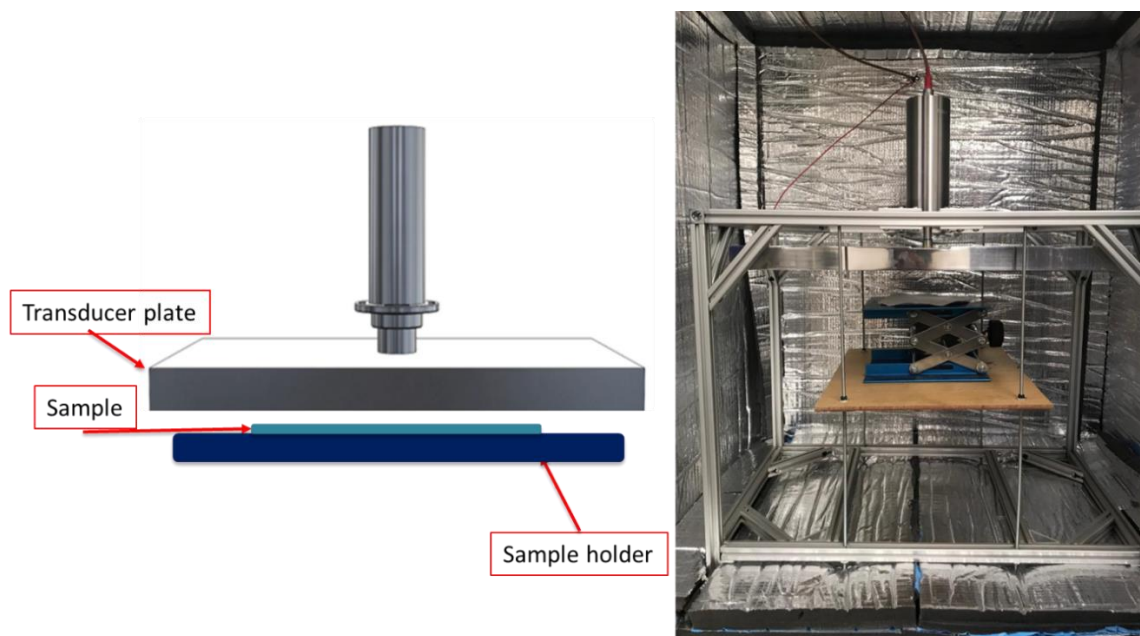


Figure 64. Schematic of the airborne ultrasound transducer and the sample holder (left side). Side view of Al plate (right side).

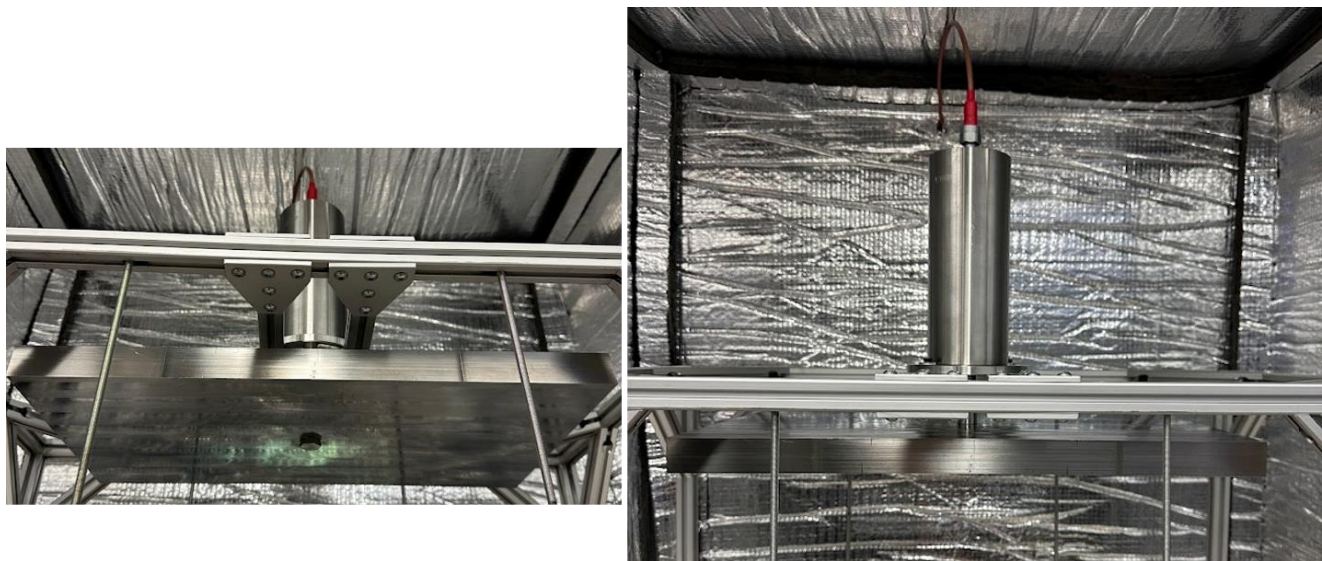


Figure 65. Bottom view and side view of Ti plate.

Two different types of sample holders are studied. The first sample holder is a solid plate, which only allows drying to occur from the top side of the sample. The second sample holder is a mesh which allows drying from both sides (top and bottom). In addition, in the case of solid sample holder, the gravity prevents the water to escape from the sample but in the case of the mesh sample holder, it works in favor of water removal. The weight of the samples was measured intermittently at about 2 - 3 min intervals using a microbalance (Sartorius BCE6200 with 0.001 g accuracy). The samples' thickness was gauged using a digital thickness gauge with 0.002 mm accuracy.

The pulps used in this study, hardwood and softwood, both refined and unrefined, were Northern Bleached Hardwood Kraft (NBHK) and Northern Bleached Softwood Kraft (NBSK). The hand-sheet making procedure was followed according to TAPPI T205 standard to reach to 150% dry-basis moisture content (DBMC). For the cases with 120% initial DBMC, the samples were dried at ambient to reach to the desired moisture content. The hardwood pulps and refined softwood pulp were slurries with 4% consistency and by adding water, the targeted initial weight was obtained. However, the unrefined softwood pulp was a dried sheet that was disintegrated in water to reach to the desired consistency. The pulp consistency is defined as the percentage by weight of oven-dry fibers in a stock suspension (slurry). The diameter of the hand-sheets was 15.9 cm.

The uncertainty analyses for the derived quantities are represented in Table 16 and was done according to Kline and McClintock [114].

Table 16. The derived uncertainty of the experimental data.

Derived Quantity	Maximum Uncertainty
DBMC	± 6.2%
Whiteness index	± 0.5%
Permeability	± 5.7%
Energy factor	± 4.24%

An FLIR infrared camera along with fiber optic temperature sensors (Micronor, TS3) and a signal conditioner (Micronor, FOTEMP4-PLUS) are used for temperature measurements.

For colorimeter measurements, ColorFlex EZ is used based on CIELAB color space ($L^*a^*b^*$). For paper drying, Whiteness Index (WI) is the most important criteria depending on the application of the paper and it can be calculated using the following equation:

$$WI = 100 - \sqrt{(100 - L^*)^2 + (a^{*2} + b^{*2})} \quad (5-1)$$

where L^* is the lightness index, a^* is red-greenness index and b^* is yellow-blueness index. For the tensile strength measurements, Multitest-dV Mecmesin device is employed for rectangular samples. To be able to compare the results with direct-contact ultrasonic drying, the samples are 19.8 mm in length and 5 mm in width. The distance between the grips is fixed at 9 mm.

In addition, Model 4340 Automatic Densometer & Smoothness Tester is used to measure Gurley seconds for each sample, following the procedure of Gurley methods (TAPPI standard T460). The Gurley second or Gurley unit is a unit that describes air permeability as a function of the time required for a specified amount of air to pass through a specified area of a separator under a specified pressure. Darcy's law then is used to calculate the permeability of the paper samples:

$$Q = \frac{ka}{\mu b} \Delta P \quad (5-2)$$

where Q is the volumetric air flow (m^3/s), k is permeability (m^2), a is the opening area (m^2), μ is dynamic viscosity of fluid ($\text{kg}/(\text{m}\cdot\text{s})$), b is the sample thickness (m), and ΔP is the pressure drop across the sample (Pa). The value of Q is 100 cc and a is 6.45 cm^2 (for a circular area of paper) using a pressure differential of 1.22 kPa.

5.1.2 Experimental Method

The method applied for analyzing the experimental results was 2^3 factorial design of experiments. This method allows to understand the individualized effect of the controlling factors as well as their interactive effects. The three main factors in this research include initial DBMC, basis weight, and refining condition. Table 17 and Table 18 indicate the high and low levels for these three factors for hardwood and softwood samples, respectively. For simplicity, the abbreviations provided in Table 17 and Table 18 are employed in this paper. The last row in this table is the center point of the cube. The center points are halfway between the low and high levels and their importance comes to play when replicating the cube is expensive and time consuming. Analysis of Variance (ANOVA) was applied for the statistical analysis using Minitab software and p-values less than 0.05 were considered statistically significant. Linear regression analysis was done to investigate the effect of the controlling factors on the total time of ultrasonic drying.

The data for direct-contact ultrasonic drying of paper samples are used from the previous chapter.

Table 17. High and low levels of factors for 2³ factorial design of experiments for hardwood (H). R defines refined and unR defines unrefined.

Abbreviations	Factors		
	Initial DBMC (%)	Basis Weight (g/m ²)	Refining Condition
H-unR-120-160	120	160	Unrefined
H-unR-150-160	150	160	Unrefined
H-unR-120-325	120	325	Unrefined
H-unR-150-325	150	325	Unrefined
H-R-120-160	120	160	Refined
H-R-150-160	150	160	Refined
H-R-120-325	120	325	Refined
H-R-150-325	150	325	Refined
H-Center Point	135	242	50% R & 50% unR

Table 18. High and low levels of factors for 2³ factorial design of experiments for softwood (S). R defines refined and unR defines unrefined.

Abbreviations	Factors		
	Initial DBMC (%)	Basis Weight (g/m ²)	Refining Condition
S-unR-150-160	150	160	Unrefined
S-unR-200-160	200	160	Unrefined
S-unR-150-325	150	325	Unrefined
S-unR-200-325	200	325	Unrefined
S-R-150-160	150	160	Refined
S-R-200-160	200	160	Refined
S-R-150-325	150	325	Refined
S-R-200-325	200	325	Refined
S-Center Point	175	242	50% R & 50% unR

5.2 Results and Discussion

5.2.1 Acoustic Characterization of the Transducer Plate in Near Field

The information discussed in this section are provided by Pusonics S.L. and the copyright has been received.

5.2.1-a Aluminum Plate

For the Al plate, the characterizations are based on the experiments conducted at Pusonics facilities. The Al plate has 12 nodal lines, and the stationary field is characterized by the measurement of the sound pressure level (SPL) generated by the transducer. The measurements are done by placing a microphone over a reflecting plate and the acoustic pressure is recorded by changing the distance between the plate and the reflector. Figure 66 shows the experimental setup used by Pusonics to do the acoustic pressure measurements.



Figure 66. The experimental setup used by Pusonics to measure the acoustic pressure at different distances from the Al plate [120].

Figure 67 shows the acoustic pressure distribution at a plane placed at 3 mm from the Al plate and the applied power is 50 W. This figure shows the 12 nodal lines across the plate.

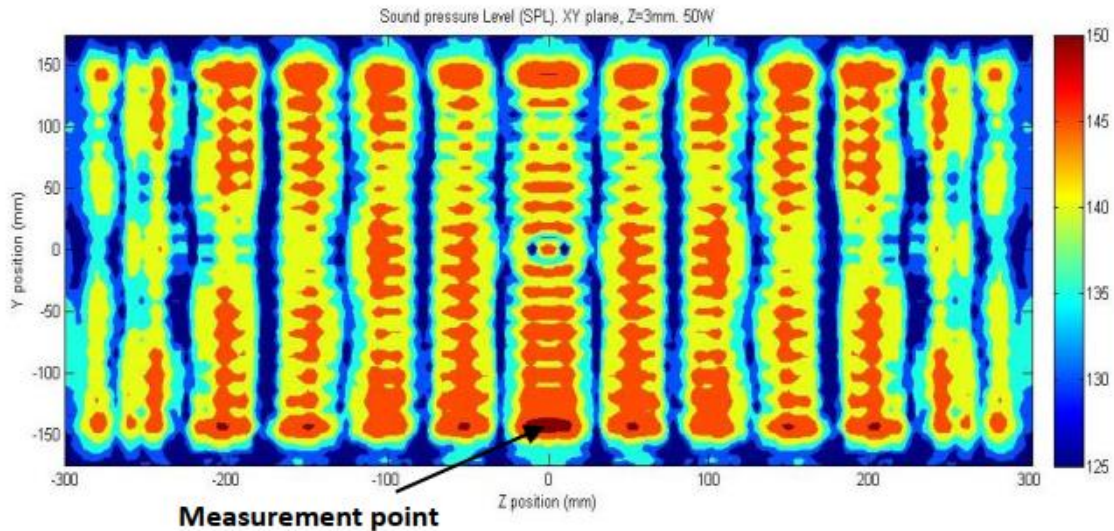


Figure 67. Sound pressure distribution at a plane parallel to the Al plate at 3 mm from the plate [120].

The pressure distribution in the free field under the transducer is not uniform and it varies with distance from the plate. This can be seen in Figure 68.

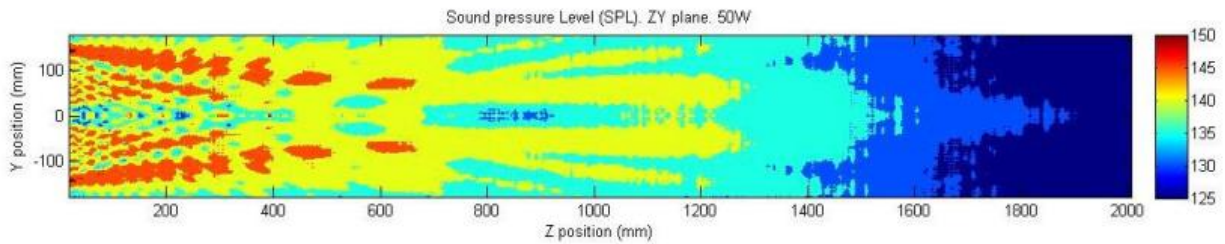


Figure 68. Pressure distribution in a transversal – perpendicular plane of the rectangular Al plate, in free field [120].

The average pressure at distances from the Al plate is plotted in Figure 69. This figure illustrates that there are a series of maximum and minimum peaks at different distances from the Al plate. However, the highest values of the average acoustic pressure are obtained at distances very close to the Al plate, with the first maximum being at 15 mm [120]. Therefore, in all the experiments conducted using the Al plate, the distance from the plate is fixed at 15 mm, unless otherwise is specified.

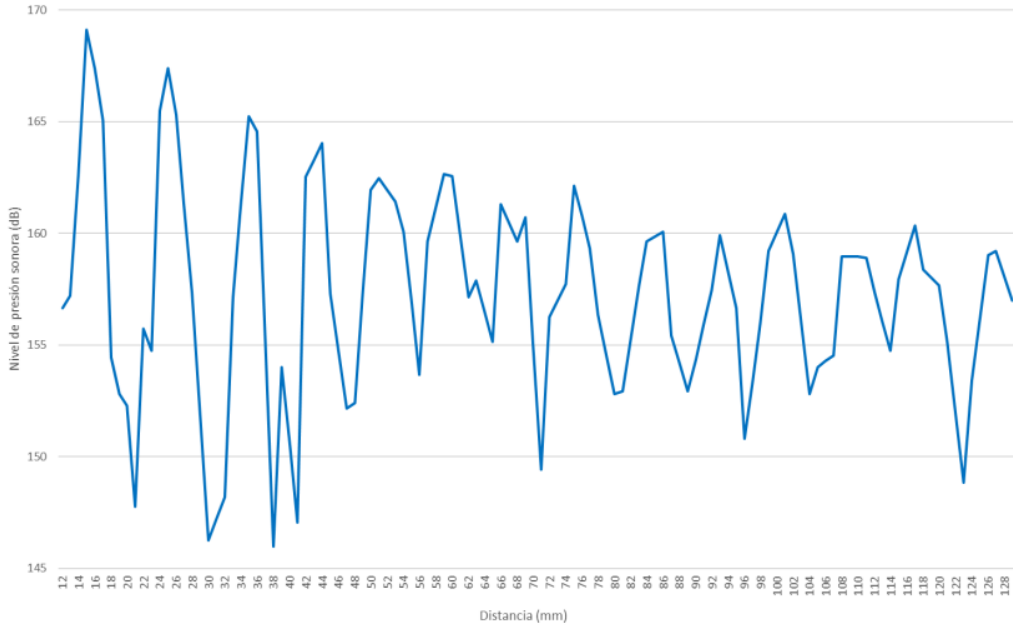


Figure 69. The average pressure from the Al plate at different distances [120].

5.2.1-b Titanium Plate

For the Ti plate, the characterizations are based on numerical simulations conducted by Pusonics [121]. Figure 70 shows the pressure distribution along the axis of the plate.

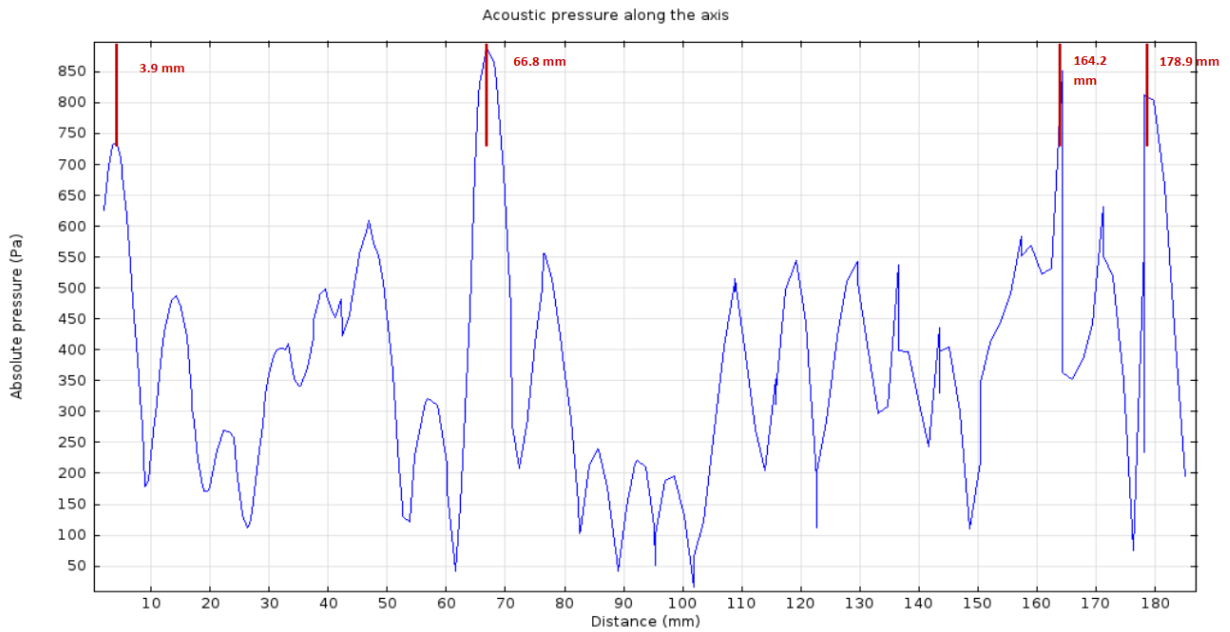


Figure 70. Pressure distribution along the axis of the Ti plate [121].

These measurements are done at the center of the plate and at different distances from the plate. This plot shows that the maximum of acoustic pressure occurs at 3.9 mm, 66.8 mm, 164.2 mm, and 178.9 mm from the Ti plate [121]. To have a better understanding of the pressure distribution at these peaks, the contours of pressure at planes parallel to the plate are illustrated in Figure 71.

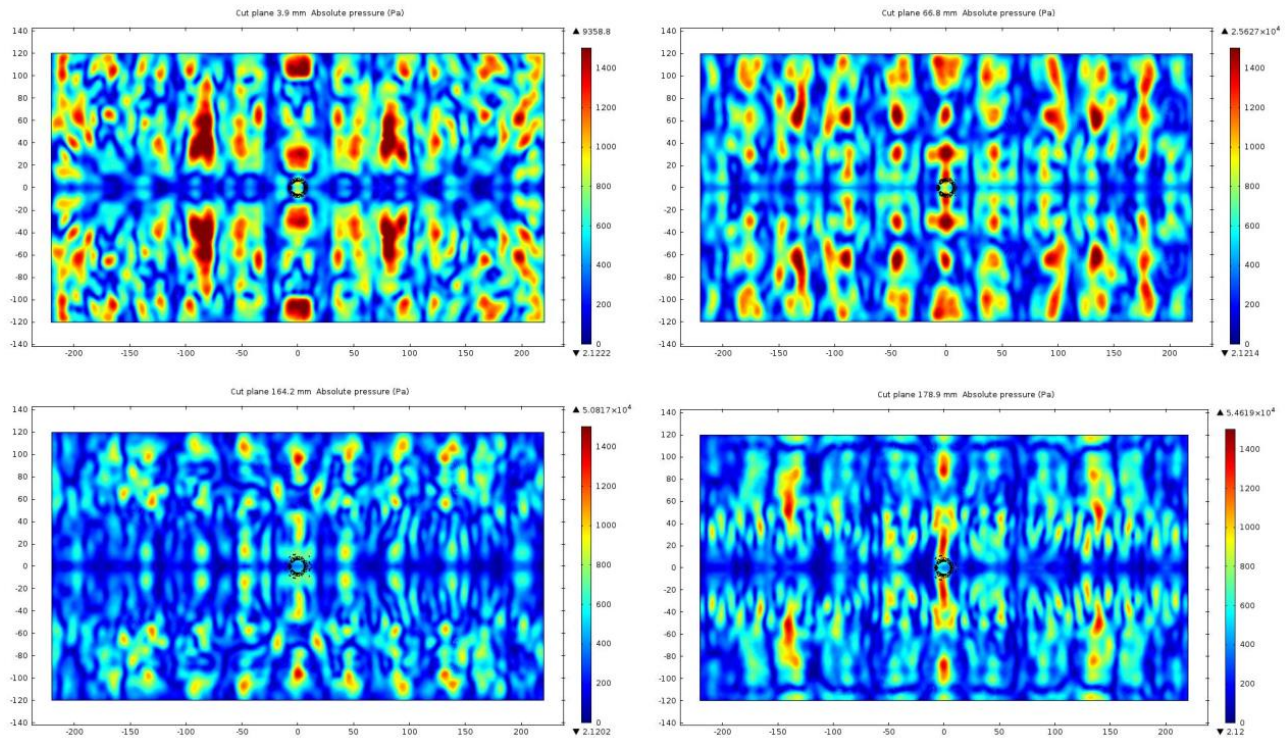


Figure 71. Contours of pressure at planes parallel to the Ti plate at different distances]: 3.9 mm, 66.8 mm, 164.2 mm, and 178.9 mm [121].

Figure 71 shows that at each plane, the pressure values are maximum near the center of the transducer plate and the high-pressure regions are more uniform at 3.9 mm distance. To support these observations, the average pressure in planes parallel to the Ti plate is plotted in Figure 72. According to this plot, the average sound pressure is maximum at near field of the transducer plate. This graph is different than the pressure distribution along the axis, because in this case, the energy contained in the whole plane parallel to the Ti plate is plotted. Based on the information provided by Pusonics, the maximum energy is at 3.9 mm from the Ti plate and the second peak for this plot is at 12.4 mm. The contours of pressure at this distance are shown in Figure 73. According to these results, Pusonics recommended to place the transducer as close as possible to the sample,

preferably at a distance about 4 mm [121]. Hence, in all the experiments conducted by this transducer plate, the distance is fixed at 4 mm, unless otherwise is specified.

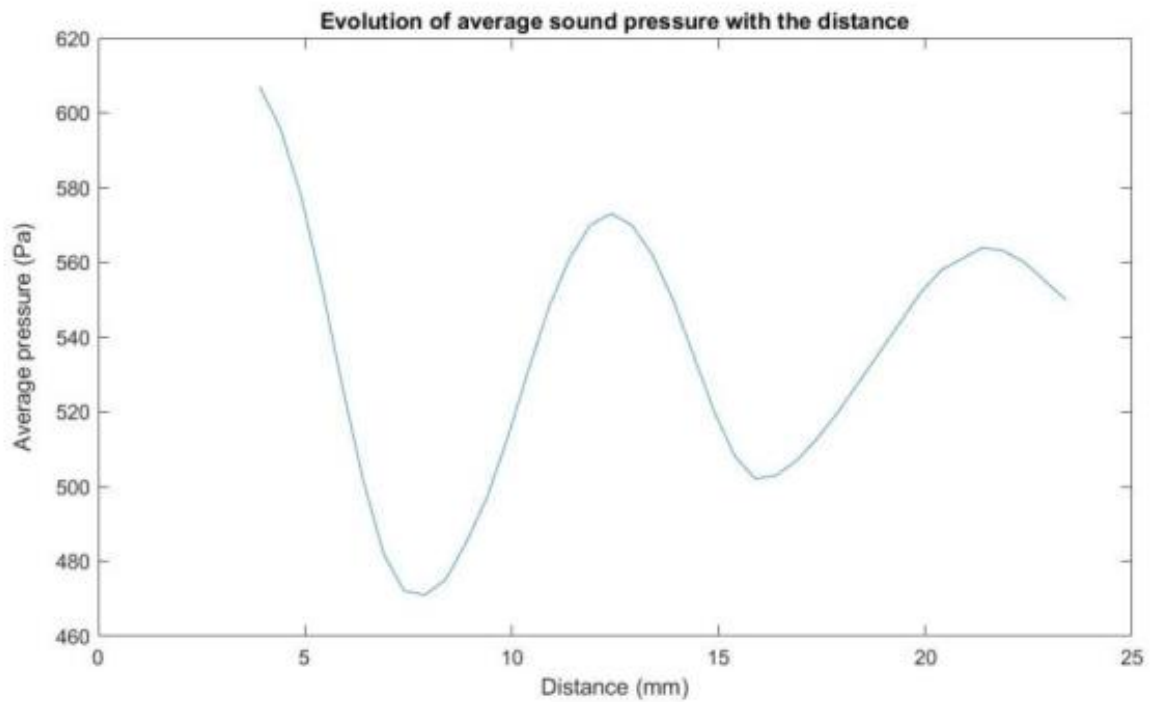


Figure 72. Evaluation of average sound pressure with distance from Ti plate [121].

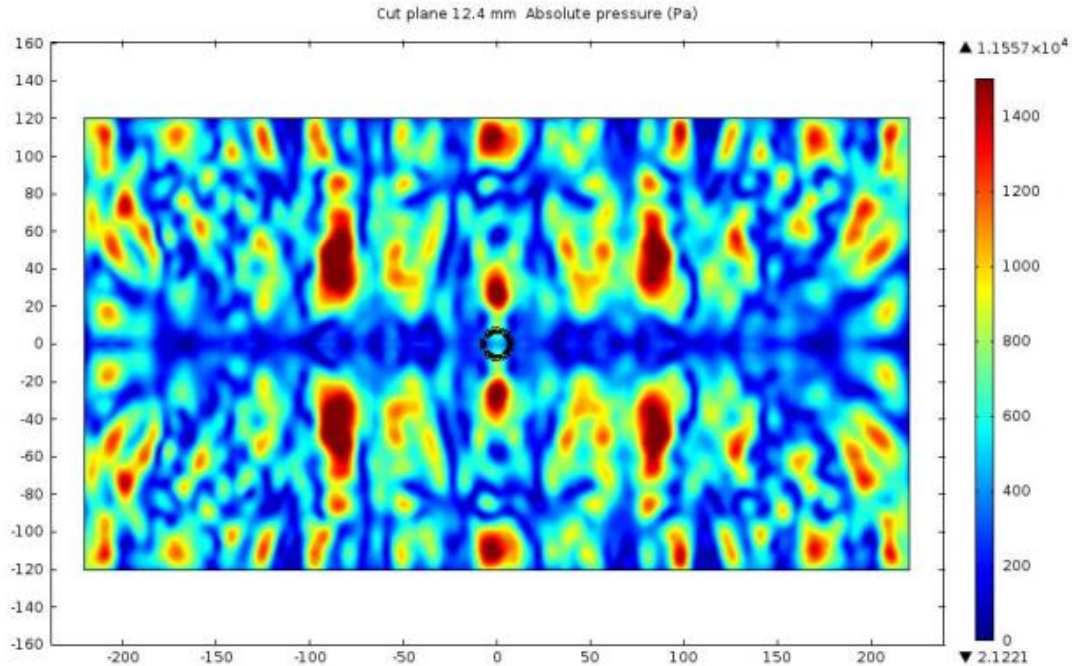


Figure 73. Contours of pressure at 12.4 mm plane parallel to the Ti plate [121].

5.2.2 Effect of Sample Holder

Two different sample holders are employed in this study. The first sample holder is a solid plate that is placed underneath the sample. In this case, the drying can only occur from the top surface of the sample. In this study, all the experiments for hardwood samples using Al plate are conducted using the solid sample holder. After receiving the Ti plate, two experiments were conducted using a solid sample holder and using a mesh sample holder. The mesh sample holder is shown in Figure 74. The size of the holes are about 5 mm.

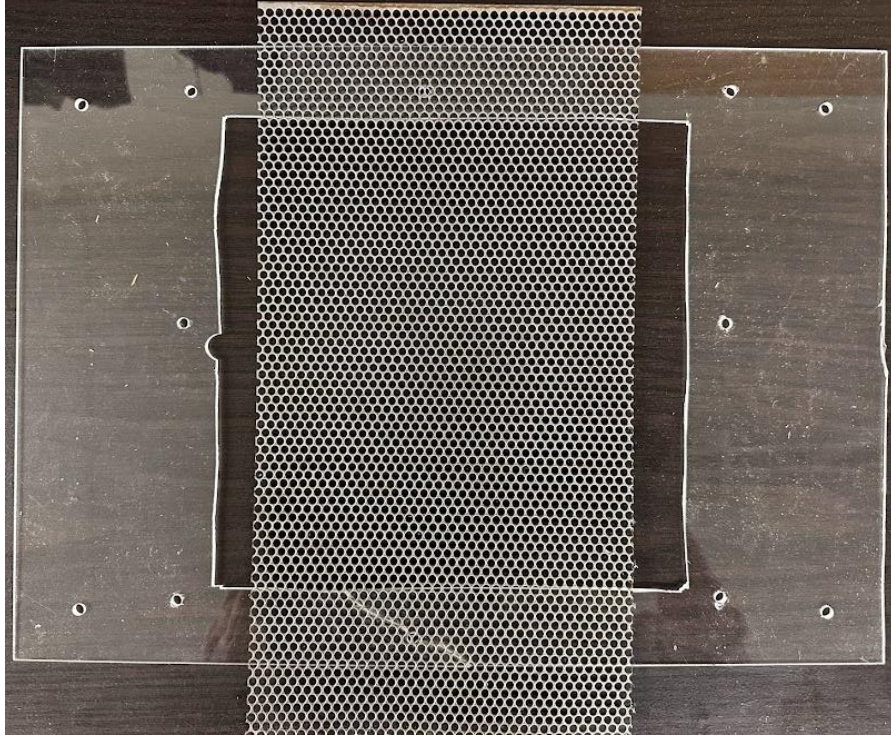


Figure 74. Mesh sample holder used in the drying experiments with the Ti plate.

In order to compare the drying performance using the solid sample holder and mesh sample holder, two drying experiments are conducted for a similar sample. The results are plotted in Figure 75. As it is illustrated, the drying time reduces by using the mesh sample holder instead of the solid sample holder. The reason for it is that in the case of a mesh sample holder, the drying can occur from both top and bottom of the sample and therefore, the drying rate enhances significantly.

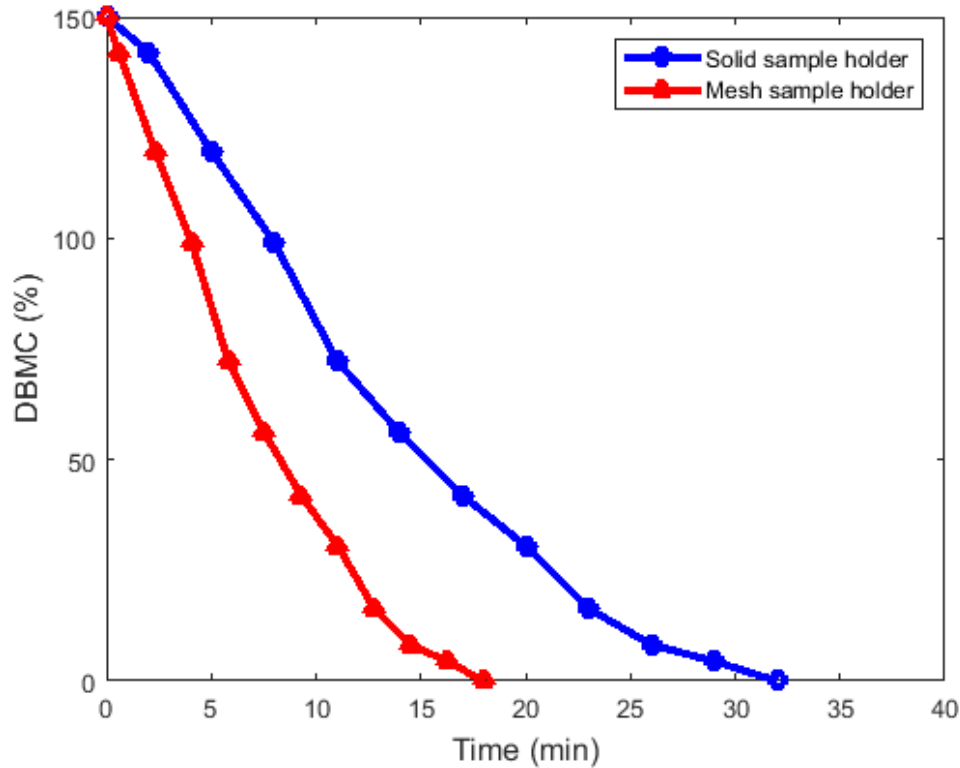


Figure 75. Comparing the drying curve for a sample dried using solid holder and a sample dried using mesh holder. Ti plate is used for these experiments and the sample is S-R-150-160.

5.2.3 Thermal Effect of Airborne Ultrasonic Drying

In this section, the Ti plate is used to investigate the thermal effects of airborne ultrasonic drying. Infrared images of the transducer plate from the bottom view and side view are shown in Figure 76 and Figure 77, respectively. The maximum temperature at the bottom of the plate is 40 °C. Figure 78 shows the measured temperatures at different distances underneath the transducer plate at three different locations. The temperature measurements are conducted using fiber optic sensors. Figure 78 shows that at a fixed distance, the temperature difference between the center and the two sides of the rectangular plate is about 2 °C and the temperature decreases as the distance increases. In addition to the conversion of electrical power to heating energy in the plate, part of the temperature rise underneath the transducer plate is due to the absorption of ultrasonic waves and the other part is caused by the turbulent flow generated near the sample surface due to the vibrations, which enhances heat and mass transfer. These observations agree with literature such

as [122-124]. Therefore, unlike the direct-contact ultrasonic drying, which the transducer's temperature increased up to 80 °C during drying (chapter 4), non-contact ultrasonic drying is a lower-temperature technology. Hence, as stated by Zhang and Abatzoglou [47], the heating effect can be much more important in direct-contact ultrasonic drying and depending on the application, it may be beneficial or disadvantage for the process.

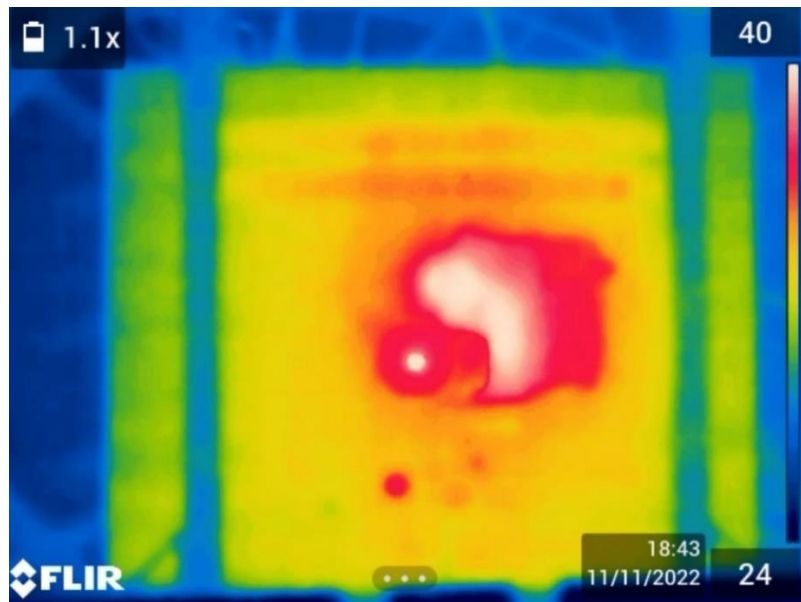


Figure 76. Infrared image of the bottom view of the transducer plate (Ti plate).

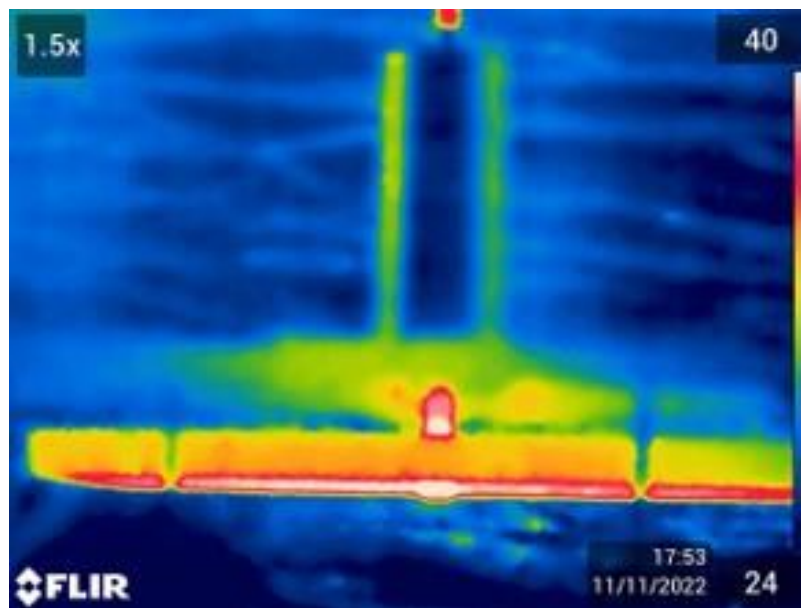


Figure 77. Infrared image of the side view of the transducer plate (Ti plate).

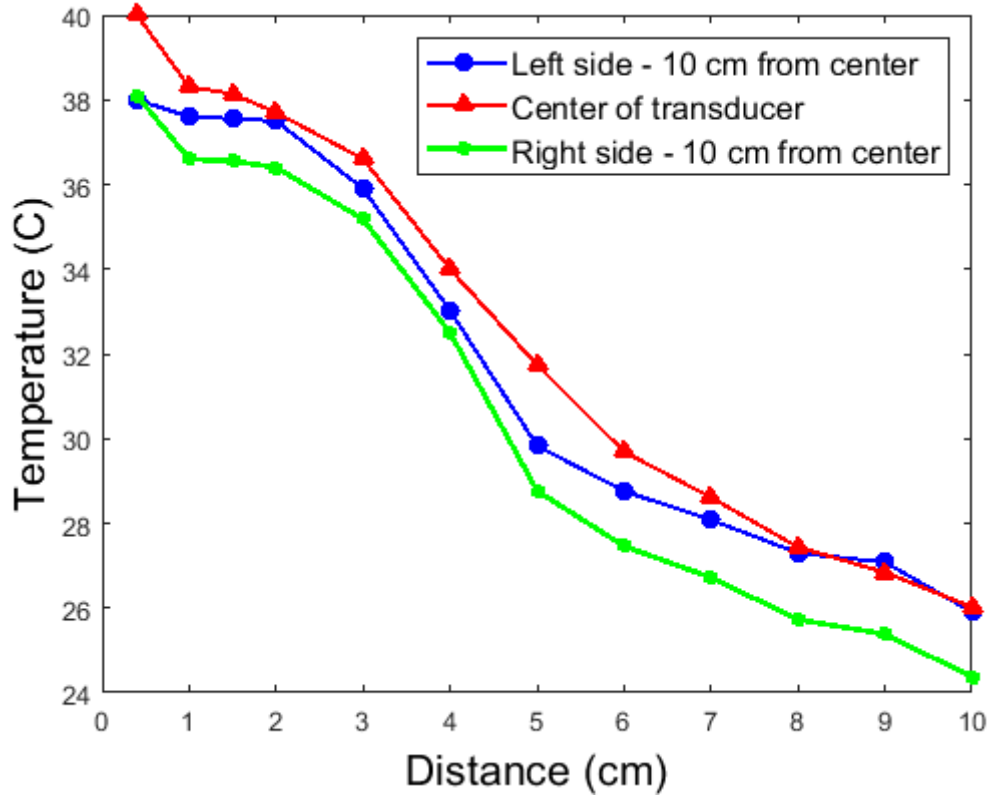


Figure 78. The effect of distance from the plate on temperature (Ti plate).

The decrease in the temperature by increasing the distance from the plate is due to the fact that the average sound pressure level at planes parallel to the plate decreases by increasing the distance. As it was discussed above, from the information provided by Pusonics S.L., the maximum sound energy for the Ti plate is at about 4 mm distance from the plate. To confirm this observation, the drying curves of a similar sample at different distances from the transducer plate are illustrated in Figure 79. It is obvious that the drying curve slope is maximum at 4 mm distance from the plate and the drying time increases by increasing the distance.

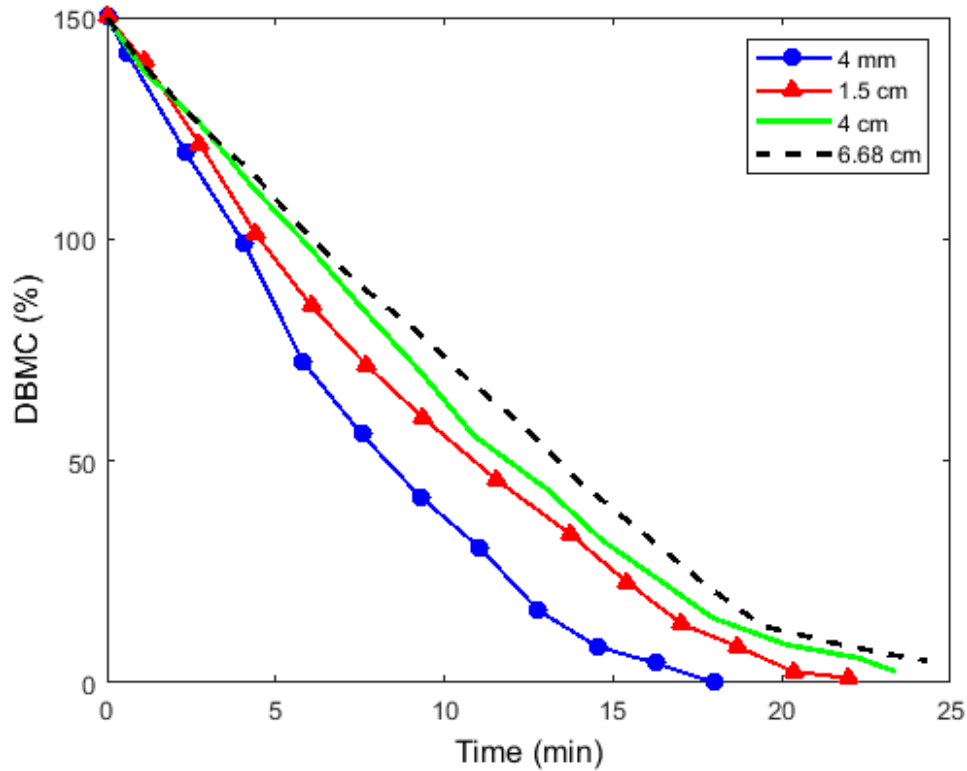


Figure 79. The effect of distance from the plate on drying curves for S-R-150-160 sample dried using Ti plate.

5.2.4 Comparing Airborne Ultrasonic Drying with Conductive Heat Drying

Since the temperature rises up to 40 °C at 4 mm underneath the transducer, the airborne ultrasonic drying is compared with conductive drying at 40 °C in Figure 80. It is illustrated that airborne ultrasonic drying decreases the drying time by 9% compared to hot plate drying. The favorable impact of airborne ultrasonic drying on quality of the dried sample will be discussed in the next sections.

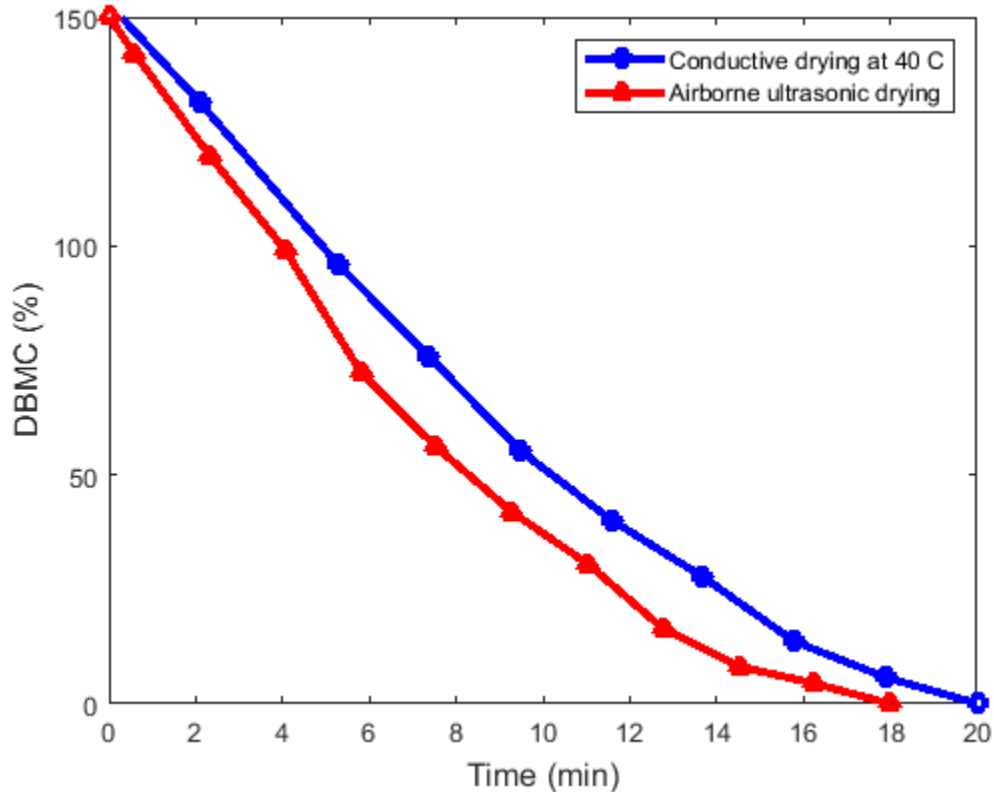


Figure 80. Comparing the drying curves for airborne ultrasonic drying (Ti plate) and conductive heating at 40 °C for S-R-150-160.

5.2.5. Temperature Inside the Sample

To measure the temperature inside the sample underneath the transducer, a sandwich of two identical handsheets are made and three fiber optic thermocouples are mounted in between them. The two handsheets are refined softwood with initial moisture contents of 150%. The weight of each sample is chosen such that the total basis weight of the sandwich is 325 g/m². One thermocouple is placed at the center and two other thermocouples are placed 7 cm away from the center in the diameter of the handsheet. The sandwich sample is placed underneath the transducer in the longitudinal direction. Figure 81 shows the results of temperature measurements inside the sandwich. There are some instabilities in the temperatures in time. One reason for these fluctuations is the movement of air (compression and expansion cycles) by the ultrasonic waves underneath the transducer in addition to the possible impact of the changes in the moisture content of the sample. The temperature at the center of the sample has the maximum value compared to

the other two temperatures. The trend is that initially the thermocouples are at room temperature but when it is placed underneath the transducer, the temperature increases. As the sample gets dried, the amount of energy consumed for evaporation decreases and as a result, the temperature increases by time. At the end, when the sample is completely dried, the temperature reaches to the maximum temperature measured in free field from Figure 78 above.

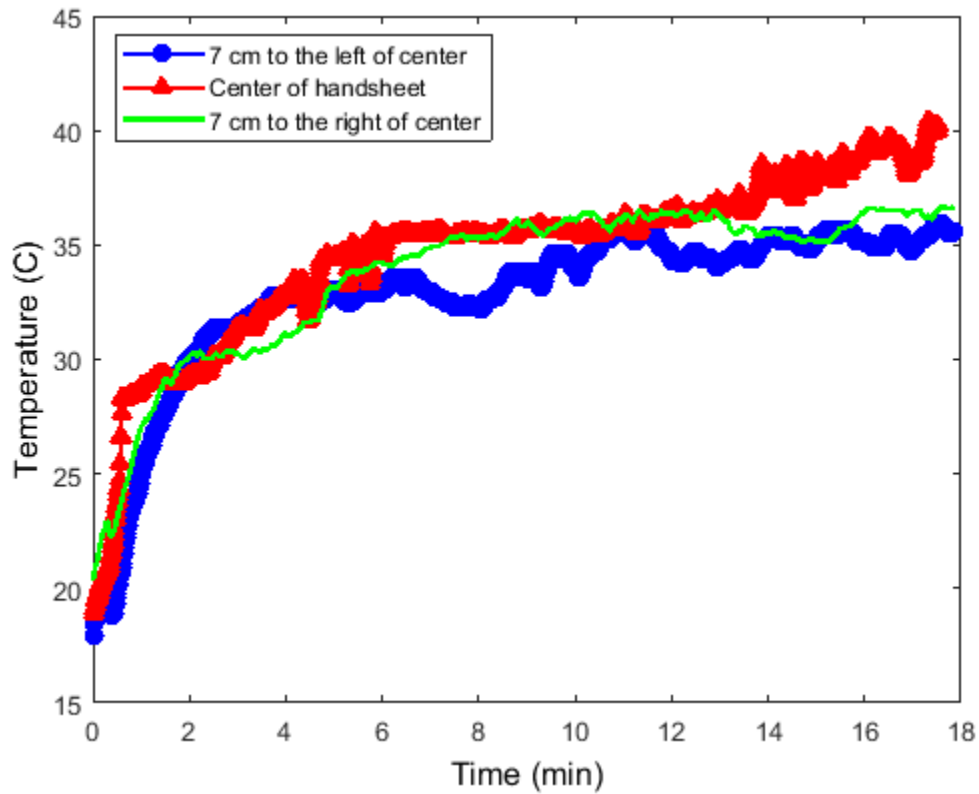


Figure 81. Temperature measurements inside a sandwich sample during airborne ultrasonic drying for S-R-150-325 (Ti plate).

5.2.6 Analysis of the Factorial Design of Experiments

The experiments for the hardwood samples are conducted using the Al plate and the solid sample holder. After that due to the ultrasonic fatigue the transducer stopped functioning. Therefore, Pusonics manufactured the Ti plate and the experiments for the softwood are conducted using the Ti plate. In addition, since the drying rate enhanced by using the mesh sample holder, the experiments for softwood samples are conducted using the mesh holder. It should be mentioned

that the results from the two plates cannot be compared one by one as the transducers have different characteristics. However, the qualitative behavior will be compared.

The drying curves for the ultrasonically dried hardwood and softwood samples are shown in Figure 82 and Figure 83. The final DBMC of the dried samples is ~3%. The experiments are repeated three times, and the error is less than 5%. Each drying curve can be split into a constant drying rate region followed by a falling drying rate region. The constant drying rate corresponds to free water removal and the falling drying rate is governed by the removal of the associated water (also known as bound water). The same behavior was observed for the direct-contact ultrasonic drying (chapter 4) and this is typical regardless of the drying mechanism.

For both hardwood and softwood, increasing the initial moisture content, slightly increases the drying time, especially at higher basis weights, since the thickness of the sample is higher, the water removal is slower. In general, unrefined samples dry faster than refined samples and it is predicted due to the difference in pore structure and fiber characteristics (i.e., sheet formation). The unrefined fibers are longer in length and larger in diameter compared to refined fibers and it results in higher pore volume and thickness in unrefined samples. In general, the pores allow the ultrasonic waves to easily reach the inner structure of the paper being dried; hence, higher open pore porosity makes the ultrasonic drying to be more efficient. More details on the effect of pore characteristics and permeability measurements will be discussed in section 5.2.9-c.

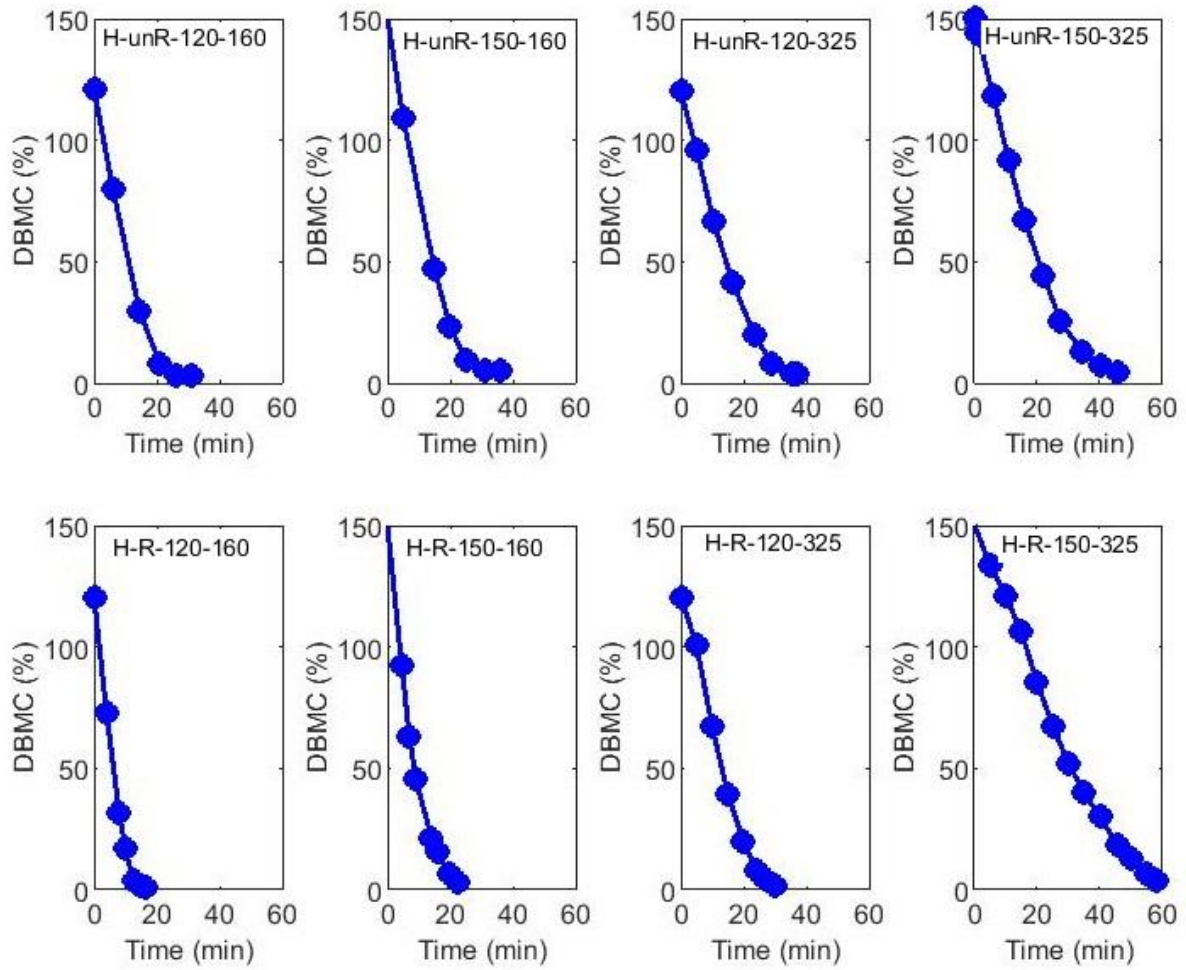


Figure 82. Airborne ultrasonic drying curves for hardwood samples dried using Al plate.

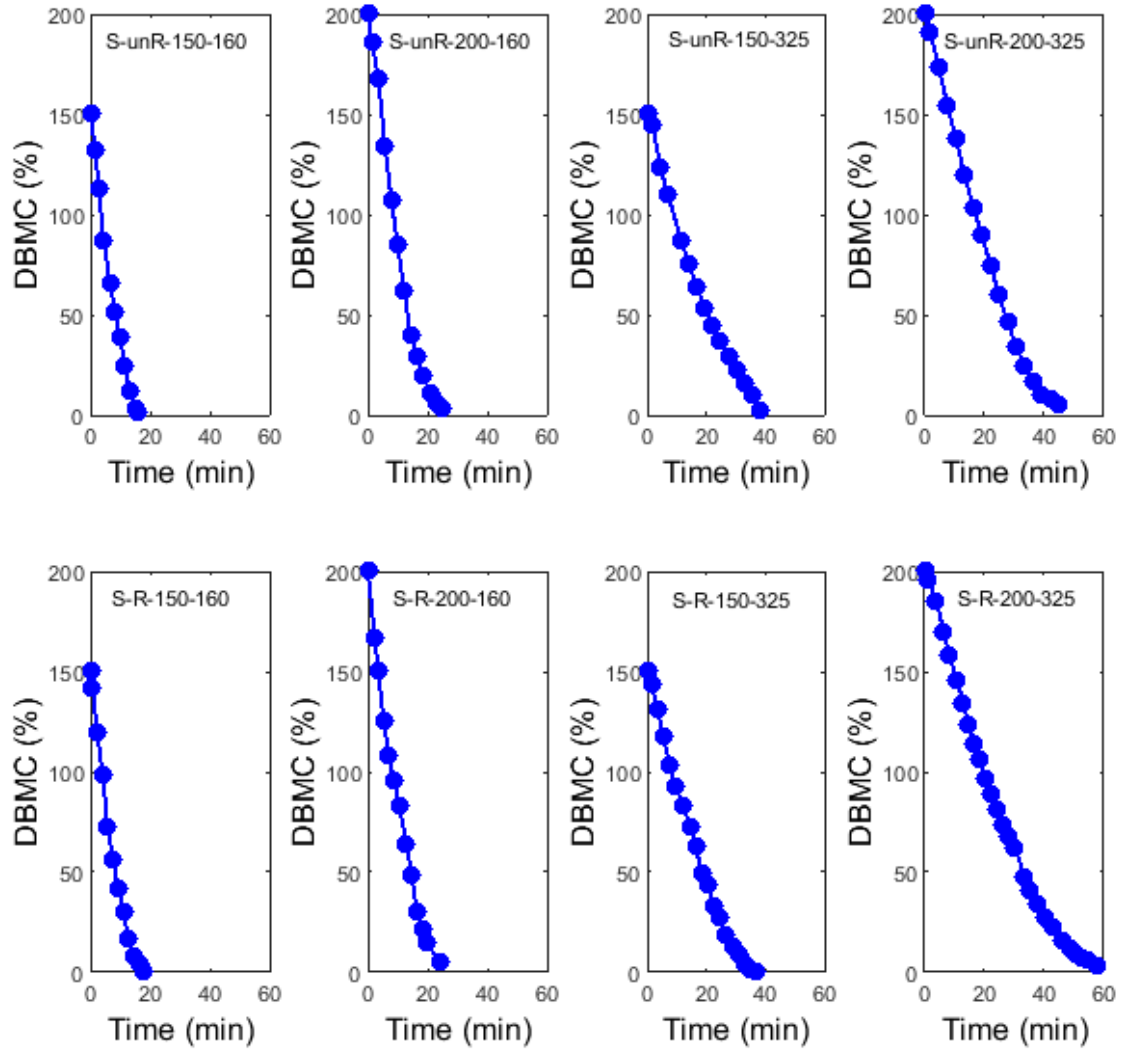


Figure 83. Airborne ultrasonic drying curves for softwood samples dried using Ti plate.

In order to analyze the results more systematically, 2^3 factorial design of experiments are used for the total time of ultrasonic drying.

5.2.7 Importance of the Controlling Factors on Total Time of Ultrasonic Drying

ANOVA analysis for the total time of ultrasonic drying for both hardwood and softwood are summarized in the pareto charts of the standardized effects in Figure 84 and Figure 85. The pareto charts allow to detect the factor and the interactive effects that are most important to the design optimization and the absolute values are shown from the largest effect to the smallest effect.

According to Figure 84 and Figure 85, in the range of the studied parameters, basis weight has the maximum effect on the total time of ultrasonic drying and after that initial moisture content. The interactive effects of the factors are less important in this analysis. This agrees with the results of direct-contact ultrasonic drying from chapter 4. The outcome of linear regression analysis for the total time of drying is reported in Table 19. The coefficient of determinations for these analysis are above 99.6% and p-values less than 0.01, implying that the predicted correlations by linear regression analysis are adequate for describing the total time of ultrasonic drying. Since the refining condition is a qualitative data, the numeric values of -1 and 1 are considered for unrefined and refined, respectively. The relationship between the total time of ultrasonic drying and the factors is described as:

$$Total\ Drying\ Time = \beta_0 + \sum_{i=1}^k \beta_i X_i + \sum_{i=1}^k \sum_{j=1}^k \beta_{ij} X_i X_j + \beta_{123} X_1 X_2 X_3 \quad (5-3)$$

where k is the number of factors, and X_i ($i = 1, 2, 3$) are the controlling factors. β_0 is the constant coefficient, β_{ij} are the coefficients for the interactive effects of factors and β_{123} captures the interactive effect of all the three factors. Factors 1, 2, and 3 are defined as initial DBMC, basis weight, and refining condition, respectively.

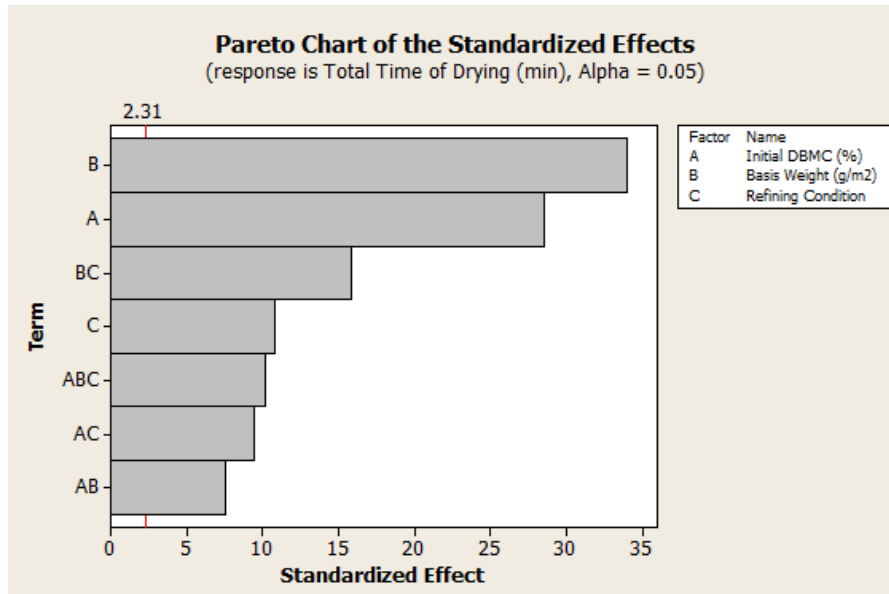


Figure 84. Pareto chart of the standardized effects for total time of ultrasonic drying for hardwood samples (dried using Al plate).

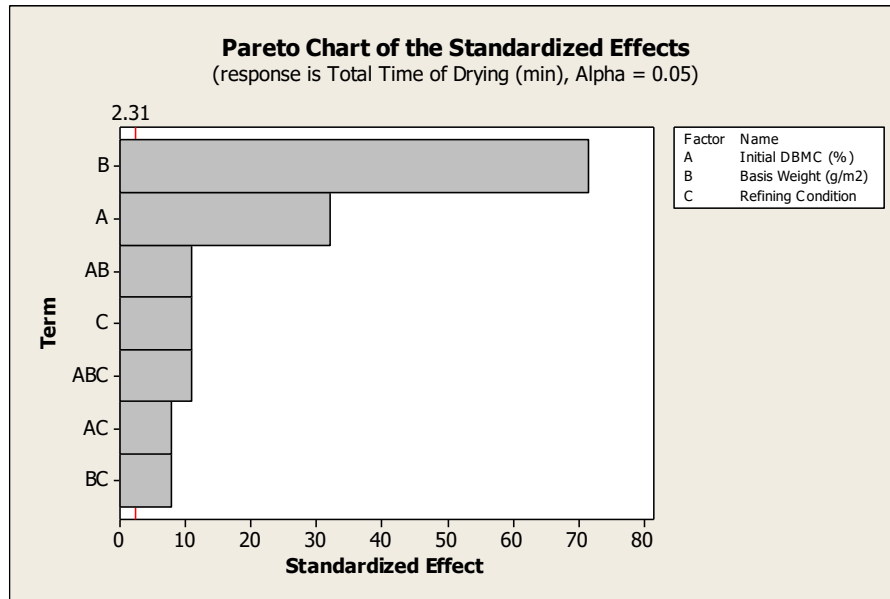


Figure 85. Pareto chart of the standardized effects for total time of ultrasonic drying for softwood samples (dried using Ti plate).

Table 19. Coefficients for equation (5-3) calculated from linear regression analysis.

		β_0	β_1	β_2	β_3	β_{12}	β_{13}	β_{23}	β_{123}	R^2 (%)
Hardwood (Al plate)	Drying time (min)	-8.170	0.112	-0.109	33.413	0.002	- 0.360	- 0.242	0.002	99.69
	Area under drying curve (%.min)	2395.9	-17.28	-21.73	2892	0.213	- 27.67	-18.1	0.16	99.74
	Whiteness index	69.730	0.012	-0.006	-5.121	0.0001	0.031	0.016	-9.839	99.58
Softwood (Ti plate)	Drying time (min)	-6.47	0.024	0.006	31.68	0.0008	- 0.194	- 0.163	0.001	99.8
	Area under drying curve (%.min)	- 638.74	1.68	-7.43	1581	0.105	- 10.28	- 10.01	0.063	99.62
	Whiteness index	79.32	0.0126	0.0088	6.08	6.27×10^{-6}	-0.03	- 0.026	9.97×10^{-5}	99.7

5.2.8 Importance of the Controlling Factors on Area Under Drying Curve

In addition to the total time of ultrasonic drying, the area under the drying curves is analyzed using ANOVA. The area under the drying curve represents the total change in DBMC over the total time of drying. Figure 86 and Figure 87 represent the pareto charts of the standardized effects for hardwood and softwood, respectively. Similar to the total time of ultrasonic drying, the basis weight has the maximum effect on the area under the drying curve and after that the effect of initial moisture content is important. The outcome of linear regression analysis for the area under the drying curve is reported in Table 19.

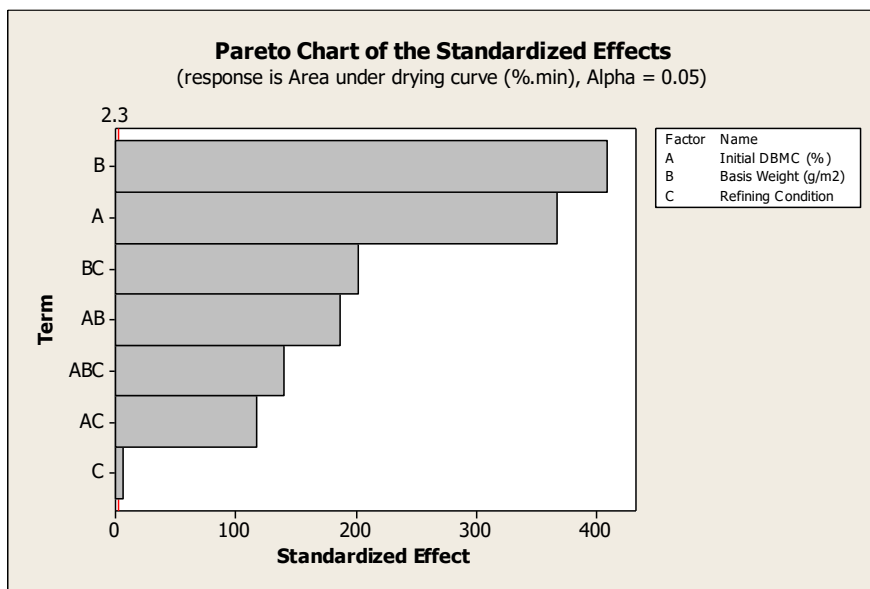


Figure 86. Pareto chart of the standardized effects for area under the drying curve for hardwood samples (dried using Al plate).

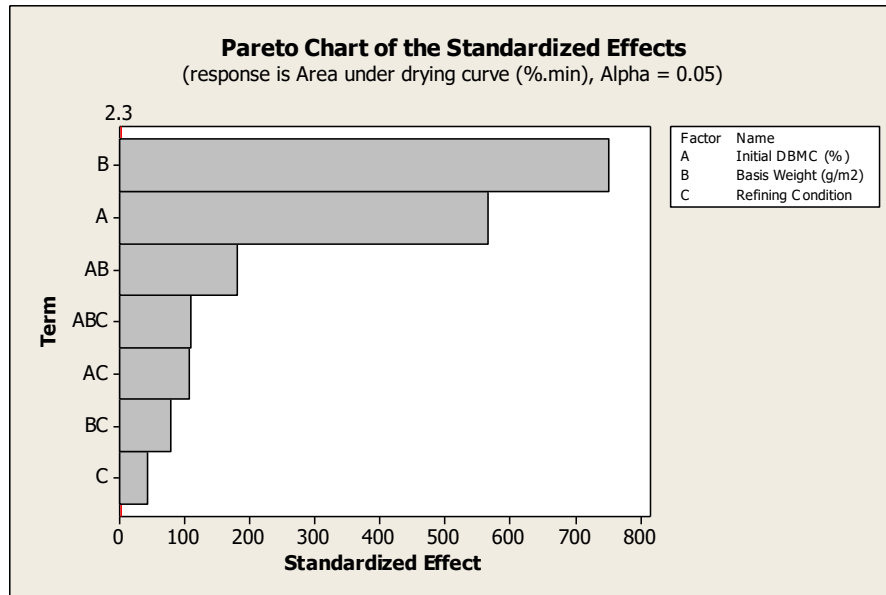


Figure 87. Pareto chart of the standardized effects for area under the drying curve for softwood samples (dried using Ti plate).

5.2.9 Quality measurements

The quality of the ultrasonically dried samples such as the color and tensile strength plays a significant role in terms of application of the paper. This section is devoted to the quality measurements of the hand-sheet papers dried by non-contact ultrasound mechanism. In addition, in support of the above discussions to relate the pore characteristics and the drying behavior, permeabilities of the samples are measured.

It should be mentioned that since the source of the pulps for the direct-contact and non-contact ultrasonically dried samples and the sample dimensions are different, the results are compared qualitatively.

5.2.9-a Colorimeter Measurements

Figure 88 and Figure 89 show the measurements for L^* (lightness index), a^* (red-greenness index), and b^* (yellow-blueness index) for hardwood and softwood samples, respectively. The lightness indices for softwood samples are higher than that of hardwood samples. These measurements are used to calculate the whiteness index of the samples.

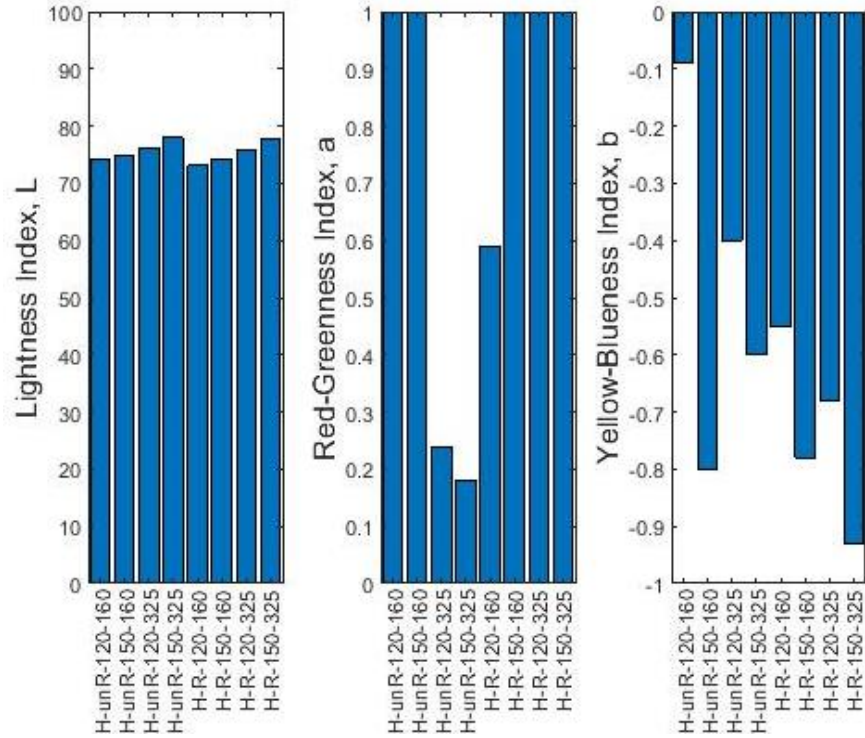


Figure 88. L^* , a^* , and b^* for hardwood samples, dried using Al plate.

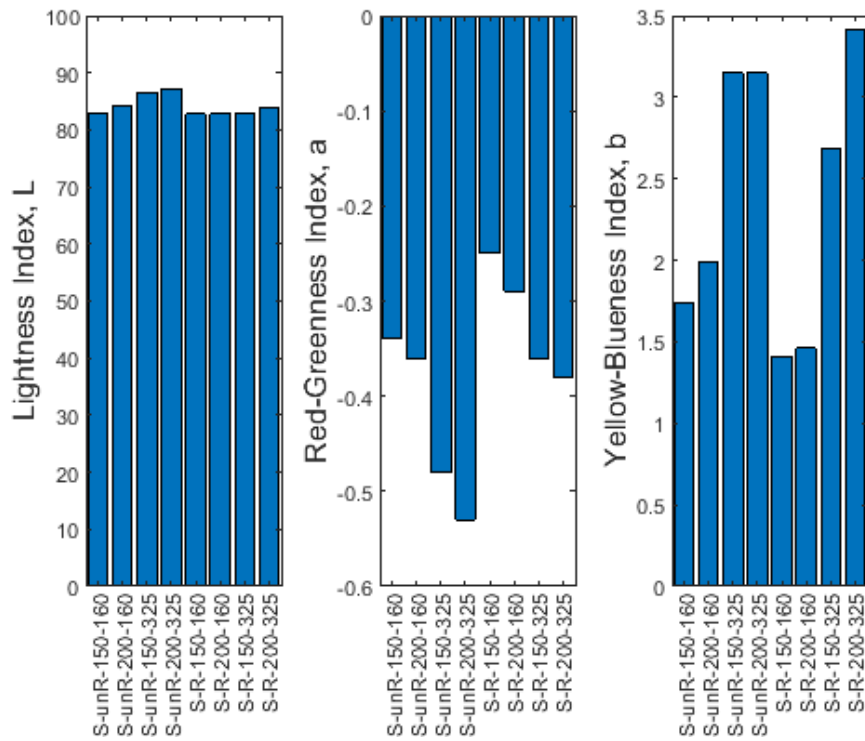


Figure 89. L^* , a^* , and b^* for softwood samples, dried using Ti plate.

To compare the impact of drying method, Figure 90 compares the L^* , a^* , and b^* for a softwood sample dried by airborne ultrasonic drying and a sample dried using conductive drying.

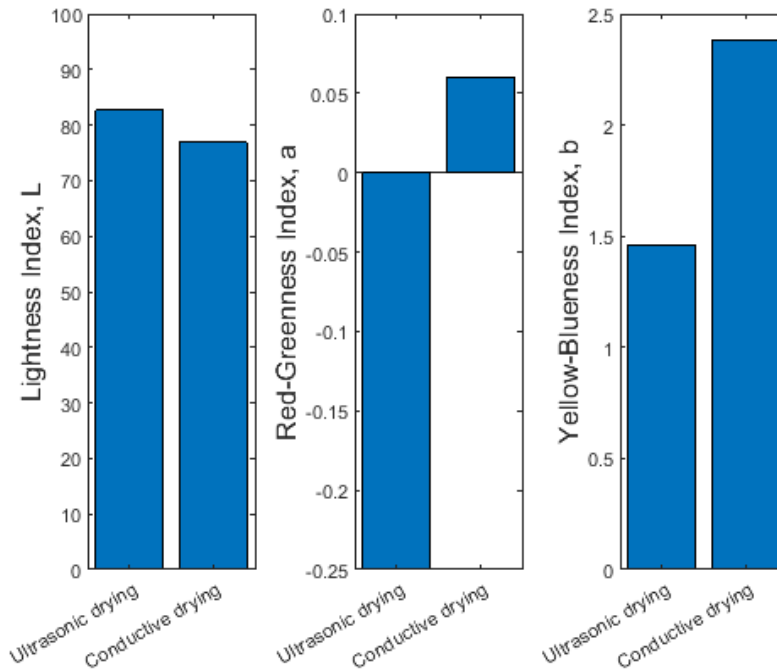


Figure 90. Comparison of L^* , a^* , and b^* for S-R-150-160 dried using airborne ultrasonic drying (Ti plate) and a similar sample dried using conductive drying.

Using these measurements, whiteness indices of a sample dried using airborne ultrasonic drying and a similar sample dried by conductive drying are compared in Figure 91. It is shown that direct heating in conductive drying reduces the whiteness index of the sample compared to airborne ultrasonic drying. This is due to the thermal effects when the sample is in direct contact with the hot plate. The reported data for colorimeter measurements are an average of three measurements from each side of the handsheet.

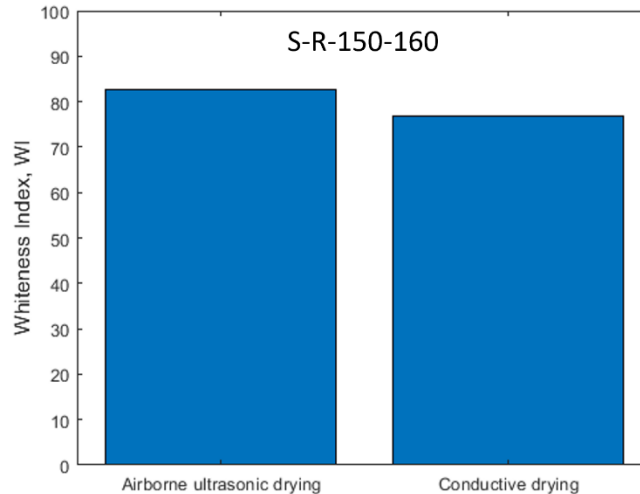


Figure 91. Comparing the whiteness indices of an ultrasonically dried sample (Ti plate) with a sample dried using conductive heating at 40 °C. The maximum standard deviation is 0.04.

It is shown that direct heating in conductive drying reduces the whiteness index of the sample compared to airborne ultrasonic drying.

Figure 92 and Figure 93 show the whiteness indices for hardwood and softwood samples, respectively dried using airborne ultrasonic drying. The maximum standard deviation for the reported numbers is 0.04. For both hardwood and softwood, the unrefined samples have higher whiteness index and by increasing the initial moisture content and basis weight, the whiteness index increases, slightly. These observations are due to increasing the porosity of the sample by increasing the initial moisture content and basis weight. In addition, the whiteness indices for the softwood samples used in this study are higher than hardwood samples. It should be noted that the source of the softwood pulp used in this study are dried sheets, which influences the sheet formation and the porosity of the samples. In fact, lightness is a subjective measure of perceived light and higher porosity leads to higher lightness and therefore higher whiteness index. The results generally agree with the results for the direct-contact ultrasonic drying from chapter 4. In that paper, the whiteness index of an ultrasonically dried sample with a sample dried using conductive heating at 80 °C was compared and observed that direct-contact ultrasonic drying slightly improves the whiteness index.

The results of linear regression for Whiteness index are reported in Table 19. For these samples, basis weight followed by the initial DBMC have the highest effects on the whiteness index.

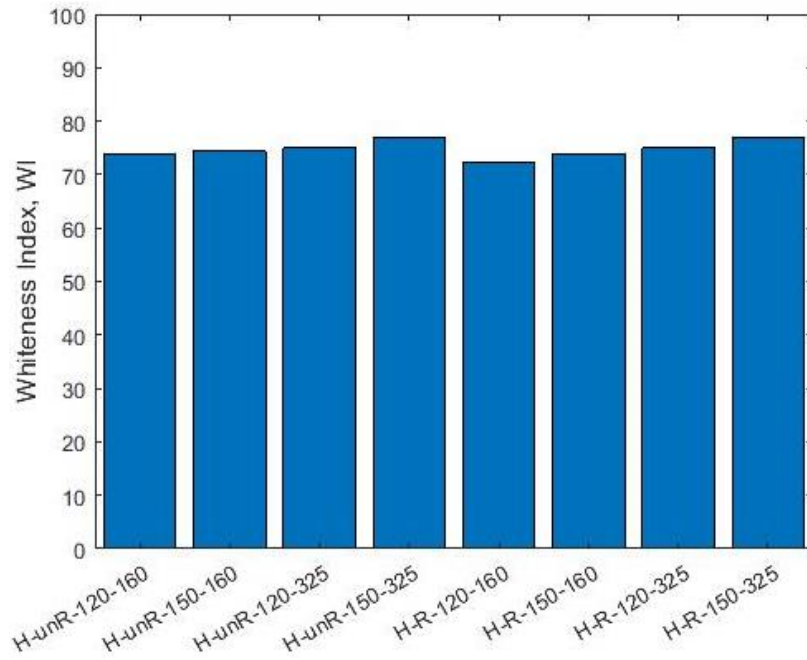


Figure 92. Whiteness index of ultrasonically dried hardwood samples (dried using Al plate).

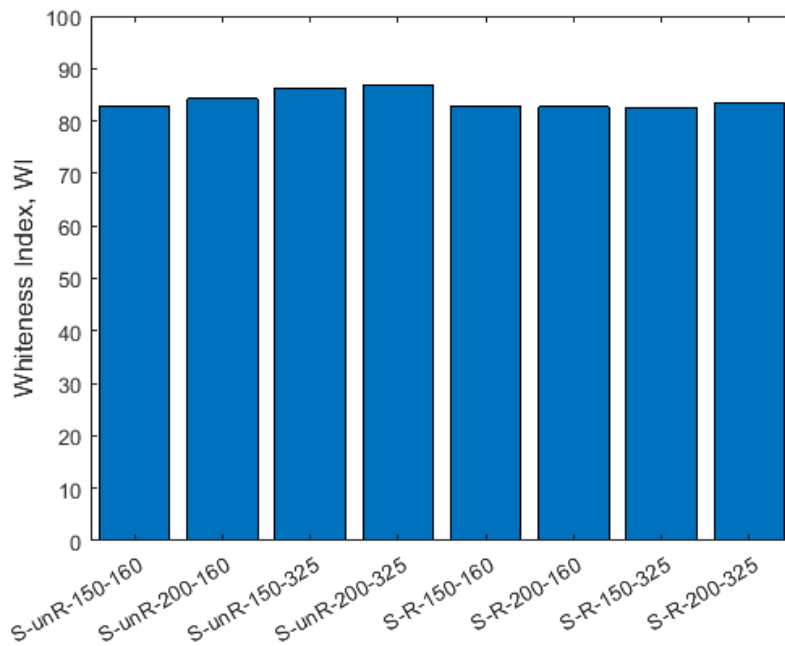


Figure 93. Whiteness indices of ultrasonically dried softwood samples (dried using Ti plate).

5.2.9-b Tensile Strength Measurements

Figure 94 compares the tensile strength of a sample dried using airborne ultrasonic drying with a sample thermally dried at 40 °C in contact with a hot plate. The tensile strain is almost the same for the two samples, but the sample dried using ultrasonic drying has a slightly higher tensile stress, which is favorable for the end product. This could be explained by the difference in the mechanism of heat transfer in airborne ultrasonic drying versus contact heat drying. In airborne ultrasonic drying, convection is the dominant mechanism and hence, it maintains the fiber structure and the sheet formation. Whereas in contact heat drying, the dominant mechanism is conduction which directly impacts the properties of the sample. Therefore, the product quality is slightly higher for the sample dried using airborne ultrasonic drying.

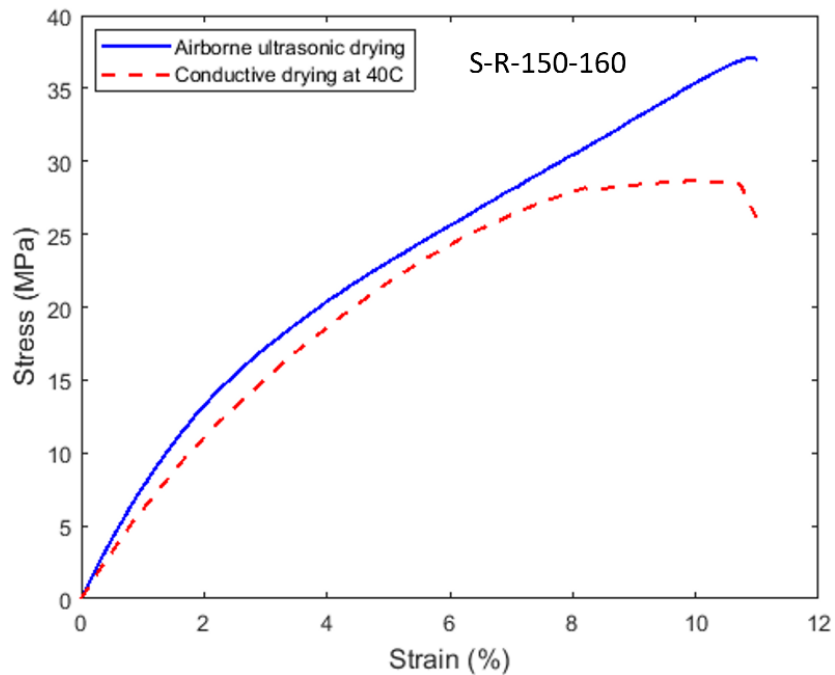


Figure 94. Comparing stress-strain curves for an ultrasonically dried sample (Ti plate) with a sample thermally dried sample at 40 °C. The maximum standard deviation is 2.4.

Figure 95 and Figure 96 compare the tensile strength measurements for refined and unrefined hand-sheet samples, respectively. The maximum standard deviation for the measurements is 3.1. The effect of initial moisture content on the tensile strength behavior is not significant. The refined samples have higher ultimate tensile strength (UTS) compared to that of unrefined samples. This

is due to the fact that refining of the pulp results in better sheet formation and thus, better tensile strength. Similar to the direct-contact ultrasonically dried samples, due to the effect of the grips, the sample with higher basis weight and thickness has a lower UTS. As expected, UTS for the center point is between the values for refined and unrefined pulps. It should be mentioned that the quantitative difference between the tensile strength of the samples dried using direct-contact and non-contact ultrasonic drying comes from the difference in the thickness and tensile strength of the samples. Table 20 and Table 21 summarize the mechanical strengths for hardwood and softwood samples, respectively.

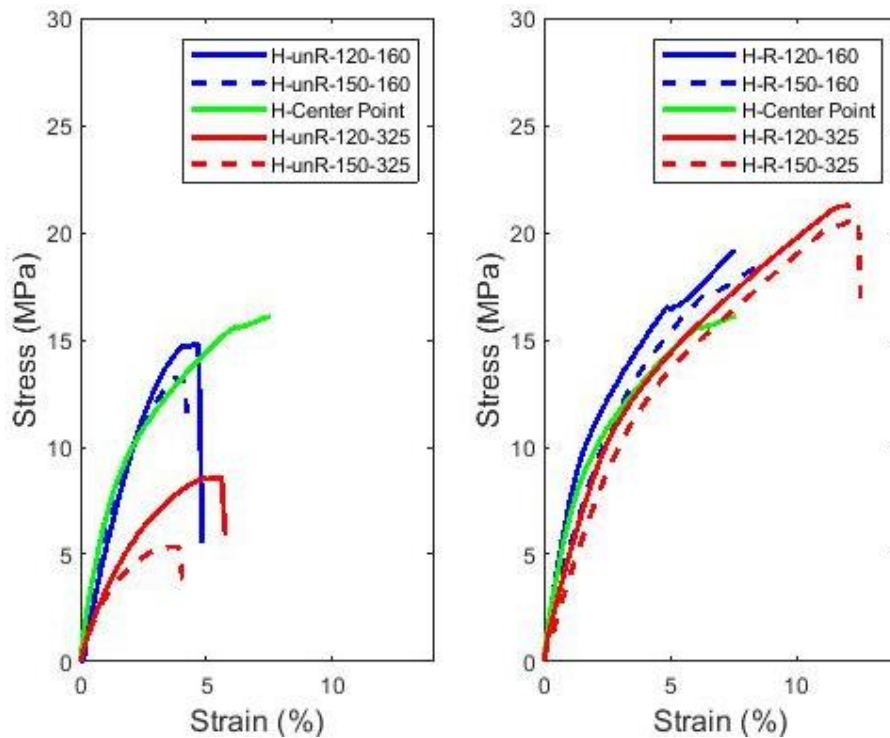


Figure 95. Stress-strain curves for (a) unrefined hardwood samples and (b) refined hardwood samples. The samples are dried using Al plate.

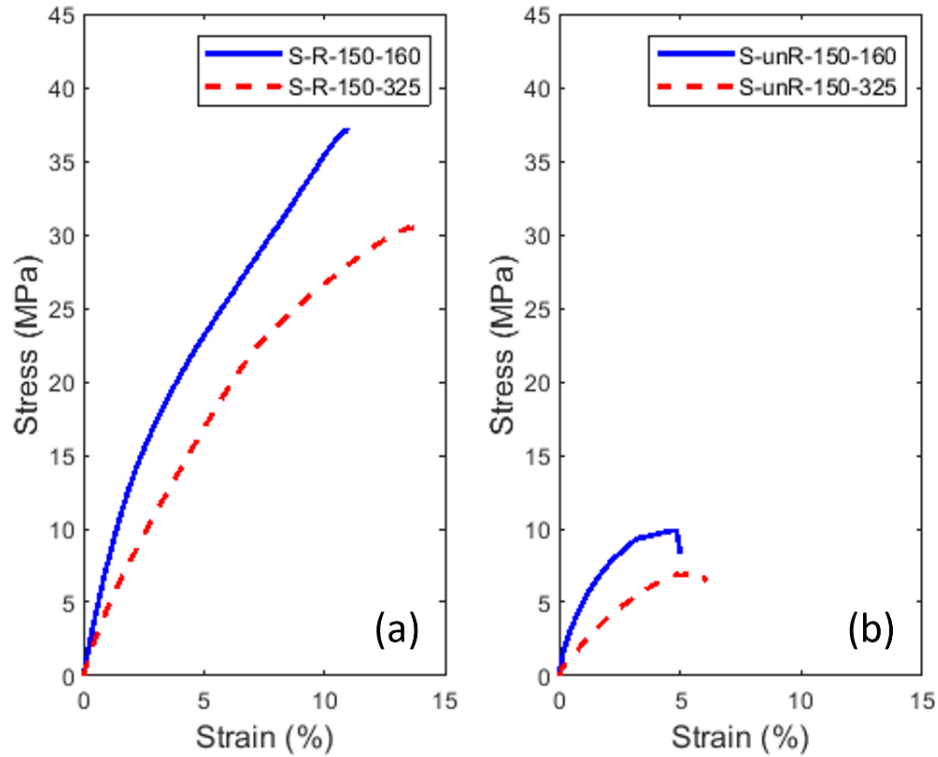


Figure 96. Stress-strain curves for (a) unrefined softwood samples and (b) refined softwood samples. The samples are dried using Ti plate.

Table 20. Ultimate tensile strain and ultimate tensile stress for different hardwood samples (dried using Al plate).

Sample	Ultimate Tensile Strain (%)	Ultimate Tensile Stress (MPa)
H-unR-120-160	4.85	14.79
H-unr-150-160	4.25	13.23
H-unR-120-325	8.76	8.57
H-unR-150-325	4.09	5.36
H-R-120-160	7.58	19.19
H-R-150-160	8.34	18.31
H-R-120-325	12.13	21.25
H-R-150-325	12.52	20.62
H-Center Point	7.59	16.08

Table 21. Ultimate tensile strain and ultimate tensile stress for softwood samples (dried using Ti plate).

Sample	Ultimate Tensile Strain (%)	Ultimate Tensile Stress (MPa)
S-unR-150-160	5.01	9.86
S-unR-150-325	6.06	6.92
S-R-150-160	11	37.13
S-R-150-325	14	30.43
S-R-150-160 (Conductive drying)	10.73	28.64

5.2.9-c Permeability Measurements

One of the pore characteristics of the paper that has a significant impact on its drying behavior is permeability. Permeability is a paper property that allows gasses (air) or liquids to pass through it under a pressure difference across a sheet. Permeability is determined by measuring the rate of airflow through a known area of the paper sheet. Table 22 and Table 23 show the mean values and standard deviations of the Gurley seconds for 5 measurements and the calculated permeability for hardwood and softwood samples, respectively.

Table 22. Permeability measurements for non-contact ultrasonically dried hardwood samples (Al plate).

Sample	Gurley Seconds (mean)	Std. Dev. for 5 tests	Permeability (m²)
H-unR-120-160	29.4	0.4	2.19×10^{-14}
H-unR-150-160	31.4	1.3	2.27×10^{-14}
H-unR-120-325	46.4	0.2	2×10^{-14}
H-unR-150-325	51.8	0.5	3.07×10^{-14}
H-R-120-160	85.9	3.2	6.42×10^{-15}
H-R-150-160	80.1	2.3	8.61×10^{-15}
H-R-120-325	240.8	5.7	4.89×10^{-15}
H-R-150-325	258.7	16.7	5.44×10^{-15}
H-Center Point	98.7	4.6	1.07×10^{-14}

Table 23. Permeability measurements for non-contact ultrasonically dried softwood samples (Ti plate).

Sample	Gurley Seconds (mean)	Std. Dev. for 5 tests	Permeability (m ²)
S-unR-150-160	12.6	0.4	5.84×10 ⁻¹⁴
S-unR-200-160	12.2	0.2	6.03×10 ⁻¹⁴
S-unR-150-325	42.5	1.3	3.62×10 ⁻¹⁴
S-unR-200-325	40.2	3	3.83×10 ⁻¹⁴
S-R-150-160	2025.1	93.7	2.27×10 ⁻¹⁵
S-R-200-160	1778.31	115.5	2.58×10 ⁻¹⁵
S-R-150-325	2859.2	156.8	1.78×10 ⁻¹⁵
S-R-200-325	2755.1	110.2	1.92×10 ⁻¹⁵

The permeability of the unrefined samples is 10 times higher than refined samples. This comes from the fact that refining of the pulp leads to a better sheet formation and the refined handsheet is more compact. Permeability is determined by the fraction of open pores and the size of the pores and in general, higher porosity results in higher permeability. The permeability decreases by increasing the basis weight. These measurements are in agreement with Figure 82 and Figure 83, which H-R-120 or 150%-325 g/m² and S-R-150 or 200%-325g/m² have the maximum drying time.

5.2.10 Energy Analysis and Drying Rate

In order to analyze the energy efficiency of non-contact ultrasonic drying of hand-sheet papers, energy factor (EF) is defined as following:

$$EF = \frac{(m_i - m_t)h_{fg}}{P_{US-rad} \times t} \quad (5-4)$$

where m_i is the initial mass, m_t is the instant mass at time t , h_{fg} is the latent heat of evaporation for water at atmospheric pressure and P_{US-rad} is the radiated ultrasonic power to the sample. This factor is determined as the ratio of the energy required for evaporation to the ultrasonic power that is radiated to the sample. The surface area of the paper sample is 0.019856 m². For the Ti plate, the surface area of the sample is 0.101 m². If it is assumed that the waste of the acoustic energy from the surrounding is negligible, out of the total applied power to the Ti plate (225 W), the energy radiated to the sample can be estimated as 44 W.

Figure 97 and Figure 98 compare the drying rate and energy factor for hardwood and softwood samples, respectively.

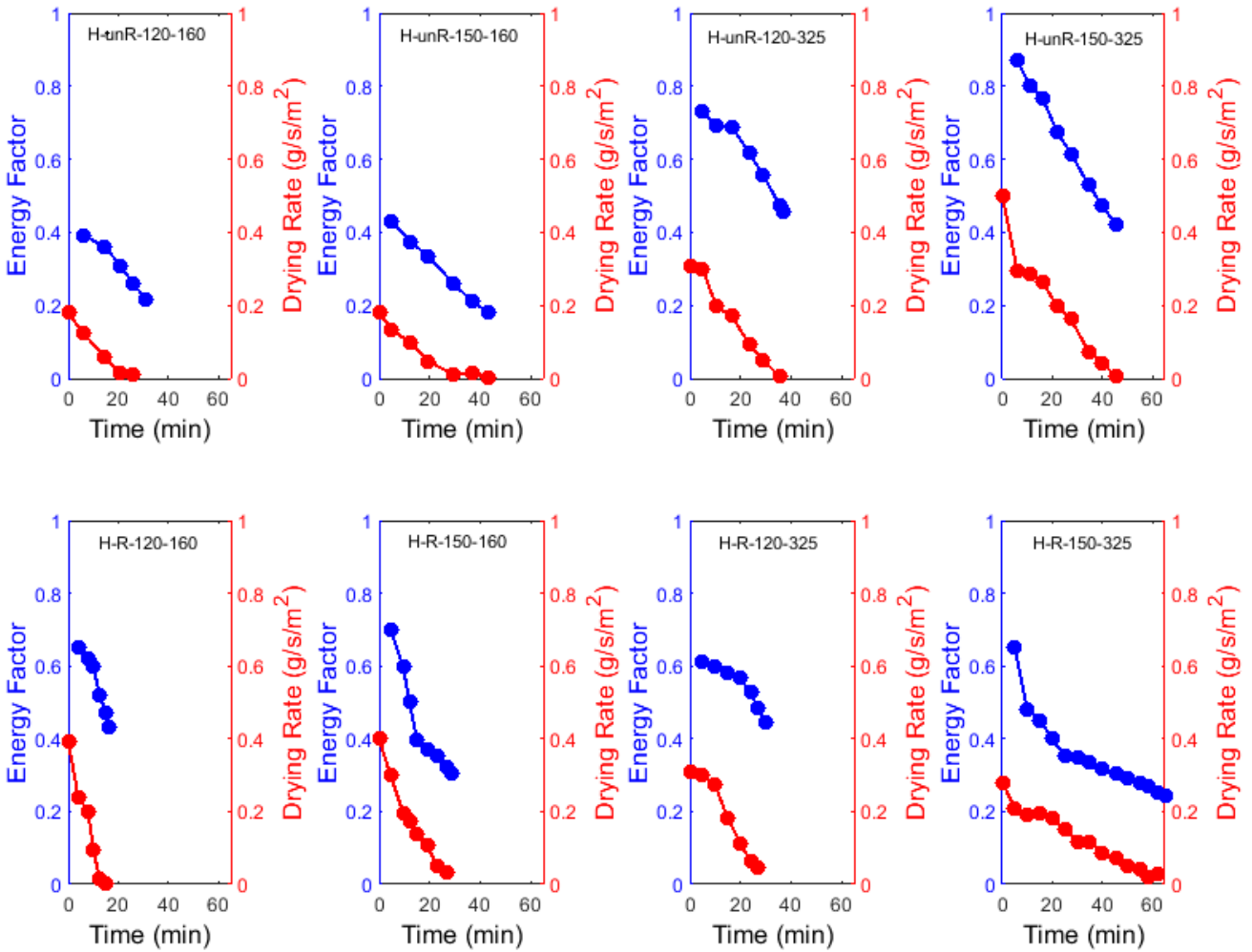


Figure 97. Energy factor and drying rate for different hardwood samples (dried using Al plate). Red curve is for drying rate and blue curve is for energy factor.

The drying rate is calculated through second-order central differencing. For hardwood with the Al plate, the energy efficiency can be as high as 0.87 and the maximum drying rate is $0.5 \frac{g}{m^2 \cdot s}$. For the softwood with the Ti plate, the energy efficiency can be as high as 0.5 and the maximum drying rate is $0.58 \frac{g}{m^2 \cdot s}$.

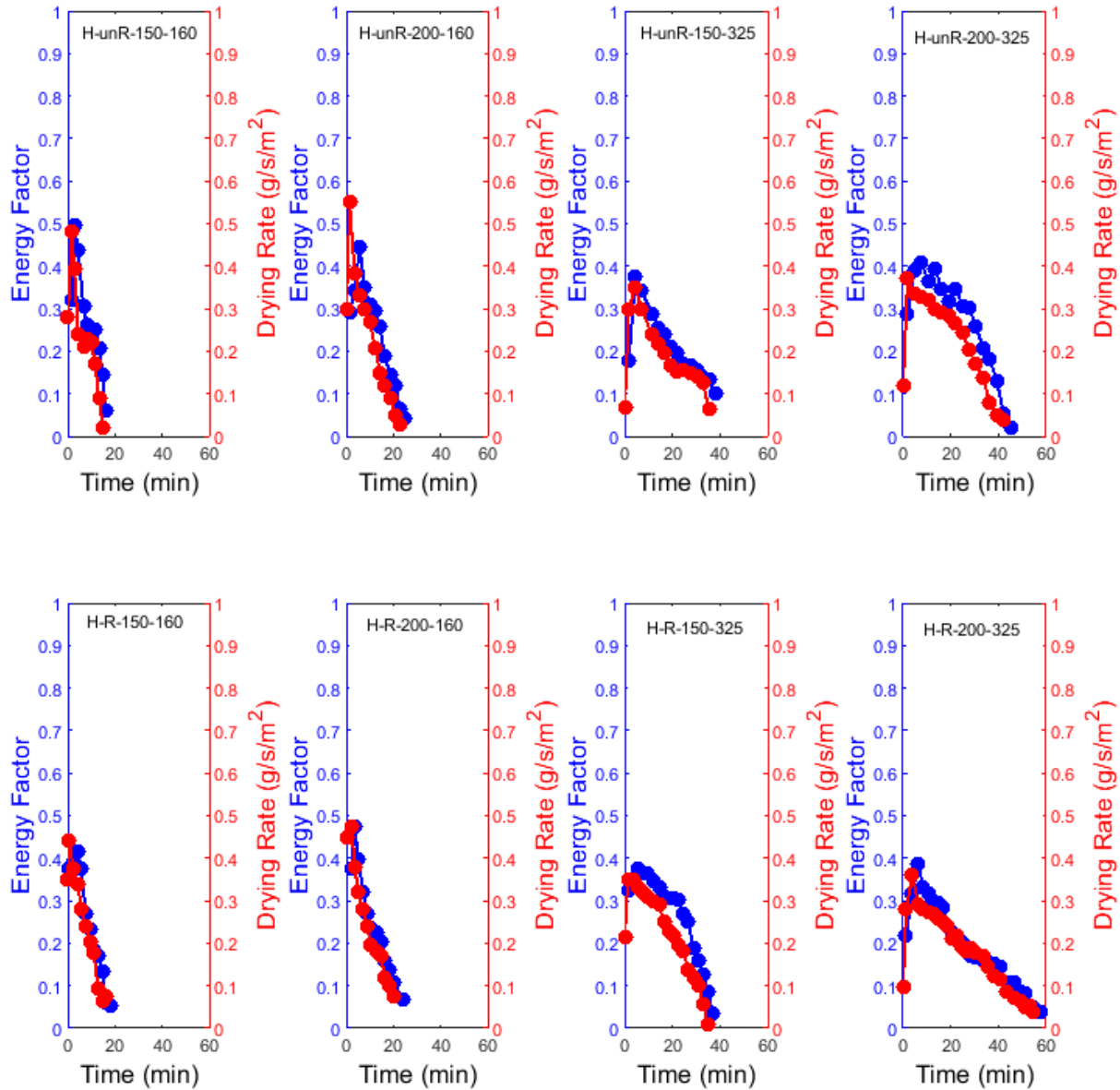


Figure 98. Energy factor and drying rate for different softwood samples (dried using Ti plate). Red curve is for drying rate and blue curve is for energy factor.

It can be confirmed that non-contact ultrasonic drying has higher drying rate and energy efficiency at higher moisture contents. These findings agree with literature such as [48 and 68] for direct-contact ultrasonic drying. As the sample gets dried and moisture content decreases, the drying rate and energy efficiency decreases. A correlation is fitted to the drying curve for different samples and Table 24 summarizes the outcome. The unique advantage of these correlations is that they can

be applied in physics based numerical models representing the mass flux due to ultrasound mechanism.

Table 24. Correlation for drying rate of different samples (dried using Ti plate) obtained using curve fitting. For simplicity, DBMC is shown as x . R^2 for all the correlations is 0.99.

Sample	Correlation for Drying Rate (g/(m².s))
S-R-160	$10^{-7}x^3 - 3 \times 10^{-5}x^2 + 0.0035x + 0.0318$
S-R-325	$2 \times 10^{-11}x^5 - 9 \times 10^{-9}x^4 + 2 \times 10^{-6}x^3 - 0.0001x^2 + 0.0066x + 0.0007$
S-unR-160	$3 \times 10^{-9}x^4 - 8 \times 10^{-7}x^3 + 6 \times 10^{-5}x^2 + 0.0017x - 0.0239$
S-unR-325	$10^{-7}x^3 - 5 \times 10^{-5}x^2 + 0.0066x - 0.0094$

To confirm the effectiveness of ultrasonic drying at high moisture contents, an additional test was conducted at 700% DBMC (S-R-700-160) using the Ti plate. For this sample, the energy factor reaches to about 0.9, illustrating the impact of higher moisture content on increasing the energy factor (Figure 99). In addition, the maximum drying rate for this sample is 0.9 g/(m².s). It is expected that for pure water or low consistency slurries the energy factor exceeds 1, which could have various potential applications. It should be mentioned that in the above calculations (see equation (5-4)), the evaporation energy considered for water present in a moist paper is simply the mass times the latent heat of water. This is too idealistic as significantly more energy is needed in a conventional drying process to evaporate the water from a moist paper. This is especially true at low moisture content levels (i.e., falling drying rate zone). Thus, the energy ratios for ultrasonic drying will be much higher than those presented in Figures 96-98. Nevertheless, the ultrasonic drying will be more effective when applied to a product with a high moisture content.

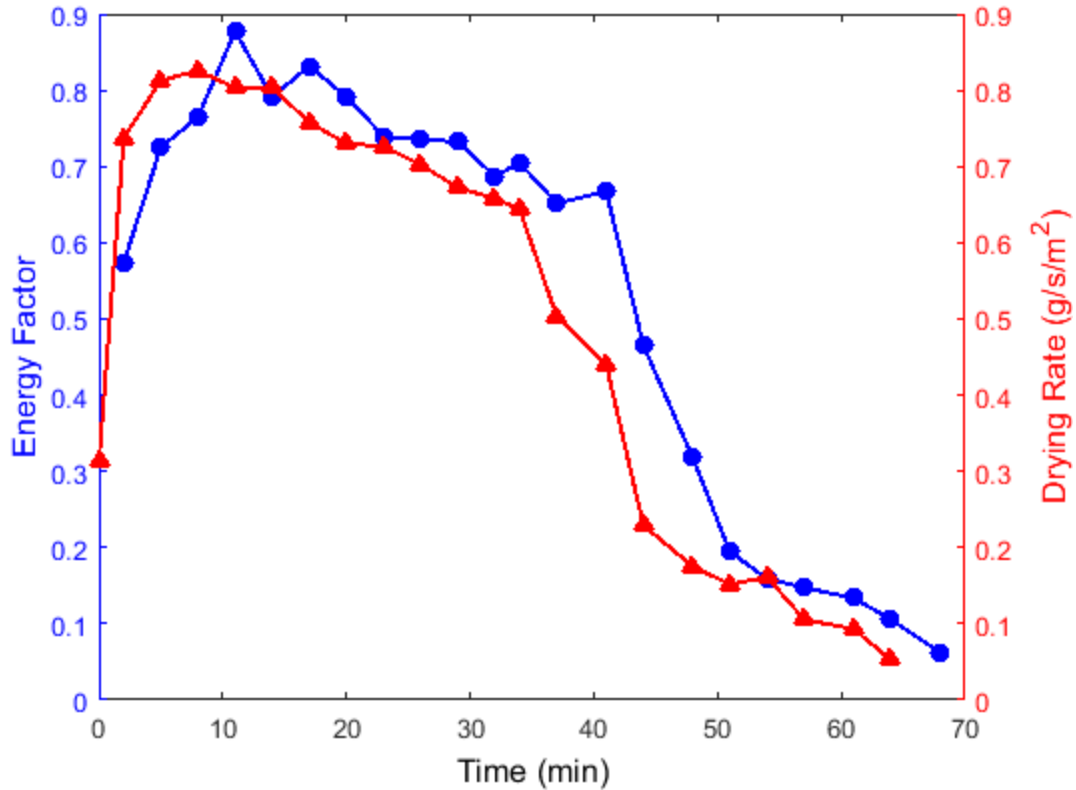


Figure 99. Illustration of the effect of high moisture content on drying behavior and energy factor for S-R-700-160 (dried using Ti plate).

5.2.11 Comparing Direct-Contact and Non-Contact Ultrasonic Drying

In direct-contact ultrasonic drying, the moist sample must be directly in contact with the transducer, while in non-contact ultrasonic drying, the moist sample is placed underneath the transducer plate. The experiments for direct-contact ultrasonic drying are carried out at 1.7MHz with 10 W power and non-contact ultrasonic drying experiments with Ti plate are conducted at 21 kHz and 225 W. For airborne ultrasound setup, the power per unit area is 1.14 W/cm² and for direct-contact ultrasound setup, this flux is equal to 3.30 W/cm². The thermal heating for these two setups is compared in section 5.2.3 and concluded that in direct-contact ultrasonic drying, the maximum temperature of the transducer plate is 80 °C, while in airborne ultrasonic drying, the maximum temperature is 40 °C. Therefore, the heating effect in direct-contact mechanism is substantially higher compared to that of non-contact mechanism. In the following, other aspects

of drying, i.e., drying rate and energy efficiency, are compared for these two setups. The data for direct-contact ultrasonic drying is attained from the previous chapter.

Since the diameter of the samples in direct-contact and non-contact ultrasonic drying is 1.98 cm and 15.9 cm, respectively, the drying rates are reported in $\frac{g}{m^2.s}$. Figure 100 compares the drying rate and energy factor for S-R-150%-160g/m² dried using direct-contact ultrasonic drying and non-contact ultrasonic drying (Ti plate).

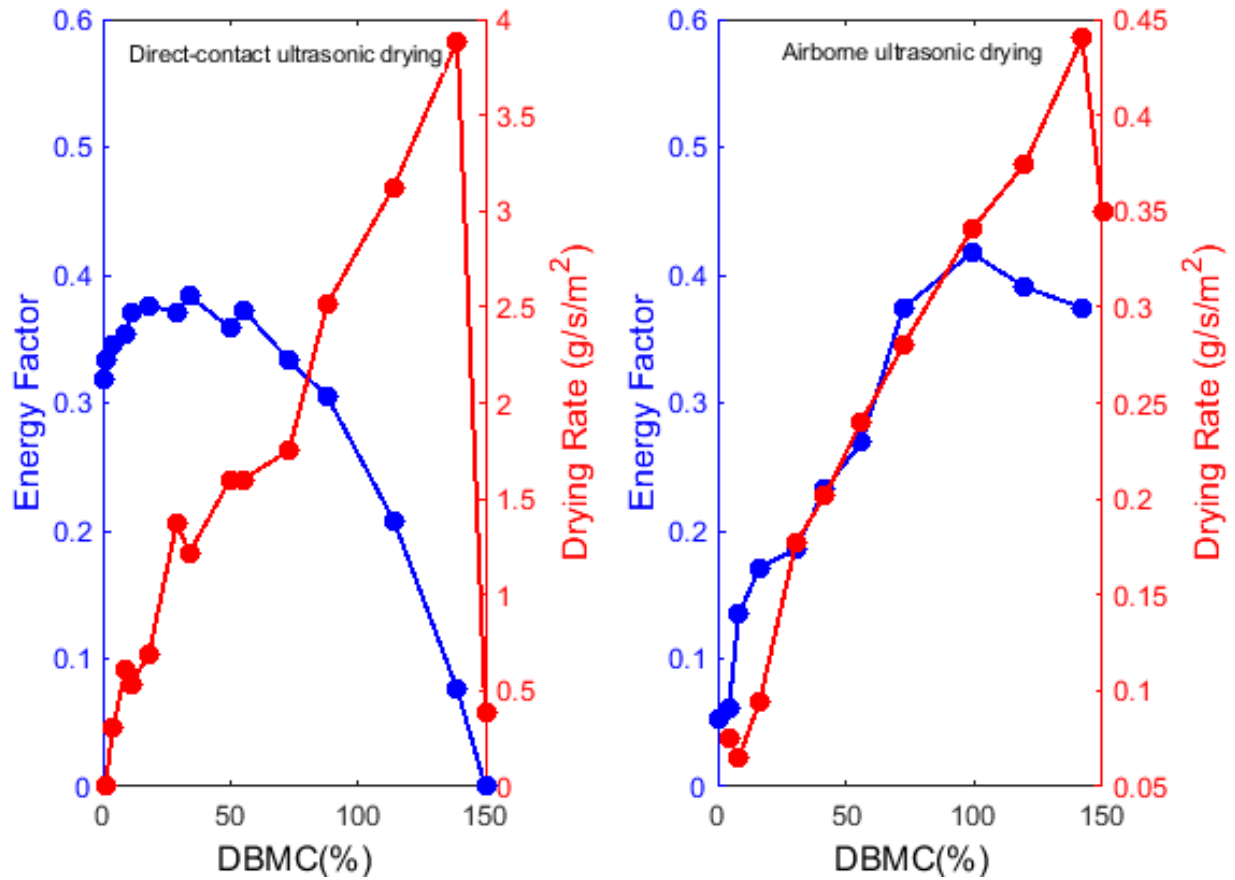


Figure 100. Comparing the drying rate and energy factor for S-R-150%-160g/m², dried by direct-contact (left) and non-contact (right) ultrasonic drying (Ti plate). Red curve is for drying rate and blue curve is for energy factor.

The general trend for both mechanisms is that the drying rate is higher at higher moisture contents. However, by decreasing the moisture content, propagation of ultrasonic waves inside the sample is harder and as a result, the drying rate decreases. The low drying rate in the beginning for direct-

contact ultrasonic drying could be due to the fact that higher frequencies have lower depth of penetration inside the sample and therefore, drying has a “warm-up” period, initially. In addition, the drying rate for direct-contact ultrasonic drying is an order of magnitude higher than non-contact ultrasonic drying. This observation may also largely be influenced by the significant heating effect generated in direct-contact ultrasonic drying, as discussed above. Although this heating effect may not be always desirable, it has a major impact on the drying rate. Whilst the papermaking machine is in a much larger scale, it should be notified that the evaporation rate in papermaking machine is about 10 times higher than the drying rate for direct-contact ultrasonic drying according to [125].

The energy factors for direct-contact and non-contact ultrasonic drying are in the same order of magnitude. One reason for low energy factor in ultrasonic drying might be due to the bulging effect of the sample during drying, which results in imperfect contact with the transducer in direct-contact drying and increase in thickness at the edges in airborne ultrasonic drying. The energy factor could be higher and part of the loss of energy could be resolved by developing more efficient designs for the transducers. Despite the higher drying rate for direct-contact ultrasonic drying, one of the biggest challenges with this technology is that the sample must be in direct contact with the transducer and therefore it is not adaptable to the current convective dryers. In this regard, non-contact (airborne) ultrasonic drying is the most ideal in terms of adapting to the convective dryers. For paper drying, one potential application of this technology is in the up-stream of papermaking machine to control moisture profile in the cross-direction and reduce overheating. For batch processes, in the cases that low temperature drying is required to preserve the properties of the products being dried, ultrasonic drying could be suitable, and it can be more efficient in hybrid with other types of drying mechanisms. Nonetheless, the outcome of this research is that at the current state, this technology is not ready for replacing the current continuous drying technologies in industrial applications, such as paper drying, and more robust and efficient designs are required. The biggest challenge in developing more efficient ultrasonic transducers is to overcome the significant impedance mismatch between air and dense mediums, which leads to substantial energy loss. There are several research groups such as [119 and 126] exploring more efficient and novel designs for ultrasonic transducers.

5.3 Summary and Conclusions

In this study, a straightforward comparison between high-power airborne ultrasonic drying (21 kHz and 225 W) and direct-contact ultrasonic drying (1.7 MHz and 10 W) for hand-sheet papers was provided. In conclusion, the results of 2^3 factorial design of experiments showed that for both mechanisms, basis weight/thickness of the sample has the maximum effect on total time of ultrasonic drying and after that the initial moisture content. One of the most important take-aways from this research is that ultrasonic drying is more effective at higher moisture content and as the sample gets dried and the moisture content decreases, the drying rate and energy efficiency decrease. Two correlations for predicting the total time of ultrasonic drying and the area under the drying curve were obtained using linear regression analysis. Quality measurements for the dried samples by airborne ultrasonic drying agreed with the measurements for the samples dried with direct-contact ultrasound. Compared to the hot plate drying, the whiteness index and tensile strength of the samples were slightly improved by using ultrasound mechanism. It was shown that permeability plays an important role in ultrasonic drying behavior and the effect of ultrasound for samples with higher permeability is higher. In addition, the thermal effect in direct-contact ultrasonic drying is very significant and it enhances the drying rate but may also have undesirable impact on product properties. The energy efficiency of airborne ultrasonic drying was in the same order of magnitude as direct-contact ultrasonic drying. More efficient designs for ultrasound transducers are required to be able to use this technology in industrial applications.

Chapter 6: Fundamental Understanding of Ultrasonic Atomization and Resultant Droplet Size: A Numerical Study

Ultrasonic atomization for aerosol droplet formation has been attracting interest in the past few decades due to its great applications such as fuel injection in internal combustion engines, ink-jet printing, agricultural sprays, mass spectroscopy, pulmonary drug delivery, and DNA microarray printing. In this chapter, a comprehensive parametric study is conducted by varying the fluid thermophysical properties, liquid height, gravity, and ultrasound characteristics to shed light on the mechanism of ultrasonic atomization. Ultrasonic atomization is studied in the presence of gravity, surface tension, and viscous forces. To elucidate the mechanism of ultrasonic atomization at low and high frequencies, multiphase CFD simulations are performed. The onset of ultrasonic atomization as a function of non-dimensional numbers (including Reynolds number, Weber number, Froude number, and Strouhal number) is investigated and the critical non-dimensional numbers required for ultrasonic atomization are evaluated. The capillary waves formed on the interface are studied, the frequency and wavelength at different conditions are measured, and the detailed dynamics of the droplet ejection (including secondary droplet formation and droplet collision) from the interface are discussed. Based on the analysis, a correlation for predicting the mean droplet size in two dimensional is proposed. The effect of different parameters on onset atomization amplitude and the resultant droplet size are found to be in qualitative agreement with the experimental data. In addition, the ultrasonic atomization phenomenon for the direct-contact mechanism is compared to the non-contact mechanism. The outcome of this research provides insights on the formation of capillary waves, the mechanism of ultrasonic atomization, the onset of ultrasonic atomization, and droplet ejection.

Keywords: capillary waves; ultrasonic atomization; onset atomization amplitude; CFD; droplet ejections

6.1 Theoretical Model

The solution domain is presented in Figure 101. In this 2D physical problem, a liquid layer of height H covers the flat surface of the vibrator at $y = 0$, above which is a layer of dry air.

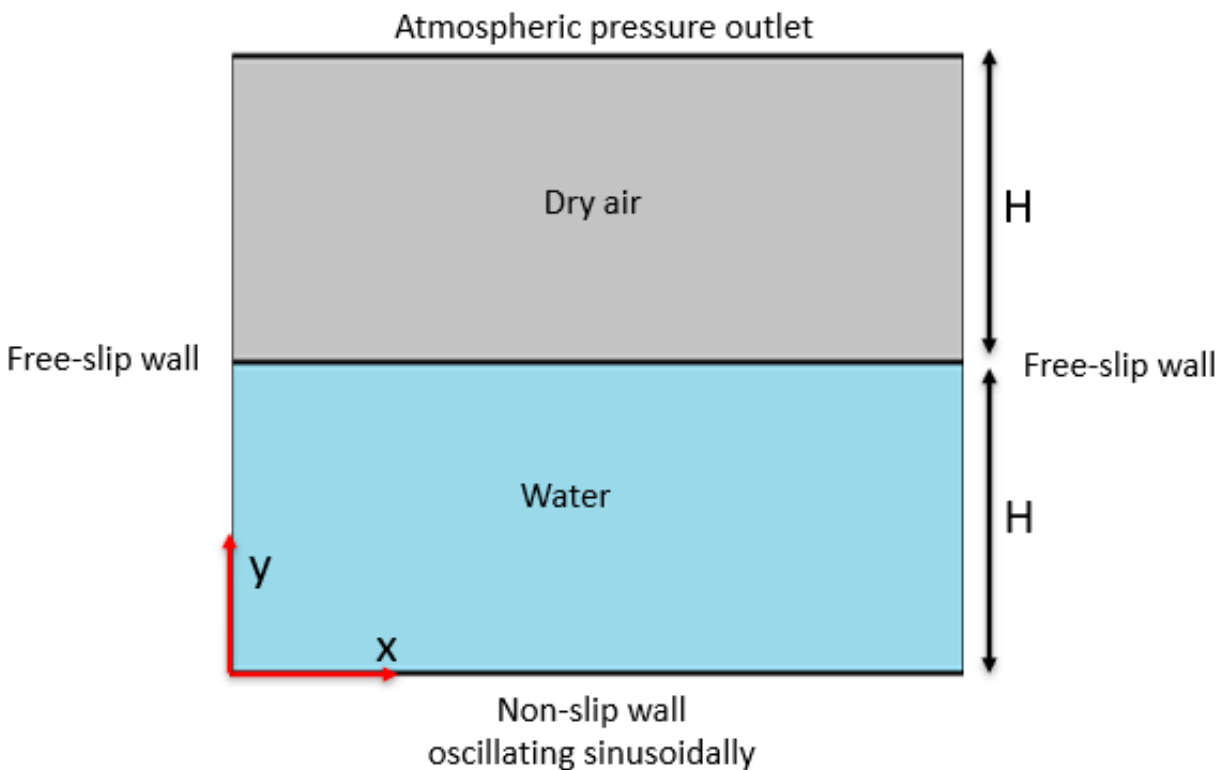


Figure 101. 2D schematic of the problem in numerical simulation for direct-contact ultrasonic atomization (not to scale).

The system is initially stationary, and the liquid-gas interface is located at $y = H$. Volume of fluid (VOF) model is applied to track the interface by defining α as the volume fraction of water. The length of the domain is set as 100λ , unless otherwise is stated, (λ is calculated using equation (1-2)) and the domain height is twice the height of water. The air region on top of the interface has the same height as the liquid, since any interface motion that occurs during the simulation should be contained within the simulation domain.

The numerical model presented below incorporates the following assumptions:

- 1- Fluid is Newtonian.
- 2- Flow is laminar.
- 3- The numerical domain is two dimensional (2D).
- 4- Liquid phase is water and gas phase is dry air.
- 5- Incompressibility and immiscibility are applied for both liquid and gas phases.
- 6- The energy equation is not included in the analysis and thus, the change in temperature and evaporation of the droplets are not considered in this model.

6.1.1 Dimensionless Governing Equations

The governing equations are non-dimensionalized using the parameters in Table 25.

Table 25. Dimensionless parameters for governing equations.

Parameter	Dimensionless parameter	Normalization factor
Spatial coordinates	x^*, y^*	H
Time	t^*	$\sqrt{\frac{H}{g}}$
Velocity	u^*, v^*	\sqrt{gH}
Pressure	P^*	$\rho_L g H$
Density	ρ^*	ρ_L

Superscript * is used to specify the dimensionless parameters. The liquid and gas phases satisfy the continuity and momentum equations as below

$$\frac{\partial u^*}{\partial x^*} + \frac{\partial v^*}{\partial y^*} = 0 \quad (6-1)$$

$$\frac{\partial U^*}{\partial t^*} + U^* \cdot \nabla^* U^* = \frac{1}{\rho^*} \nabla^* (P^* + \rho^* y^*) + \frac{1}{Re} \nabla^{2*} U^* + \frac{1}{0.5\beta We} \rho^* \kappa^* \nabla^* \alpha \quad (6-2)$$

where u and v are scalar velocity components and U is the velocity vector. The last term in equation (6-2) is the dimensionless volumetric force due to surface tension at the interface. This force is described as following in the dimensional format

$$F_{surface\ tension} = \sigma \frac{\rho \kappa \nabla \alpha}{0.5(\rho_l + \rho_g)} \quad (6-3)$$

$$\rho = \alpha \rho_l + (1 - \alpha) \rho_g \quad (6-4)$$

κ is the interface curvature, which is defined as the divergence of the unit normal (\mathbf{n}) to the interface obtained from the volume fraction field

$$\kappa = \nabla \cdot \hat{\mathbf{n}} = -\nabla \cdot \left(\frac{\nabla \alpha}{|\nabla \alpha|} \right) \quad (6-5)$$

Three non-dimensional numbers appear in the momentum equation, which are Reynolds, Weber, and non-dimensional density numbers, respectively.

$$Re = \frac{\sqrt{gH}H}{\nu} \quad (6-6)$$

$$We = \frac{\rho_l (gH)H}{\sigma} \quad (6-7)$$

$$\beta = \frac{\rho_l + \rho_g}{\rho_l} \quad (6-8)$$

Reynolds number is the ratio of inertial forces to viscous forces and Weber number is a measure of the relative importance of inertial forces compared to surface tension forces. Combining the effect of Reynolds number and Weber number results in Ohnesorge numbers as follows

$$Oh = \frac{\sqrt{We}}{Re} \quad (6-9)$$

Ohnesorge number is a dimensionless number that compares viscous forces with inertial and surface tension forces.

6.1.2 Boundary Conditions and Interface Tracking Strategy

The lateral boundary conditions are considered as free-slip walls to minimize their effects on the system. The upper boundary condition is constrained as pressure outlet with atmospheric pressure. At $y = 0$, no-slip boundary condition for fluid is assumed and the wall is sinusoidally oscillating in the vertical direction with the velocity described by the following equation

$$v = A\omega \sin(\omega t) \quad (6-10)$$

where A is amplitude, ω is angular frequency, and t is time. For instance, Figure 102 shows the oscillating velocity for 1.7 MHz and 0.55 μm amplitude for 10 periods.

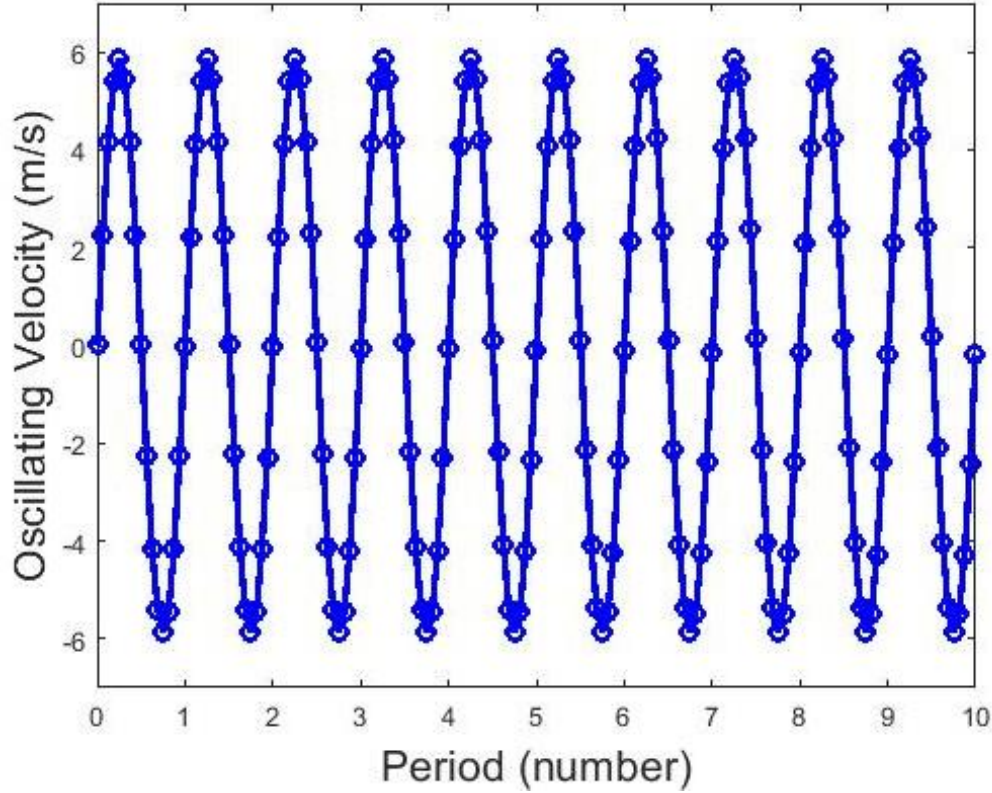


Figure 102. Oscillating velocity for 1.7 MHz and 0.55 μm amplitude.

The non-dimensional form of the boundary condition at $x = 0$ and $x = L$ are

$$\frac{\partial u^*}{\partial x^*} = \frac{\partial v^*}{\partial y^*} = 0 \quad (6-11)$$

At $y = 0$

$$u^* = 0 \quad (6-12)$$

$$v^* = Fr \times \sin(St.t) \quad (6-13)$$

where Froude and Strouhal numbers are defined as

$$Fr = \frac{A\omega}{\sqrt{gH}} \quad (6-14)$$

$$St = \omega \sqrt{\frac{H}{g}} \quad (6-15)$$

Froude number is the non-dimensional amplitude defined by the ratio of ultrasonic acceleration forces to the gravitational forces. Strouhal number is the non-dimensional frequency. In addition, Strouhal and Froude numbers can be related to each other as

$$Fr = St \times \frac{A}{H} \quad (6-16)$$

Therefore, in the analysis, we can consider either Froude number or the non-dimensional amplitude as $\frac{A}{H}$. As previously stated, in this study, the volume of fluid (VOF) technique is used to represent the instabilities, motion, and mass exchange across the interface. The advantage of the VOF method is its relatively easy programming with common finite difference discretization methods while it provides precise measurement of the interface profile under various operating conditions. This method tracks volumes of fluid, not the interface itself and hence, changes in the topology are handled automatically. In this method, the jump mass balance at the interface is defined as

$$\rho_l^*(U_l^* - V_{in}^*) \cdot \mathbf{n}^* = \rho_g^*(U_g^* - V_{in}^*) \cdot \mathbf{n}^* \quad (6-17)$$

where V_{in} is the velocity at the interface, which represents the momentum transfer across the interface due to capillary instabilities and atomization. The complete set of equations for VOF method can be found in [127]. In this method, the continuity equation across the interface must reflect the interfacial motion and mass transfer. This equation can be written as

$$(\rho_l - \rho_g) \left(\frac{\partial \alpha}{\partial t} + U \cdot \nabla \alpha \right) + \rho \nabla \cdot U = (\rho_l - \rho_g) (U - V_{in}) \cdot \nabla \alpha \quad (6-18)$$

where α is the volume fraction of liquid phase. The equation can be split into a pure continuity equation, $\nabla \cdot U = 0$, and a complementary counterpart represented by the topological equation

$$\frac{\partial \alpha}{\partial t} + U \cdot \nabla \alpha = (U - V_{in}) \cdot \nabla \alpha \quad (6-19)$$

This equation in dimensionless form would be

$$\frac{\partial \alpha}{\partial t^*} + U^* \cdot \nabla^* \alpha = (U^* - V_{in}^*) \cdot \nabla^* \alpha \quad (6-20)$$

6.1.3 Numerical Technique

The transient governing equations are solved both in the liquid and air using Fluent 2022 R1. The effect of ultrasonic vibrations is modeled by oscillating the lower wall using a sinusoidal velocity by applying dynamic mesh movement. The capillary surface waves are modeled as laminar flow. The SIMPLE algorithm is employed for pressure-velocity coupling and the geometric reconstruction scheme is used to determine the face fluxes for VOF. Convergence criteria is set as 10^{-5} for continuity and momentum equations. The mesh size is considered as $1/20^{\text{th}}$ of the wavelength, calculated by Kelvin's capillary formula (equation (1-2)), which depends on the base excitation frequency. This criteria for the mesh size does not change the results of the simulation. In addition, the time step is set as $1/16^{\text{th}}$ of the oscillation periods (τ), for each exciting frequency, to ensure the convergence. All calculations are based on the properties of water at room temperature (about 20 °C). Table 26 presents the properties of liquid and air for the base case study.

Table 26. Properties of liquid and air for the base case study at 1.7 MHz frequency.

Property	Surface tension, σ_{base}	Liquid viscosity, μ_{base}	Liquid density, ρ_{base}	Air viscosity, μ_g	Air density, ρ_g
Value	0.072 N/m	0.001 kg/(m.s)	998 kg/m ³	1.7894×10^{-5} kg/(m.s)	1.225 kg/m ³

In order to break the liquid into droplets using ultrasonic vibrations, the amplitude must be above a threshold value. The threshold amplitude for vibrating the interface is given as [128].

$$A_{th} = \left(2 \frac{\mu}{\rho_l}\right) \left(\frac{\rho_l}{\pi \sigma f}\right)^{1/3} \quad (6-21)$$

Lierke and Griesshammer [129] suggested that the atomization inception amplitude is between 3 to 6 times the critical amplitude. In this study, the theoretical amplitude (A_{th}) is calculated using equation (6-21) for water at room temperature. Then, the amplitude is increased in increments of 0.05 times of A_{th} and at each amplitude, sufficient time is allowed to make sure all the transient

states have passed. The onset amplitude for atomization is then determined when a vigorous droplet ejection is produced.

The droplet sizes are evaluated using ImageJ software. The numerical model is evaluated against the available experimental data for ultrasonic atomization of liquid water, and it will be discussed in detail.

6.1.4. Buckingham Pi Method

In order to validate the non-dimensionalization of the Navier Stokes equations, Buckingham Pi theorem also was used to predict the non-dimensional numbers. In this analysis, the variables include f , H , A , σ , μ , ρ_L , U , and g . Therefore, there is 8 variables in this analysis. We chose the independent variables to be H , ρ_L , and U and there is 3 dimensions (length, time, and mass). Thus, the number of Pi terms would be $8 - 3 = 5$. After applying the Buckingham Pi theorem, the following non-dimensional numbers appear in the equations:

$$\Pi_1 = \frac{\mu}{\rho_l U H} = \frac{1}{Re} \quad (6-22)$$

$$\Pi_2 = \frac{\sigma}{H U^2 \rho_l} = \frac{1}{We} \quad (6-23)$$

$$\Pi_3 = \frac{A}{H} \quad (6-24)$$

$$\Pi_4 = \frac{FH}{U} = St \quad (6-25)$$

$$\Pi_5 = \frac{\sigma g H}{U^2} = \frac{1}{Fr} \quad (6-26)$$

The above non-dimensional numbers from Buckingham Pi theorem confirm the non-dimensionalization performed in the previous sections.

6.2 Experimental Method

In chapter 4, a mist generation type of piezoelectric transducers (SMIST25F16RR112) was used for direct-contact ultrasonic drying of paper samples. For these transducers the dominant displacement mode is in the vertical direction. The outer diameter and thickness of the transducer

are 1.9 cm and 1 mm, respectively. The working frequency is 1.7 MHz, and this high frequency ultrasonic transducer helps to push the limits for understanding of ultrasonic atomization at high frequencies.

6.3 Results and Discussion

Ultrasonic atomization is studied experimentally by placing a 50 μL water droplet on the surface of a mist generation transducer at 1.7 MHz and 10 W power is applied. Figure 103 presents the time sequence of this experiment. The upward mechanical motion of the transducer results in flattening the water droplet and it causes the formation of a crater in the center of the droplet. Then as the transducer moves downward, the droplet collapses toward the center due to the surface tension forces and it results in a high-pressure region at the center which forces the liquid upward. This high-momentum spike in the center of the droplet leads to pinch off of secondary droplets from the end of the spike. This process continues until the water droplet is totally atomized. These observations are in agreement with literature such as James et al. [89 and 130]. They studied water drop atomization at 61 kHz and 987 Hz. The authors presented visualizations of vibration induced atomization including close-ups of crater formation.

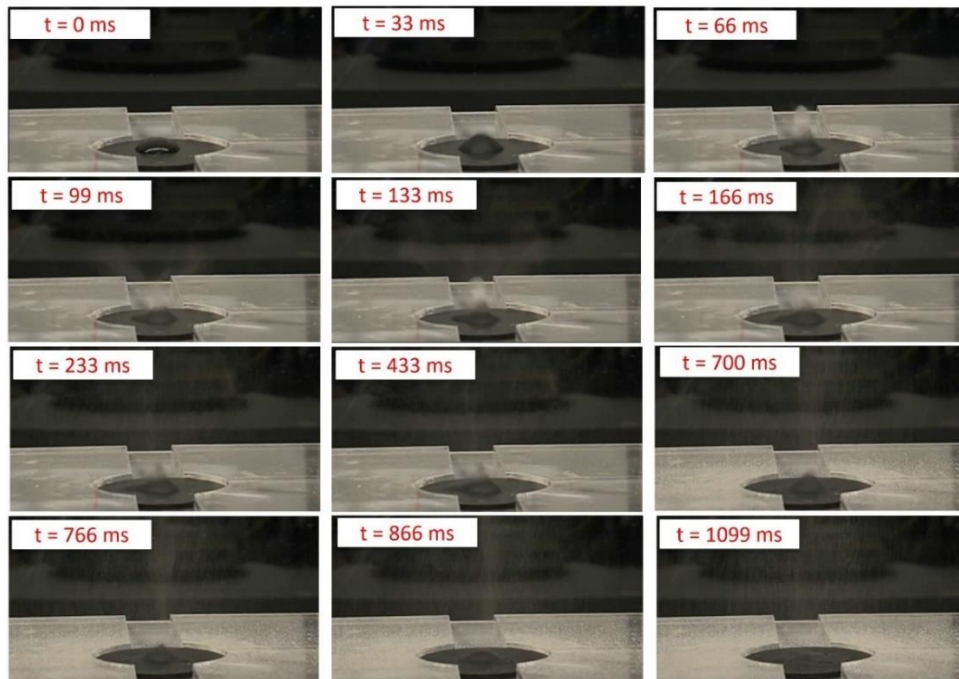


Figure 103. A time sequence of an experimental video for atomization at 1.7 MHz excitation frequency and 10 W power.

Experimental investigation of all the details and aspects related to ultrasonic atomization is very difficult and challenging in experiments and requires high-tech and expensive equipment, especially at MHz frequencies. Thus, CFD simulations are used in this study to evaluate the atomization nature under different operating conditions. In the following, the effect of each of the thermophysical properties of liquid, liquid height, gravity, and exciting frequency on ultrasonic atomization of a liquid film is discussed.

6.3.1 Effect of Exciting Amplitude on Ultrasonic Atomization

The liquid layer needs to be deep enough such that the surface can oscillate freely without interference from the actuating base on which the liquid is held. Hence, the minimum liquid depth can be of the same length order as the surface waves. For liquid height 3λ , the onset amplitude for atomization is $1.1A_{th}$. At lower amplitudes, the liquid free surface oscillates without ejection occurring, meaning that the surface waves don't have enough kinetic energy to overcome the resistance forces associated with the fluid interface. Figure 104 represents the interface region for $0.5 A_{th}$ amplitude. As this figure shows, this amplitude is not high enough to overcome the surface tension and the capillary waves cannot be formed at the interface. Figure 105 shows the changes in free surface at different times (in terms of the oscillation period) for $1A_{th}$ amplitude. For this case, capillary waves are formed at the interface however, no atomization occurs even up to more than 200 periods and only phenomenon is acoustic streaming. After that, the numerical instabilities at the interface are large enough that results in divergence of the simulation.

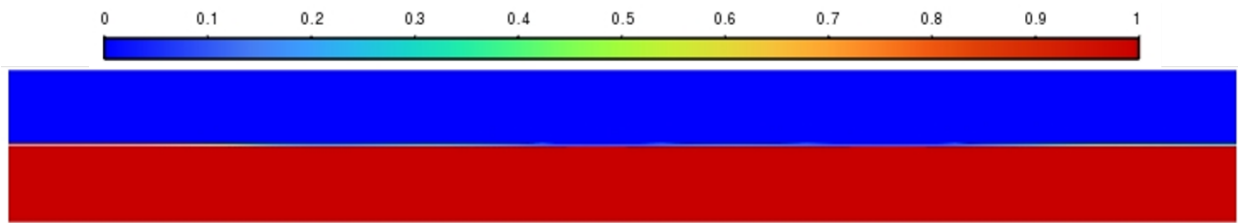


Figure 104. Volume fraction of water for $0.5A_{th}$ amplitude, 3λ liquid height and 1.7 MHz frequency after 1000τ .

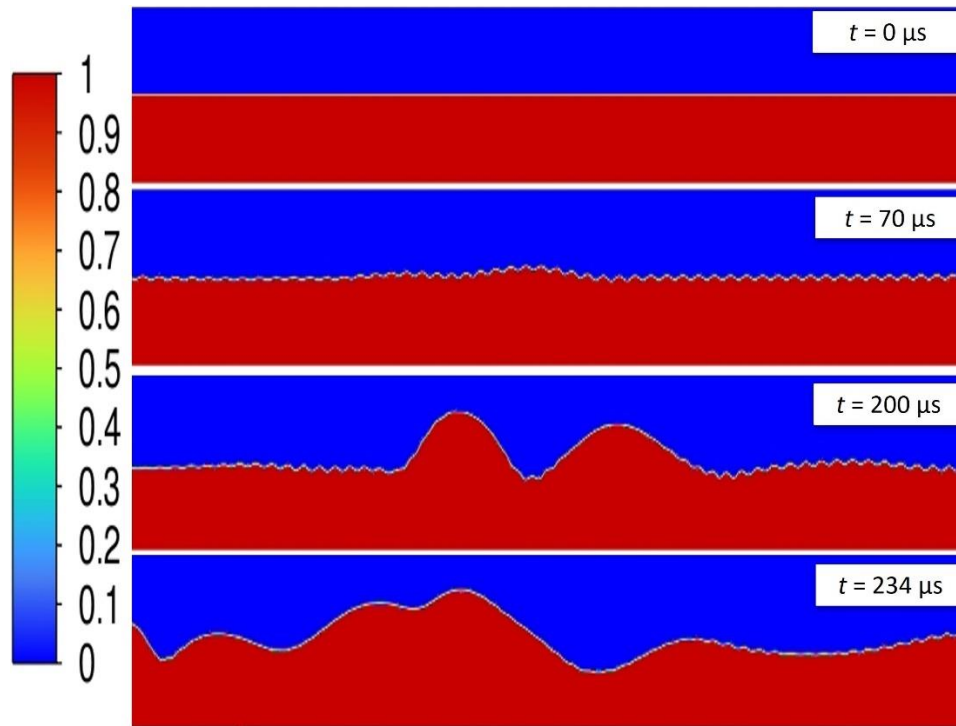


Figure 105. Volume fraction of water at the interface region for $1A_{th}$ amplitude, 3λ liquid height and 1.7 MHz frequency.

As the amplitude approaches the onset atomization amplitude, the motions on the free surface start at a lower time period. For example, Figure 106 is representing the motion at the interface region for the case of $1.1A_{th}$ amplitude. For this case, atomization starts after about 10 periods. The mechanism of droplet formation is that under a sufficiently strong exciting vibration, surface capillary waves are generated at the liquid/gas interface. These waves are weak initially and the wave formation can be generally approximated linearly. However, as the amplitude of the waves become larger and surface waves progress to the waves capable of ejecting droplets, the behavior is highly nonlinear. At this point, if the oscillating forces are higher than surface tension forces, axisymmetric conical shapes are created at the interface. The capillary waves quickly destabilize and elongate to form individual jets, each of which eventually breaks up to form one or more droplets. This jetting or pinch-off occurs rapidly across the interface and generates “a mist” of droplets. After ejection of the droplets and as this becomes more vigorously, the droplet ejection becomes a chaotic phenomenon. These observations highly agree with the experimental data from Sindayihebura and Bolle [83] for atomization of liquid water at 32 - 60 kHz frequencies. Figure

107 shows the droplet formation and droplet jets in more details. A ligament protrudes from the upward movement of the wave and a droplet forms at the end of the ligament. This droplet initially maintains the upwards velocity of the wave. However, as the wave moves downwards, the ligament is stretched to produce a ‘neck’ and surface tension decelerates the droplet. This eventually results in rupturing the droplet. The droplets get ejected from the free surface of water and the ultrasonic acceleration moves the droplets upward. Nevertheless, some of the larger droplets break into smaller droplets and generate secondary droplets as it is shown in Figure 107. After pinching off the droplets and generating mist, the droplet diameter is in the range of 1.3-3.2 μm . These observations are difficult or impossible to catch in experiments and require in-situ measurements of high-speed cameras with high resolutions.

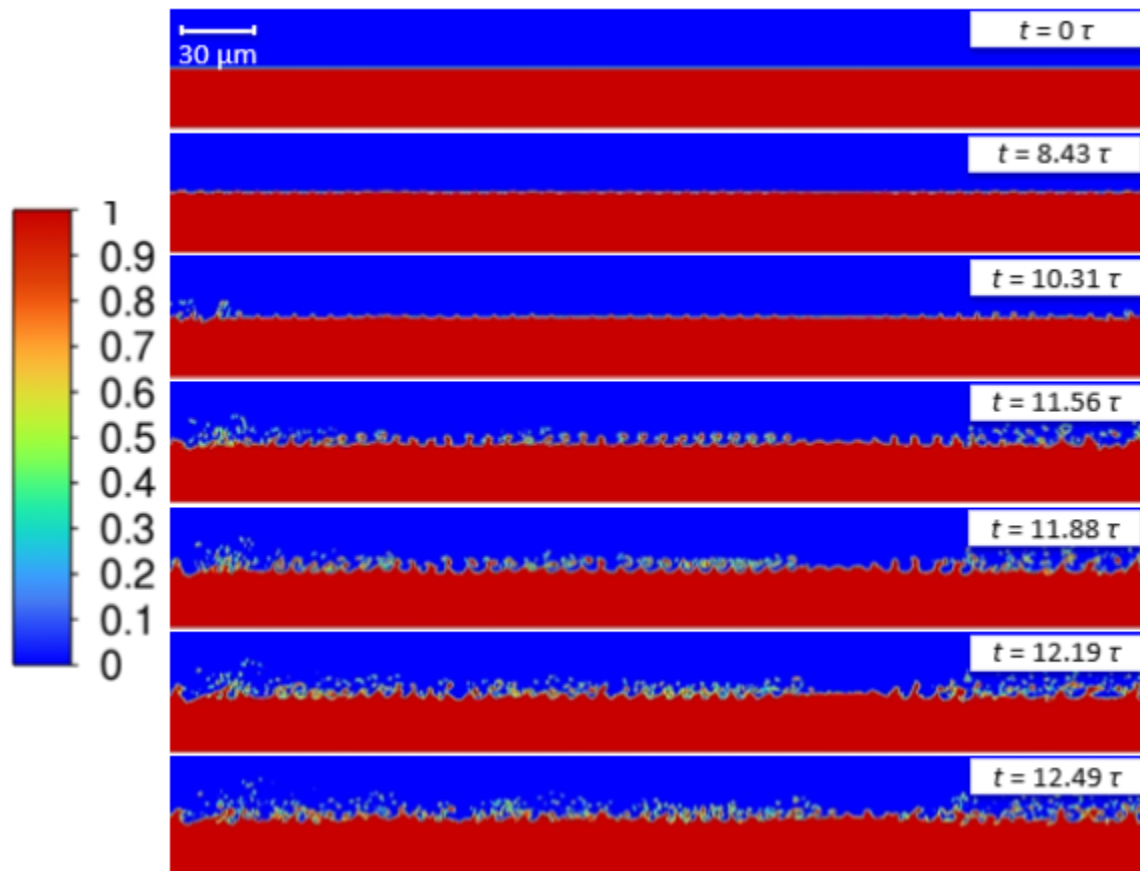


Figure 106. Volume fraction of water at the interface region for 1.1Ath amplitude, 3 λ liquid height and 1.7 MHz frequency.

The peak-to-peak measurements of the capillary surface waves confirm that at each time step, the frequency of the capillary waves is smaller than the excitation frequency and it will be discussed more in the next sections.

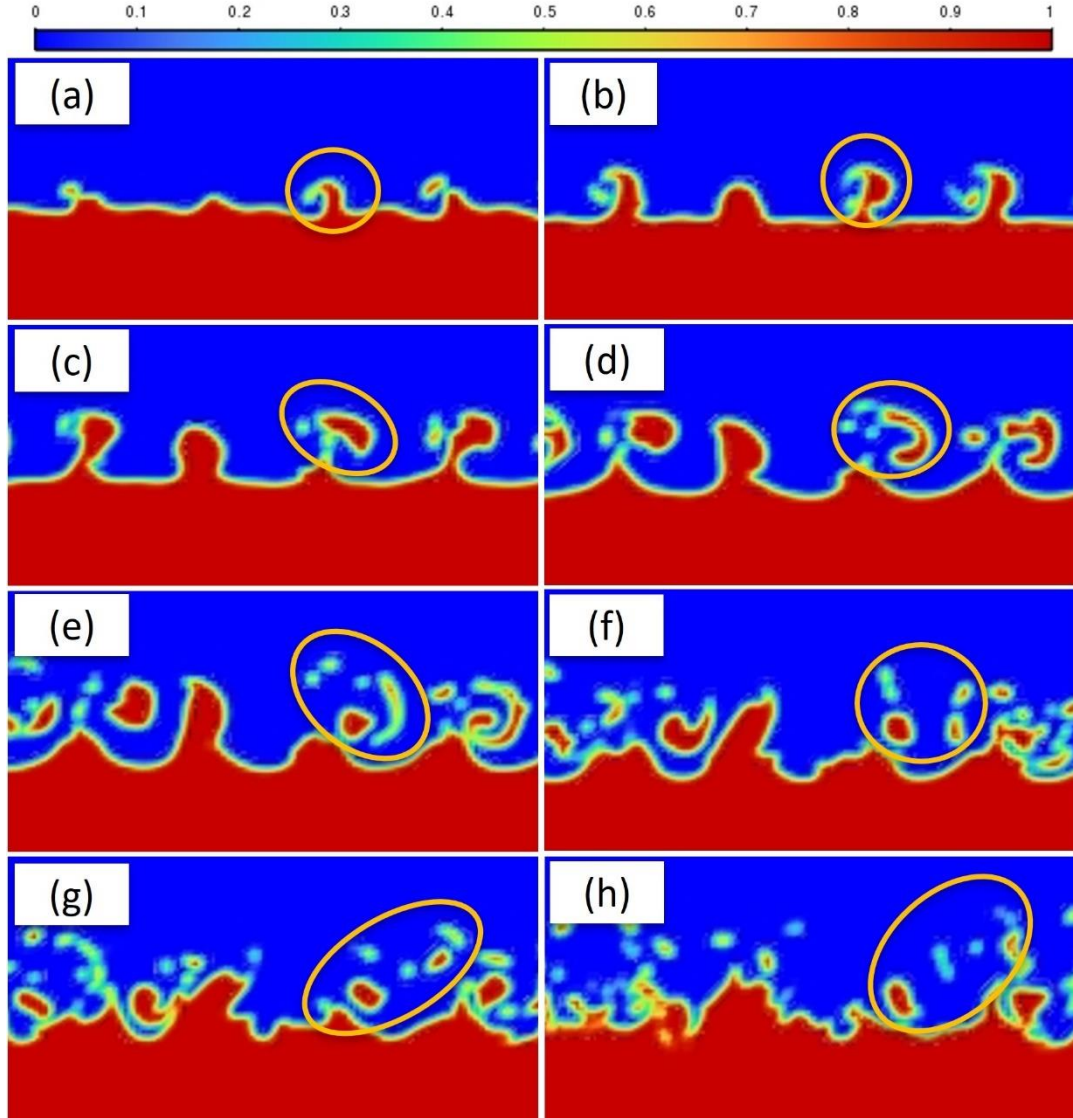


Figure 107. Droplet formation for $1.1A_{th}$ amplitude, 3λ liquid height and 1.7 MHz frequency at different times: (a) $6.62 \mu\text{s}$, (b) $6.73 \mu\text{s}$, (c) $6.84 \mu\text{s}$, (d) $6.95 \mu\text{s}$, (e) $7.06 \mu\text{s}$, (f) $7.17 \mu\text{s}$, (g) $7.24 \mu\text{s}$, and (h) $7.35 \mu\text{s}$. The colormap is based on the volume fraction of liquid.

At higher amplitudes, the rate of atomization increases. For instance, Figure 108 shows the changes at the interface region at $1.2A_{th}$ and in this case, the atomization starts at about 8 time periods instead of 10 time periods.

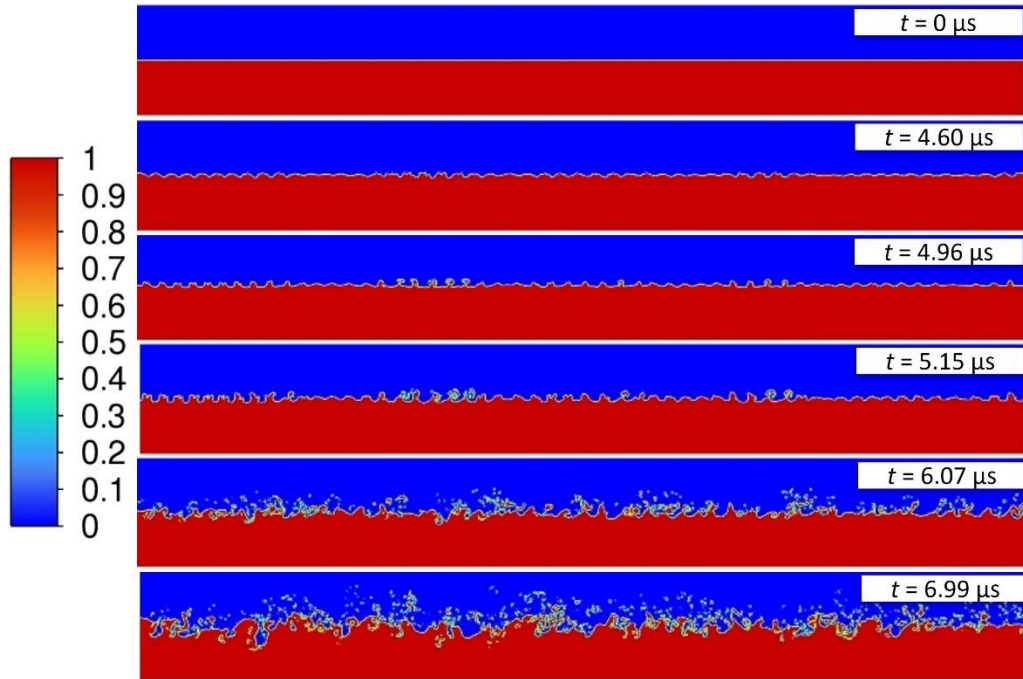


Figure 108. Volume fraction of water at the interface region for $1.2A_{th}$ amplitude, 3λ liquid height and 1.7 MHz frequency.

6.3.2 Effect of Liquid Height on Ultrasonic Atomization

In cases that the liquid height is smaller than the wavelength of the surface waves, the liquid does not oscillate and in this case the interface simply just rides along with the actuator. It is shown in Figure 109 for 0.5λ liquid height at $1A_{th}$ amplitude and 1.7 MHz frequency at 200τ .

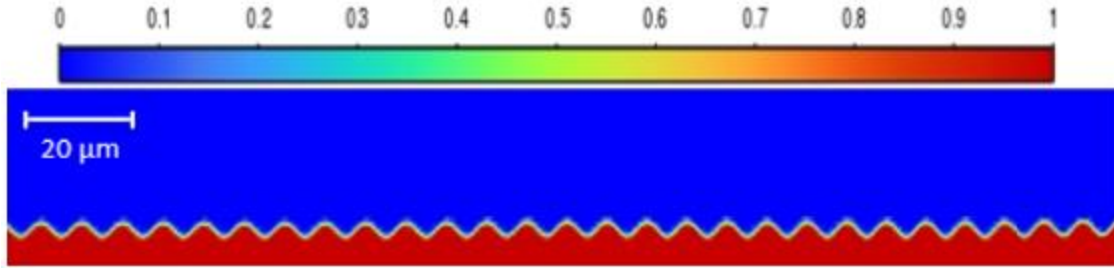


Figure 109. Volume fraction of water at the interface region for $1A_{th}$ amplitude, 0.5λ liquid height and 1.7 MHz frequency.

According to Ehrhorn and Semke [91], if a vibrating film produces atomized droplets at a given depth, increasing this depth beyond a certain threshold will lead to sporadic droplet production and increasing it further will lead to excessive damping in the system which halts the process entirely. In this study, by increasing the liquid height, the onset atomization amplitude is increasing. For the liquid height of 50λ , the onset atomization is found to be $2A_{th}$. Similar to the case of 3λ , at lower amplitudes, the liquid free surface oscillates without any droplet formation. The changes in the free surface at different time periods for $1.2A_{th}$ amplitude are shown in Figure 110. For clarity, only the region near the interface is shown in the picture.

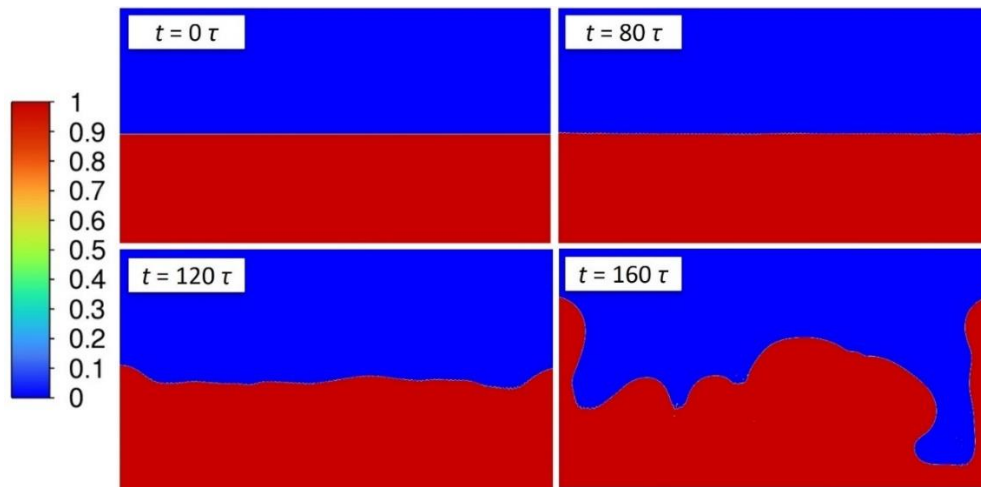


Figure 110. Volume fraction of water at the interface region for $1.2A_{th}$ amplitude, 50λ liquid height and 1.7 MHz frequency.

As the amplitude approaches the onset amplitude, the motion on the free surface starts at an earlier time. For example, the motion at the interface region for the case of $1.8A_{th}$ amplitude is shown in Figure 111. In this case, the motion at the interface starts after about 40τ however, no atomization occurs even up to 90 periods.

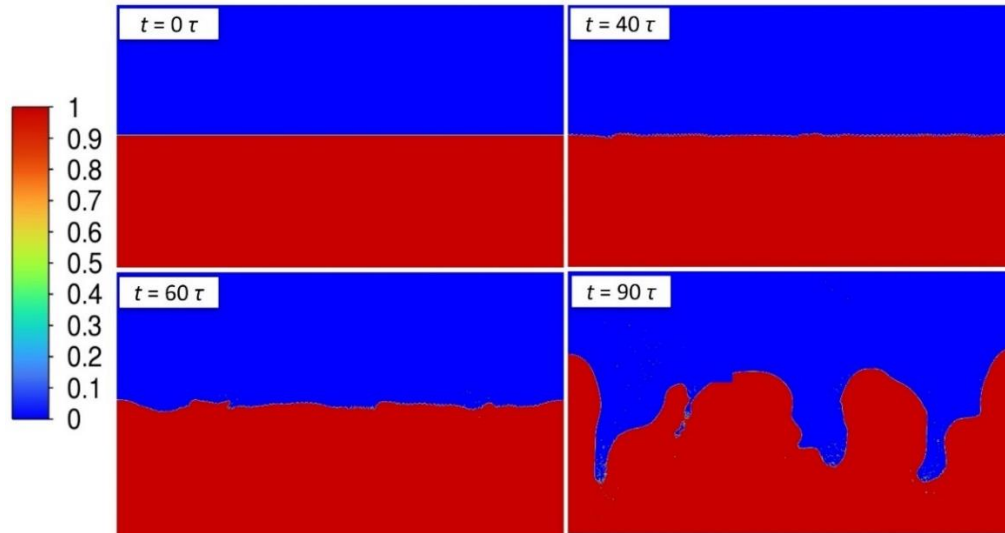


Figure 111. Volume fraction of water at the interface region for $1.8A_{th}$ amplitude, 50λ liquid height and 1.7 MHz frequency.

As it stated above, for this liquid height, the onset of atomization is observed at $2A_{th}$. The changes in volume fraction of water for this case are shown in Figure 112 and Figure 113. After pinching off the droplets and generating mist, the droplet diameter for this studied case is in the range of $1.6\text{-}3.3\ \mu\text{m}$ and the droplets move with an average velocity of 6 m/s.

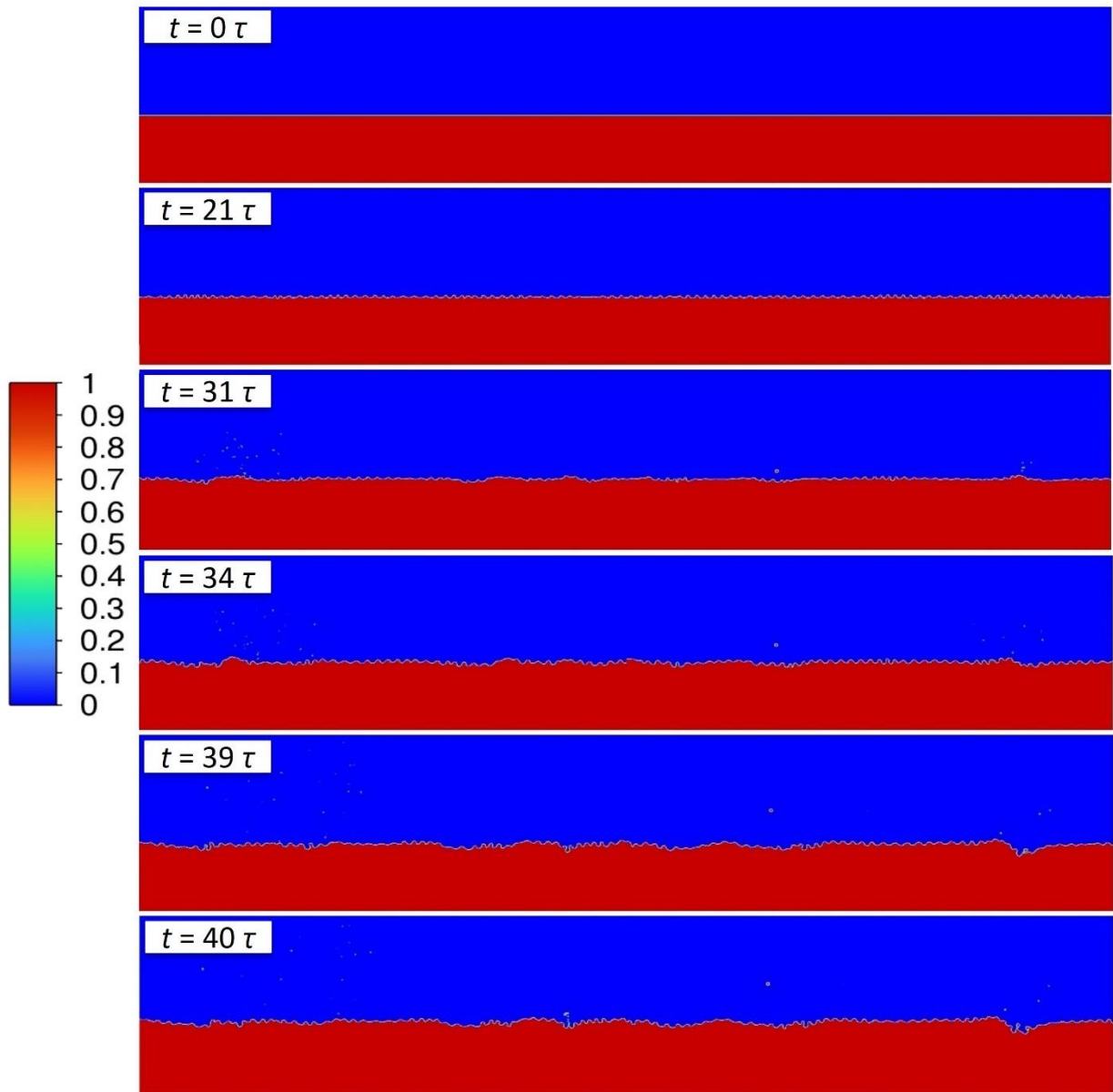


Figure 112. Volume fraction of water at the interface region for $2A_{th}$ amplitude, 50% liquid height and 1.7 MHz frequency.

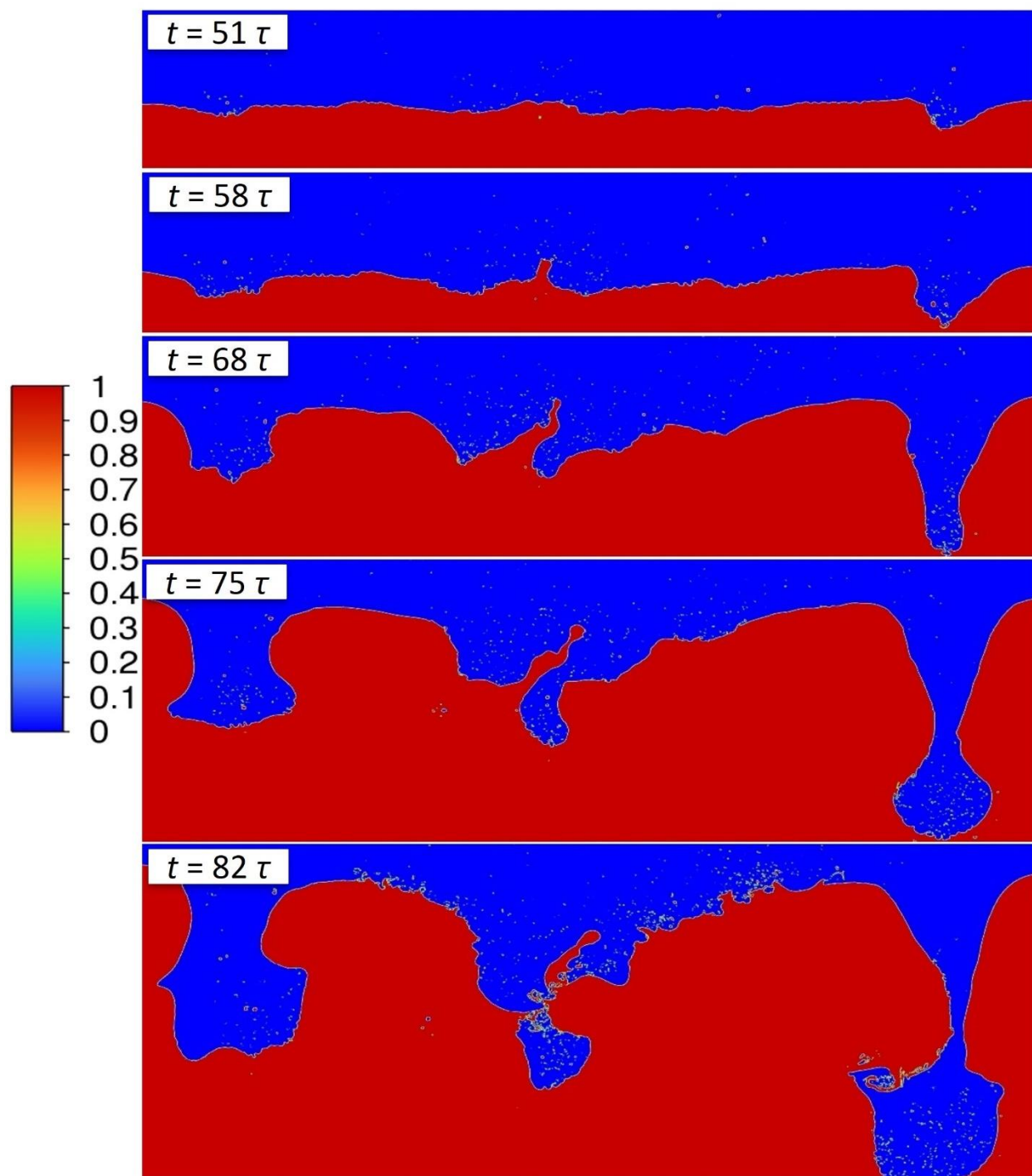


Figure 113. Volume fraction of water at the interface region for $2A_{th}$ amplitude, 50% liquid height and 1.7 MHz frequency.

For $H \gg \lambda$, the mechanism of droplet formation is similar to the case of 3λ and $1.1A_{th}$, except that the phenomenon is more non-linear and thus, with increasing the liquid height, it takes longer to atomize. Furthermore, it is distinguished that at higher liquid heights, the droplets are more uniform in shape (50λ vs 3λ liquid height), which the difference could be due to the faster atomization rate (shorter time) for lower liquid height compared to the higher liquid height. The phenomenon of secondary droplet formation is more noticeable at higher liquid heights. In general, the droplets are either ejected from the free surface of the liquid and travel away from the surface, staying the same size or a larger droplet gets ejected first and then secondary droplets get generated due to the breakdown of the larger droplet. Figure 114 reveals the formation of the secondary droplets during ultrasonic atomization. Initially, a large droplet gets ejected from the free surface of water and the ultrasonic acceleration moves the droplet upward. However, some of the larger droplets, as large as $8 \mu\text{m}$ in diameter, break into smaller droplets and generate secondary droplets. The velocity of the highlighted droplet in Figure 114 is about 6.6 m/s . This high inertia overcomes the surface tension and results in breaking up of the droplet into smaller droplets. In addition to formation of secondary droplets, another observation is the collision of droplets. In this study, the outcome of collision of single-fluid droplets with similar sizes is observed to be either coalescence or separation. For instance, in Figure 114, in times $31.43 \mu\text{s}$ and $31.62 \mu\text{s}$ coalescence of the formed secondary droplets occurs.

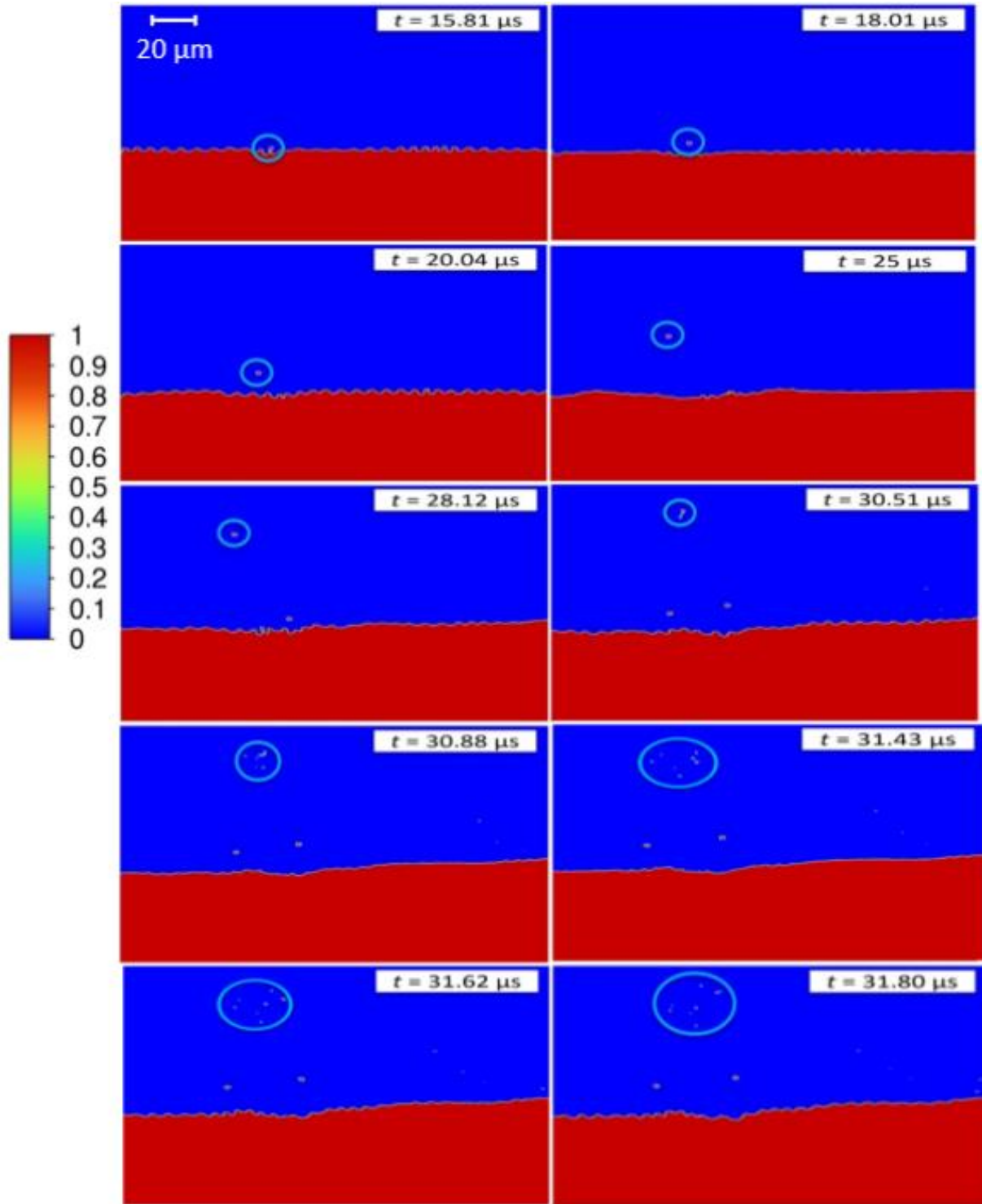


Figure 114. Secondary droplets formation and droplets' collisions. $2A_{th}$ amplitude, 50λ liquid height and 1.7 MHz frequency. The colormap is based on volume fraction of liquid.

The vertical coordinate of the center point of the interface (Figure 115) was tracked and monitored with time. To do this, an Iso-Surface was defined in Fluent for volume fraction of water when the value is 0.5. Then an Iso-Clip was set on the x -coordinate of the mesh for the previously defined Iso-Surface. After that, an Iso-Surface was defined for the mesh in the x -direction at the middle point (centerpoint) and the surface was chosen as the previously defined Iso-Clip.

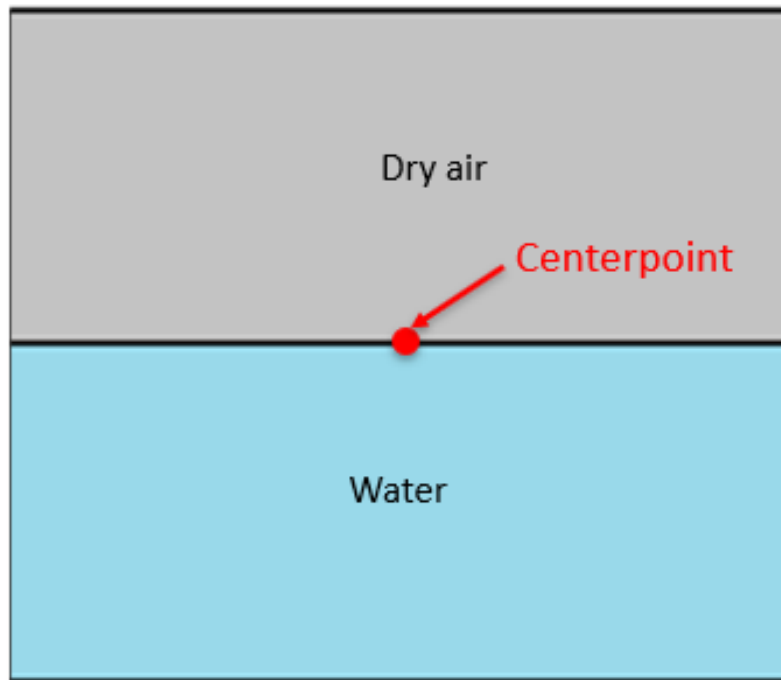


Figure 115. Vertical coordinate of the centerpoint of the interface vs time period.

Figure 116 shows the changes of the vertical coordinate for the centerpoint of the interface.

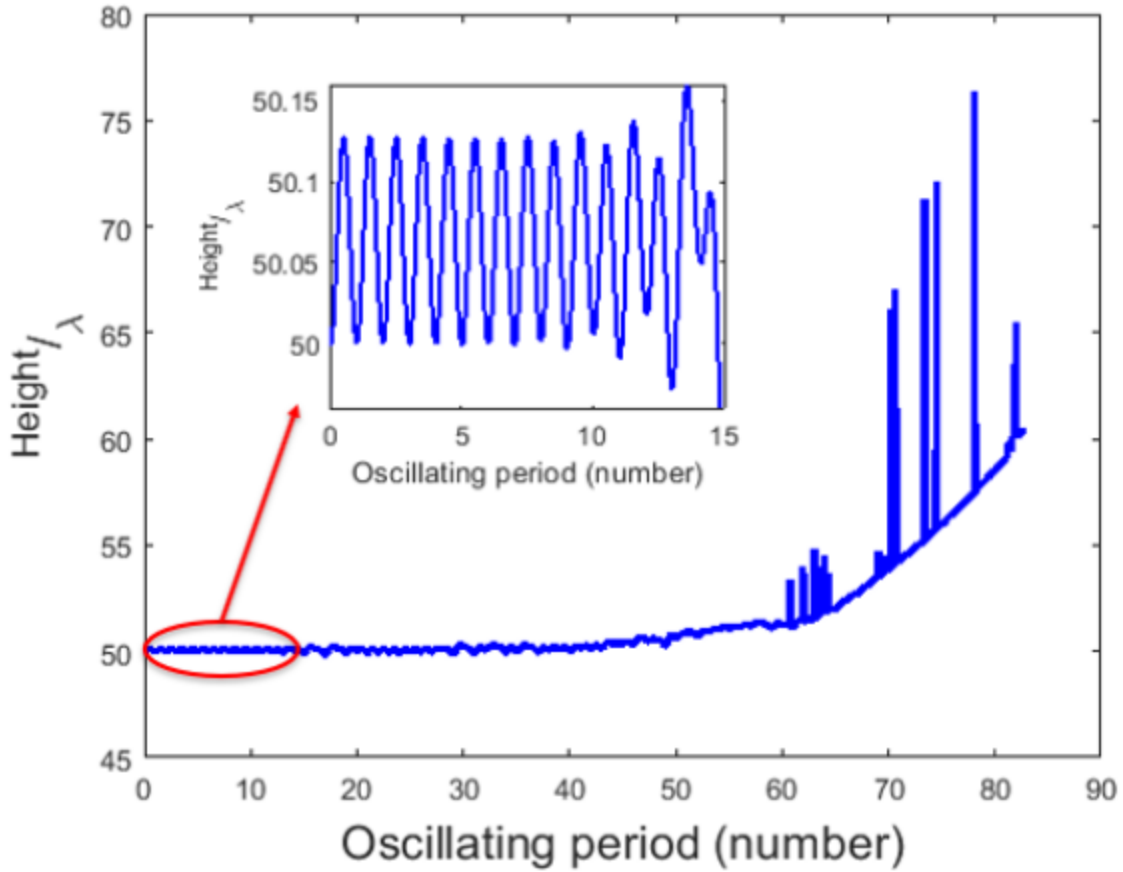


Figure 116. Vertical coordinate of the centerpoint of the interface vs time period. $2A_{th}$ amplitude, 50λ liquid height and 1.7 MHz frequency.

In the beginning for about 10 oscillation periods, the displacements of the interface are almost linear and uniform but as the waves progress, the behavior becomes non-linear and at the end when the droplet ejection occurs vigorously, the fluctuations at the interface become very unpredictable. In the linear wave zone, the frequency of the waves is half of the base frequency (1.7 MHz) which corresponds to the wavelength of $8.56 \mu\text{m}$.

The same observations can be made using the velocity and pressure at the centerpoint of the interface in Figure 117 and Figure 118, respectively. Beside the sinusoidal movements at the interface, these figures represent the chaotic behavior of the surface waves after starting the pinch off of the droplets.

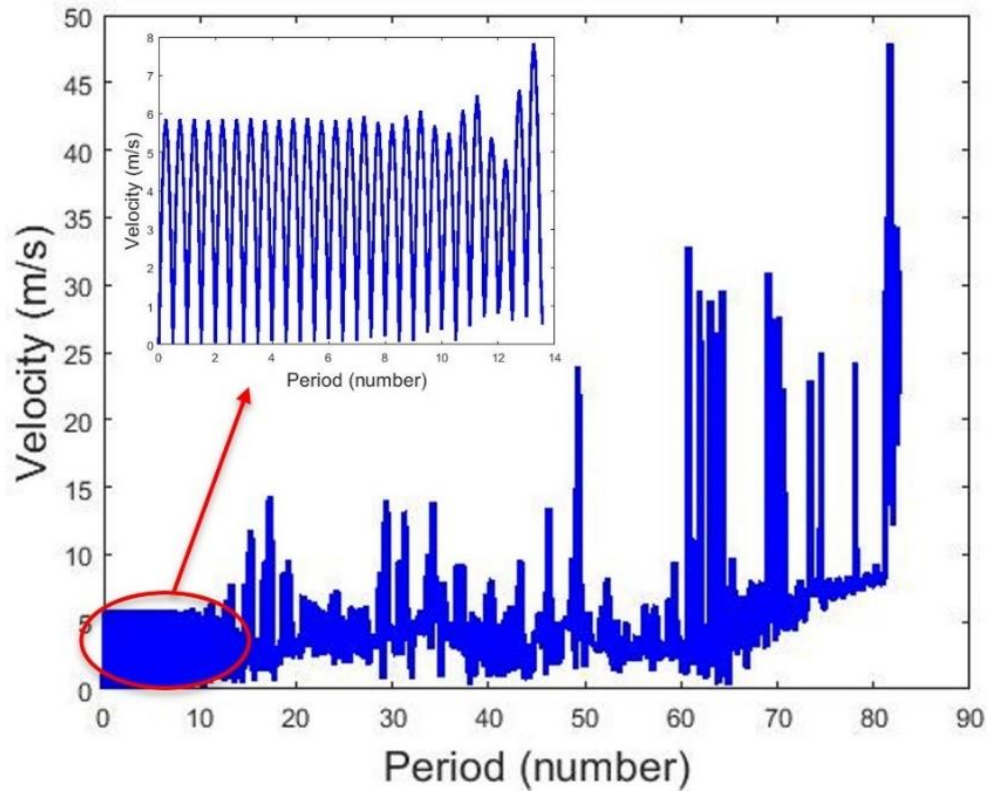


Figure 117. Velocity of the centerpoint of the interface vs oscillation period. $2A_{th}$ amplitude, 50% liquid height and 1.7 MHz frequency.

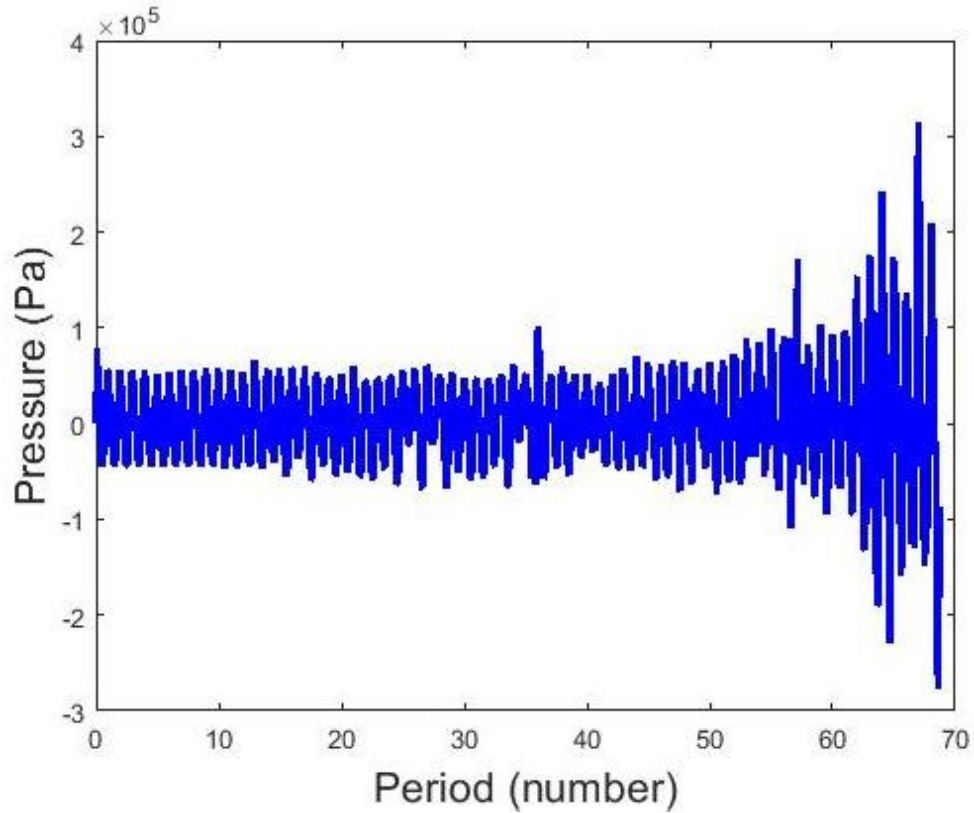


Figure 118. Pressure of the centerpoint of the interface vs time period. $2A_{th}$ amplitude, 50λ liquid height and 1.7 MHz frequency.

For this case also, increasing the exciting amplitude results in droplet ejection at lower time periods and higher atomization rate. Comparing Figure 119 for $2.2A_{th}$ and Figure 120 for $3A_{th}$ with Figure 112 and Figure 113 for $2A_{th}$ supports this claim.

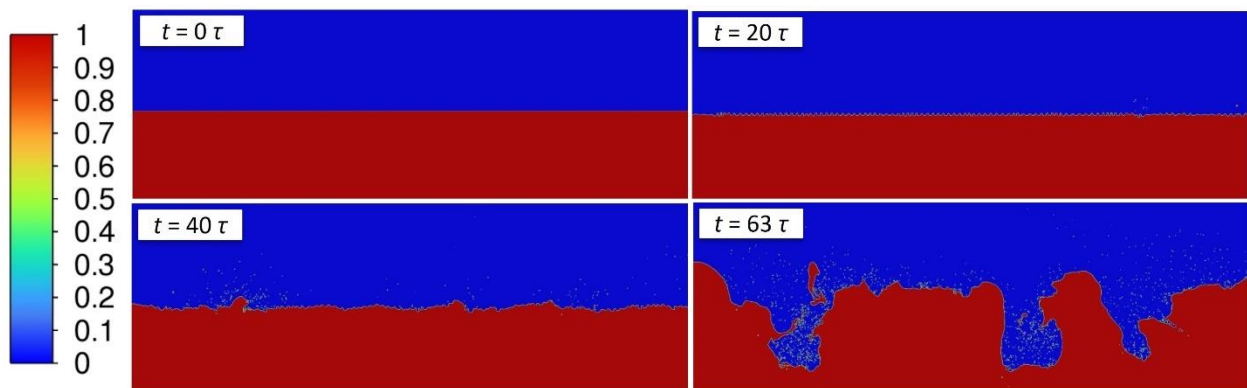


Figure 119. Volume fraction of liquid at the interface region for $2.2A_{th}$ amplitude, 50λ liquid height and 1.7 MHz frequency.

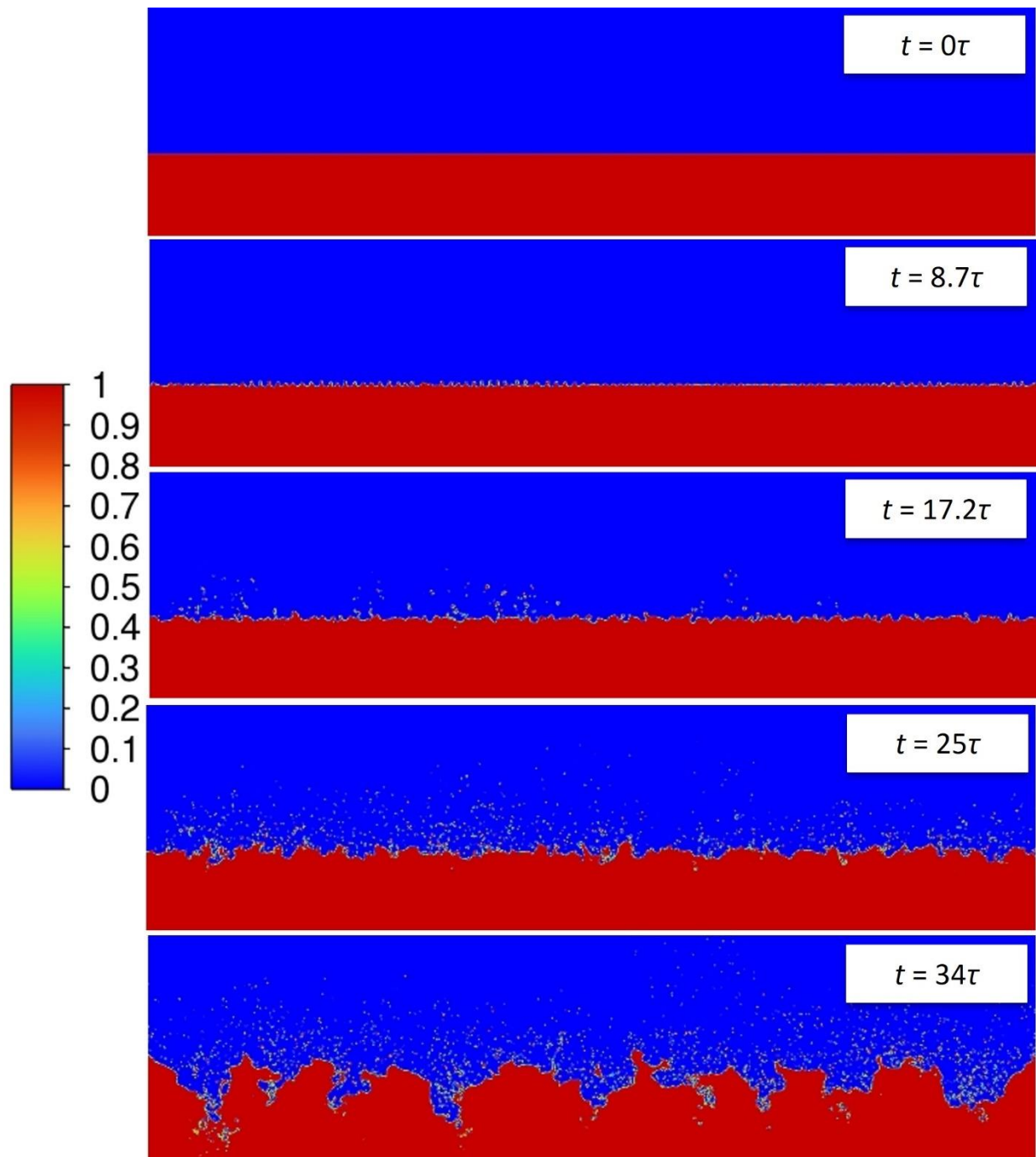


Figure 120. Volume fraction of liquid at the interface region for $3A_{th}$ amplitude, 50λ liquid height and 1.7 MHz frequency.

Comparing the average velocity of the interface versus time for different amplitudes for 50λ liquid height (Figure 121) reveals that the velocity of the interface is oscillating sinusoidally and by

increasing the amplitude, the average velocity of the interface increases. In addition, as the amplitude increases, the chaotic behavior of the waves starts at an earlier oscillation period.

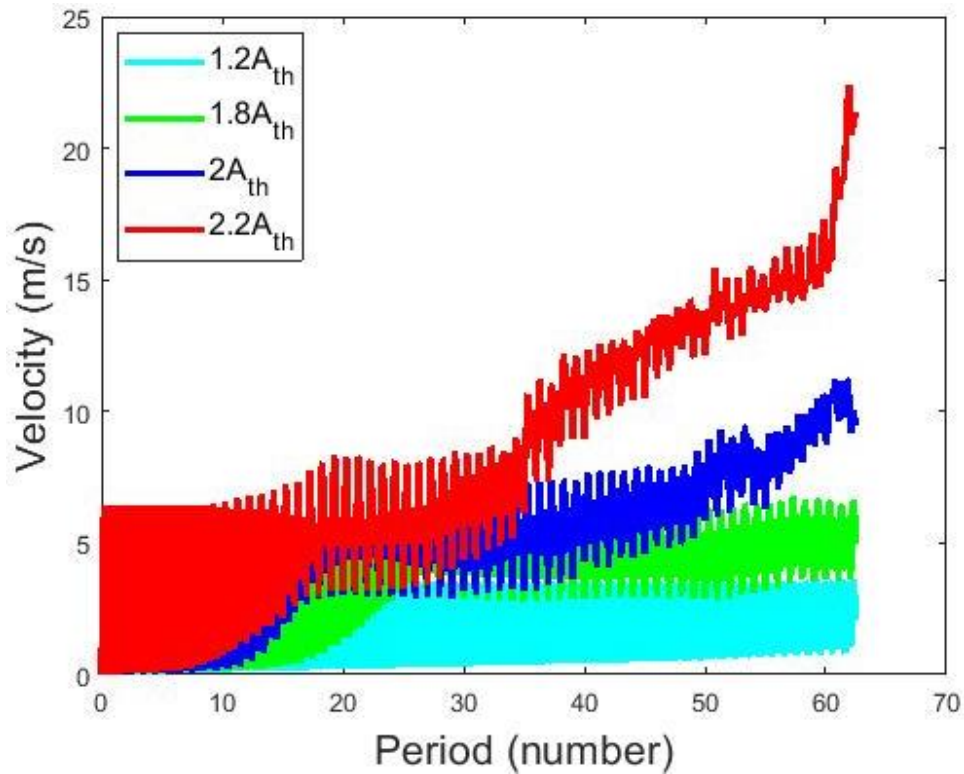


Figure 121. Average velocity of interface for different excitation amplitudes.

The effect of liquid height is studied for different values (3λ , 30λ , 50λ , 100λ and 200λ). The onset atomization amplitude is slightly increasing by liquid height. For instance, Figure 122 and Figure 123 show the changes in volume fraction of water for 30λ and 100λ .

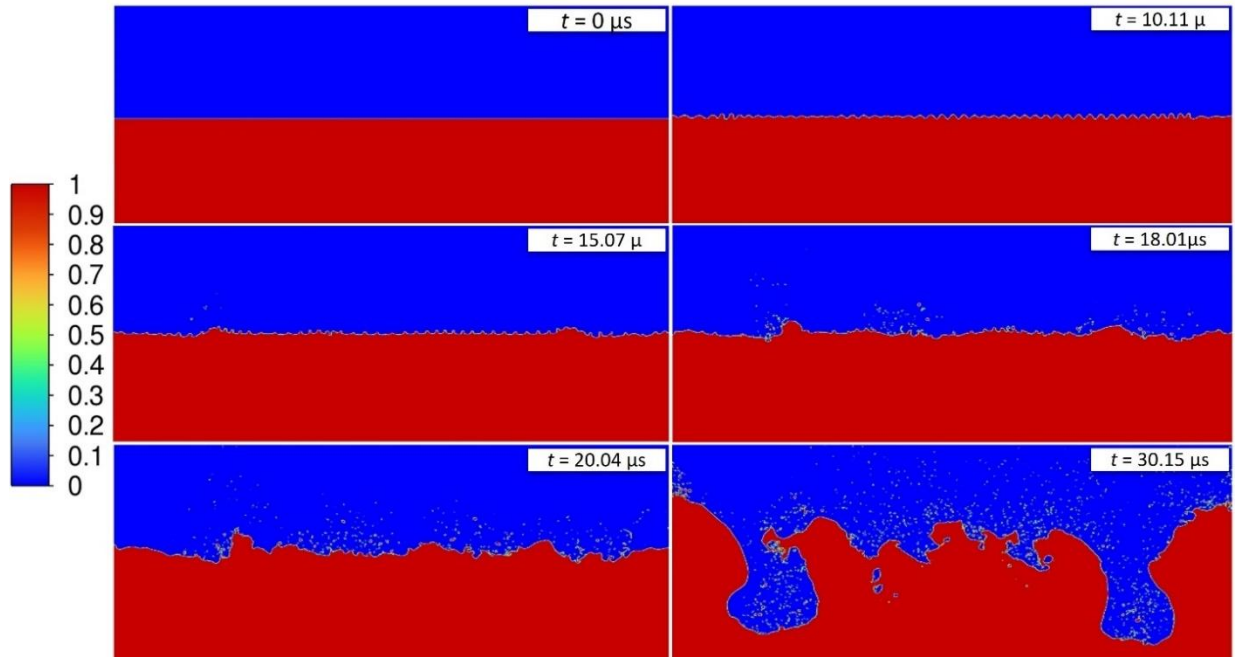


Figure 122. Volume fraction of water for 2A_{th} amplitude, 30λ liquid height and 1.7 MHz frequency.

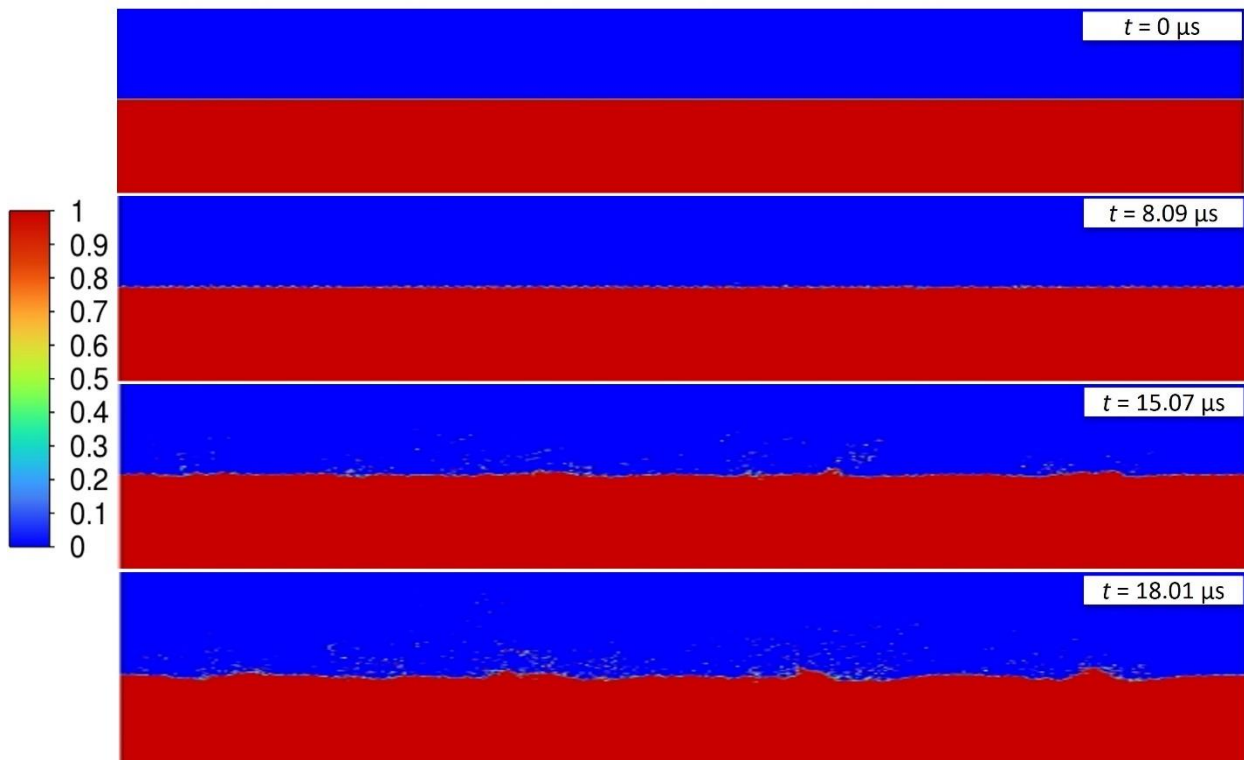


Figure 123. Volume fraction of water for 2.05A_{th} amplitude, 100λ liquid height and 1.7 MHz frequency.

The summary of the results is represented in Figure 124. This figure exhibits the effect of liquid height on the onset amplitude for atomization at 1.7 MHz frequency. According to this plot, increasing the liquid height one order of magnitude almost doubles the onset atomization amplitude. In addition, increasing the liquid height from 30λ to 200λ , does not change the onset amplitude significantly. In the following analysis in this research, the liquid height is considered to be 50λ for each excitement frequency.

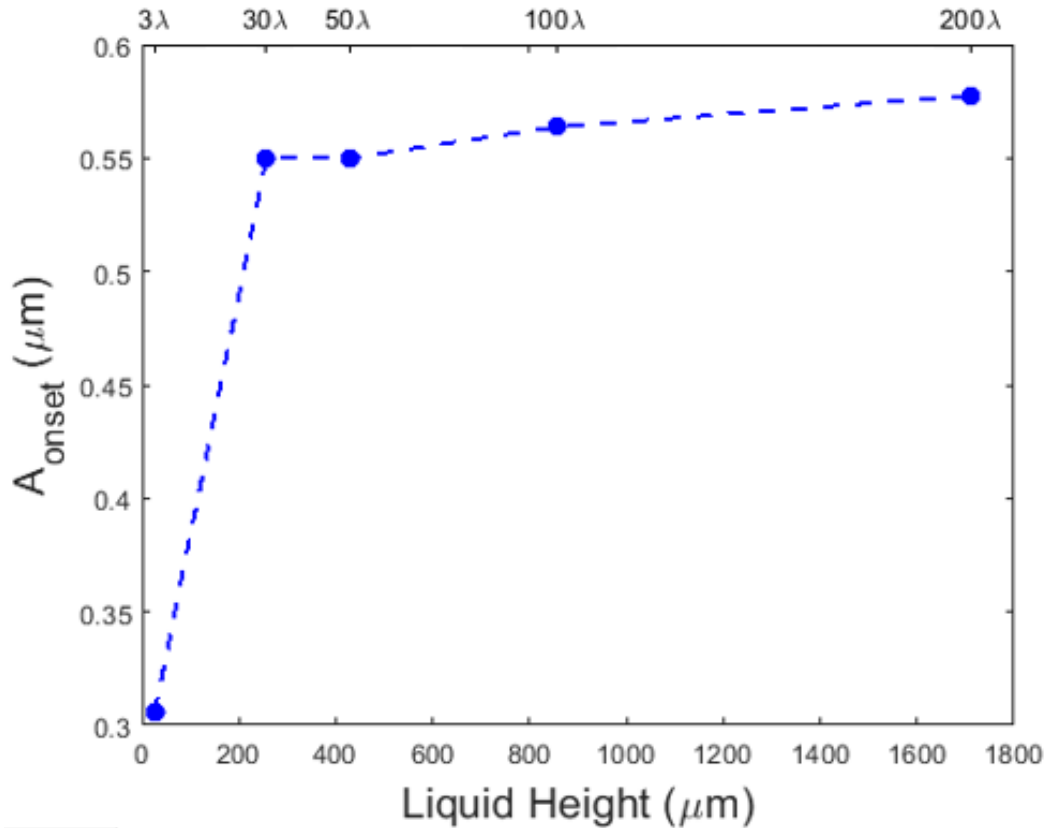


Figure 124. The effect of liquid height on onset amplitude for atomization at 1.7 MHz frequency.

Table 27 shows the non-dimensional numbers for the cases with different liquid heights at 1.7 MHz frequency.

Table 27. Non-dimensional numbers for different liquid heights.

Liquid height ($\times \lambda_{th}$)	$Re = \frac{\rho_l \sqrt{gHH}}{\mu}$	$We = \frac{\rho_l (gH^2)}{\sigma}$	$Fr = \frac{A\omega}{\sqrt{gH}}$	$St = \omega \sqrt{\frac{H}{g}}$	$Oh = \frac{\sqrt{We}}{Re}$
3	0.4	8.99×10^{-5}	205.6	17282	0.023
30	12.8	0.009	117	54650	0.007
50	27.6	0.25	90.7	70554	0.006
100	78	0.1	65.7	99778	0.004
200	220.8	0.4	47.6	141108	0.003

Many experiments have been conducted on the formation of the droplets using ultrasonic atomization. Most of these studies are based on the theory of Lang [73] in 1962 who used Kelvin's expression for capillary wavelength as a function of frequency and related the droplet size to the capillary wavelength. However, as Peskin and Raco [131] in 1963 stated, Kelvin's theory does not consider the effect of parameters such as liquid film height and amplitude. Rajan and Pandit [93] in 2001, provided correlations for predicting the droplet size as a function of thermophysical properties of liquid (flow rate, viscosity, density, and surface tension) and ultrasonic properties like amplitude, frequency, and the area of vibrating surface by introducing non-dimensional numbers for an ultrasonic nozzle. Their proposed correlation is for a continuously operating atomizer and in that case, the film thickness is directly related to the liquid flow rate. However, in the case of a liquid film on a vibrating surface, there is a gap in the literature to describe the droplet size as a function of both thermophysical properties of liquid as well as ultrasonic properties. In this research, the effect of liquid height on the capillary wavelength and droplet size is studied and the results are shown in Figure 125.

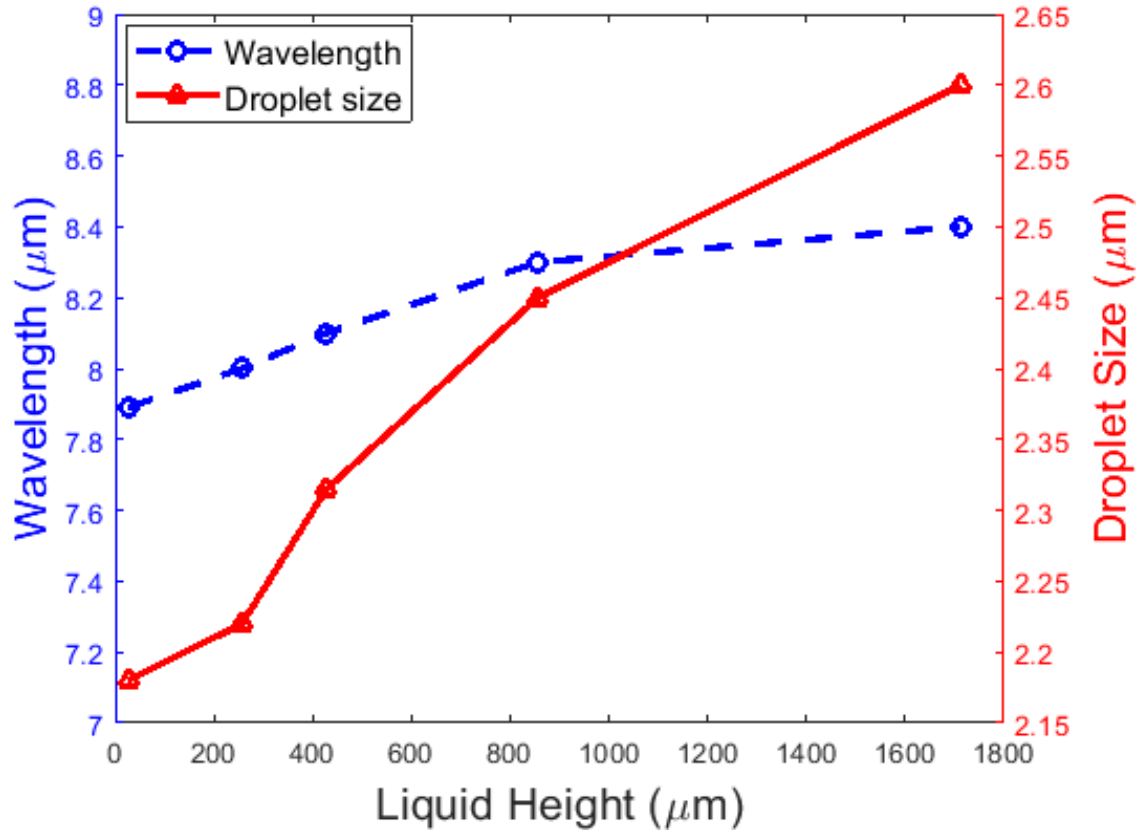


Figure 125. The effect of liquid height on capillary wavelength and droplet size at 1.7 MHz frequency.

The overall trend is that by increasing the liquid height, the mean droplet size increases. Similar to the effect of liquid height on the onset amplitude for atomization, there is a decrease in slope in Figure 125 as the liquid height increases. It is predicted that after a large enough liquid height, the droplet size changes slightly by further increase in liquid height. However, at very large liquid heights, surface instabilities are limited, and atomization does not occur.

It should be stated that within the length of time considered in this study, the impact of droplet ejection on the liquid film height is negligible.

6.3.3 Effect of Surface Tension on Ultrasonic Atomization

The energy required for overcoming the forces at the interface depends on the properties of the liquid, such as surface tension and it plays a major role in determining potential droplet size. The liquid/air surface tension is varied to $0.5\sigma_{\text{base}}$, $1\sigma_{\text{base}}$, $2\sigma_{\text{base}}$, and $4\sigma_{\text{base}}$ in the simulations at 1.7 MHz

frequency and 50λ liquid height. It should be mentioned that the liquid/air surface tension can be changed by adding impurities and surfactants to the liquid in different applications. Figure 126 shows the effect of surface tension on the onset atomization amplitude. As the surface tension decreases, the onset amplitude for atomization increases. In equation (6-21), surface tension is related to onset amplitude as $\sigma^{-1/3}$ and this relation is projected in Figure 126.

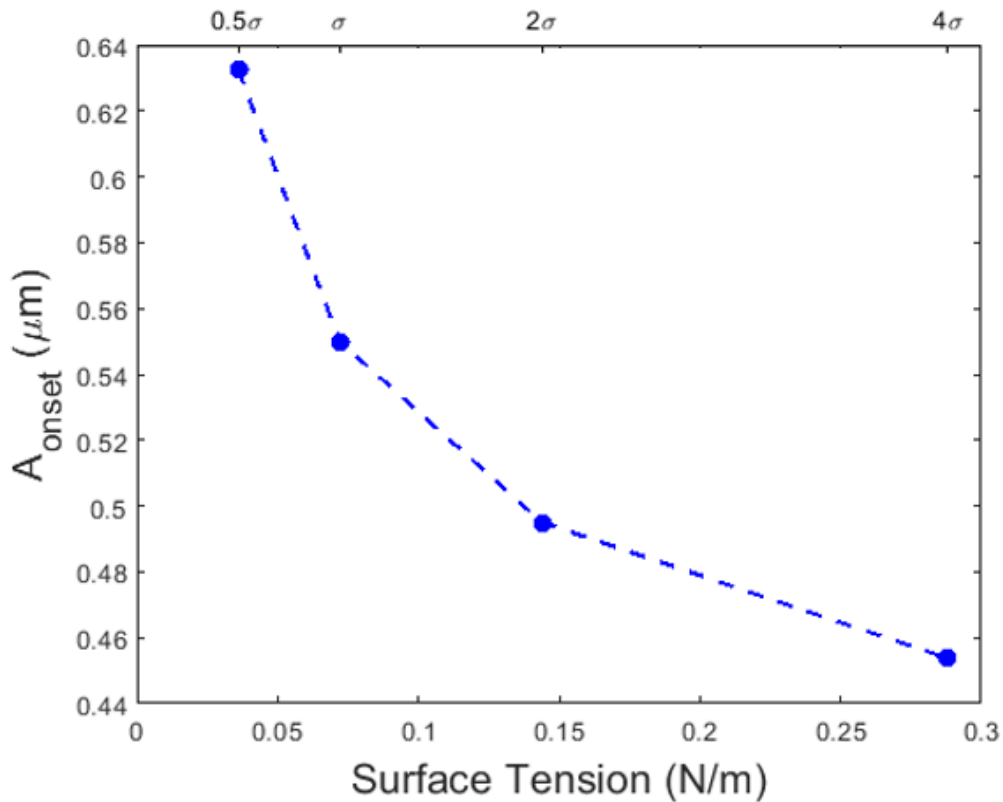


Figure 126. The effect of surface tension on onset amplitude for atomization at 1.7 MHz frequency and 50λ liquid height.

Surface tension tends to minimize the free surface area of the liquid and since increasing surface tension leads to increase in surface capillary wavelength, it is easier to atomize to reduce the surface area. In fact, higher surface tension makes the interface more susceptible to capillary instabilities. Table 28 shows the non-dimensional numbers for different values of surface tension. At constant Reynolds and Strouhal numbers, changes in Weber number changes Froude number. The onset atomization amplitude versus Weber number is plotted in Figure 127 and it reveals that by decreasing surface tension, Weber number increases. In addition, the values for Weber number

are less than 1, meaning that the surface tension forces are dominating the inertial forces and therefore, Froude number increases due to the resistance energy acting upon the interface. Figure 128 shows the combined effect of Reynolds and Weber numbers as Ohnesorge number.

Table 28. Non-dimensional numbers for different values of surface tension.

Surface tension ($\times \sigma_{base}$)	Re = $\frac{\rho_l \sqrt{gHH}}{\mu}$	We = $\frac{\rho_l (gH^2)}{\sigma}$	Fr = $\frac{A\omega}{\sqrt{gH}}$	St = $\omega \sqrt{\frac{H}{g}}$	Oh = $\frac{\sqrt{We}}{Re}$
0.5	27.6	0.05	104.3	70554	0.008
1	27.6	0.025	90.7	70554	0.0057
2	27.6	0.012	81.6	70554	0.004
4	27.6	0.006	74.8	70554	0.0029

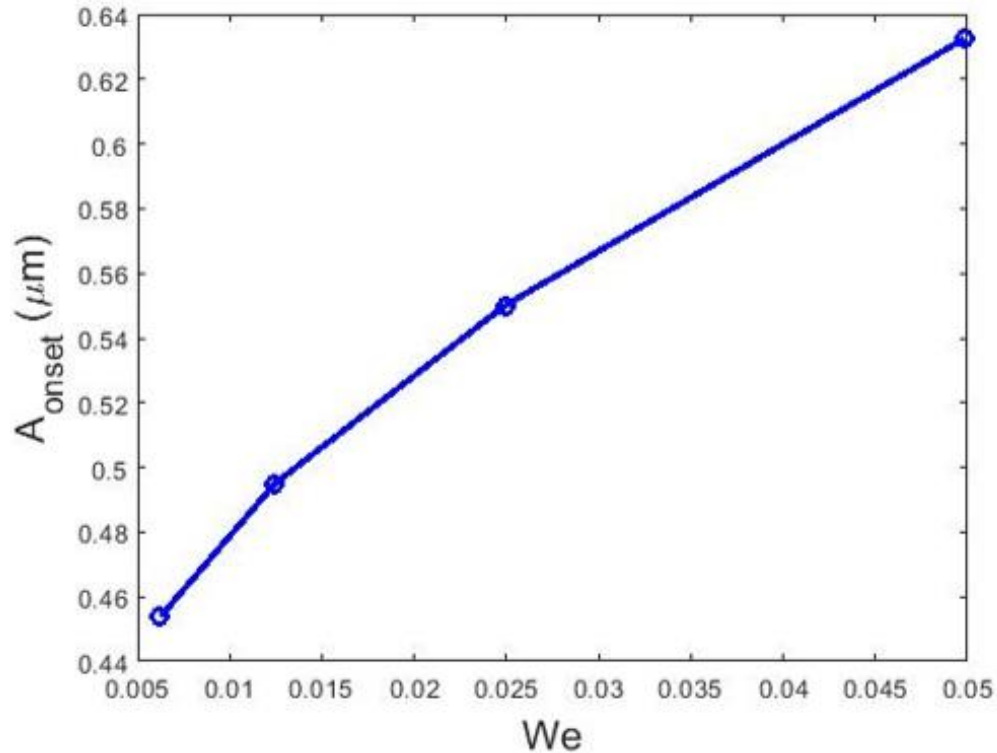


Figure 127. Onset atomization amplitude vs Weber number at different surface tension values at 1.7 MHz frequency and 50λ liquid height.

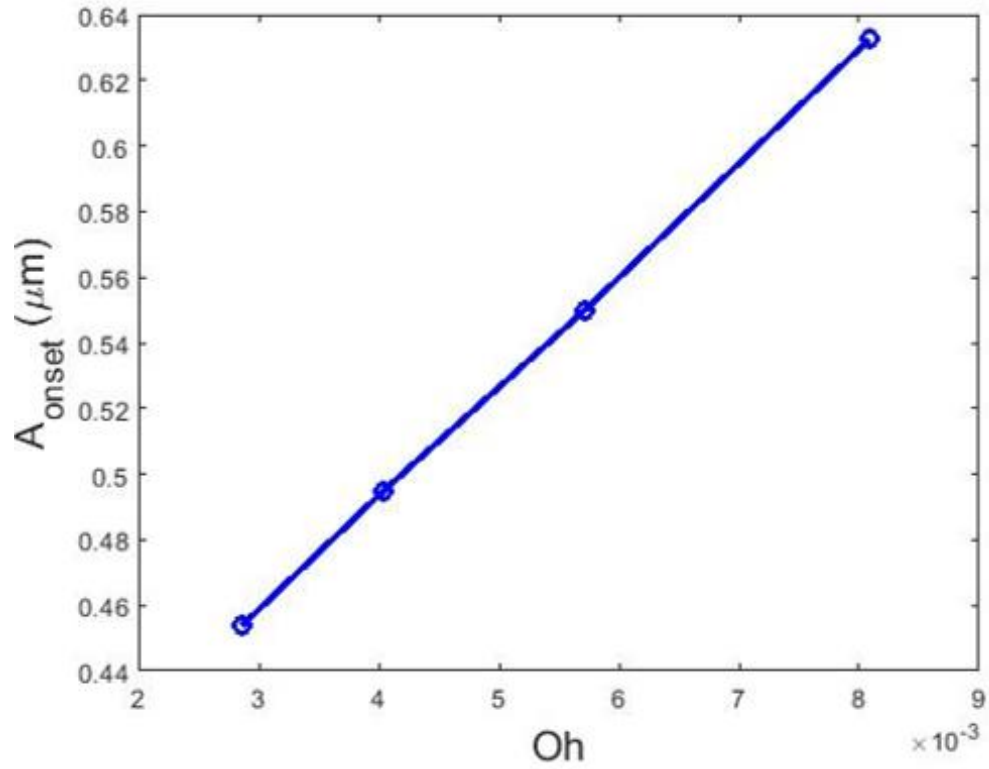


Figure 128. Onset atomization amplitude vs Ohnesorge number at different surface tension values at 1.7 MHz frequency and 50 μ liquid height.

The effect of surface tension on the mean size of the atomized droplets as well as the capillary wavelength is shown in Figure 129.

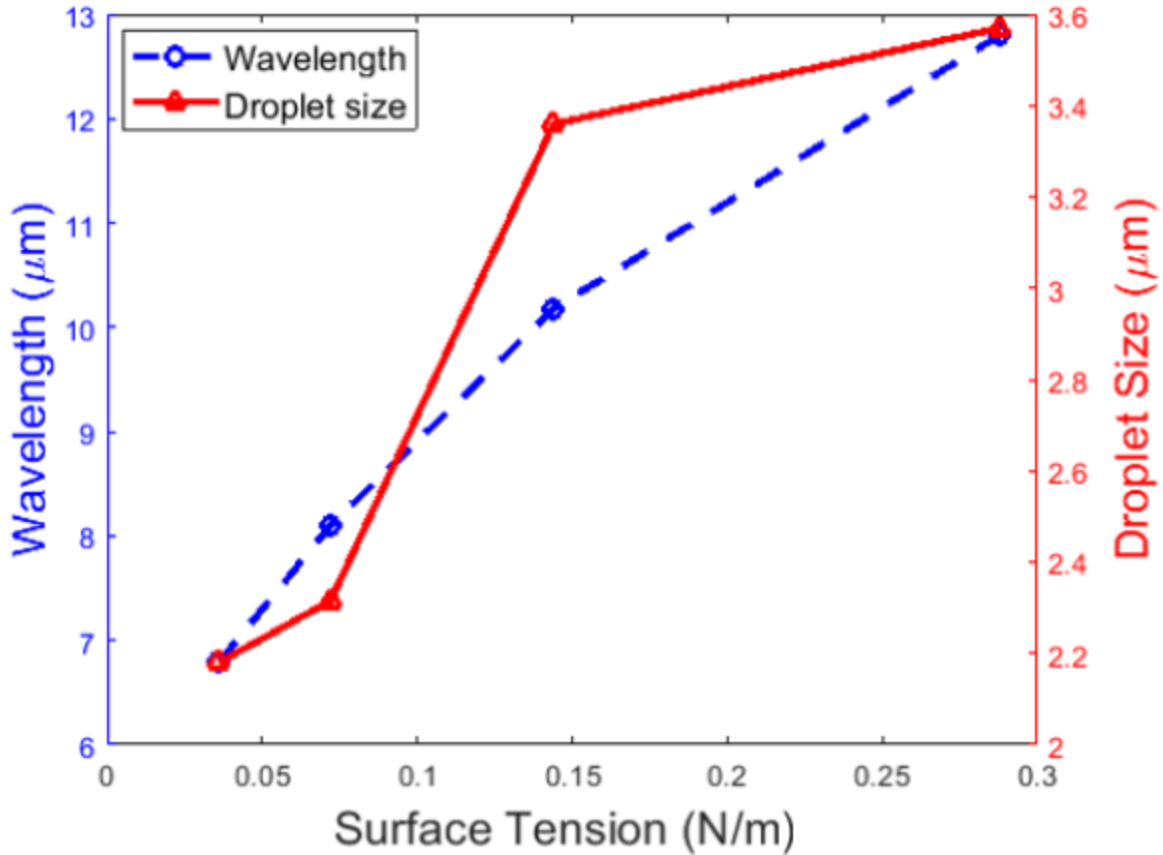


Figure 129. The effect of surface tension on droplet size and capillary wavelength at 1.7MHz frequency and 50 λ liquid height.

With decreasing the surface tension from $4\sigma_{base}$ to $0.5\sigma_{base}$, the droplet size is changed from $3.5 \mu\text{m}$ to $2.187 \mu\text{m}$. The decrease in the surface tension leads to decrease in the capillary wavelength and hence, the number of capillary waves per unit vibrating area increases with higher amplitudes, making the droplet ejection from the crests easier. Thus, the number of ejected droplets, i.e., the atomization rate, is higher at lower surface tension and the droplet sizes are smaller. Ramisetty et al. [85] stated that the increase in the kinetic energy of the liquid droplets is associated with the decrease in the droplet sizes. The difference in the capillary wavelength, atomization rate and ease of droplet ejection for two cases of $0.5\sigma_{base}$ and $4\sigma_{base}$ are illustrated in Figure 130.

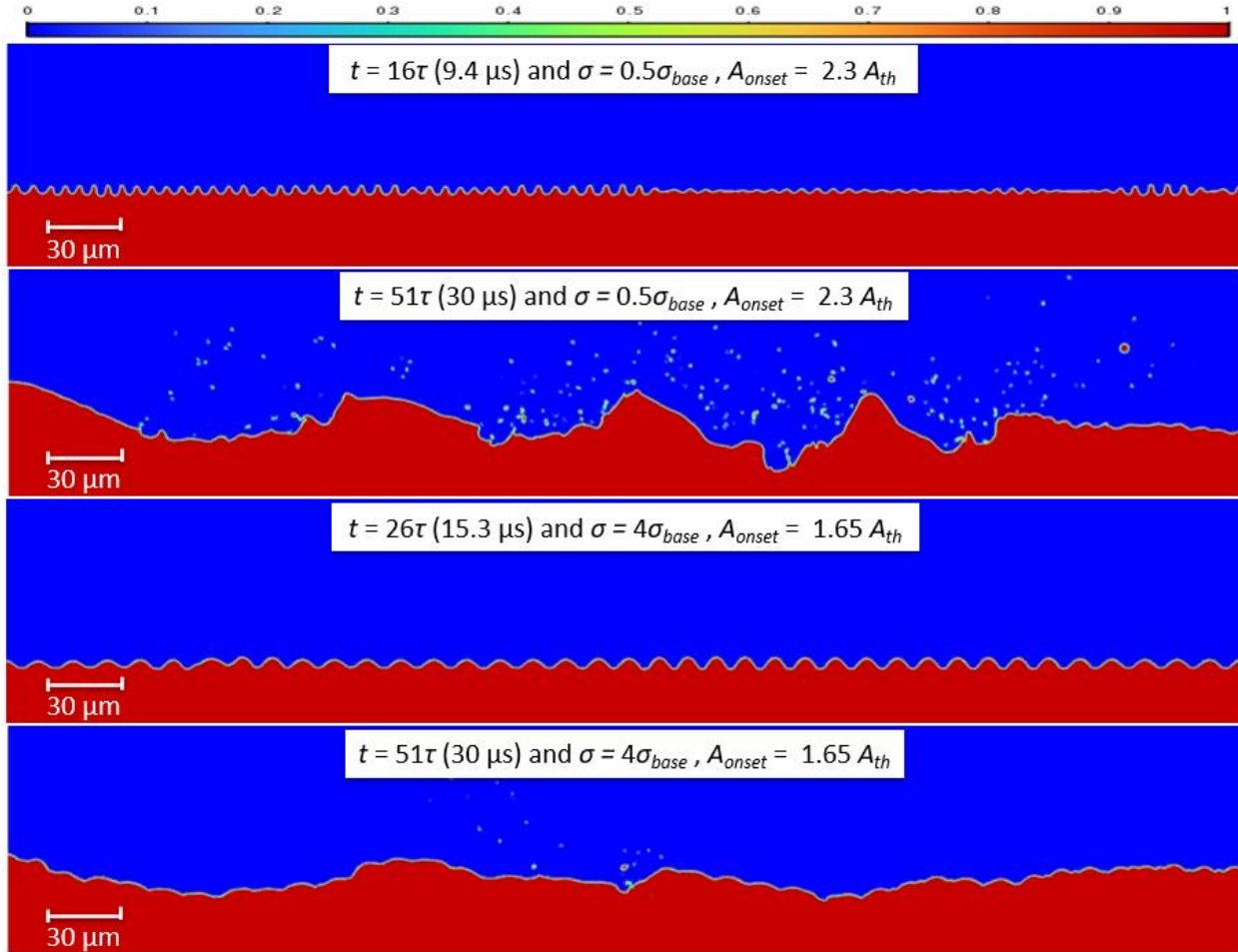


Figure 130. Comparison of the wavelength and atomization rate for two cases of $0.5\sigma_{base}$ and $4\sigma_{base}$ at 1.7 MHz frequency and 50λ liquid height. The colormap is based on liquid volume fraction.

6.3.4 Effect of Liquid Viscosity on Ultrasonic Atomization

Viscosity is a measure of a fluid's resistance to change in shape and it quantifies the internal frictional force between adjacent layers of fluid that are in relative motion. According to equation (6-21), the onset amplitude linearly increases with dynamic viscosity of the liquid. Different values of dynamic viscosity including $0.5\mu_{base}$, $1\mu_{base}$, $2\mu_{base}$, and $4\mu_{base}$ for 50λ liquid height and 1.7 MHz frequency are studied. Figure 131 shows the onset atomization amplitude for each case. This plot confirms the linear relationship between dynamic viscosity and onset atomization amplitude. In general, for highly viscous liquids, large values of amplitudes are needed to generate the unstable perturbations responsible for the droplet formation. Hence, higher electrical power and energy is

required for atomizing the liquid, i.e., disintegrating liquid into droplets, with higher viscosity due to the increase in liquid's resistance to change in shape. These results agree with the experimental results in the literature such as [87 and 88].

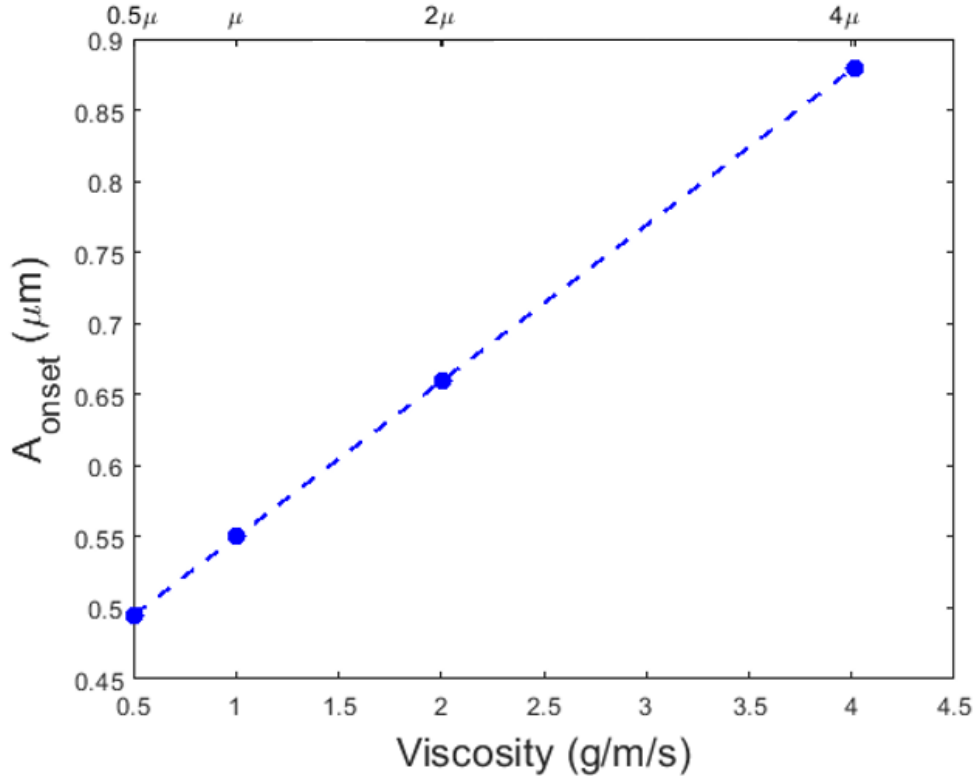


Figure 131. The effect of viscosity on onset amplitude for atomization at 1.7 MHz frequency and 50λ liquid height.

Figure 132 shows the interface region for a low and a high viscosity cases. Comparing both cases at 18τ , it is obvious that the growth rate of the crest height of the capillary waves at $4\mu_{\text{base}}$ is much lower compared to that at $0.5\mu_{\text{base}}$ and hence, the capillary wave number decreases at higher viscosities which results in the rise of both capillary wavelength and droplet sizes. Avvaru et al. [86] showed this behavior schematically as presented in Figure 133. This is another confirmation that the growth of capillary waves is the prerequisite for atomization and depends on the supplied energy.

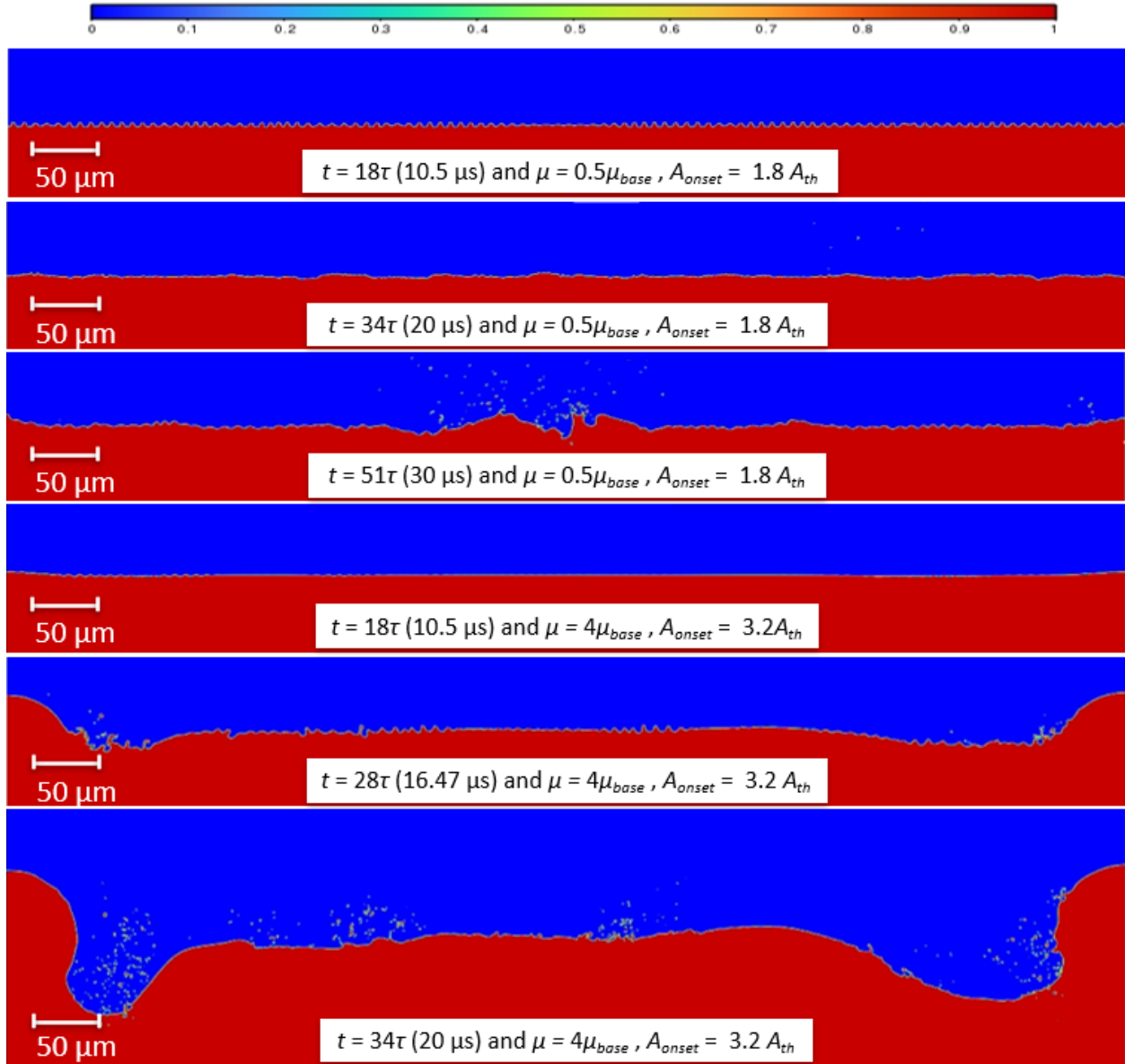


Figure 132. Comparison of the interface region for two cases with viscosities $0.5\mu_{base}$ and $4\mu_{base}$ at different time steps. The colormap is based on liquid volume fraction.

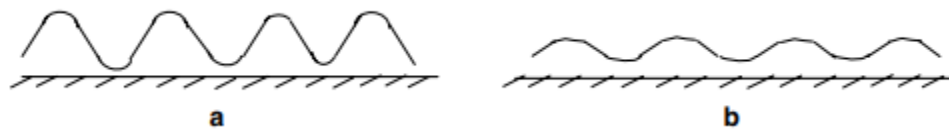


Figure 133. Capillary wave formation for low and high viscous liquids [86].

Among the non-dimensional numbers, viscosity only appears in Reynolds number. Weber and Strouhal numbers are constant and are equal to 0.0249 and 70554, respectively. The non-dimensional numbers are provided in Table 29. Figure 134 displays onset atomization amplitude as a function of Reynolds number and it reflects the μ^{-1} relation in Reynolds number. It should be mentioned that the values for Froude number confirm that the inertial forces are greater than gravitational forces at the free surface of the liquid film. In addition, the inertial forces dominate the viscous forces at these amplitudes and therefore, atomization happens.

Table 29. Non-dimensional numbers for different values of liquid viscosity.

Viscosity ($\times \mu_{base}$)	Re = $\frac{\rho_l \sqrt{gH} H}{\mu}$	We = $\frac{\rho_l (gH^2)}{\sigma}$	Fr = $\frac{A\omega}{\sqrt{gH}}$	St = $\omega \sqrt{\frac{H}{g}}$	Oh = $\frac{\sqrt{We}}{Re}$
0.5	55.2	0.025	81.6	70554	0.0029
1	27.6	0.025	90.7	70554	0.0057
2	13.8	0.025	108.8	70554	0.0114
4	6.9	0.025	145	70544	0.0229

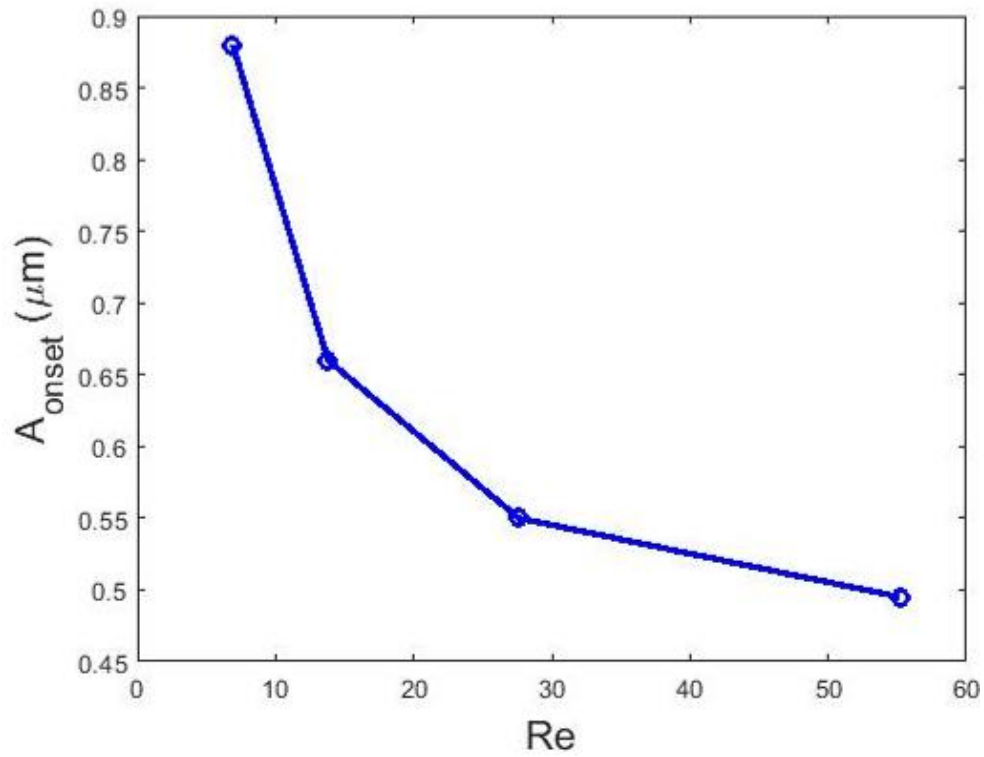


Figure 134. Onset atomization amplitude vs Reynolds number at different viscosity values at 1.7 MHz frequency and 50 λ liquid height.

The combined effect of Reynold number and Weber number is shown in Figure 135 as Ohnesorge number.

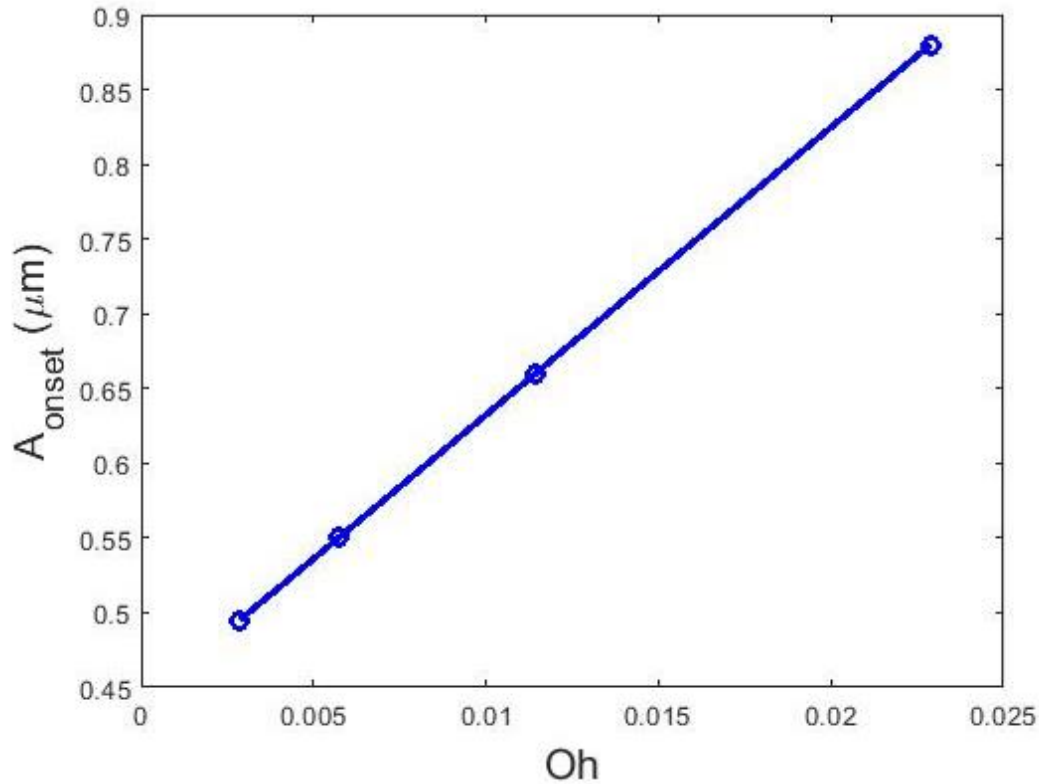


Figure 135. Onset atomization amplitude vs Ohnesorge number at different viscosity values at 1.7 MHz frequency and 50 λ liquid height.

The relationship between liquid viscosity and the droplet size has become one of the concerns in the recent years. Rajan and Pandit [93] reported that as the liquid viscosity increases, the droplet size increases. However, Avvaru et al. [86] experimentally observed a reverse trend. They explained their observations based on the change in viscosity by temperature. As the viscosity of the liquid increases, it is harder for the liquid to come out of the atomizer nozzle and therefore, the residence time of the liquid on the surface of the atomizer increases which results in increasing the temperature of the liquid due to the vibrational energy dissipation. As a result, the viscosity decreases and at some critical viscosity depending on the operating ultrasound intensity, the liquid film finally gets atomized. In contrary, Zhang et al. [87], observed that the droplet size and standard deviation gradually rise with increasing viscosity but after a peak at 0.00788 kg/(m.s), the trend become reverse and the droplet size and the standard deviation decreases with continuous increase in viscosity. Their results indicate that when the viscosity value of the liquid is small or large, the droplet diameter becomes more uniform and smaller, and the droplet size distribution also becomes

narrower. The authors explained the change in behavior for high viscous liquids using the cavitation hypothesis. At low liquid viscosity, the damping of cavity shock-wave is also low and thus, with a continuous supply of energy, cavity shock-wave intensity becomes high, which contributes to a high droplet velocity and a large droplet size. Nevertheless, by continuing to increase the liquid viscosity, cavitation becomes suppressed because it needs much more energy to produce cavitation collapse and therefore, the droplet size decreases. The range of the viscosities studied in this research are below the peak value described by Zhang et al. [87]. In this research, the effect of cavitation on ultrasonic atomization is not studied. Figure 136 shows the effect of liquid viscosity on droplet size and capillary wavelength. Both droplet size and wavelength increase by increasing viscosity, which agrees with the observations in the literature.

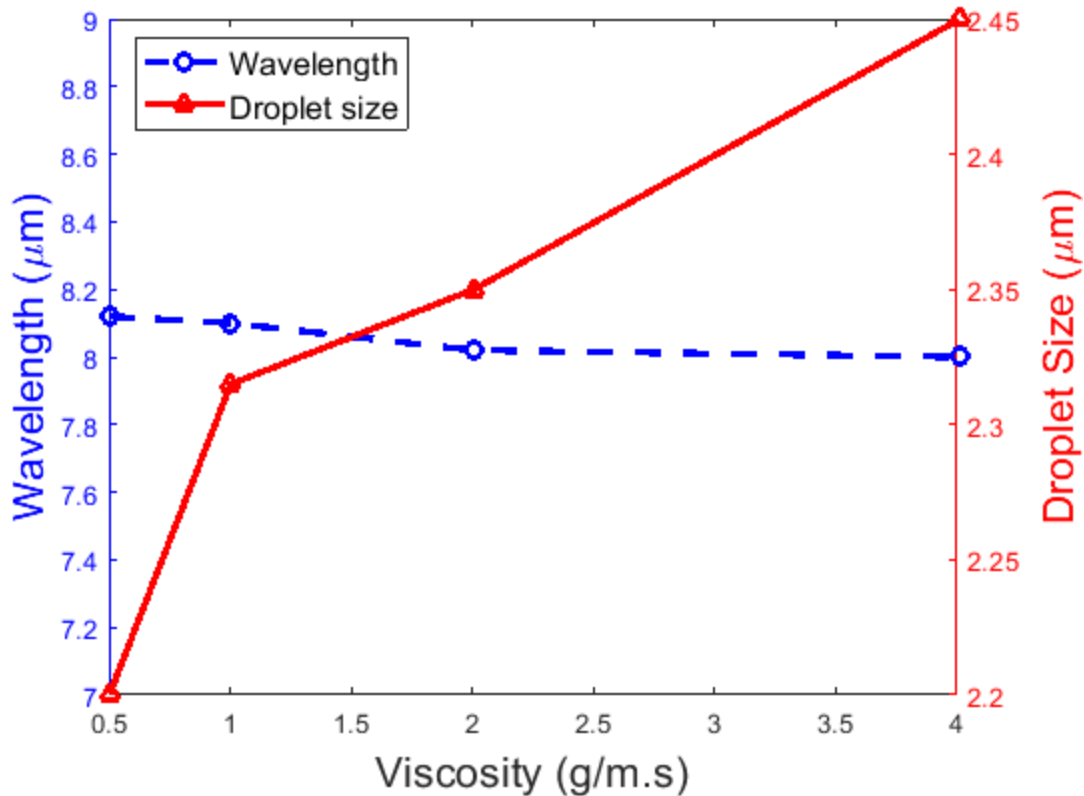


Figure 136. The effect of viscosity on droplet size and capillary wavelength at 1.7MHz frequency and 50λ liquid height.

It should be mentioned that since the onset amplitude is inversely related to the frequency and the amplitude is high at low frequencies (will be discussed in detail in section 06.3.6, highly viscous

liquids are very difficult or impossible to atomize using low frequency atomizers and therefore, MHz frequencies are suitable for atomizing high viscous liquids.

6.3.5 Effect of Liquid Density on Ultrasonic Atomization

One of the advantages of numerical simulations is that the effect of each parameter can be analyzed isolated from other parameters. In this section, the density of liquid is changed to values of $0.5\rho_{\text{base}}$, $1\rho_{\text{base}}$, $2\rho_{\text{base}}$, and $4\rho_{\text{base}}$ for 1.7 MHz frequency and 50λ liquid height. Increasing density decreases the capillary wavelength, which reduces the size of the droplets ejected from the crests. Figure 137 shows the effect of density on droplet size and capillary wavelength. Equation (6-21) implies that the onset amplitude is proportion to the liquid density as $\rho_L^{-2/3}$ and this behavior is reflected in Figure 138. From the non-dimensional numbers (Table 30), higher density corresponds to higher inertial forces and higher values for Reynolds and Weber numbers. This results in ease of droplet ejection. Figure 139 illustrates the differences between the droplet size and wavelength for a case with low density and a case with high density. At density of $2\rho_{\text{base}}$, the capillary waves are formed at the interface at 15.3τ , while for the $0.5\rho_{\text{base}}$, the capillary forces are produced at 21.5τ and the wavelength is smaller compared to that of $2\rho_{\text{base}}$. At 21.5τ for $2\rho_{\text{base}}$, the capillary waves have evolved and have higher amplitudes.

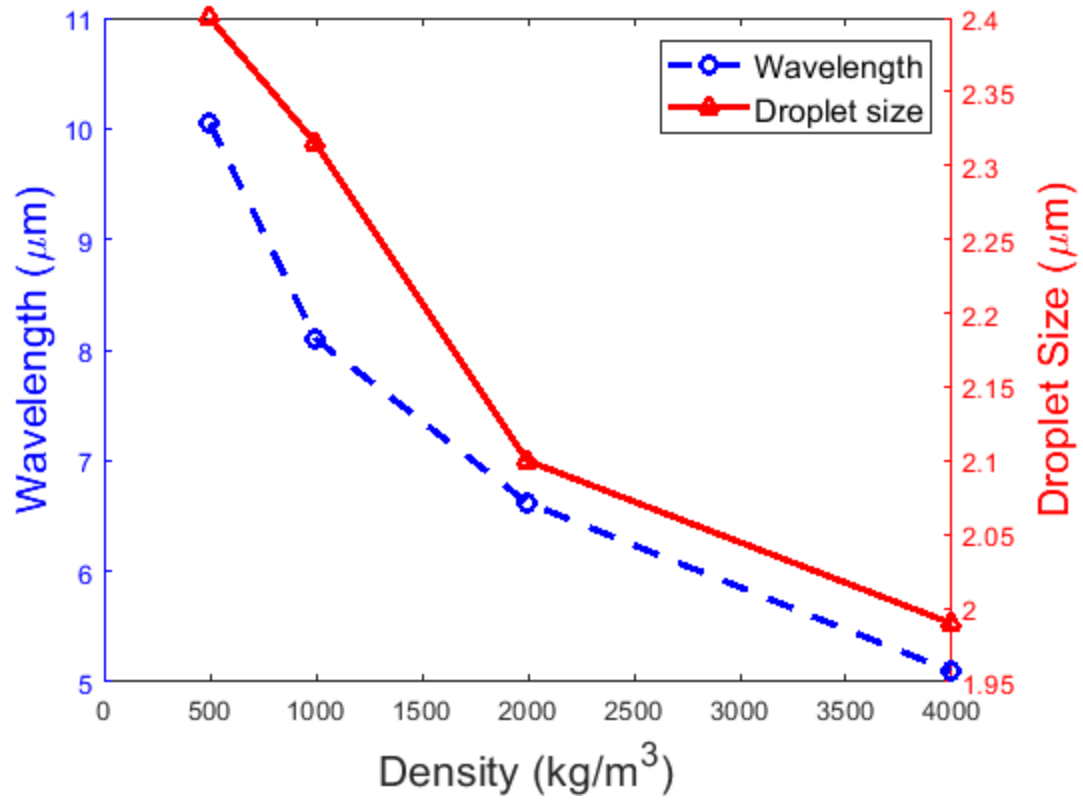


Figure 137. The effect of density on droplet size and capillary wavelength at 1.7MHz frequency and 50 μ l liquid height.

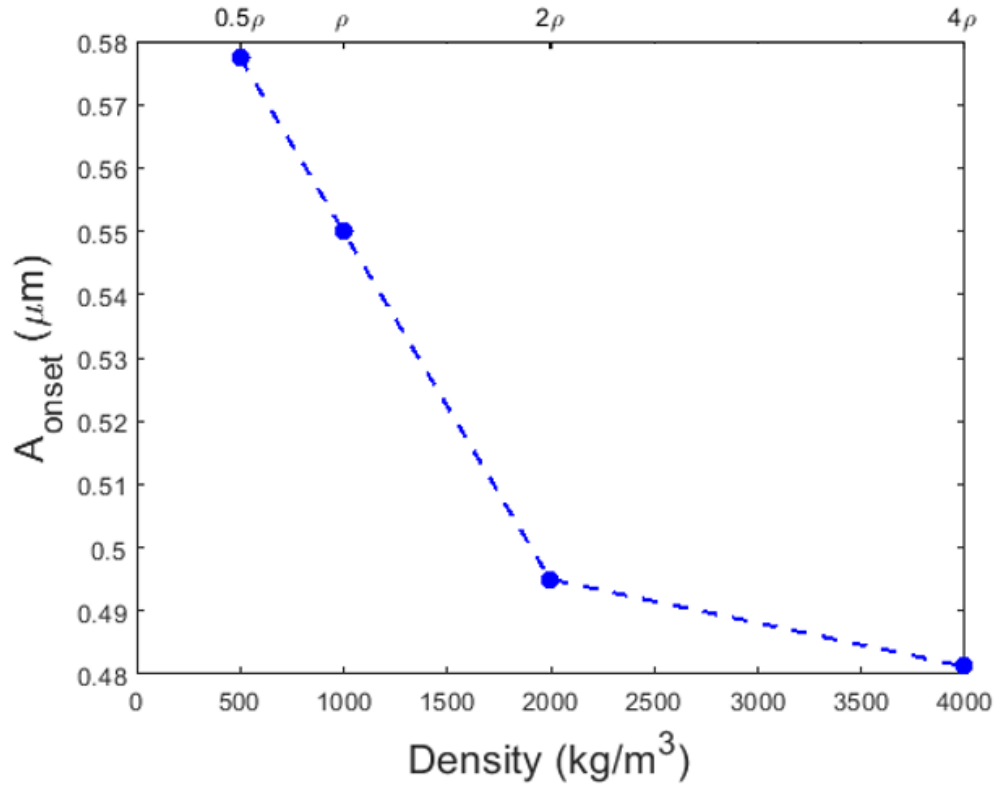


Figure 138. The effect of density on onset amplitude for atomization at 1.7 MHz frequency and 50 λ liquid height.

Table 30. Non-dimensional numbers for different values of liquid density.

Density ($\times \rho_{base}$)	$Re = \frac{\rho_l \sqrt{gH} H}{\mu}$	$We = \frac{\rho_l (gH^2)}{\sigma}$	$Fr = \frac{A\omega}{\sqrt{gH}}$	$St = \omega \sqrt{\frac{H}{g}}$	$Oh = \frac{\sqrt{We}}{Re}$
0.5	13.8	0.0125	95.2	70554	0.008
1	27.6	0.0249	90.7	70554	0.0057
2	55.2	0.0498	81.6	70554	0.004
4	110.4	0.0997	79.3	70544	0.0029

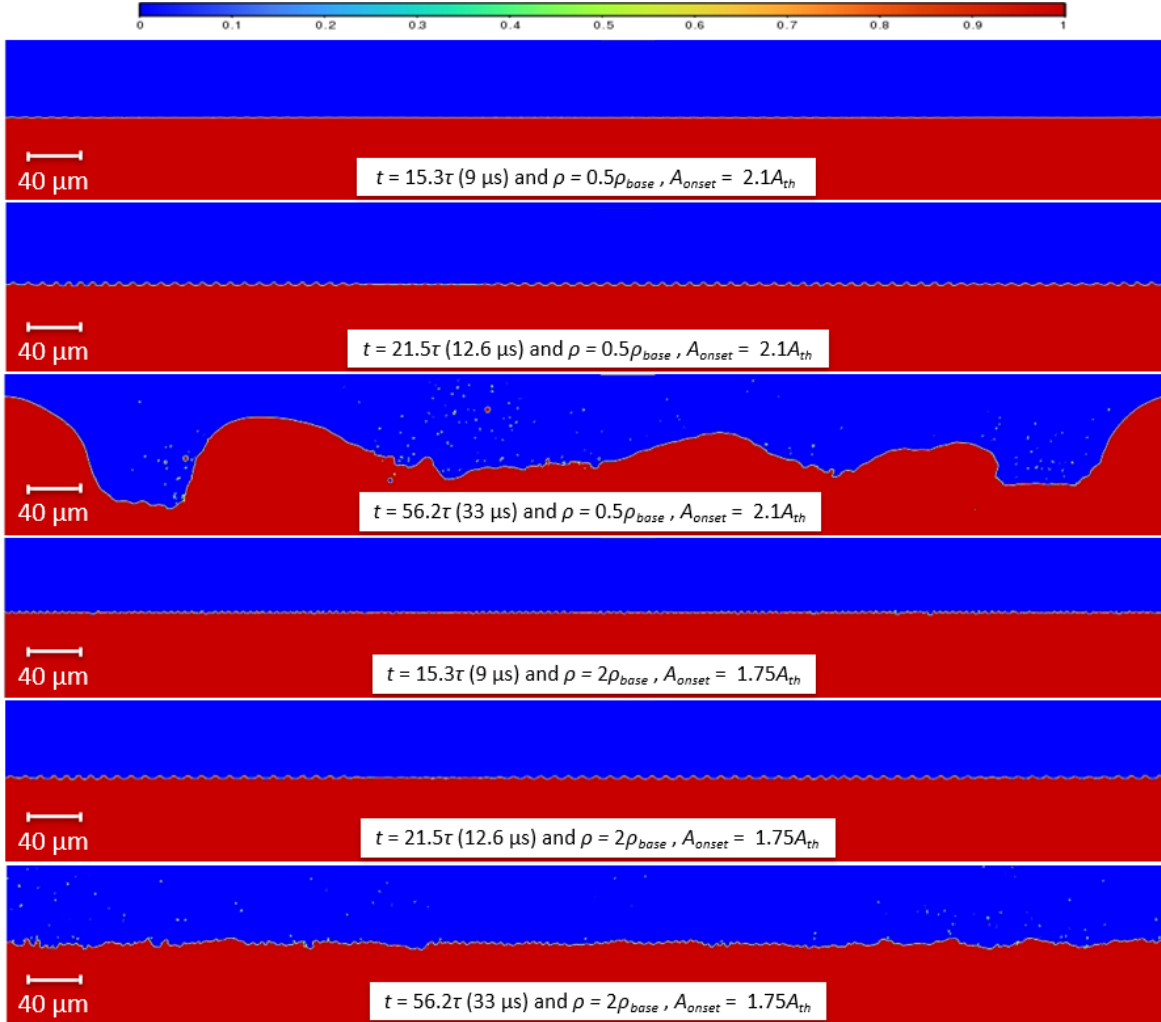


Figure 139. Comparison of the interface region for two cases with densities $0.5\rho_{base}$ and $2\rho_{base}$ at different time steps. The colormap is based on liquid volume fraction.

Figure 140 shows a 3D plot for the effect of Reynolds and Weber numbers on ultrasonic atomization amplitude. The combined effect of these two non-dimensional numbers is shown in Figure 141 as Ohnesorge number. For the cases studied here, the changes in Reynolds number compared to that of Weber number is appreciable. By increasing Ohnesorge number, the viscous forces become dominant compared to inertial and surface tension forces and hence, higher energy is required for atomization, which results in increasing the onset ultrasonic atomization.

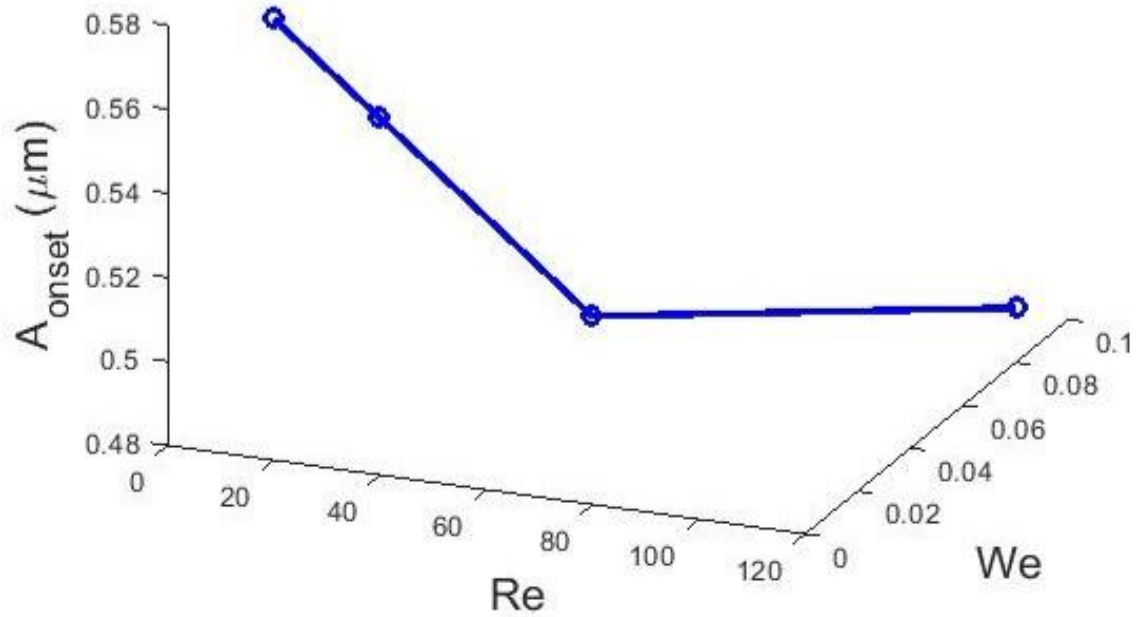


Figure 140. Onset atomization amplitude vs Weber number and Reynolds number at different density values at 1.7 MHz frequency and 50 λ liquid height.

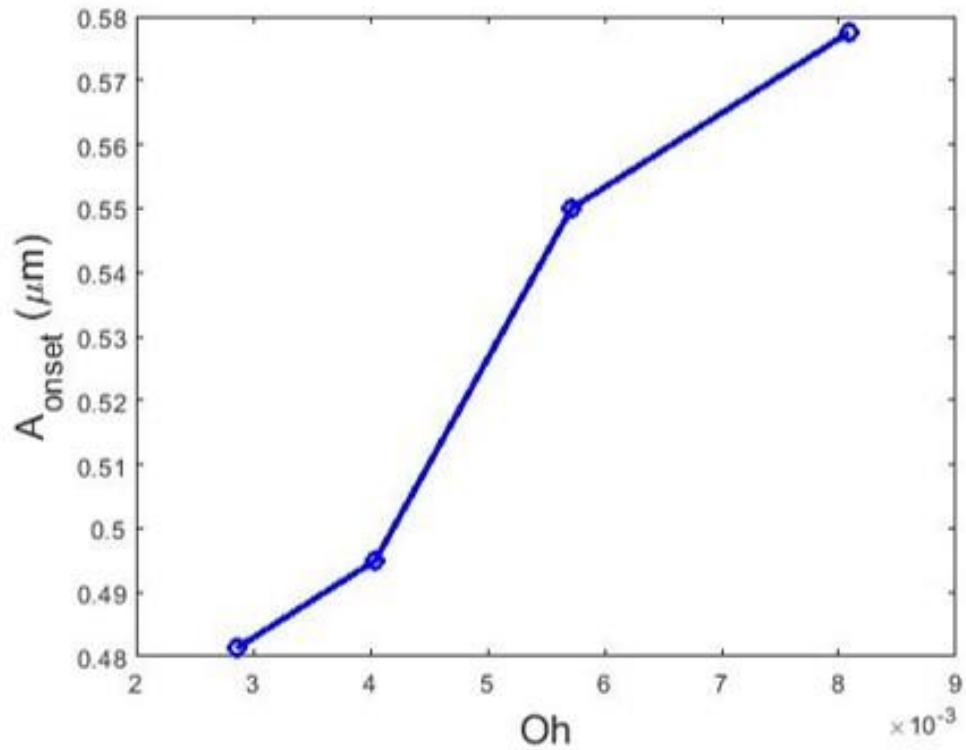


Figure 141. Onset atomization amplitude vs Ohnesorge number at different density values at 1.7 MHz frequency and 50 λ liquid height.

6.3.6 Effect of Exciting Frequency on Ultrasonic Atomization

The effect of frequency on the onset atomization amplitude is studied by using several ultrasonic atomizers of different frequencies in the range of 50-2000 kHz. The liquid height for these case studies is 50λ , for each frequency and the other controlling parameters are constant. Comparing between the results of different cases revealed that all the ultrasonic atomizers create the same forms of standing wave configurations. An example of surface wave patterns for 50 kHz and 2 MHz are presented in Figure 142 at their onset atomization amplitudes. Comparing the surface waves for these two frequencies, it can be verified that the wavelength is larger for the lower exciting frequency compared to that of the higher exciting frequency.

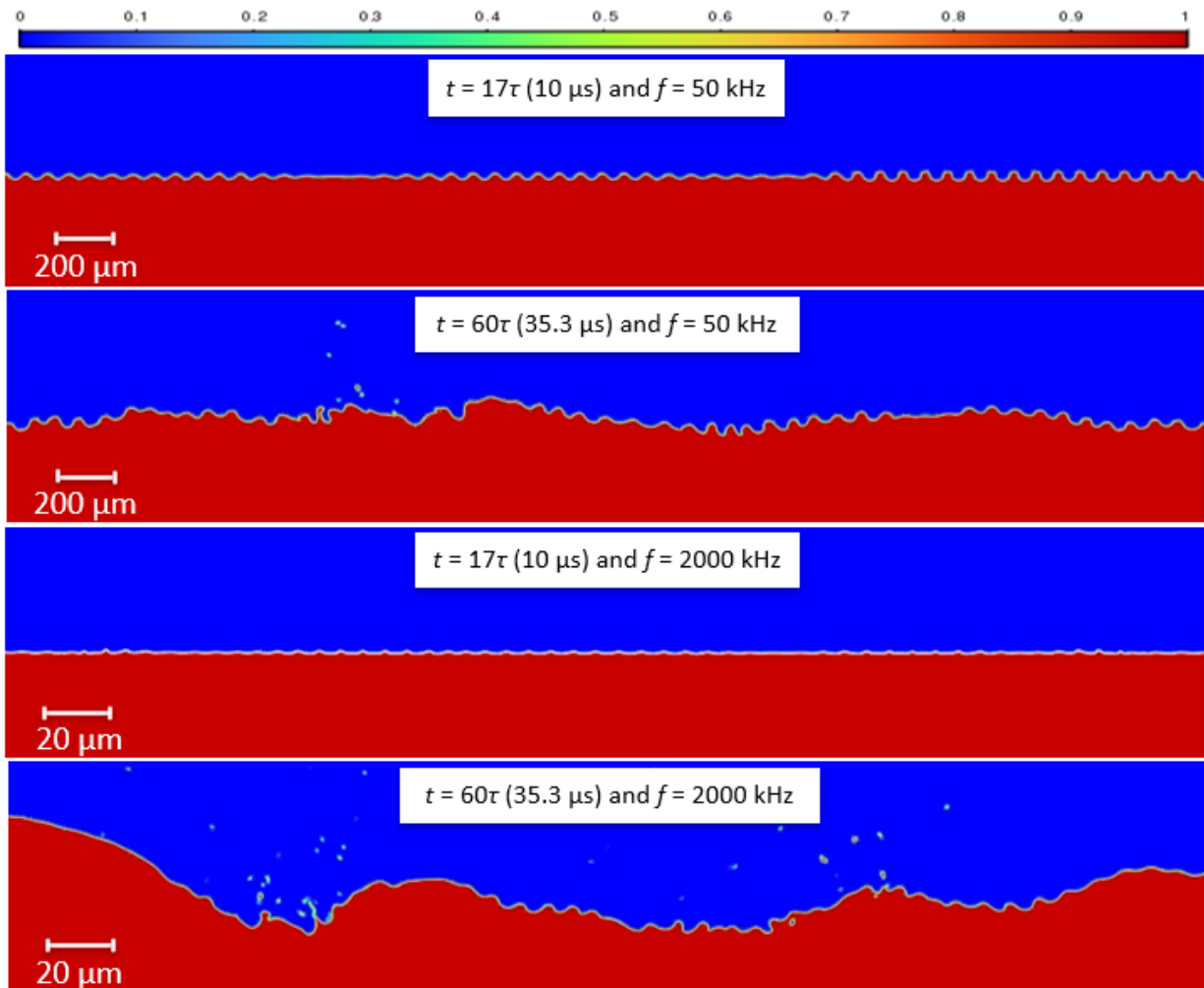


Figure 142. Comparison of the wavelength and atomization rate for two cases of 50 kHz and 2MHz frequencies. The colormap is based on liquid volume fraction.

Figure 143 illustrates the relationship between the wavelength and droplet size with frequency and Figure 144 shows the effect of exciting frequency on the onset atomization amplitude. As the frequency decreases, the wavelength increases and therefore, the depth of penetration is greater. The lower frequency has higher period time. Contradictory, higher frequency has lower wavelength which enables us to observe smaller details. Based on equation (6-21), the onset amplitude is proportional to f^{-3} and this relationship is displayed in Figure 144 from the numerical simulations. Furthermore, as illustrated in Figure 144, the onset atomization amplitude for 50 kHz frequency is much higher than the rest of the frequencies studied, and it is $5A_{th}$. This result is in agreement with Lierke and Greisshammer [129] for low frequency vibrations, which suggests that the atomization inception amplitude is between 3 to 6 times the critical amplitude.

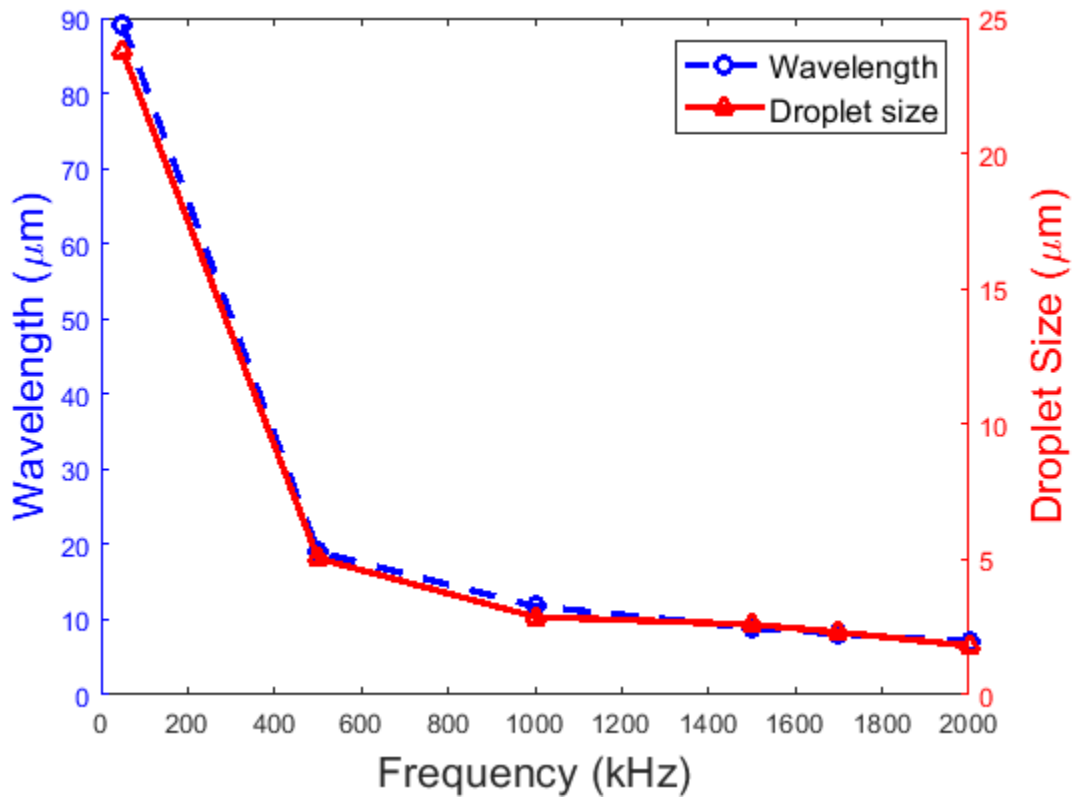


Figure 143. The effect of frequency on droplet size and capillary wavelength at 1.7MHz frequency and 50λ liquid height.

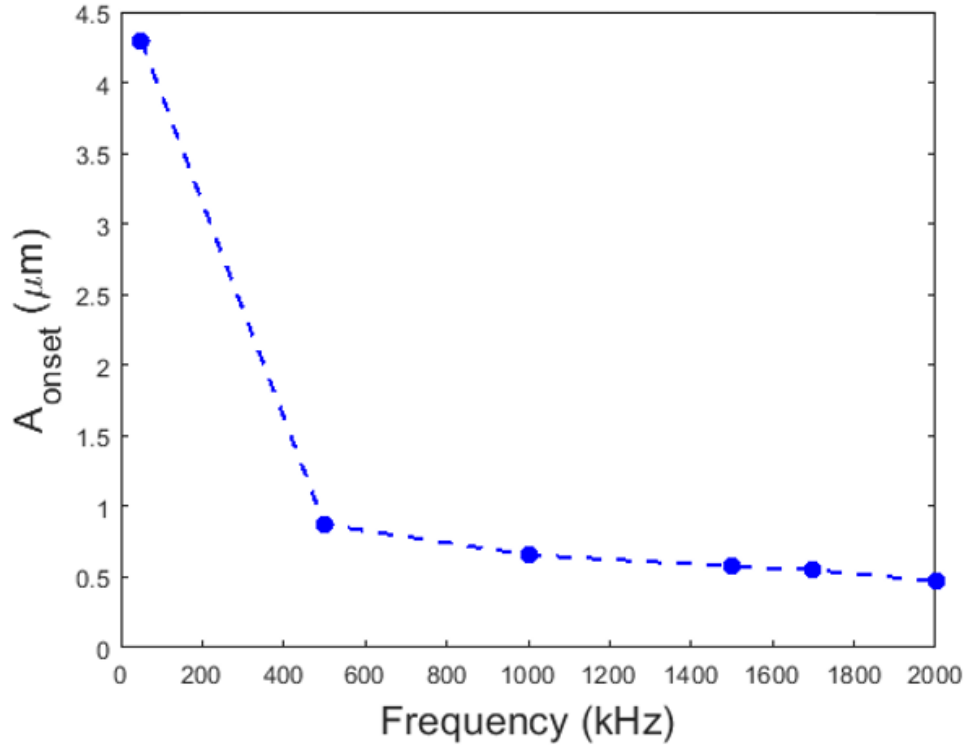


Figure 144. The effect of frequency on onset amplitude for atomization at 50 μ liquid height.

Table 31 represents the non-dimensional numbers for the cases with different frequencies.

Table 31. Non-dimensional numbers for different values of exciting frequency.

Frequency (kHz)	$Re = \frac{\rho_l \sqrt{gH} H}{\mu}$	$We = \frac{\rho_l (gH^2)}{\sigma}$	$Fr = \frac{A\omega}{\sqrt{gH}}$	$St = \omega \sqrt{\frac{H}{g}}$	$Oh = \frac{\sqrt{We}}{Re}$
50	938.5	2.74	6.49	6722	0.0018
500	93.8	0.13	28.1	31203	0.0038
1000	46.9	0.05	53.5	49532	0.0048
1500	31.3	0.029	80.4	64905	0.0055
1700	27.6	0.025	90.7	70554	0.0057
2000	23.5	0.02	96.4	78627	0.006

Reynolds and Weber numbers are proportional to H and H^2 , respectively and hence, by increasing Reynolds and Weber numbers, Froude number decreases. This is due to the fact that the liquid height is smaller for higher frequencies. Since liquid height is 50λ for each exciting frequency, this is another confirmation that the wavelength decreases as the frequency increases. On the other hand, Strouhal number is related to both frequency and liquid height. Table 31 shows that as the frequency decreases, the inertial forces due to the unsteadiness of the flow from ultrasonic oscillations dominates (higher onset amplitude) and therefore Froude number increases.

6.3.7 Effect of Gravity on Ultrasonic Atomization

The effect of reduced gravity ($0g$ and $0.5g$) and high gravity ($2g$) are studied at 1.7 MHz and the results are compared to the case of gravity (g). No difference is observed between the three cases and the onset amplitude for atomization is the same (confirming equation (6-21), which onset amplitude does not depend on gravity). These results are presented in Figure 145. In fact, the values of Froude number and Strouhal number at different studied cases (Table 32) imply that the inertial forces are greater than the gravitational forces and consequently capillary waves dominate over gravity waves. According to Edward and Fauve [132], the criteria for dominating the capillary waves over the gravity waves is defined as follows:

$$\frac{\sigma k^2}{\rho_l} \gg g \quad (6-27)$$

where k is the capillary wave number ($\frac{2\pi}{\lambda}$). According to equation (1-2), λ doesn't depend on gravity and hence it has the same value for different gravities studied here. For the gravitational value of g , the wavelength needs to be much smaller than 0.01703 m to satisfy the above criteria. This wavelength corresponds to 9.57 Hz frequency which is way out of the ultrasound range. For $2g$, the critical wavelength reduces to 0.012 and for the case of reduced gravity, it only gets worse (0.024 m for $0.5g$). Capillary wavelength decreases by increasing frequency and for 1.7 MHz frequency, wavelength is 8.56 μm . This information is useful especially in space applications and it confirms that the ultrasonic capillary waves are the same in terrestrial and spaces applications.

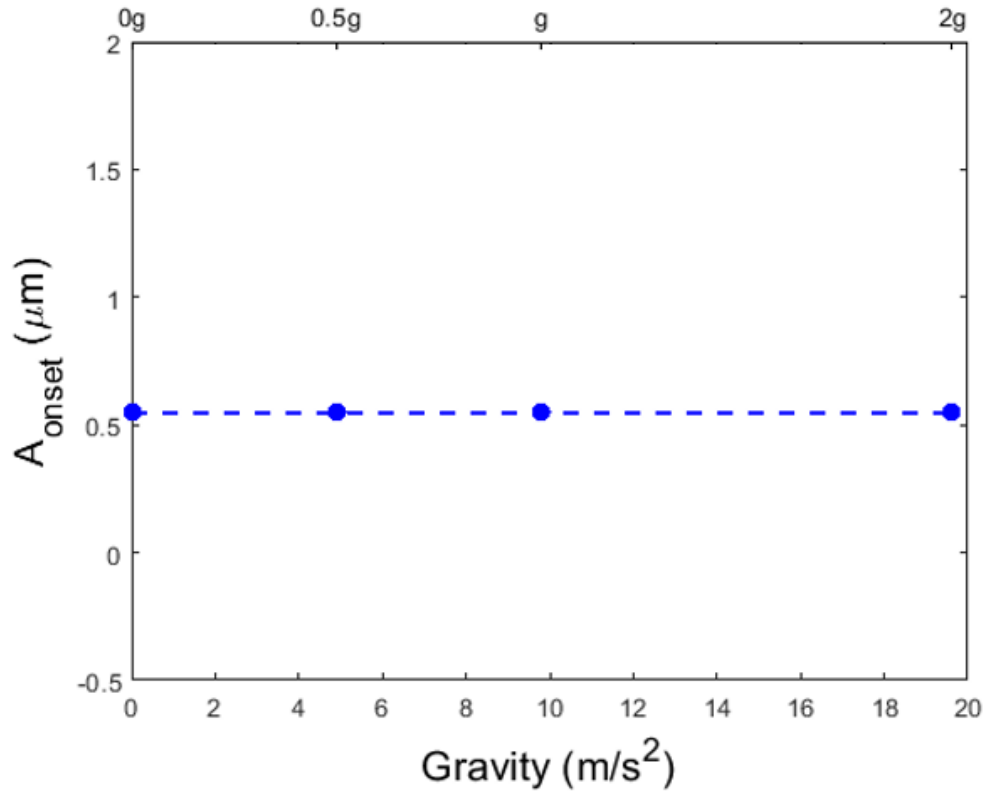


Figure 145. The effect of gravity on onset amplitude for atomization at 1.7 MHz frequency and 50λ liquid height.

Table 32. Non-dimensional numbers for different values of gravity.

Gravity (× g)	Re = $\frac{\rho_l \sqrt{gH} H}{\mu}$	We = $\frac{\rho_l (gH^2)}{\sigma}$	Fr = $\frac{A\omega}{\sqrt{gH}}$	St = $\omega \sqrt{\frac{H}{g}}$	Oh = $\frac{\sqrt{We}}{Re}$
0	27.6	0.025	-	-	-
0.5	27.6	0.025	128.2	99778	0.0057
1	27.6	0.025	90.7	70554	0.0057
2	27.6	0.025	64.1	49889	0.0057

6.3.8 Non-Dimensional Numbers

Non-dimensional numbers are introduced in this research to reduce the number of variables that describe ultrasonic atomization. Table 33 presents the non-dimensional numbers for all the studied cases above. The data shows that other than Froude number, which is related to the amplitude, for the effect of surface tension, only Weber number changes and for the effect of viscosity, only Reynolds number changes. Since Ohnesorge number is a function of both Reynolds and Weber numbers, this number is not considered in the evaluations here. However, in order to provide a universal plot for the effect of non-dimensional numbers on the ultrasonic amplitude (i.e., Froude number), the numerical simulations have to be conducted such that only one of the non-dimensional numbers changes. Hence, additional cases are modeled at constant Weber numbers and Strouhal numbers. The results of these analysis are plotted in Figure 146 and Figure 147. These plots illustrate that at a constant Weber number, by increasing Reynolds number, the required Froude number for the atomization to occur decreases. Similarly, at a constant Strouhal number, Froude number decreases as Reynolds number increases. These plots show the onset conditions for atomization to occur. Therefore, the area below each graph depicts the condition that ultrasonic atomization can arise. In another word, to have ultrasonic atomization at a specific Reynolds number, there is a critical Froude number. In addition to the critical Froude numbers, Figure 148 and Figure 149 show the critical $\frac{A}{H}$ that is required for ultrasonic atomization. The only difference is that for Figure 149 at constant Strouhal numbers, contrary to Froude number, $\frac{A}{H}$ decreases as the Strouhal number increases, confirming that by increasing the non-dimensional frequency (Strouhal number), the required amplitude for atomization decreases.

Table 33. Non-dimensional numbers for different thermophysical properties of liquid and frequencies.

Controlling parameter		Non-dimensional numbers				
		Re	We	Fr	St	Oh
Frequency (kHz)	50	938.5	2.74	6.43	6722	0.0018
	500	93.8	0.127	28.1	31203	0.0038
	1000	46.9	0.05	53.46	49532	0.0048
	1500	31.3	0.029	80.35	64905	0.0055
	1700	27.6	0.025	90.7	70554	0.0057
	2000	23.5	0.02	96.43	78627	0.006
Liquid height (\times λ_{th})	3	0.41	8.97×10^{-5}	205.6	17282	0.023
	30	12.83	0.0089	117	54650	0.007
	50	27.6	0.0249	90.7	70554	0.0057
	100	78.1	0.0997	65.7	99778	0.004
	200	220.8	0.3986	47.6	141108	0.0029
Surface tension (\times σ_{base})	0.5	27.6	0.0498	104.3	70554	0.008
	1	27.6	0.0249	90.7	70554	0.0057
	2	27.6	0.01246	81.6	70554	0.004
	4	27.6	0.006	74.8	70554	0.0029
Viscosity (\times μ_{base})	0.5	55.2	0.0249	81.6	70554	0.0029
	1	27.6	0.0249	90.7	70554	0.0057
	2	13.8	0.0249	108.8	70554	0.0114
	4	6.9	0.0249	145	70554	0.0229
Density (\times ρ_{base})	0.5	13.8	0.01246	95	70554	0.008
	1	27.6	0.0249	90.7	70554	0.0057
	2	55.2	0.0498	81.6	70554	0.004
	4	110.4	0.0997	79	70554	0.0029

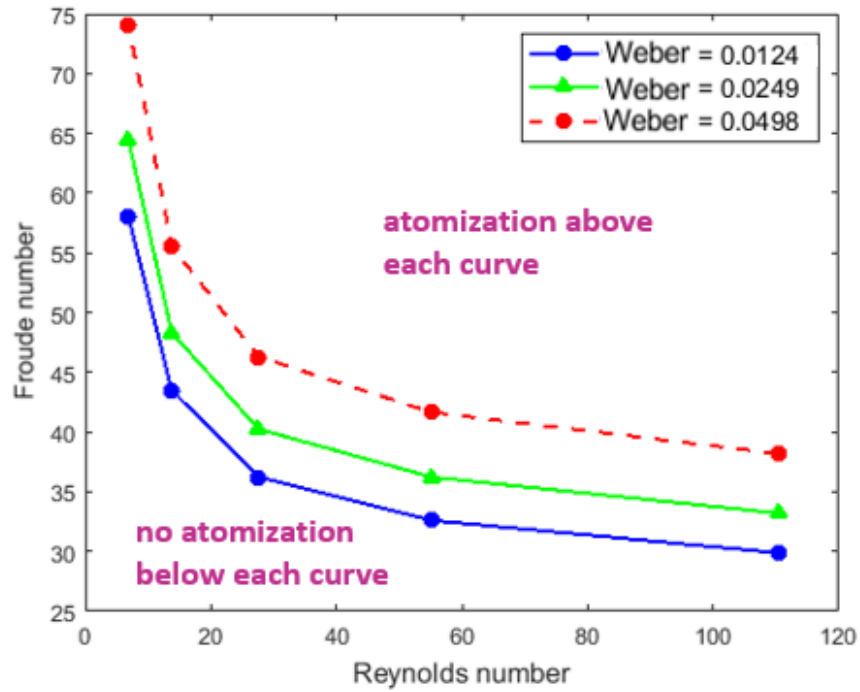


Figure 146. Critical Froude number for atomization as a function of Reynolds number at different Weber numbers. Strouhal number for all cases is 20751.

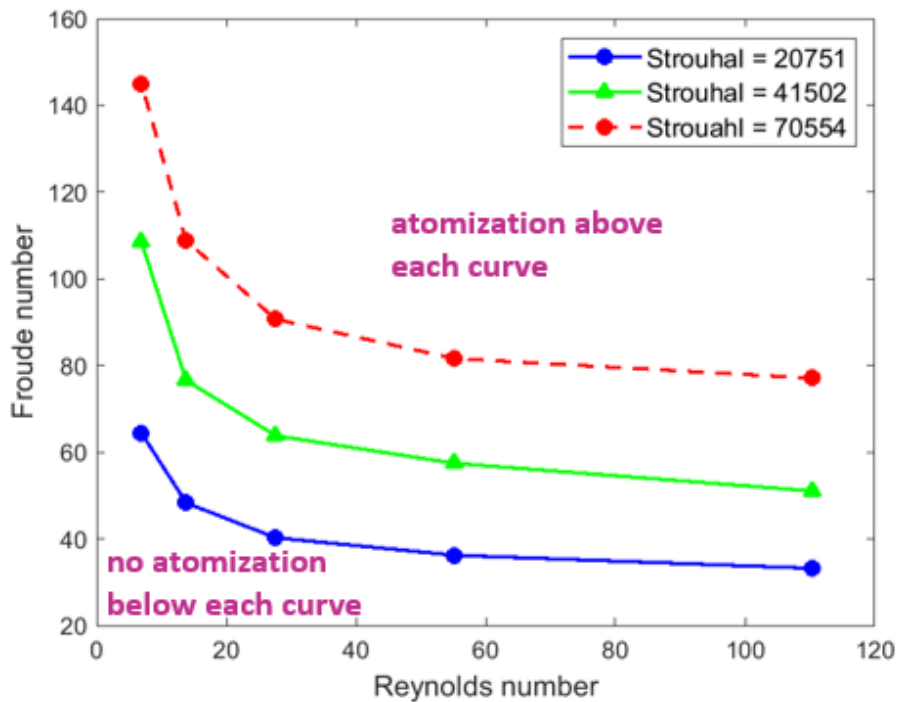


Figure 147. Critical Froude number for atomization as a function of Reynolds number at different Strouhal numbers. Weber number for all cases is 0.0249.

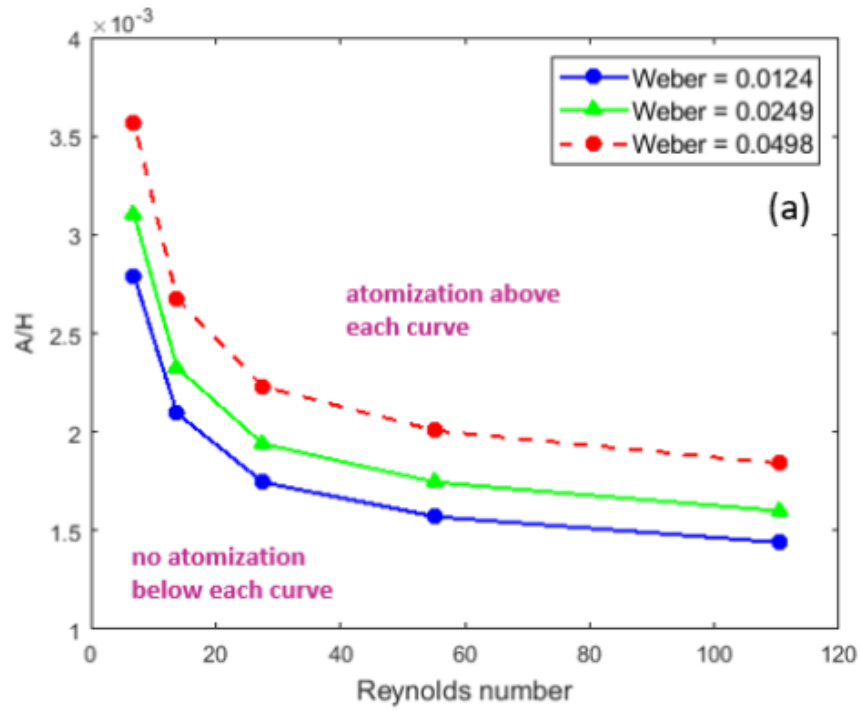


Figure 148. Critical $\frac{A}{H}$ for atomization as a function of Reynolds number at different Weber numbers. Strouhal number for all cases is 20751.

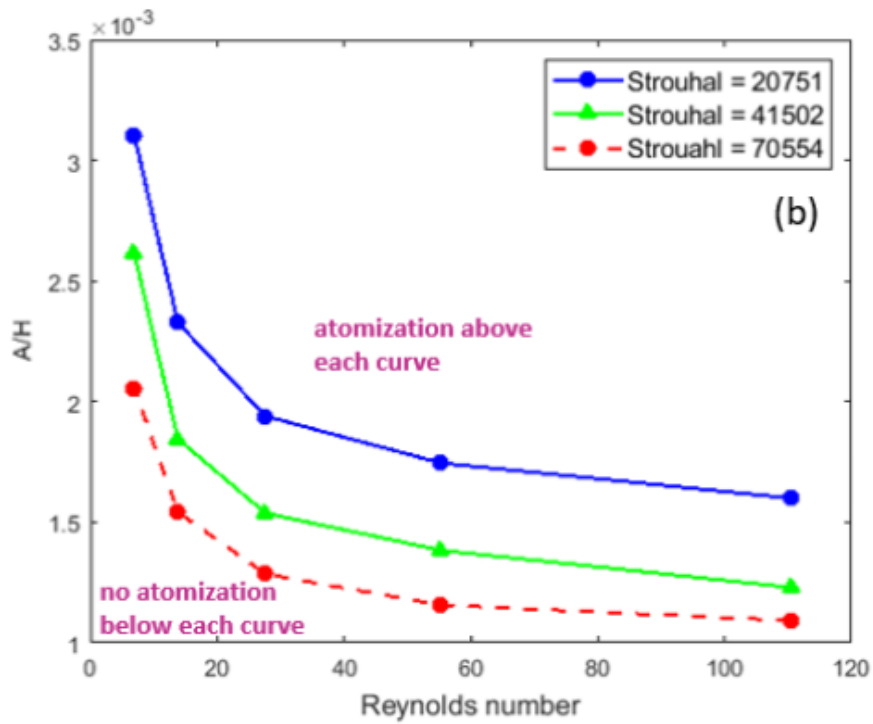


Figure 149. Critical $\frac{A}{H}$ for atomization as a function of Reynolds number at different Strouhal numbers. Weber number for all cases is 0.0249.

The physical meaning behind the above plots is that in order to have ultrasonic atomization, the applied amplitude/energy has to overcome the gravitational, viscous, and surface tension forces. The significance of these plots is that they can assist in designing and optimizing ultrasonic atomizers. To confirm the advantage of the non-dimensional curves, water, cow's milk, and sunflower oil are chosen and the non-dimensional numbers are calculated for them. In these calculations, the frequency is assumed to be 1.7 MHz and the liquid height is 50λ and therefore, the Strouhal number is the same for all the liquids. The properties of the cow's milk are taken from [133] and the properties of sunflower oil are from [134 and 135]. Table 33 summarizes the related calculations. By finding the corresponding Reynolds and Weber numbers for each liquid on the graphs, it can be confirmed that the non-dimensional amplitude required for atomizing cow's milk ($\sim 2.1 \times 10^{-3}$) is higher than water ($\sim 1.3 \times 10^{-3}$). For the case of sunflower oil, Reynolds number is smaller than the range of the numbers reported in the above figures. But it can be estimated that the non-dimensional amplitude for sunflower oil can be close to 3.5×10^{-3} . Figure 150 shows the non-dimensional amplitudes required for atomization for the studied liquids.

Table 34. Non-dimensional numbers for water, cow's milk, and sunflower oil.

Liquid	Re	We	St
Water	27.6	0.0279	70554
Cow's milk	6.6	0.0357	70554
Sunflower oil	0.56	0.049	70554

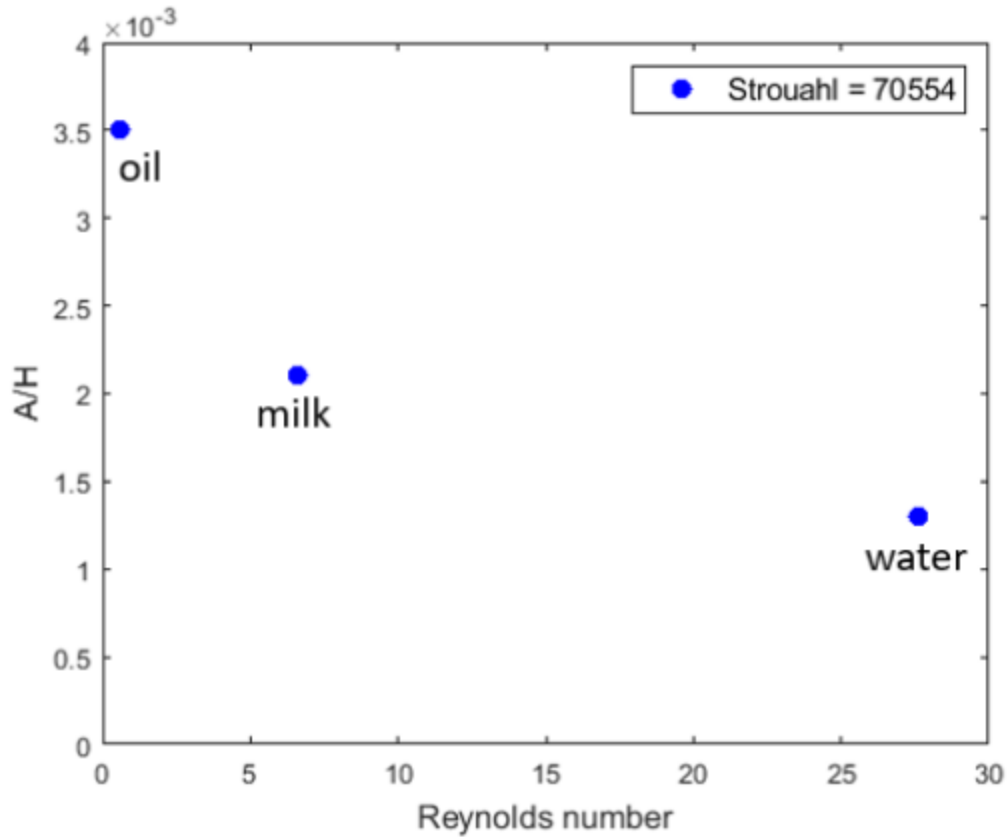


Figure 150. The estimated non-dimensional numbers for the liquids specified in Table 34.

6.3.9 Capillary Wavelength in Ultrasonic Atomization

The capillary wavelengths are measured by the peak-to-peak distance of the developed free surface waves. Figure 151 shows the schematic of the peak-to-peak measurements.

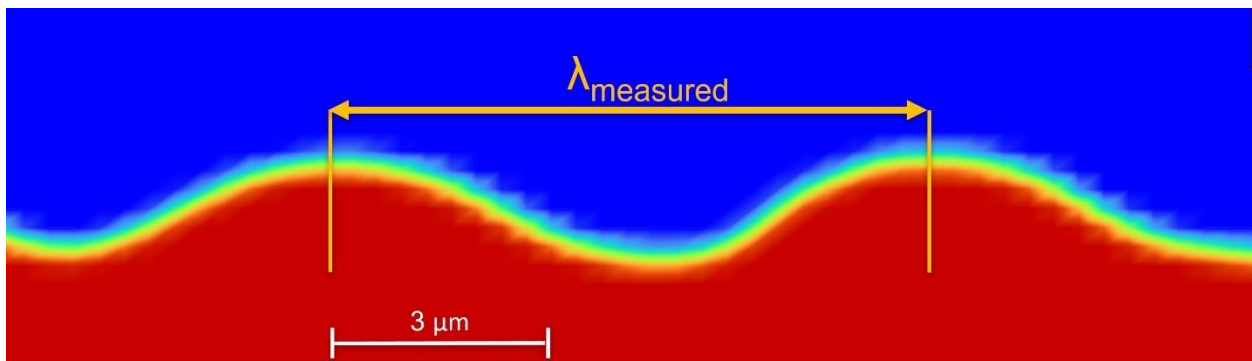


Figure 151. Peak-to-peak measurements for $\lambda_{\text{measured}}$ from simulations for $2A_{\text{th}}$ amplitude, 50λ liquid height and 1.7 MHz frequency.

Figure 152 summarizes the results of the measured surface waves versus the capillary wavelengths calculated by equation (1-2). The interesting results is that the measured and calculated values are exactly the same. This finding declares that the assumption for the frequency of the surface capillary waves being half of the excitation frequency is valid in the range of the parameters studied in this research (50 kHz – 2 MHz frequency). The maximum error in measuring the capillary wavelength in the simulations is 2.81% which could be related to the accuracy of the measurements. This finding is another validation for the accuracy of the numerical simulations reported in this research.

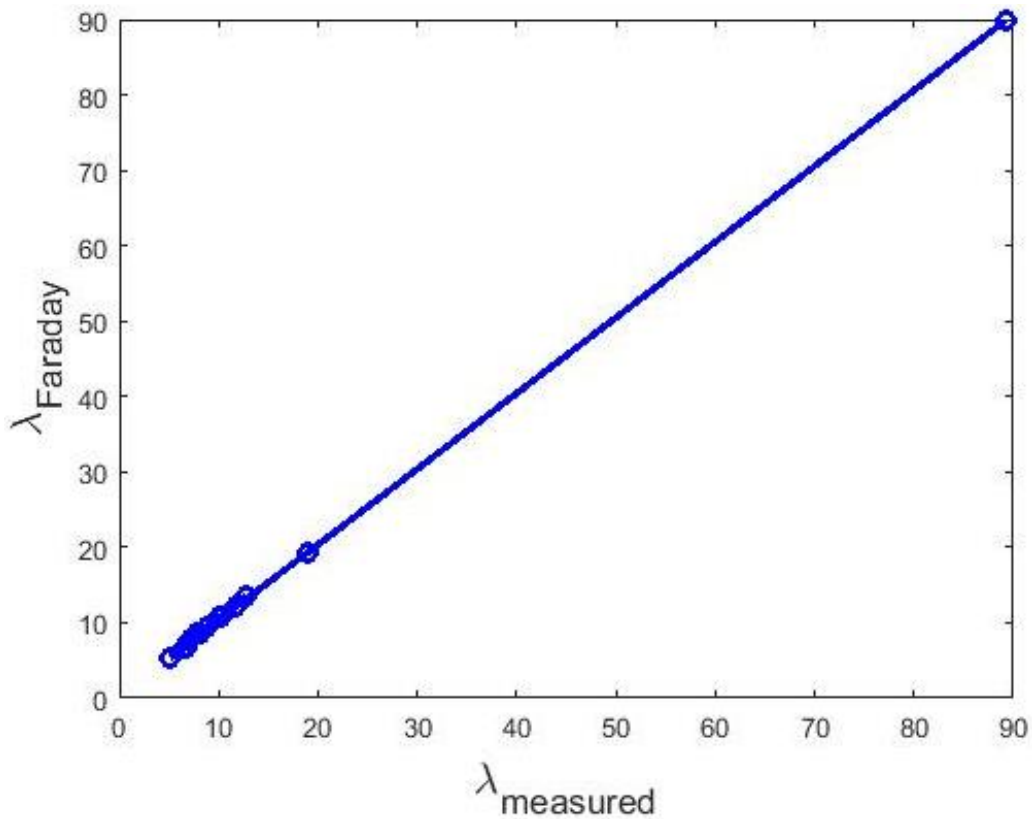


Figure 152. Measured vs calculated (equation (1-2)) capillary wavelengths.

6.3.10 Droplet Size in Ultrasonic Atomization

The droplet sizes are measured using the available features in Fluent and using ImageJ software. The results are summarized in

Table 35 along with the calculated droplet sizes using equation (1-3) from Lang [73]. Since the measurements in ImageJ are semi-automatic, it appears that the results of measurements using ImageJ are more accurate and hence, these results are used in further analysis.

Table 35. Comparing the measured droplet sizes with Lang model [73] for various parameters.

Controlling parameter		Droplet size (μm)		
		Measured		Lang model
		Fluent	ImageJ	
Frequency (kHz)	50	21.5	21.41	30.54
	500	5.85	4.976	6.58
	1000	3.39	3.122	4.14
	1500	2.36	2.654	3.16
	1700	1.85	2.241	2.91
	2000	1.77	1.735	2.61
Liquid height ($\times \lambda_{th}$)	3	-	1.895	2.91
	30	-	2.13	2.91
	50	-	2.241	2.91
	100	-	2.3	2.91
	200	-	2.401	2.91
Surface tension ($\times \sigma_{base}$)	0.5	1.61	2.187	2.31
	1	1.85	2.241	2.91
	2	1.88	3.01	3.67
	4	1.92	3.5	4.62
Viscosity ($\times \mu_{base}$)	0.5	-	2.139	2.91
	1	-	2.241	2.91
	2	-	2.3	2.91
	4	-	2.318	2.91
Density ($\times \rho_{base}$)	0.5	2.31	2.41	3.67
	1	1.85	2.241	2.91
	2	1.77	2.02	2.31
	4	1.68	1.961	1.83

Table 36 extends the results of the measurements by ImageJ and represents the standard deviation (SD), minimum and maximum droplet sizes for various operating conditions. The small values of standard deviations confirm the monodispersity of the produced droplets.

Table 36. Measured droplet sizes and their distributions using ImageJ.

Controlling parameter		Droplet size from ImageJ (μm)			
		Mean	SD	Min	Max
Frequency (kHz)	50	21.41	5.277	14.969	36.534
	500	4.976	0.928	3.893	8.36
	1000	3.122	0.776	1.945	5.886
	1500	2.654	0.612	1.868	4.832
	1700	2.241	0.468	1.644	3.365
	2000	1.735	0.319	1.16	2.689
Liquid height (\times λ_{th})	3	1.895	0.38	1.353	3.241
	30	2.13	0.39	0.971	2.564
	50	2.241	0.468	1.644	3.365
	100	2.3	0.332	1.52	3.34
	200	2.401	0.436	1.378	3.495
Surface tension (\times σ_{base})	0.5	2.187	0.433	1.471	3.673
	1	2.241	0.468	1.644	3.365
	2	3.01	0.677	1.395	3.978
	4	3.5	0.563	1.82	4.945
Viscosity (\times μ_{base})	0.5	2.139	0.395	1.605	3.73
	1	2.241	0.468	1.644	3.365
	2	2.3	0.472	1.529	4.128
	4	2.318	0.336	1.66	3.048
Density (\times ρ_{base})	0.5	2.41	0.577	1.725	3.366
	1	2.241	0.468	1.644	3.365
	2	2.02	0.513	1.383	4.031
	4	1.961	0.507	1.274	4.518

Comparing the measured droplet sizes from the simulation with the droplet sizes calculated by Lang model, it is clear that Lang model predicted the droplet sizes larger than the measured droplet sizes. One possible reason for this is that the simulations are in 2D which the droplet sizes could be slightly different from 3D. Lang model is developed for low frequency ultrasound and therefore, it may not be able to predict the droplet size in high frequency ultrasound, accurately. In addition, Lang [73] measured the droplet size by cooling the molten wax droplets and solidifying them. The solidification and the volume expansion associated with that also could be another reason for higher droplet size predicted by Lang model. Another possible reason for this difference is that as it was mentioned above, a good portion of the generated droplets have secondary breakups and it is important to consider the final average droplet size, which is the case in this study. Furthermore, the droplet size distribution is strongly dependent on the frequency. It also significantly depends on the thermophysical properties of the liquid including the surface tension, viscosity, and density. In addition, the height of the liquid film slightly changes the droplet size and distribution. Obviously, as it was mentioned before, not all these effects are considered in Lang model. Hence, by applying the non-dimensional numbers in this study, a correlation for describing the droplet size as a function of all the controlling parameters is developed. This correlation with $R^2 = 0.924$ is given as follows

$$D = \left(\frac{\pi\sigma}{\rho_l f^2} \right)^{0.333} [0.5 + 0.001 \times Fr^{0.15} We^{0.22} St^{0.1} Re^{-0.12}] \quad (6-28)$$

The range of the variables in this correlation includes $f = 50 \text{ kHz} - 2 \text{ MHz}$, $\sigma = 0.036 - 0.288 \text{ N/m}$, $\rho_l = 499 - 3992 \text{ kg/m}^3$, $\mu = 0.0005 - 0.004 \text{ kg/m/s}$, and $H = 256 - 1712 \text{ }\mu\text{m}$, which corresponds to $Fr = 28 - 145$, $We = 0.006 - 0.398$, $St = 31203 - 141108$, and $Re = 6.9 - 220$. The first term in the above correlation is representative of the ultrasonic atomization based on capillary phenomena and the second term is the representative of the dependency of the droplet size on thermophysical properties of the liquid. The positive sign of the power for Weber number shows the dependency of the droplet size on surface tension for the range of the studied parameters ($We \ll 1$). The negative sign of the power for Reynolds number implies that the droplet size increases by viscosity. The positive signs of the power for Froude number and Strouhal number are attributed to the simultaneous dependency of the droplet size on the amplitude, frequency, and liquid height. Comparison between the measured droplet size and the predicted droplet size is represented in

Figure 153. Figure 154 and Figure 155 show the non-dimensional droplet size (D/λ) as a function of Reynolds number for the non-dimensional numbers plotted in Figure 146 and Figure 147, respectively.

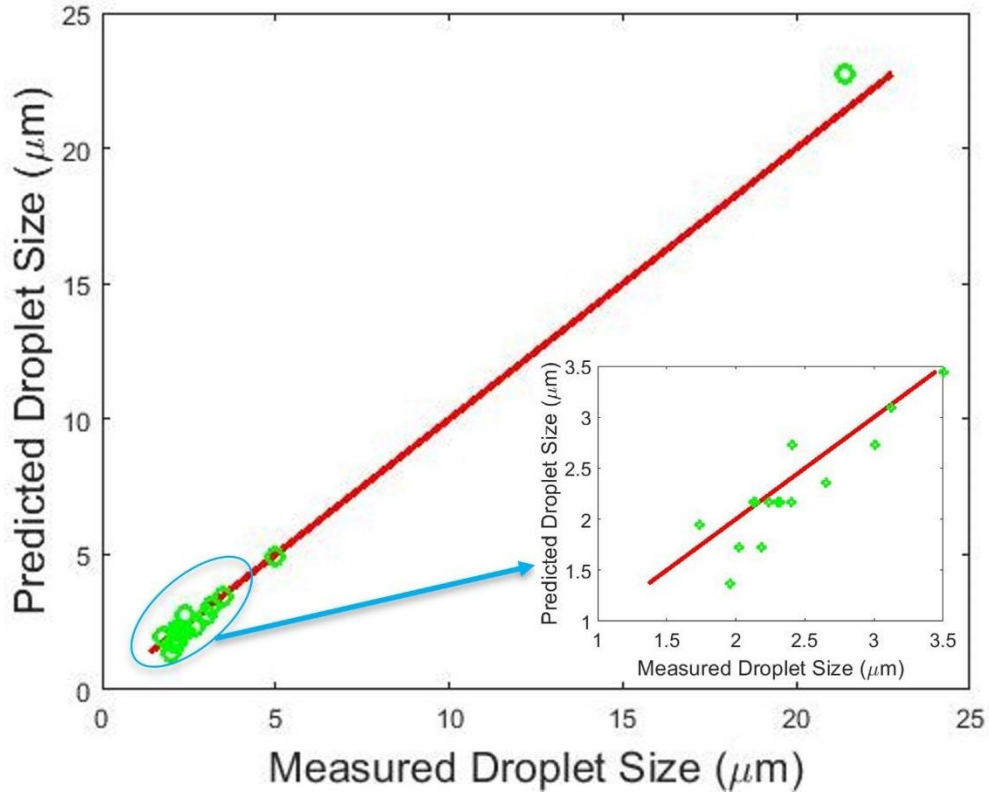


Figure 153. Comparison between the measured droplet size vs the predicted droplet size.

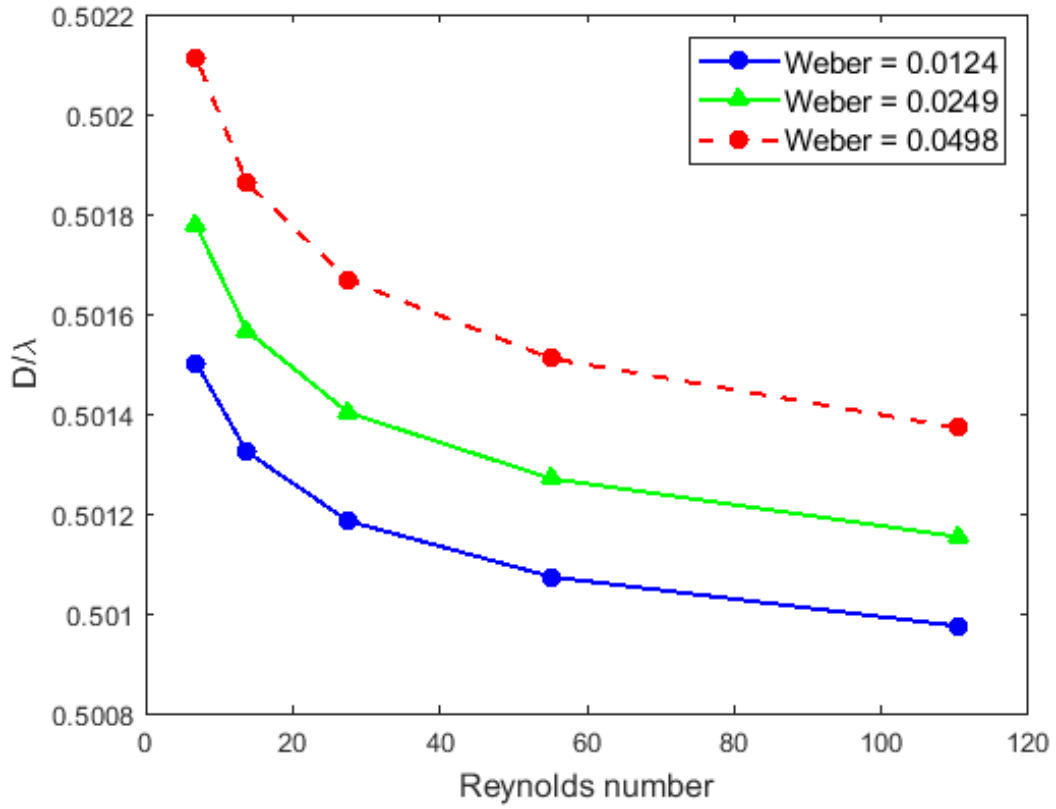


Figure 154. Non-dimensional droplet size as a function of Reynolds number at different Weber numbers. Strouhal number for all cases is 20751.

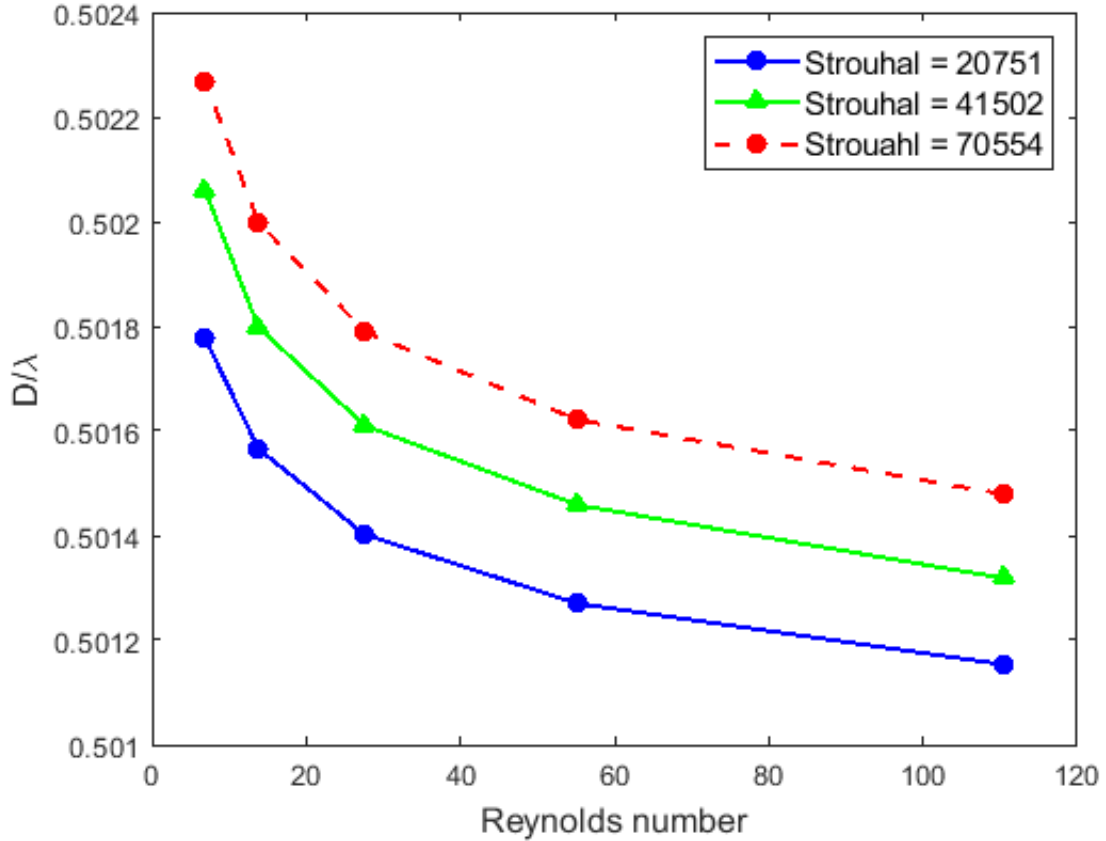


Figure 155. Non-dimensional droplet size as a function of Reynolds number at different Strouhal numbers. Weber number for all cases is 0.0249.

In the above calculations and measurements of the droplet sizes, a size average of about 150 droplets is used. Therefore, some of the droplets were generated in the previous time steps and some of the droplets were being produced at the targeted time steps. Therefore, the range of the droplet sizes and the standard deviation for some of the measurements is relatively large. Another way for the measurements, is looking at different time steps and at each time step only consider the size of the droplets at the inception point. This avoids the inclusion of droplet collision and generation of secondary droplets in estimating the mean droplet size. Using these analysis, the correlation provided in equation (6-28) for predicting the droplet size can be modified as

$$D = \left(\frac{\pi\sigma}{\rho_l f^2} \right)^{0.333} \left[0.52 + 0.086 \times \left(\frac{A}{H} \right)^{-0.75} We^{0.8} St^{0.054} Re^{-1.546} \right] \quad (6-28)$$

This new correlation is based on $\frac{A}{H}$ instead of Froude number and the R^2 for this correlation is 0.93. The range of the variables is the same as the correlation in equation (6-28) and $\frac{A}{H}$ is in the range of 0.00034 – 0.0119.

It should be noted that the reported plots for the effect of various properties on the droplet size in the previous sections, are based on this method of measuring the droplet size.

Figure 156 compares the predicted droplet sizes from equation (6-28) with the droplet sizes calculated by Lang model. This figure shows that Lang model predicted the droplet sizes larger than the droplet sizes observed in this study. One possible reason for this is that the simulations are in 2D and therefore, the analysis does not directly represent a 3D droplet configuration. However, Lang [73] measured the droplet size by cooling the molten wax droplets and solidifying them. The solidification and the volume expansion associated with that could be one reason for higher droplet size predicted by Lang model. It should be noted that the deviation from Lang model increases as the wavelength increases.

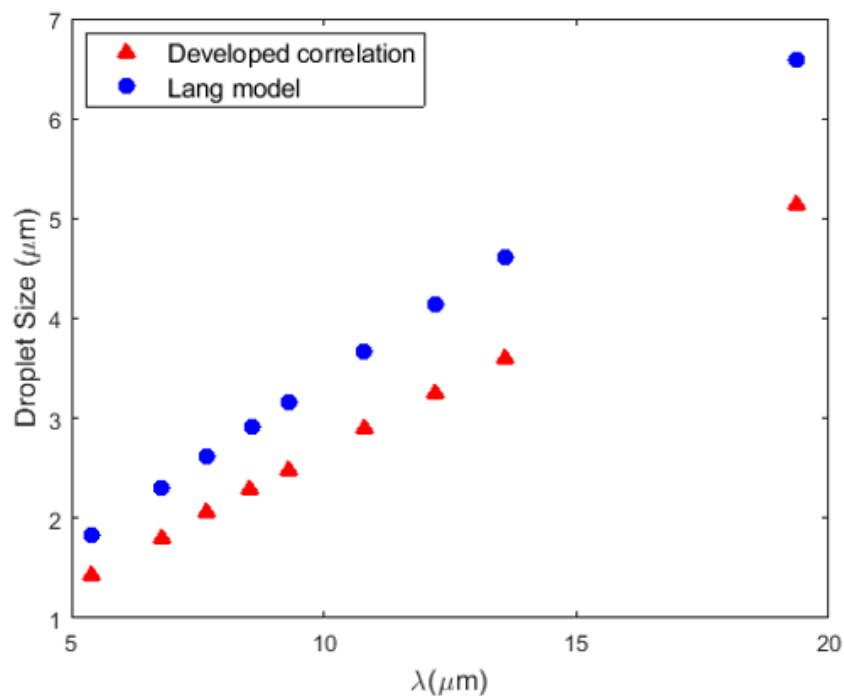


Figure 156. Comparing the predictions from equation (6-28) developed from the numerical simulations and the calculated droplet sizes from Lang model.

Figure 157 and Figure 158 show the non-dimensional droplet size (D/λ), calculated by equation (6-29), as a function of Reynolds number for the non-dimensional numbers plotted in Figure 146 and Figure 147, respectively. These plots show that at a constant Weber number or a constant Strouhal number, by increasing Reynolds number, the non-dimensional droplet size decreases. These plots can assist in predicting the droplet size in ultrasonic atomizers.

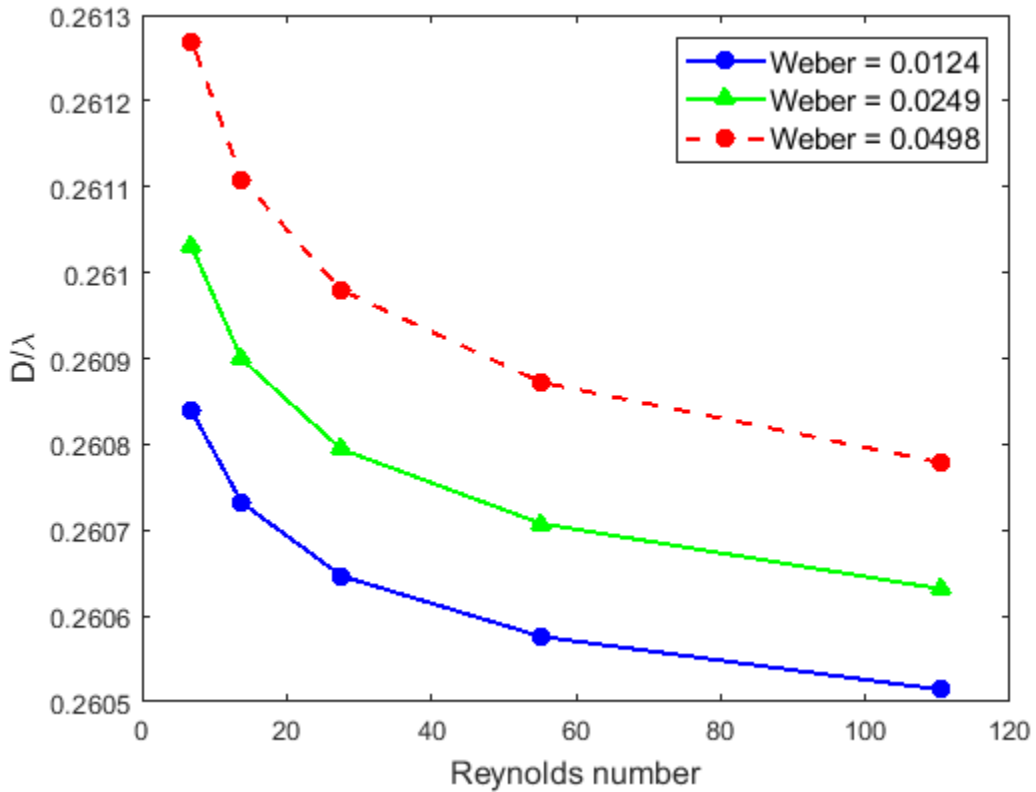


Figure 157. Non-dimensional droplet size as a function of Reynolds number at different Weber numbers. Strouhal number for all cases is 20751.

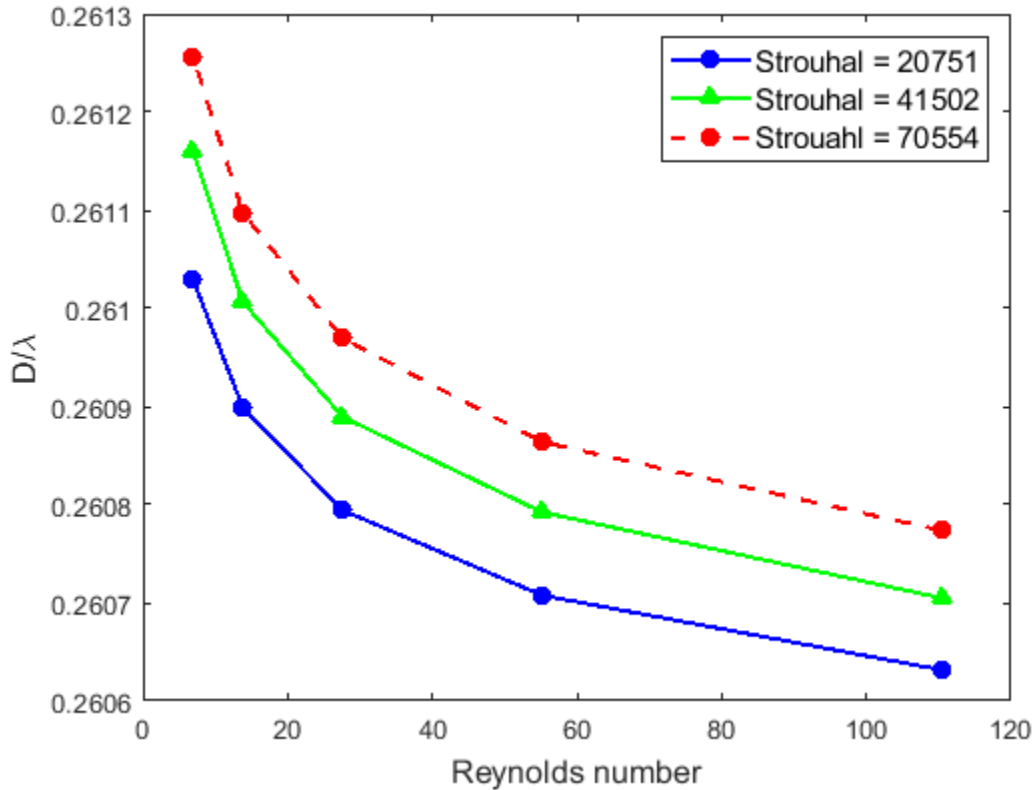


Figure 158. Non-dimensional droplet size as a function of Reynolds number at different Strouhal numbers. Weber number for all cases is 0.0249.

It should be noted that the droplet size analysis is limited in terms of applications since the numerical simulations are conducted in 2D.

6.3.11 Ultrasonic Atomization of a Water Droplet

To extend the numerical simulations, ultrasonic atomization of a water droplet sitting on a vertically vibrating flat plate instead of a liquid thin film is studied. The radius of the droplet is 4.7 mm. The governing equations are the same as described in section 6.1 and the boundary conditions and dimensions are illustrated in Figure 159. For simplicity, the fluid motion and the interface shape are symmetrical with respect to the vertical axis. A sinusoidal acceleration-oscillation with 0.55 μm amplitude at 1.7 MHz frequency is applied to the vibrating plate. One of the challenges in numerical simulation of droplets is the use of proper contact angle. In this study, the contact angle of the gas-liquid interface with the horizontal plate is assumed to be constant and it is considered to be 84° similar to Suzuki and Mitsubishi [136]. At the start of the simulation, a water

droplet with the shape of $1/8^{\text{th}}$ sphere is placed on the plate. Figure 160 shows the volume fraction of water after $26.10 \mu\text{s}$. The significant difference between the simulation of a water droplet and a liquid film is that the droplet ejection starts from the edges of the water droplet in contact with the vibrating wall since the minimum thickness of the liquid is at this area.

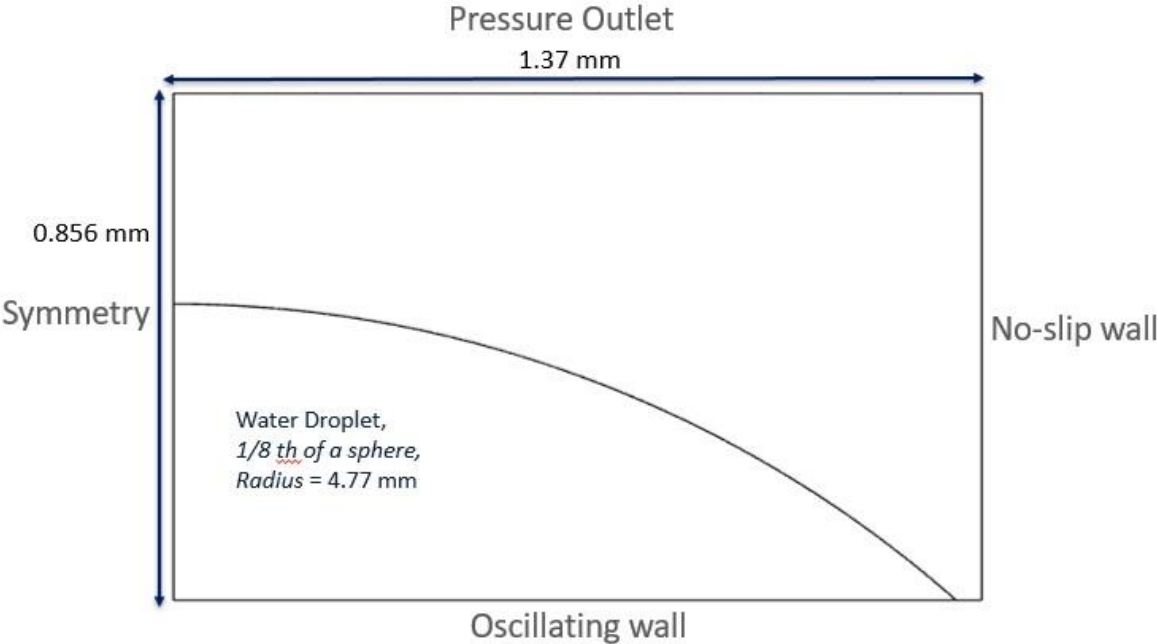


Figure 159. 2D schematic of the problem in numerical simulation for direct-contact ultrasonic atomization of a water droplet sitting on a vibrating wall (not to scale).

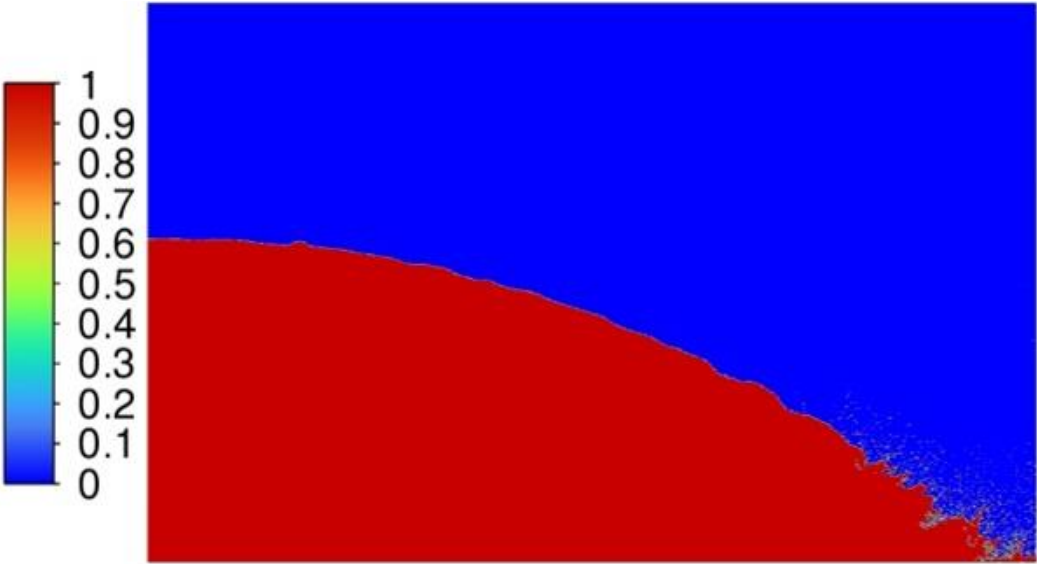


Figure 160. Volume fraction of water at $26.10 \mu\text{s}$.

6.3.12 Airborne Ultrasonic Atomization

In the previous sections, the mechanism, and fundamentals of ultrasonic atomization for a direct-contact ultrasound setup was discussed in great details. However, there is a lack of understanding and knowledge for the mechanism of ultrasonic atomization and droplet formation in an airborne ultrasound setup and there is no information that can be found in the literature. This is mostly due to the complex hydrodynamic nature of ultrasonic atomization. Airborne ultrasonic atomization is relatively new compared to direct-contact ultrasonic atomization. In addition, equation (6-21) for the onset of capillary waves only applies for direct-contact ultrasonic atomization and this is necessary to explore the impact of fluid properties and ultrasound characteristics on onset amplitude for atomization in airborne ultrasound. As it was mentioned above, experimentally investigating the surface waves and the droplet characteristics requires very high resolution and high-speed cameras and laser diffraction devices. CFD is an alternative tool for characterizing the ultrasonic atomization phenomenon. The behavior of oscillatory flow could be further complicated if more than one fluid is present (e.g., water-air two phase flow). Hence, by applying the developed 2D CFD model in section 6.1, the process of airborne ultrasonic atomization of liquid water and the droplet formation are studied. The described numerical modeling strategy allows for better visualization and understanding of the oscillatory two-phase flow than experiment alone.

In this section, the same governing equations as described in section 6.1 are applied. Figure 161 represents the 2D schematic of the problem.

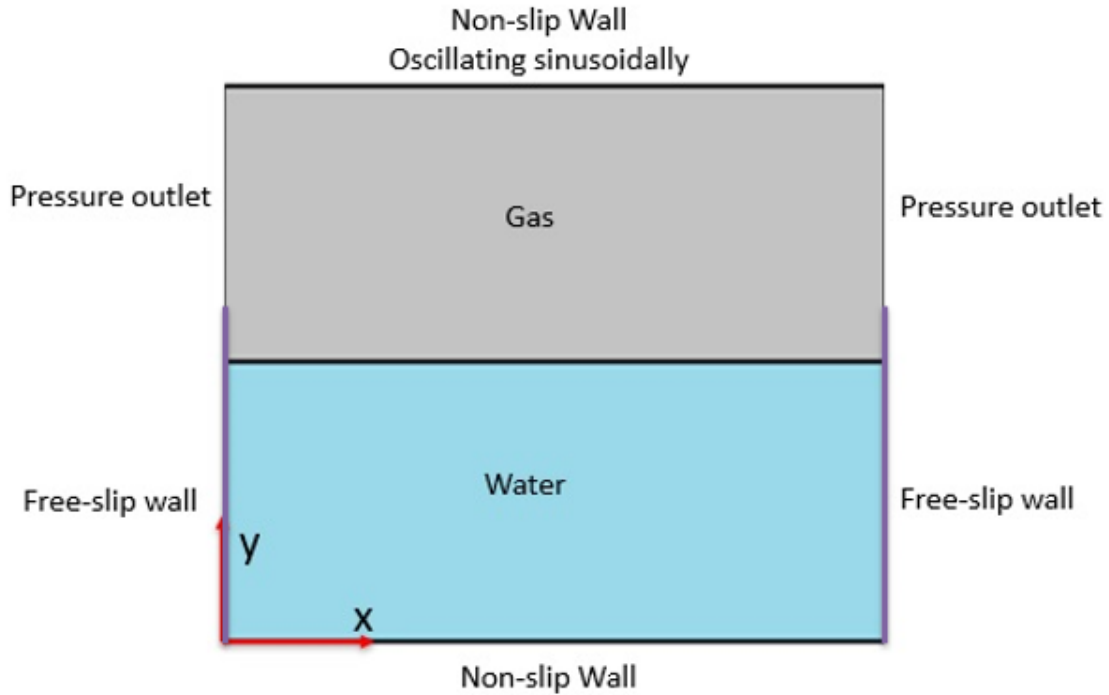


Figure 161. 2D schematic of the problem in numerical simulation for non-contact ultrasonic atomization (not to scale).

In this case, the upper boundary is oscillating sinusoidally by applying dynamic mesh. Dynamic mesh means that the computational mesh is not the same but can change during computation. The lower boundary is a non-slip wall. The liquid layer covers the lower wall, and the ultrasonic waves propagate to the interface of liquid/gas through air. The lateral boundary conditions, adjacent to the liquid, are free-slip walls and the parts adjacent to the air are pressure outlets. The lateral walls adjacent to the liquid are taller than the interface of gas/liquid, otherwise the liquid overflows to the outlet boundaries. The same assumptions as previous sections are applied to this 2D numerical model. Flow is laminar, and both liquid and air are considered to be Newtonian and incompressible.

To explore the differences between the mechanisms of direct-contact and airborne ultrasonic atomization, one case of non-contact ultrasonic atomization at 21 kHz frequency is discussed in detail. Table 37 shows the geometrical parameters related to this case.

Table 37. Geometrical dimension for the base case studied for airborne ultrasonic atomization at 21 kHz frequency.

Parameter	Dimension
Domain horizontal length	8 mm
Domain vertical width	2.48 mm
Liquid height	0.48 mm
Lateral wall	0.96 mm
Distance between the oscillating wall and gas/liquid interface	2 mm

Figure 162 shows the contours of absolute pressure in the domain at 0 , $\tau/4$, $\tau/2$, $3\tau/4$, and τ for the first oscillating period in the simulation at this amplitude. The applied amplitude for this case is $75 \mu\text{m}$. Initially, the pressure is zero at the beginning of the simulation ($t = 0$). With the oscillations of the upper wall, the pressure inside the domain increases and has a peak at $\tau/4$ (compression cycle). After the peak, the pressure decreases. At $\tau/2$, the maximum pressure is at the oscillating wall and as the distance increases, the pressure decreases, resulting in contours of pressure in the domain. At this time, the expansion cycle initiates. At $3\tau/4$, the expansion is at maximum and at τ , the expansion cycle ends, leading to minimum pressure at the oscillating wall and increase of pressure as the distance from the wall increases. These compression and expansion cycles can be observed more clearly in Figure 163. In this figure, to have a better comparison of the changes in pressure at different time steps, the contours of absolute pressure are plotted with the same colormap.

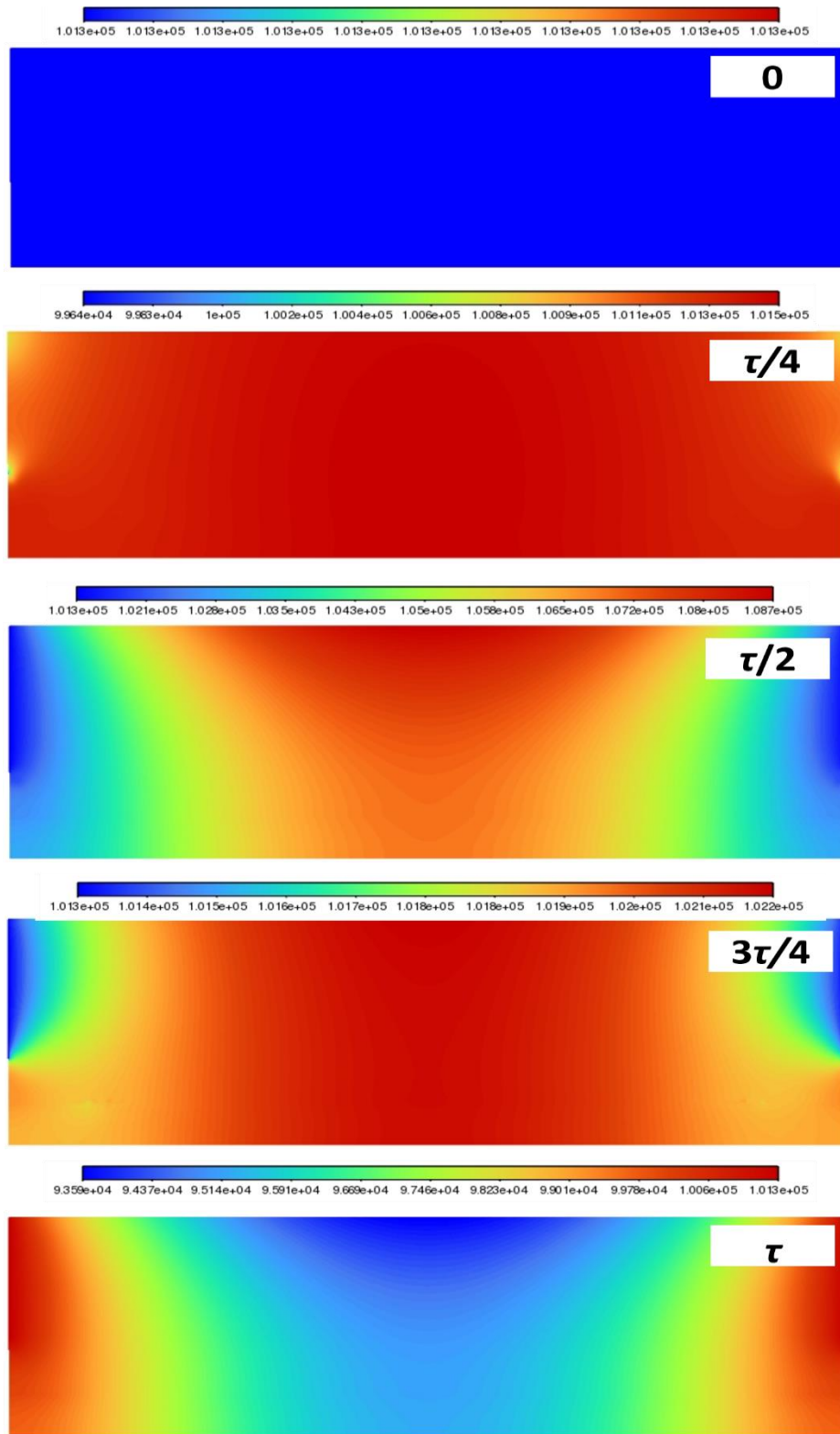


Figure 162. Contours of absolute pressure (Pa) in the domain at different oscillation periods (for 75 μm amplitude and 21 kHz frequency).

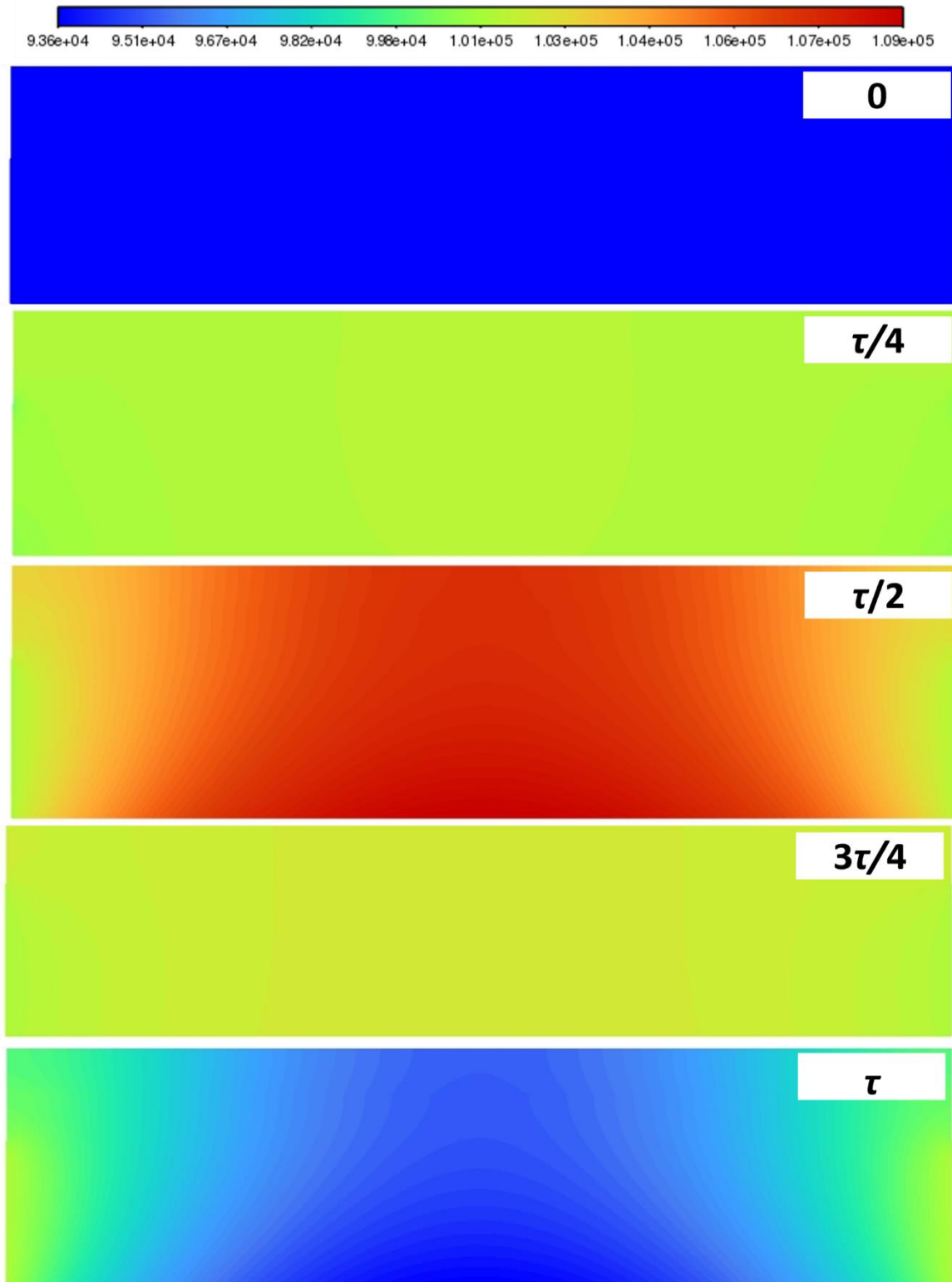


Figure 163. Contours of absolute pressure (Pa) in the domain at different oscillation periods (for 75 μm amplitude and 21 kHz frequency).

The contours in Figure 163 show the pressure oscillation in the horizontal direction in the liquid layer and confirm sinusoidal behavior of the pressure in the simulations.

The changes in volume fraction of water at different time steps and the contours of velocity are shown in Figure 164 and Figure 165, respectively. For the case of airborne, the mechanism of ultrasonic atomization and the propagation of ultrasonic waves in the liquid/gas interface is different from the case of direct-contact ultrasonic atomization. The ultrasonic waves start from the upper wall and travel through the air to reach to the interface and then reflect back to the air. This reflection of the waves from the interface is due to the impedance mismatch between water and air. The density (ρ) of liquid water (998.2 kg/m^3) is three orders of magnitudes higher than the density of air (1.225 kg/m^3) and the speed of sound (c) in water (1480 m/s) is 4.47 times higher compared to that in air (331 m/s). Therefore, there is a significant difference between the impedance in water ($1477336 \text{ kg/m}^2/\text{s}$) and in air ($405.475 \text{ kg/m}^2/\text{s}$). This impedance mismatch is the factor that determines the efficiency of airborne ultrasonic atomization, and it is responsible for the fact that higher amplitudes are required for atomization in an airborne setup compared to that in a direct-contact setup. Figure 165 shows that the instabilities at the interface initiate from the walls of the domain. Since the fluid is considered to be incompressible, the compression and expansion cycles of the moving wall at the top result in compressing the air out of the domain and sucking the air into the domain, respectively. From Figure 165, it appears that the motion of air generates some vortices in the outlets and in the contact points with the lateral walls of the domain. The vortices induced by air flow in and out of the domain disturb the liquid interface. On the other hand, the reflection of the waves from the interface results in vortices in the air domain. These vortices push the water upward in the vicinity of the walls and push it downward in the middle and make peaks at the interface. This results in thinning of the liquid film in the center of the domain. As these vortices get stronger by time and push the water upward more, the peaks at the interface become larger until the tip of the peaks is very thin. At this point, the upward motion of the peaks overcomes the surface tension forces and leads to necking and eventually breaking up of the peaks. This airborne ultrasonic atomization highly depends on the exciting amplitude. At low amplitudes, the ultrasonic waves may create motion at the interface however, the generated vortices are not strong enough to cause atomization. On the other hand, at amplitudes higher than the critical amplitude, the vortices are stronger and can push the water away from the walls. In this case, the

ultrasonic atomization occurs earlier and faster. For example, Figure 166 represents the changes in volume fraction of water and the movements of the interface for a similar case but at $100\ \mu\text{m}$ amplitude. Figure 167 shows the changes in the contours of velocity in the domain. Comparing Figure 167 with Figure 165 reveals that the velocity magnitude is higher for $100\ \mu\text{m}$ amplitude compared to that of $75\ \mu\text{m}$ amplitude. Figure 168 shows the velocity vectors of the vortices and the direction of flow at 4.75 ms, 5 ms, and 5.25 ms. These velocity vectors show how the compression and expansion cycles result in change in the direction of the velocity in the domain and hence, induces vortices imposed on the interface that make the instabilities leading to atomization and droplet formation.

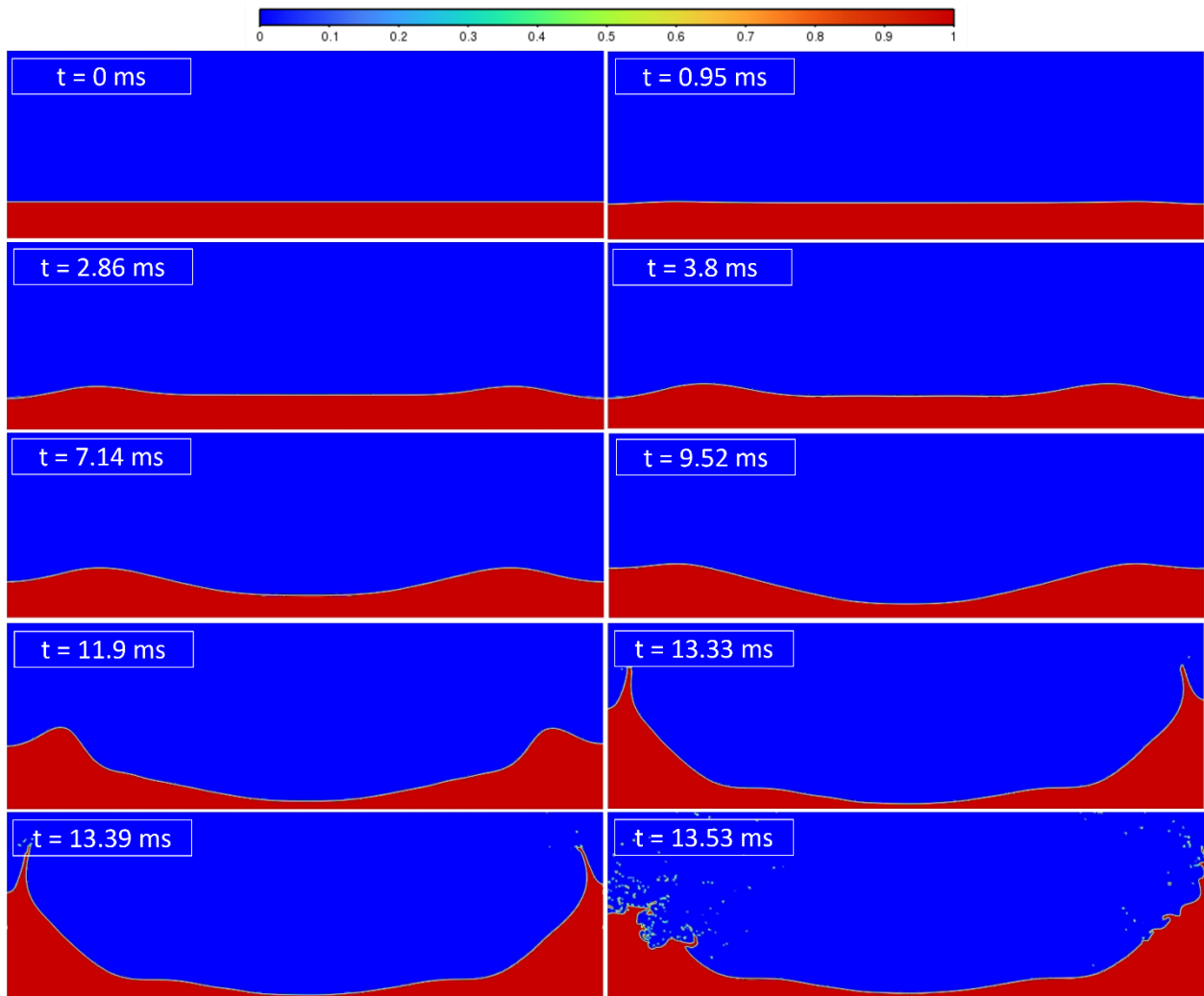


Figure 164. Volume fraction of water for the case of $75\ \mu\text{m}$ amplitude, 3λ liquid height and 21 kHz frequency (airborne).

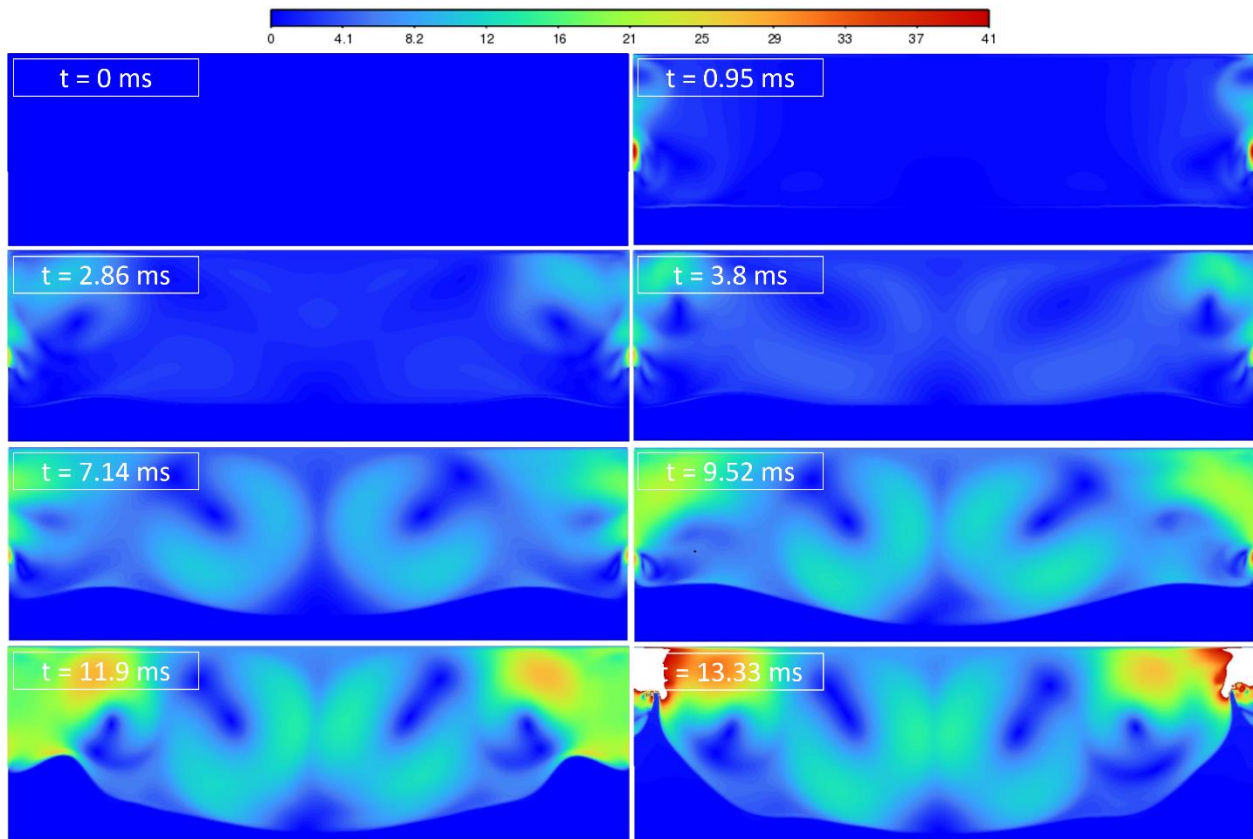


Figure 165. Contours of velocity (m/s) for the case of 75 μm amplitude, 3λ liquid height and 21 kHz frequency (airborne). At 13.33 ms, the velocity at the upper corners of the domain is higher than 41 m/s.

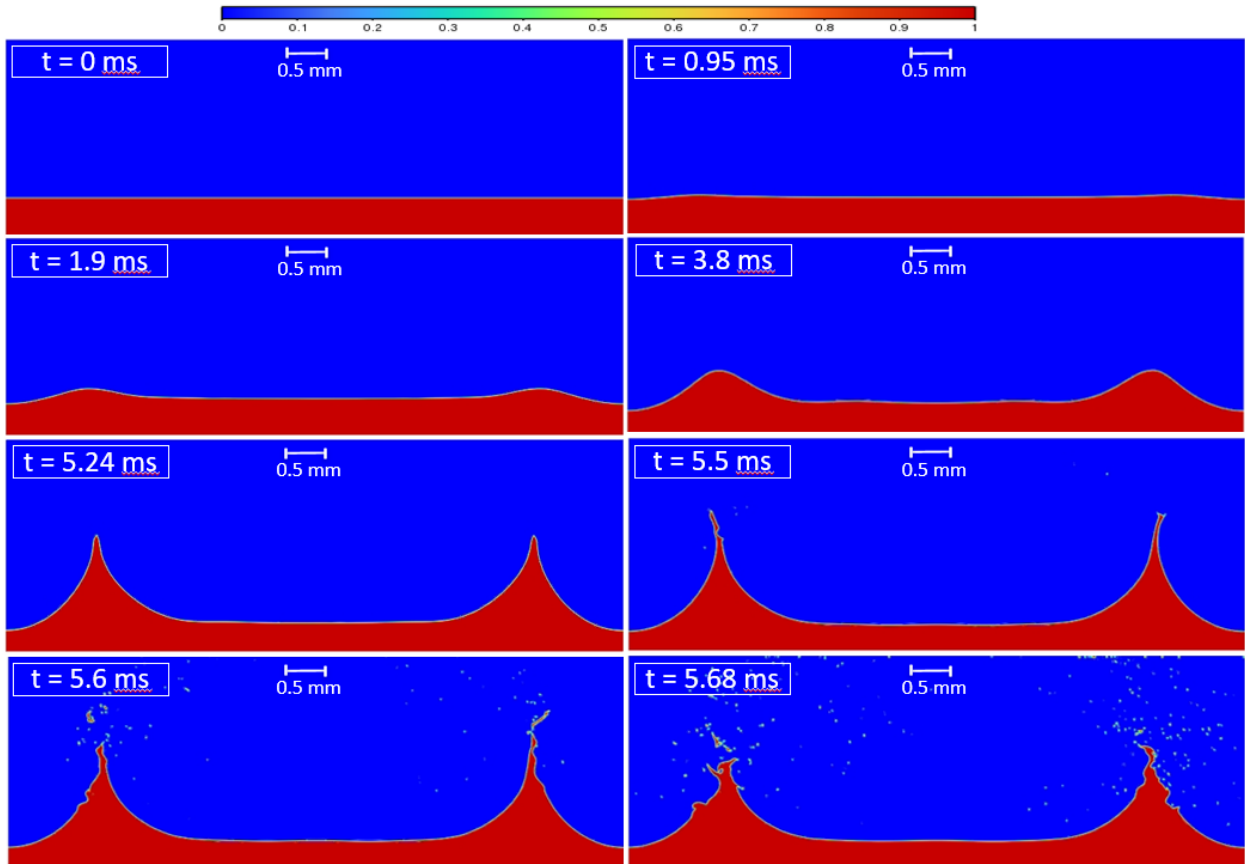


Figure 166. Volume fraction of water for the case of $100\ \mu\text{m}$ amplitude, 3λ liquid height and 21 kHz frequency (airborne).

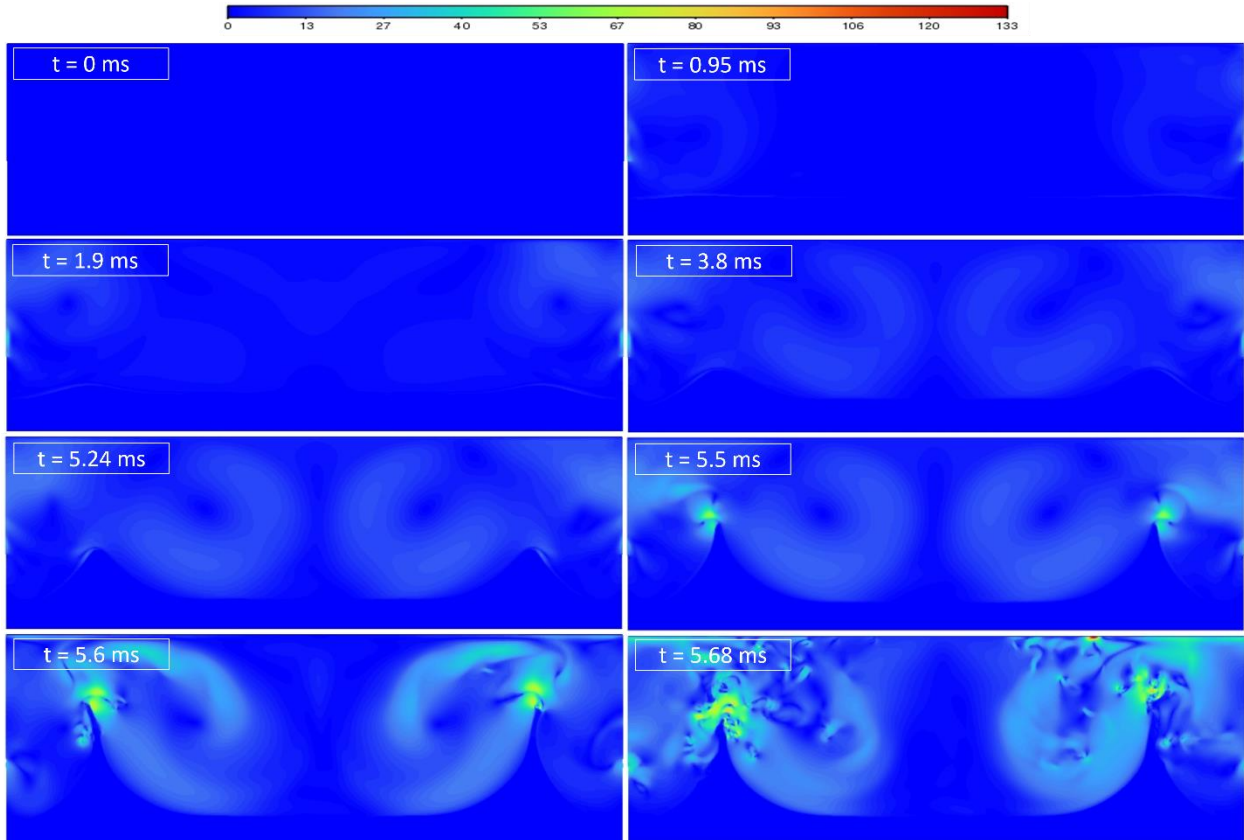


Figure 167. Contours of velocity (m/s) for the case of $100\ \mu\text{m}$ amplitude, 3λ liquid height and 21 kHz frequency (airborne).

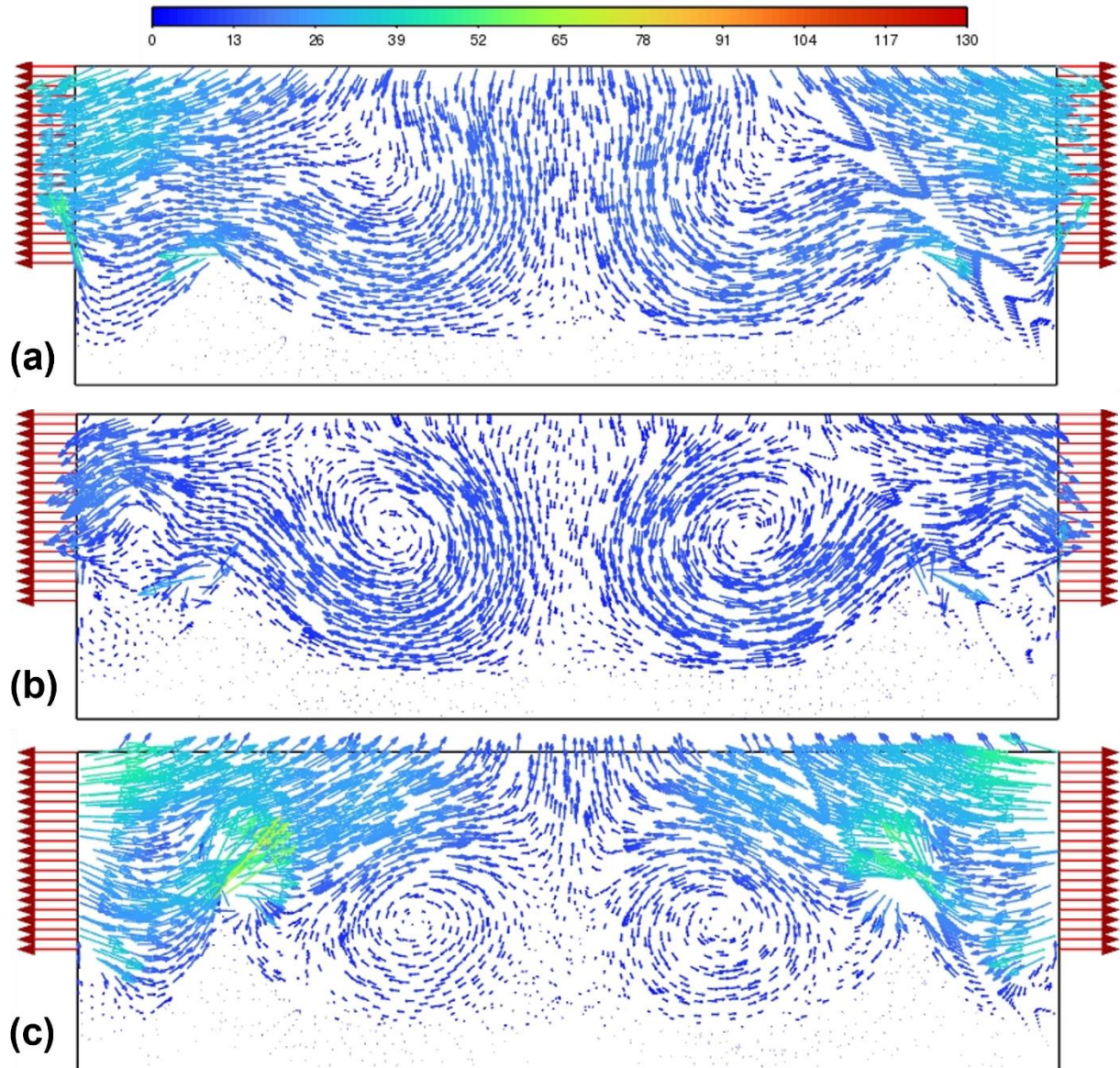


Figure 168. Velocity vectors (m/s) at: (a) 4.75 ms, (b) 5 ms, and (c) 5.25 ms for the case of 100 μm amplitude, 3λ liquid height and 21 kHz frequency (airborne).

It should be noted that the geometry used in the simulations for airborne ultrasonic atomization is different than the experimental setup described in chapter 5. In the experimental setup, the ultrasonic vibrations from the piezoelectric transducer are transferred to the plate. The vibrations then get distributed on the surface of the plate. The plate used in the experiments in chapter 5 have 12 nodal lines. Therefore, the resonant frequency of the plate itself is different than the transducer. In addition, the sample underneath the transducer plate receives the waves that are a sum of all the

generated waves from different nodal lines (Fourier transform). However, in the numerical simulations, the waves that are propagating from the upper wall are uniform sinusoidal waves.

6.4 Summary and Conclusions

In this study, the importance of controlling parameters and thermophysical properties of liquid on ultrasonic atomization over a wide range of parameters and frequencies (50 kHz – 2 MHz) was explored. Multiphase CFD simulations were conducted to further understand the atomization process. The liquid inside the container experienced vertical vibration from the bottom wall that propagates waves on the stationary surface of the liquid. At a high enough amplitude, the applied ultrasonic vibrations disturbed the surface of the liquid film and generated waves that are called capillary surface waves. The energy to disturb the liquid interface needs to be higher than the surface tension, viscous, and gravitational forces. The unstable surface waves, which are responsible for the droplet formation, were visualized by the multiphase CFD simulations. As the applied amplitude increases, at a critical amplitude, ultrasonic atomization begins by forming ligaments at the interface and eventually breakups to form droplets. It appeared that the mechanism and dynamics of atomization is similar for high and low frequencies. In addition to the droplets' collisions, another observation was that the ejected droplets showed a secondary breakup which could be due to their high inertial energies to form multiple droplets. The results confirmed that the onset atomization amplitude depends on the liquid height, surface tension, viscosity, density as well as the frequency of the vibrations. Increasing surface tension, density, and frequency decreased the onset atomization amplitude, whereas increasing liquid height and viscosity increased the onset atomization amplitude. The importance of the effect of viscosity is higher than surface tension (μ vs $\sigma^{1/3}$). Therefore, by selecting a proper surfactant to modulate surface tension it is possible to decrease the energy required for ultrasonic atomization and to increase the energy efficiency. Using non-dimensional numbers, the minimum Froude number for ultrasonic atomization at different values of Reynolds number, Weber number, and Strouhal number were provided. Furthermore, a correlation for predicting the droplet size as a function of thermophysical properties of liquid and controlling parameters was provided. The number of droplets increased, and the droplet size decreased with increasing the vibration frequency. The qualitative effect of different parameters on onset atomization amplitude and resultant droplet size agreed with the experimental data in the literature. In addition, the peak-to-peak measurements of the wavelengths

for the capillary waves showed that the frequency of the capillary waves at the surface of liquid film is half the exciting frequency. This matches with the experimental observations in the literature and thus, is another validation for the accuracy of the proposed numerical model. Furthermore, this numerical model was employed to study the mechanism of airborne ultrasonic atomization, which is different than the direct-contact ultrasonic atomization. In an airborne setup, the ultrasonic waves propagate through air to reach to the interface. The compression and expansion cycles of the ultrasonic waves induce vortices in the air above the interface and result in disturbing the interface. These disturbances, at a sufficiently high imposed amplitude, lead to atomization and ejection of droplets from the interface. The proposed numerical model has great potentials in investigating atomization under different conditions. Some of the other applications will be discussed in chapter 7 (recommendations).

Chapter 7: Summary and Recommendations

7.1 Summary

In this dissertation, the conducted research covered five subjects as follow,

- 1- Numerical study of removal of water trapped between fibers in paper drying;
- 2- Numerical study of removal of water trapped inside a single cellulose fiber;
- 3- Experimental study of drying of paper with direct-contact ultrasound mechanism;
- 4- Experimental study of drying of paper with airborne ultrasound mechanism;
- 5- Numerical study of the onset of ultrasonic atomization of a liquid film and resultant droplet size (direct-contact and airborne).

In chapters 2 and 3, the removal of water at the intermediate stage of paper drying was studied, numerically. Specifically, the water was trapped in between fibers and inside a single micro-scale fiber. The properties of the fibers are associated with the cellulosic fibers. Two separate multiphysics and multiphase numerical models were developed and the impact of geometrical characteristics of the fibers, physical properties of the liquid, the applied heat flux, and the velocity and temperature of air on drying rate were investigated. These two chapters provide fundamental understanding of removal of water in the microscale in paper drying. One of the takes aways from these two chapters is the effect of instabilities induced by Marangoni flows on enhancement of drying rate. Other possibilities for increasing the drying rate at the intermediate stage of drying curve include increasing the applied heat flux on the outer surface of the fiber or increasing the inlet air temperature and impinging jet air velocity. The results showed that for removal of water trapped between the fibers or the water trapped inside a fiber, fibers with larger diameter, length, and thickness dry slower as the total volume of liquid increases in these cases. Additionally, increasing the thickness of the fiber wall, reduces the heat transfer rate and thus, the fiber dries slower. The outcome of these simulations provides remarkable insights on the fundamentals of the effective factors on removal of water during the intermediate stage of drying curve.

Chapters 4 and 5 systematically explored the potentials of direct-contact and airborne (non-contact) ultrasonic drying. ANOVA analysis was used to investigate the impact of different

controlling factors on ultrasonic drying, both direct-contact and airborne. Both mechanisms showed that basis weight/thickness of the sample has the maximum effect on the total time of ultrasonic drying and it is followed by the effect of initial moisture content and refining condition. Comparison of the microscopic images and air permeability measurements for different samples revealed that the sheet formation and pore characteristics of the paper samples have significant impacts on the drying behavior. Softwood fibers dry faster compared to that of hardwood fibers and unrefined fibers dry faster than refined fibers, due to higher permeabilities of air in softwood and unrefined paper samples. By increasing the basis weight and hence, the thickness of the sample, the air permeability decreases, resulting in a longer path for water removal from the pores. Furthermore, two correlations for predicting the total time of ultrasonic drying and area under the drying curve were provided. Ultrasonic drying is a green and sustainable technology and can guide the industry toward electrification of their processes. The prominent outcome of this research is that ultrasonic drying is most efficient, in terms of drying rate and energy factor, at higher moisture contents. This conclusion can help industry to develop ultrasonic assisted drying technologies. For example, ultrasonic drying can be installed in the upstream of the dryer section, when the moisture content is high and as the moisture content decreases, another technology can be employed. This technology can also be applied in the beginning of the dryer for the purpose of making the moisture content to be uniform in the cross section (C-D) of the paper. Ultrasonic drying/dehydration is either a low heat drying process in the case of direct-contact or a negligible thermal heating for airborne ultrasonic drying and hence, this technology not only assists in improving the efficiency of the process, but also improves the product quality, such as whiteness index and tensile strength. Direct-contact ultrasonic drying is applicable for a batch process, while airborne ultrasonic drying is suitable for a continuous drying process. The drying rate for direct-contact ultrasonic drying is an order of magnitude higher than the drying rate in airborne mechanism. This is mostly due to the impedance mismatch between the media in airborne ultrasonic drying. Nevertheless, the energy efficiency of drying for both the transducers employed in this study for direct-contact and airborne ultrasonic drying were the same. The outcome of these studies will help in the design and retrofitting of ultrasonic drying in various processes.

In chapter 6, a sophisticated numerical model was developed to fundamentally understand the physics behind ultrasonic atomization. The related mechanism for propagation of ultrasonic waves

inside the liquid, generation of the instabilities at the interface, and ejection of the droplets were observed by implementing numerical simulations. The onset amplitude for ultrasonic atomization was determined for different thermophysical properties of liquid and operating conditions. The results showed that to reduce the onset atomization amplitude, one can increase surface tension or reduce viscosity, density, and liquid height. Furthermore, increasing the exciting frequency reduces the onset amplitude for atomization and thus, the required electrical power for atomizing the liquid film decreases. The critical non-dimensional numbers for atomization were also obtained and a unique map for onset of ultrasonic atomization was provided. The numerical simulations revealed details that are difficult to capture in the experiments including secondary droplets formation and collision of the droplets. It appeared that the mechanism and dynamics of atomization is similar for high and low frequencies. Additionally, the effect of different parameters on the droplet size was studied. These results provide the essential conditions in controlling the droplet size. A correlation for predicting the droplet size as a function of non-dimensional numbers was provided. The measured frequency of the surface waves in the simulations was half of the exciting frequency which agrees with the literature. This multiphase numerical model for the first time provided fundamental insights on ultrasonic atomization at a wide range of parameters.

7.2 Recommendations

The removal of water at the final stages of drying is numerically studied in this research. The experimental validation of this numerical simulation requires high resolution and high-temperature microscopes. If there is an accessibility of the high-resolution equipment at micro-scale, the experimental validation is recommended. In addition, the numerical model for free water removal is available in the literature, however numerical study of bound water removal is more challenging and not available as continuum does not apply in nano-scale. It is recommended to develop a numerical model for this case. Another recommendation would be to combine the numerical model developed in this research with the model for free water removal.

For direct-contact ultrasonic drying, there are a few recommendations. Firstly, the measurements of the energy consumption by the power amplifier revealed that the actual power consumed by the power amplifier is 400 W more than the applied power to the transducer (10 W). This is due to the fact that the commercial power amplifiers are designed to cover a wide range of powers and

frequencies and therefore, there are lots of energy loss in the internal components of the power amplifier. Hence, it is recommended to design and build power amplifiers with a narrower range of frequencies and powers regarding the transducers used in this study in order to increase the energy efficiency of the setup itself. Secondly, the size of the samples used in the direct-contact ultrasonic drying had almost the same size as the transducer (19.8 mm in diameter) to cover the surface of the transducer. To be able to conduct the experiments for a larger sample, it could be recommended to connect several transducers. These transducers can be connected in series or parallel and their performance could be compared to each other.

For airborne ultrasonic drying, study of the impact of different shapes and hole sizes of the mesh sample holder on ultrasonic drying is recommended. The ultrasonic wavelength at 21 kHz frequency is about 17 mm and the size of the holes for the mesh sample holder used in this research was about 5 mm. It may be worthwhile to answer to the question of what if the hole sizes are larger than the ultrasonic wavelength and to explore the impact of that on the drying rate and efficiency. Furthermore, in-situ measurements of the changes in pore sizes and volumes during drying could help in understanding the impact of pore characteristics on ultrasonic drying behavior. In conducting the experiments, a few ideas have come up that could be applied to make the experimental testing fixture more robust. The first recommendation is to design an automatic arm that is connected to the transducer from the top in a way that it can move intermittently. In the experiments conducted in this research, the weight of the sample was measured at intermittent of about 2 min. The challenge was that if the scale was placed under the sample, the ultrasonic pressure would have caused the weight to change artificially and consequently, the weight had to be measured intermittently instead of continuously. This was done by removing the sample from under the transducer, quickly measure the weight and put it back on the sample holder. Considering the possible impact of this method of measurement on the evaporation, the automatic arm could be a smart way to remove the transducer away, measure the weight and bring back the transducer to the original location for the purpose of reducing the “wasted” time, enhancing the consistency in measurements, and automating the procedure. Another improvement for the experimental testing fixture could be to rebuild the setup with stronger and heavier aluminum rails or build the setup on a benchtop to minimize the influence of external vibrations on the experiments. Moreover, the design of airborne ultrasonic transducers is a hot topic since there is an urge to improve the

impedance mismatch between the transducer plate and air and also between air and the sample. In my opinion, one reason is that there is a knowledge/communication gap between the engineers who design and build the transducers and the engineers who use the transducers to develop technologies. In addition, the requirements, the needs, and the limitations of the technology development must be communicated and considered in the design. Hence, one recommendation would be to bring a group of multidisciplinary scientists and engineers (physics, electronics, mechanical, and materials backgrounds) to collaborate on building the next generation of the transducers. Combining ultrasonic drying, especially airborne mechanism, with other drying technologies including hot air drying is highly recommended as the results of this research confirms that ultrasonic drying is more efficient at higher moisture contents and the efficiency of drying decreases as the sample gets dried. Combining this technology with other drying technologies and optimizing the efficiency of drying using machine learning and artificial intelligence algorithms can be applied in development of the next generation of smart dryers. On the other hand, since the experiments in this research are conducted stationary, the application of ultrasonic transducers for a moving belt setup could be explored as the future direction of this research. The effect of the hot air temperature, hot air velocity, and speed of the belt can be investigated. This will be beneficial for further optimization of the drying process. In addition, the ultrasonic drying, both direct-contact and airborne, could be applied for drying products other than paper hand-sheets for instance cookies, vegetables, fruits, and other porous media. The results of drying rates for both direct-contact and non-contact ultrasonic drying could also be used as source terms or fluxes at the boundary conditions in development of numerical models for drying. Another aspect of ultrasonic drying that worth exploring is its application in space (both reduced gravity and high gravity). In space applications, this is very necessary to remove the water from food waste and human waste to be able to reuse this water. Ultrasound technology could have great potentials in this regard.

For numerical simulation of ultrasonic atomization, the developed model has great potentials for modeling various scenarios, and it is recommended to extend the application of the numerical model to:

- Study of the ultrasonic atomization behavior for different liquids, for example oil, milk, alcohol, etc.

- Include the effect of ultrasonic waves on heat transfer enhancement inside the liquid and counting for evaporation
- Study the porous media drying using ultrasound mechanism, with both direct and non-contact mechanisms
- Extend the model to 3D
- Simulate spray drying
- Combine free water removal and the other numerical models for removal of water at the final stages of drying with ultrasonic drying
- Numerically simulate the atomization due to shear by applying an oscillating air pressure at the inlet boundary condition
- Study the impact of different controlling parameters and thermophysical properties of liquid on airborne ultrasonic atomization

Additionally, study of the effect of cavitation on ultrasonic atomization at high power intensities is recommended. Visualization of the ultrasonic atomization using Laser Doppler Vibrometer and PIV, measuring the diameter of the droplets and comparing the results to the results of the numerical simulations could also be another step forward for this project.

Chapter 8: Impact

With the advancements of the modern technologies, the planet Earth is heating up and the science clearly has shown that to avert the worst impacts of climate change and preserve a livable planet, global temperature needs to be controlled. For this purpose, there has been a call by the United Nation to reduce the CO₂ emissions by 45% by 2030 and reach to net zero by 2050 [137]. The industry sector is the source of 24% of greenhouse emissions in the USA and it holds one of the keys in controlling the global warming [138]. Drying is a common process for energy intensive sectors and thus, fundamental understanding of this process can assist in improving industry to reach zero carbon footprint by 2050. The expected impact of this thesis is to provide the related industry with fundamental understanding of water removal in the absence and presence of ultrasound mechanism. Fundamental understanding of the effect of different controlling parameters on drying at the final stages assist in improving the current drying technologies. In terms of energy savings, ultrasonic drying is a green and sustainable technology, and it is expected that it will have a significant impact on energy saving and reducing CO₂ emissions, globally. This technology moves the related industries toward electrification as it does not use any fossil fuels. Electrification is important in reduction of carbon footprint and thereby mitigates climate change and contributes to the mission of zero net carbon footprint by 2050. Department of Energy estimates that using novel non-thermal drying technologies, it is possible to save 0.5 quad/year energy in drying industries (1.2 quad/year). If it is assumed that the energy saving in paper drying is 0.1 quad/year, therefore, it is anticipated that energy savings by ultrasonic drying of paper is at least 1% of 0.1 quad/year. This amount of energy is equivalent to 264,550,000 kg/year reduction in CO₂ emission according to the calculator provided in [139]. Furthermore, ultrasonic drying improves the product quality as it operates at low temperatures. This technology can contribute to the design of smart dryers. In addition, ultrasonic drying could be applied to industries other than paper industry including food, waste food, chemical, and pharmaceuticals. This study can assist in the design and retrofitting of ultrasonic drying in various processes.

The impact and importance of the numerical simulation of ultrasonic atomization is in optimal design of spray atomizers/dryers. The droplet generation is known to have a variety of applications

and has continued to be an area of broad interest. For the food and paper industry, knowing the impact of the operating conditions and thermophysical properties of liquid on the ultrasonic atomization behavior and the droplet sizes, could advantage in optimizing the setup to enhance the drying efficiency. For example, the results of this research revealed that increasing frequency, surface tension, and density decreases the required input power for ultrasonic atomization. On the other hand, increasing the viscosity and the liquid height has an opposite effect. This information could help the industry to select the proper additives/surfactants and to come up with a “secret” recipe to improve the efficiency of their process and control the desired characteristics. Furthermore, ultrasonic atomization has other applications. For instance, inhalation or pulmonary is a vitally important rote for noninvasive drug delivery. The size of the aerosol particles for each application has an optimum size range which plays a significant role in the efficient and effective delivery of inhaled medications to the lung (1 to 5 μm). The results of the current research provide the basis for viable devices in pulmonary drug delivery. Other applications of ultrasonic atomization could be in coating and processing of nano-electronic structures and devices. Fundamental understanding of ultrasonic atomization provides insights for evaluating the performance and optimal design of atomizers in terms of cost and energy efficiency.

Appendix A: Kinetic Models for Ultrasonic Drying Curves

In Chapters 4 and 5, 2^3 factorial design of experiments was employed to describe the kinetics of ultrasonic drying and to come up with a correlation for predicting the total time of drying. Another method that can be applied to predict ultrasonic drying curves is using kinetic models. Table 38 represents the semi-theoretical and empirical models that are often applied to ultrasonic drying curves. Each of these models has its own model constants that are specified in the table.

Table 38. Semi-theoretical and empirical models applied to ultrasonic drying curves from Inyang et al. [140].

Model name	Model	Model parameter (s)
Lewis (Newton)	$M_r = \exp(-kt)$	k
Page	$M_r = \exp(-kt^n)$	k, n
Modified Page	$M_r = \exp(-(kt)^n)$	k, n
Midilli et al	$M_r = \exp(-kt^n) + bt$	k, n, b
Henderson and Pabis	$M_r = A \exp(-kt)$	A, k
Logarithmic	$M_r = A \exp(-kt) + c$	A, k, c
Two-term	$M_r = A \exp(-k_0t) + B \exp(-k_1t)$	A, k_0, B, k_1
Two-term exponential	$M_r = A \exp(-kt) + (1 - A) \exp(-kAt)$	A, k
Weibull	$M_r = \exp(-(\frac{t}{\beta})^\alpha)$	α, β
Gaussian	$M_r = a \exp(-(\frac{t-b}{c})^2)$	a, b, c
Wang and Singh	$M_r = 1 + at + bt^2$	a, b

In these models, M_r is the average moisture content at time t and is defined as follows

$$M_r = \frac{m_t - m_{bone-dry}}{m_0 - m_{bone-dry}} \quad (A-1)$$

where m_t is the mass at time t , $m_{bone-dry}$ is the mass of dried sample, and m_0 is the initial mass. In these analyses, the drying curves from direct-contact ultrasonic drying are used, as an example. By fitting each model to the drying curves for different softwood and hardwood samples, the model parameters are obtained. Table 39 summarizes the outcome of curve fittings and Table 40 shows the kinetic models prediction evaluation in terms of R^2 (coefficient of determination), RMSE (root mean squared error), and PE (percent error). PE can be calculated as following

$$PE(\%) = \frac{100}{n} \sum_{i=1}^n \frac{M_{r_{experiment,i}} - M_{r_{model,i}}}{M_{r_{experiment,i}}} \quad (A-2)$$

Figure 169 compares the goodness of each model prediction by using the PE values. Page model, modified page model, Midilli et al. model, and Weibull model show the minimum PE values, less than 4%. This means that the predictions from these four models are the most accurate among the model studied here.

Although the goodness evaluation of the above models shows that the model predictions are acceptable and agree with the experimental data, there are a few items that need to be pointed out. First, the R^2 and PE values for factorial design of experiments are higher compared to the kinetic models. Second, by looking at Table 39, each model has a different constant value for each sample. It may be possible to combine the effect of all the factors (i.e., moisture content, thickness, and refining condition) and come up with a correlation for the model parameters as a function of the controlling factors however, this adds to the complexity of the model and also reduces the accuracy of the predictions. Third and most importantly, the kinetic models do not consider the interactive effects of the controlling factors in their calculations. Hence, in this study, 2^3 factorial design of experiments and linear regression analysis were employed for analyzing the drying curves.

Table 39. Empirical kinetic models: calculated model parameters.

Sample	Lewis model		Page model		Modified Page model		Midilli et al. model			Henderson-Pabis model		Logarithmic model			Two-term model				Two-term exponential model		Weibull model		Gaussian model			Wang and Singh model	
	k	k	n	k	n	k	n	b	A	k	A	k	C	a	k0	b	k1	a	k	alpha	beta	a	b	c	a	b	
H-unR-100-0.3	0.9760	0.8996	1.6739	0.9388	1.6740	0.8850	1.5555	-0.0227	1.1166	1.0846	1.5926	0.5002	-0.5426	0.5584	1.0850	0.5584	1.0850	2.0726	1.5774	1.6740	1.0652	1.0054	-0.1863	1.2620	-0.6768	0.0994	
H-unR-150-0.3	1.0290	0.9691	1.5347	0.9798	1.5347	0.9258	1.4243	-0.0202	1.1075	1.1313	1.3549	0.6629	-0.3035	0.5538	1.1314	0.5538	1.1314	2.0128	1.6014	1.5347	1.0207	1.0788	-0.3868	1.3737	-0.7346	0.1301	
H-unR-100-0.6	0.6330	0.4683	1.5834	0.6194	1.5834	0.5641	1.4425	-0.0230	1.1275	0.7148	1.6387	0.3207	-0.5845	0.5637	0.7148	0.5637	0.7148	2.0370	1.0199	1.5833	1.6146	1.0613	-0.5025	2.0775	-0.4388	0.0398	
H-unR-150-0.6	0.7951	0.6663	1.5128	0.7646	1.5128	0.7454	1.4631	-0.0071	1.1239	0.8886	1.3221	0.5609	-0.2522	0.5620	0.8887	0.5620	0.8887	1.0097	0.7952	1.5128	1.3078	1.1459	-0.6381	1.8428	-0.5770	0.0817	
H-R-100-0.3	1.2391	1.3114	1.6305	1.1808	1.6304	1.1247	1.5317	-0.0223	1.1187	1.3737	1.4341	0.7501	-0.3716	0.5593	1.3737	0.5593	1.3737	2.0962	2.0119	1.6303	0.8469	1.0569	-0.2352	1.0636	-0.8733	0.1777	
H-R-150-0.3	0.9577	0.8888	1.4110	0.9199	1.4110	0.8963	1.3624	-0.0079	1.1036	1.0511	1.2354	0.7361	-0.1755	0.5518	1.0512	0.5518	1.0512	1.9680	1.4646	1.4111	1.0871	1.3022	-0.8642	1.7506	-0.6990	0.1230	
H-R-100-0.6	0.6578	0.4824	1.6385	0.6409	1.6386	0.6091	1.5483	-0.0133	1.1484	0.7538	1.5687	0.3687	-0.4920	0.5742	0.7539	0.5742	0.7539	2.1018	1.0903	1.6386	1.5602	1.0751	-0.4586	1.9642	-0.4558	0.0439	
H-R-150-0.6	0.5311	0.3787	1.4474	0.5112	1.4474	0.4906	1.3743	-0.0073	1.1225	0.5937	1.2914	0.3857	-0.2258	0.5613	0.5937	0.5613	0.5937	1.9806	0.8196	1.4475	1.9561	1.2189	-1.2665	2.9721	-0.3863	0.0370	
S-unR-100-0.3	1.8008	2.1897	1.4682	1.7055	1.4682	1.6039	1.3494	-0.0360	1.0694	1.9124	1.2866	1.1857	-0.2580	0.5348	1.9128	0.5348	1.9128	0.9904	1.8008	1.4682	0.5863	106.660 0	-67.0290	28.5440	-1.2904	0.4099	
S-unR-150-0.3	1.1001	1.1004	1.6852	1.0584	1.6851	0.9579	1.5048	-0.0433	1.1091	1.2154	1.7517	0.4859	-0.7117	0.5545	1.2152	0.5545	1.2152	2.0608	1.7695	1.6851	0.9448	0.9993	-0.1545	1.1120	-0.7463	0.1124	
S-unR-100-0.6	1.2421	1.2911	1.5410	1.1803	1.5410	1.1492	1.4807	-0.0116	1.1002	1.3555	1.2943	0.8629	-0.2411	0.5501	1.3553	0.5501	1.3553	2.0226	1.9380	1.5410	0.8472	1.0743	-0.3101	1.1313	-0.8976	0.1988	
S-unR-150-0.6	0.8601	0.7676	1.4204	0.8301	1.4204	0.7638	1.2931	-0.0236	1.0918	0.9368	1.3361	0.5527	-0.3002	0.5459	0.9367	0.5459	0.9367	1.9398	1.3018	1.4204	1.2047	1.1707	-0.7298	1.8202	-0.6220	0.0945	
S-R-100-0.3	1.5852	1.7162	1.2690	1.5306	1.2690	1.5699	1.3345	0.0114	1.0536	1.6637	1.0828	1.4891	-0.0429	0.5268	1.6637	0.5268	1.6637	1.8392	2.2605	1.2690	0.6534	533.150 0	-19.7090	7.6310	-1.1368	0.3270	
S-R-150-0.3	1.2026	1.2165	1.3695	1.1538	1.3695	1.1099	1.3015	-0.0141	1.0923	1.3060	1.2134	0.9338	-0.1606	0.5462	1.3061	0.5462	1.3061	1.9424	1.8123	1.3696	0.8667	1.4286	-0.8660	1.4996	-0.8716	0.1912	
S-R-100-0.6	1.0813	1.0373	1.5502	1.0239	1.5502	0.9835	1.4628	-0.0152	1.1072	1.1865	1.3136	0.7350	-0.2585	0.5536	1.1867	0.5536	1.1867	2.0192	1.6807	1.5502	0.9767	1.0639	-0.3383	1.2921	-0.7762	0.1473	
S-R-150-0.6	0.8200	0.6937	1.5212	0.7863	1.5212	0.7408	1.4112	-0.0172	1.1074	0.9038	1.3819	0.5110	-0.3350	0.5537	0.9039	0.5537	0.9039	1.9972	1.2730	1.5212	1.2718	1.0676	-0.4703	1.7098	-0.5874	0.0827	

Table 40. Kinetic models prediction evaluation (R^2 , RMSE, and PE).

Sample	Lewis (Newton) model			Page model			Modified Page model			Midilli's model			Henderson and Pabis model			Logarithmic model			Tow-term model			Two-term exponential model			Weibull model			Gaussian model			Wang and Singh		
	Rsq	RMSE	PE	Rsq	RMSE	PE	Rsq	RMSE	PE	Rsq	RMSE	PE	Rsq	RMSE	PE	Rsq	RMSE	PE	Rsq	RMSE	PE	Rsq	RMSE	PE	Rsq	RMSE	PE	Rsq	RMSE	PE	Rsq	RMSE	PE
S-unR-100-0.3	0.9632	0.0654	7.2266	0.9956	0.0225	2.2055	0.9956	0.0225	2.2053	0.9977	0.0163	1.2370	0.9693	0.0597	8.2432	0.9931	0.0283	3.4564	0.9693	0.0597	8.2484	0.9632	0.0654	7.2244	0.9956	0.0225	2.2056	0.1613	0.3120	47.6370	0.9972	0.0180	Midilli
S-unR-150-0.3	0.9318	0.0888	10.3080	0.9938	0.0269	3.3874	0.9938	0.0269	3.3869	0.9969	0.0190	2.4445	0.9469	0.0784	9.5740	0.9907	0.0328	4.1050	0.9469	0.0784	9.5720	0.9838	0.0432	4.6513	0.9938	0.0269	3.3868	0.9966	0.0200	2.5860	0.9905	0.0331	4.1413
S-unR-100-0.6	0.9554	0.0712	9.1921	0.9977	0.0162	2.2725	0.9977	0.0162	2.2725	0.9982	0.0142	1.9667	0.9667	0.0615	8.8085	0.9895	0.0346	5.1474	0.9667	0.0615	8.8062	0.9938	0.0267	3.3812	0.9977	0.0162	2.2725	0.9987	0.0120	1.6065	0.9930	0.0283	4.1193
S-unR-150-0.6	0.9636	0.0610	7.7729	0.9967	0.0183	1.7243	0.9967	0.0183	1.7243	0.9988	0.0113	1.1780	0.9740	0.0516	7.3002	0.9960	0.0202	2.9265	0.9740	0.0516	7.2965	0.9943	0.0241	1.9746	0.9967	0.0183	1.7243	0.9982	0.0136	1.3362	0.9972	0.0169	2.3232
S-R-100-0.3	0.9828	0.0413	5.6223	0.9950	0.0223	1.9749	0.9950	0.0223	1.9749	0.9959	0.0202	2.1177	0.9860	0.0372	6.1066	0.9885	0.0337	5.0069	0.9860	0.0372	6.1067	0.9953	0.0215	2.0626	0.9950	0.0223	1.9749	0.7092	0.1694	28.7450	0.9880	0.0344	2.0401
S-R-150-0.3	0.9704	0.0563	7.5699	0.9960	0.0207	2.4643	0.9960	0.0207	2.4644	0.9968	0.0185	2.7617	0.9800	0.0463	7.1906	0.9937	0.0260	4.8201	0.9800	0.0463	7.1922	0.9954	0.0223	2.1302	0.9960	0.0207	2.4642	0.9956	0.0217	3.7040	0.9940	0.0254	4.1469
S-R-100-0.6	0.9514	0.0743	9.7763	0.9957	0.0222	2.6161	0.9957	0.0222	2.6160	0.9969	0.0189	2.1476	0.9639	0.0640	8.8967	0.9891	0.0352	4.5449	0.9639	0.0640	8.8989	0.9907	0.0325	3.5959	0.9957	0.0222	2.6160	0.9974	0.0173	2.0302	0.9925	0.0291	3.9534
S-R-150-0.6	0.9533	0.0707	9.3151	0.9975	0.0164	2.1916	0.9975	0.0164	2.1913	0.9990	0.0105	1.4661	0.9667	0.0597	8.3415	0.9935	0.0263	3.5919	0.9667	0.0597	8.3429	0.9929	0.0276	3.1529	0.9975	0.0164	2.1917	0.9994	0.0081	0.9324	0.9951	0.0230	3.3271
H-unR-100-0.3	0.9348	0.0865	10.5390	0.9962	0.0208	2.5010	0.9962	0.0208	2.5010	0.9977	0.0162	2.1090	0.9512	0.0748	9.9721	0.9892	0.0352	4.5046	0.9512	0.0748	9.9811	0.9880	0.0371	4.3749	0.9962	0.0208	2.5010	0.9981	0.0147	1.8681	0.9890	0.0354	4.3651
H-unR-150-0.3	0.9522	0.0731	9.5517	0.9963	0.0203	2.3622	0.9963	0.0203	2.3622	0.9980	0.0149	1.5267	0.9653	0.0623	8.4694	0.9921	0.0297	4.0245	0.9653	0.0623	8.4711	0.9917	0.0306	3.1617	0.9963	0.0203	2.3622	0.9979	0.0153	1.7662	0.9940	0.0259	3.5994
H-unR-100-0.6	0.9400	0.0796	10.3060	0.9952	0.0226	2.4362	0.9952	0.0226	2.4362	0.9971	0.0174	2.2035	0.9602	0.0648	8.1553	0.9932	0.0269	3.8589	0.9602	0.0648	8.1553	0.9896	0.0331	3.1577	0.9952	0.0226	2.4361	0.9967	0.0188	2.5237	0.9913	0.0303	4.2481
H-unR-150-0.6	0.9552	0.0698	9.8941	0.9989	0.0108	0.9205	0.9989	0.0108	0.9204	0.9993	0.0090	0.8942	0.9721	0.0550	7.9071	0.9926	0.0283	4.2482	0.9721	0.0550	7.9085	0.9552	0.0698	9.8953	0.9989	0.0108	0.9205	0.9989	0.0111	1.5831	0.9925	0.0285	4.4743
H-R-100-0.3	0.9410	0.0843	10.2770	0.9960	0.0219	1.7752	0.9960	0.0219	1.7749	0.9974	0.0176	1.7986	0.9571	0.0718	9.9138	0.9888	0.0367	5.5686	0.9571	0.0718	9.9143	0.9914	0.0321	2.3712	0.9960	0.0219	1.7745	0.9965	0.0206	2.3656	0.9889	0.0366	5.1460
H-R-150-0.3	0.9673	0.0588	8.2247	0.9980	0.0144	1.8270	0.9980	0.0144	1.8270	0.9984	0.0130	1.8772	0.9792	0.0469	6.8931	0.9938	0.0256	4.4864	0.9792	0.0469	6.8945	0.9972	0.0173	1.6915	0.9980	0.0144	1.8269	0.9976	0.0158	2.4921	0.9945	0.0241	3.6525
H-R-100-0.6	0.9357	0.0848	11.3230	0.9982	0.0143	1.2993	0.9982	0.0143	1.2996	0.9991	0.0103	1.3839	0.9610	0.0661	8.7174	0.9929	0.0283	4.3018	0.9610	0.0661	8.7196	0.9942	0.0255	2.2078	0.9982	0.0143	1.2996	0.9983	0.0140	1.6476	0.9886	0.0357	5.6450
H-R-150-0.6	0.9614	0.0628	9.3018	0.9989	0.0106	0.8289	0.9989	0.0106	0.8290	0.9997	0.0057	0.7765	0.9775	0.0480	6.9134	0.9957	0.0211	3.3109	0.9775	0.0480	6.9143	0.9970	0.0176	1.5001	0.9989	0.0106	0.8293	0.9992	0.0092	1.3452	0.9957	0.0210	3.5592

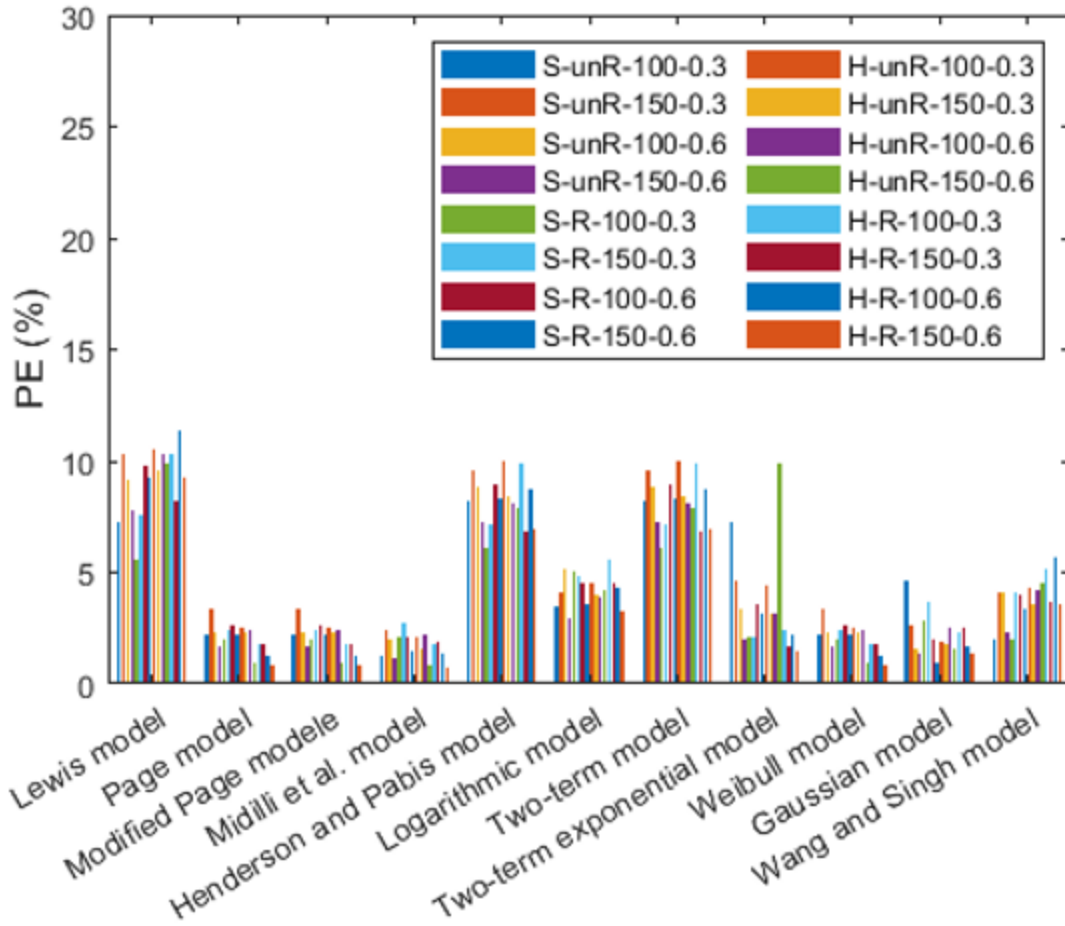


Figure 169. Model prediction evaluation under different drying conditions.

References

- [1] Department of Energy report, *Quadrennial Technology Review*. September 2015.
- [2] Bajpai, P., *Biotechnology for Pulp and Paper Processing*. Springer, 2012.
- [3] Lu, T., Shen, S., *Numerical and Experimental Investigation of Paper Drying: Heat and Mass Transfer with Phase Change in Porous Media*. *J. Appl. Therm. Eng.*, 27(8-9), 1248-1258, 2007.
- [4] Ghosh, A.K., *Fundamentals of Paper Drying—Theory and Application from Industrial Perspective*, in *Evaporation, Condensation and Heat Transfer*. IntechOpen, 2011.
- [5] Li, J., Lingbo, K., Liu, H., *Dryer Section Energy System Measurement and Energy-Saving Potential Analysis for a Paper Machine*. 45(8), 239-243, 2012.
- [6] Mujumdar, A.S., *Handbook of Industrial Drying: A Review of*, CRC Press, 2007.
- [7] Sabarez, H.T., Gallego-Juarez, A.A., Riera, E., *Ultrasonic-Assisted Convective Drying of Apple Slices*. *Dry. Tech.* 30, 989-997, 2012.
- [8] Wray, D., Ramaswamy, H.S., *Novel Concepts in Microwave Drying of Foods*. *Dry. Tech.* 33, 769-783, 2015.
- [9] Martynenko, A., Zheng, W., *Electrohydrodynamic Drying of Apple Slices: Energy and Quality Aspects*. *J. Food Eng.* 168, 215-222, 2016.
- [10] Yang, M., Yagoobi, J., *Enhancement of Drying Rate of Moist Porous Media with Dielectrophoresis Mechanism*. *Dry. Tech.* 40, 2952-2963, 2022.
- [11] Seyed-Yagoobi, J., Husain, A.N., *Experimental and Theoretical Study of Heating/Drying of Moist Paper Sheet with a Gas-Fired Infrared Emitter*. *J. Heat Trans.* 123.4, 711-718, 2001.
- [12] Loureiro, A.C., Souza, F.C.A., Sanches, E.A., *Cold Plasma Technique as a Pretreatment for Drying Fruits: Evaluation of the Excitation Frequency on Drying Process and Bioactive Compounds*. *Food Res. Int.* 147, 1-8, 2021.

- [13] Putranto, A., Chen, X.D., *Vacuum Drying of Food Materials Modeled and Explored Using the Reaction Engineering Approach (REA) Framework*. Dry. Tech., 40, 2519-2527, 2021.
- [14] Sabarez, H. T., *Airborne Ultrasound for Convective Drying Intensification*. Innov. Food Proc. Tech. Woodhead Publishing, 14, 2016. 361-386.
- [15] Geankopolis, C.J., *Transport Processes and Unit Operations*. Prentice-Hall, 1993.
- [16] Weise, U., *Characterization and Mechanisms of Changes in Wood Pulp Fibers Caused by Water Removal*. J. Acta Polytechnica Scandinavica Chemical Technology, 1997.
- [17] Schlunder, E.U., *Drying of Porous Material During the Constant and the Falling Rate Period: A Critical Review of Existing Hypotheses*. Dry. Tech. 22.6, 1517-1532, 2004.
- [18] Topgaard, D., Soderman, O., *Changes of Cellulose Fiber Wall Structure During Drying Investigated Using NMR Self-Diffusion and Relaxation Experiments*. Cellulose, 9(2), 139-147, 2002.
- [19] Caurie, M., *Bound Water: It's Definition, Estimation and Characteristics*. Int. J. Food Sci. Tech., 46(5), 930-934, 2011.
- [20] Maloney, T.C., Johansson, T., Paulapuro, H., *Removal of Water from the Cell Wall During Drying*. J. Paper Tech., 39(6), 39-47, 1998.
- [21] Perkins, E. L., Batchelor, W.J., *Water Interaction in Paper Cellulose Fibers as Investigated by NMR Pulsed Field Gradient*. Carbohydrate polymers. 87.1, 361-367, 2012.
- [22] Park, S., *Drying Behavior of Cellulose Fibers Characterized by Thermal Analysis*. North Carolina State University, 2006.
- [23] Wiberg, P., Sehlstedt S., Moren T., *Heat and Mass Transfer During Sapwood Drying Above the Fiber Saturation Point*. Dry. Tech. 18(8), 1647-1664, 2000.
- [24] Sandberg, K., Salin, G.J., *Liquid Water Absorption in Dried Norway Spruce Timber Measured with CT Scanning and Viewed as a Percolation Process*. 46, 207-219, 2012.
- [25] Sedighi-Gilani, M., et al., *Visualization and Quantification of Liquid Water Transport in Softwood by Means of Neutron Radiography*. Int. J. Heat Mass Trans. 55, 6211-6221, 2012.

- [26] Bucur, V., *Nondestructive Characterization and Imaging of Wood*. Springer Science and Business Media, 2013.
- [27] Gezici-Koc, O., et al., *Bound and Free Water Distribution in Wood During Water Uptake and Drying as Measured by 1D Magnetic Resonance Imaging*. *Cellulose*, 24(2), 535-553, 2017.
- [28] Zhou, M., et al., *Magnetic Resonance Imaging Evidences of the Impact of Water Sorption on Hardwood Capillary Imbibition Dynamics*. *J. Wood Sci. Tech.* 52(4), 929-955, 2018.
- [29] Park, S., et al., *Hard to Remove Water in Cellulose Fibers Characterized by High Resolution Thermogravimetric Analysis-Methods Development*. *Cellulose*. 13.1, 23-30, 2006.
- [30] Park, S., et al., *Changes in Pore Size Distribution During the Drying of Cellulose Fibers as Measured by Differential Scanning Calorimetry*. *Carbohydrate polymers*. 66.1, 97-103, 2006.
- [31] Polat, O., Crotofino, R.H., Murray Douglas, W.J., *Transport Phenomena Analysis of Through Drying Paper*. *Ind. Eng. Chem. Res.* 31(3), 736-743, 1992.
- [32] Chen, G., *Impingement and Through Air Drying of Paper*. McGill University, 1995.
- [33] Chen, G., Doaglas, W.J.M., *Combined Impingement and Through air Drying of Paper*. 15, 315-339, 1997.
- [34] Weineisen, H., *Through-Drying of Tissue Paper-Experiments and Modelling*. Lund University, 2007.
- [35] Forughhi, A.F., et al., *Through Air Drying of Paper—The Effect of Dryer Fabric*. 37(11), 1454-1464, 2019.
- [36] Hubbe, M., *Mini-Encyclopedia of Papermaking Wet-End Chemistry: Additives and Ingredients, Their Composition, Functions, Strategies for Use*. Naning Invelychem Co., 2011.
- [37] Mandlez, Daniel, et al., *Quantifying the Contribution of Fines Production During Refining to the Resulting Paper Strength*. *Cellulose*. 29.16, 8811-8826, 2022.
- [38] Harding, S.G., et al., *Water Transport During the Drying of Cardboard Studied by NMR Imaging and Diffusion Techniques*. *Chem. Eng. Sci.* 56.18, 5269-5281, 2001.

- [39] Kramer, R.K, Carvalho, A.J.F., *Non-Freezing Water Sobbed on Microcrystalline Cellulose Studied by High-resolution Thermogravimetric Analysis*. Cellulose. 28.16, 10117-10125, 2021.
- [40] Rashid, M.T., et al., *Numerical Simulation of Evaporation Phenomena and Heat Transfer of Liquid Hydrocarbon in a Microtube*. Int. J. Heat Mass Trans. 179, 121734, 2021.
- [41] Kandlikar, S.G., *Fundamental Issues Related to Flow Boiling in Minichannels and Microchannels*. Exp. Therm. Fluid Sci. 26, 389-407, 2002.
- [42] de Oliveira, J.D., et al., *On Flow Boiling of R-1270 in a Small Horizontal Tube: Flow Patterns and Heat Transfer*. Appl. Therm. Eng. 178, 115403, 2020.
- [43] Stenstrom, S., *Drying of Paper: A Review 2000–2018*. Dry. Tech. 38, 825-845, 2019.
- [44] Burger, F., Sollner, K., *The Action of Ultrasonic Waves in Suspensions*. Trans. Faraday Soc. 32, 1598-1603, 1936.
- [45] Legay, M., et al., *Enhancement of Heat Transfer by Ultrasound: Review and Recent Advances*. Int. J. Chem. Eng., 2011, 1-17, 2011.
- [46] Rahimi, M., Abolhasani, M. Azimi, N., *High Frequency Ultrasound Penetration Through Concentric Tubes: Illustrating Cooling Effects and Cavitation Intensity*. Heat Mass Trans. 51(4), 587-599, 2015.
- [47] Zhang, Y., Abatzoglou, N., *Fundamentals, Applications and Potentials of Ultrasound-Assisted Drying*. 154, 21-46, 2020.
- [48] Peng, C., et al., *Physics of Direct-Contact Ultrasonic Cloth Drying Process*. 125, 498-508, 2017.
- [49] Jambrak, A.R., et al., *Accelerated Drying of Button Mushrooms, Brussels Sprouts and Cauliflower by Applying Power Ultrasound and its Rehydration Properties*. J. Food Eng. 81, 88-97, 2007.
- [50] Gallego-Juarez, J.A., et al., *Application of High-Power Ultrasound for Dehydration of Vegetables: Processes and Devices*. Dry. Tech. 25, 1893-1901, 2007.

- [51] Momen, A.M., et al., *Preliminary Investigation of Novel Direct Contact Ultrasonic Fabric Drying*. ASME Int. Mech. Eng. Cong. Expo. 57434, 1-6, 2015.
- [52] Gallego-Juarez, J.A., et al., *A New High-Intensity Ultrasonic Technology for Food Dehydration*. Dry. Tech. 17(3), 597-608, 1999.
- [53] Mujumdar, A.S., *Drying Technology in Agriculture and Food Sciences*. Science Publishers, 2000.
- [54] De la Fuente-Blanco, S., et al., *Food Drying Process by Power Ultrasound*. Ultrasonics, 44, e523-e527, 2006.
- [55] Raso, J., et al., *Influence of Different Factors on the Output Power Transferred into Medium by Ultrasound*. Ultras. Sonochem., 5(4), 157-162, 1999.
- [56] Mulet, A., et al., *New Food Drying Technologies-Use of Ultrasound*. Food Sci. Tech. Int. 9(3), 215-221, 2003.
- [57] Chen, Y., et al., *Novel Ultrasonic-Assisted Vacuum Drying Technique for Dehydrating Garlic Slices and Predicting the Quality Properties by Low Field Nuclear Magnetic Resonance*. 306, 1-7, 2020.
- [58] Li, P. Chen, Z., *Experiment Study on Porous Fiber Drying Enhancement with Application of Power Ultrasound*. Appl. Acoustics, 127, 169-174, 2017.
- [59] Peng, C., Moghaddam, S., *Experimental Evaluation and Kinetic Analysis of Direct-Contact Ultrasonic Fabric Drying Process*, J. Them. Sci. Eng. Appl. 13, 1-11, 2021.
- [60] García-Pérez, J.V., *Ultrasonic Drying of Foodstuff in a Fluidized Bed: Parametric Study*. Ultrasonics, 44, e539-e543, 2006.
- [61] García-Pérez, J.V., et al., *Power Ultrasound Mass Transfer Enhancement in Food Drying*. Food Bioproducts Proc. 85(3), 247-254, 2007.
- [62] Andrés, R., et al., *Airborne Power Ultrasound for Drying Process Intensification at Low Temperatures: Use of a Stepped-Grooved Plate Transducer*. Dry. Tech. 39, 245-258, 2019.

- [63] Fairbanks, H.V., *Drying Powdered Coal with the Aid of Ultrasound*. Powder Tech. 40, 257-264, 1984.
- [64] Tao, Y.; et al., *Comparison Between Airborne Ultrasound and Contact Ultrasound to Intensify Air Drying of Blackberry: Heat and Mass Transfer Simulation, Energy Consumption and Quality Evaluation*. Ultras. Sonochem. 72, 1-15, 2021.
- [65] Wood, R.W., Loomis, A.L., *The Physical and Biological Effects of High-Frequency Sound-Waves of Great Intensity*. The London, Edinburgh, and Dublin Philosophical Magazine and Journal of Science. 4(22), 417-436, 1927.
- [66] Ashokkumar, M., *Handbook of Ultrasonics and Sonochemistry*. Springer, 2016.
- [67] Lacas, F., et al., *Design and Performance of an Ultrasonic Atomization System for Experimental Combustion Applications*. Particle and Particle Sys. Charac. 11(2), 166-171, 1994.
- [68] Noori O'Connor, Z., Yagoobi, J., Tilley, B., *Experimental Study of Drying of Paper with Direct-Contact Ultrasound Mechanism*. Dry. Tech., 2150635, 1-7, 2022.
- [69] Khaire, R.A., Gogate, P.R., *Novel Approaches Based on Ultrasound for Spray Drying of Food and Bioactive Compounds*. Dry. Tech. 39(12), 1832-1853, 2021.
- [70] Tan, S., et al., *Water Spray Cooling of Polymers*. Polymer Eng. Sci. 52(5), 1069-1080, 2012.
- [71] Gogate, P., *The Use of Ultrasonic Atomization for Encapsulation and Other Processes in Food and Pharmaceutical Manufacturing*, in *Power ultrasonics*. Elsevier, 2015.
- [72] Rodriguez, L., et al., *Description and Preliminary Evaluation of a New Ultrasonic Atomizer for Spray-Congelation Processes*. Int. J. Pharma. 183(2), 133-143, 1999.
- [73] Lang, R.J., *Ultrasonic Atomization of Liquids*. J. Acoustical Soc. America. 34(1), 6-8, 1962.
- [74] Sollner, K., *The Mechanism of the Formation of Fogs by Ultrasonic Waves*. Tran. Faraday Soc. 32, 1532-1536, 1936.
- [75] Perron, R.R., *The Design and Application of a Reliable Ultrasonic Atomizer*. IEEE Trans. Sonics Ultras. 14(4), 149-152, 1967.

- [76] Faraday, M., *On a Peculiar Class of Acoustical Figures; and on Certain Forms Assumed by Groups of Particles Upon Vibrating Elastic Surfaces*. Philos. Trans. Royal Soc. London. 121, 299-340, 1831.
- [77] Strutt, J.W., Rayleigh, L., *On the Crispations of Fluid Resting Upon a Vibrating Support*. Phil. Mag. 16, 50-53, 1883.
- [78] Qi, A., Yeo, L.Y., Friend, J.R. *Interfacial Destabilization and Atomization Driven by Surface Acoustic Waves*. Phys. Fluids. 20(7), 1-15, 2008.
- [79] Benjamin, T.B., Ursell, F.J., *The Stability of the Plane Free Surface of a Liquid in Vertical Periodic Motion*. Math. Phys. Sci. 225(1163), 505-515, 1954.
- [80] Kumar, K., Tuckerman, L.S., *Parametric Instability of the Interface Between Two fluids*. J. Fluid Mech. 279, 49-68, 1994.
- [81] Miles, J., *On Faraday Waves*. J. Fluid Mech. 248, 671-683, 1993.
- [82] Rajchenbach, J., Clamond, D., *Faraday Waves: Their Dispersion Relation, Nature of Bifurcation and Wavenumber Selection Revisited*. J. Fluid Mech., 777, 1-12, 2015.
- [83] Sindayihebura, D., Bolle, L., *Theoretical and Experimental Study of the Behaviour of Liquid Film Free Surfaces Driven by Transverse Ultrasonic Vibrations*. WIT Trans. Model. Simul. 13, 1-8, 1970.
- [84] Yule, A., Al-Suleimani, Y., *On Droplet Formation from Capillary Waves on a Vibrating Surface*. Math. Phys. Eng. Sci. 456(1997), 1069-1085, 2000.
- [85] Ramisetty, K.A., Pandit, A.B., Gogate, P.R., *Investigations into Ultrasound Induced Atomization*. Ultras. Sonochem. 20(1), 254-264, 2013.
- [86] Avvaru, B., et al., *Ultrasonic Atomization: Effect of Liquid Phase Properties*. Ultrasonics, 44(2), 146-158, 2006.
- [87] Zhang, Y., Yuan, S., Wang, L., *Investigation of Capillary Wave, Cavitation and Droplet Diameter Distribution During Ultrasonic Atomization*. Exp. Therm. Fluid Sci. 120, 1-12, 2021.

- [88] Goodridge, C.L., Shi, W.T., Lathrop, D.P., *Threshold Dynamics of Singular Gravity-Capillary Waves*. 76(11), 1824-1827, 1996.
- [89] James, A.J., Smith, M.K., Glezer, A. *Vibration-Induced Drop Atomization and the Numerical Simulation of Low-Frequency Single-Droplet Ejection*. J. Fluid Mech. 476, 29-62, 2003.
- [90] Tsai, S.C., Tsai, C.S. *Linear Theory on Temporal Instability of Megahertz Faraday Waves for Monodisperse Microdroplet Ejection*. IEEE Trans. Ultras. 60(8), 1746-1755, 2013.
- [91] Ehrhorn, J., Semke, W., *Numerical Modeling of Vibration Induced Atomization of Liquids*, in *Topics in Model Validation and Uncertainty Quantification*, Springer, 2013.
- [92] Song, Y.L., et al., *Simulation of Onset of the Capillary Surface Wave in the Ultrasonic Atomizer*. Micromachines. 12(10), 1-13, 2021.
- [93] Rajan, R., Pandit, A.B., *Correlations to Predict Droplet Size in Ultrasonic Atomisation*. Ultrasonics. 39(4), 235-255, 2001.
- [94] Barba, A.A., et al., *Intensification of Biopolymeric Microparticles Production by Ultrasonic Assisted Atomization*. Chem. Eng. Proc.: Proc. Intens. 48(10), 1477-1483, 2009.
- [95] Chen, X., Yang, V., *Direct Numerical Simulation of Multiscale Flow Physics of Binary Droplet Collision*. Phys. Fluids. 32(6), 1-22, 2020.
- [96] Sustainable Development Goals. *The United Nations*. <https://www.undp.org/sustainable-development-goals>
- [97] Asensio, M., Seyed-Yagoobi, J., *Theoretical Drying Study of Single-Tier Versus Conventional Two-Tiered Dryer Configurations*. TAPPI J. 75(10), 203-211, 1992.
- [98] Asensio, M., et al., *Comparison of several multi-cylinder paper drying simulation models*. Dry. Tech. 13(4), 945-958, 1995.
- [99] Carey, V.P., *Liquid Vapor Phase Change Phenomena: An Introduction to The Thermophysics of Vaporization and Condensation Processes in Heat Transfer Equipment*. CRC Press, 2018.
- [100] Chilton, T.H., Colburn, A.P., *Mass Transfer (Absorption) Coefficients Prediction from Data on Heat Transfer and Fluid Friction*. J. Indus. Eng. Chem. 26(11), 1183-1187, 1934.

- [101] Pakowski, Z., et al., *Evaluation of Equations Approximating Thermodynamic and Transport Properties of Water, Steam and Air for Use in Cad of Drying Processes*. Dry. Tech. 9(3), 753-773, 1991.
- [102] Petrova, T., Dooley, R., *Revised Release on Surface Tension of Ordinary Water Substance*. J. Proc. Int. Assoc. Prop. Water Steam. 63, 23-27, 2014.
- [103] Datta, A., *Porous Media Approaches to Studying Simultaneous Heat and Mass Transfer in Food Processes. I: Problem Formulations*. J. Food Eng. 80(1), 80-95, 2007.
- [104] Linstrom, P.J., Mallard, W.G., *The NIST Chemistry WebBook: A Chemical Data Resource on the Internet*. J. Chem. Eng. Data. 46(5), 1059-1063, 2001.
- [105] Ververis, C., et al., *Fiber Dimensions, Lignin and Cellulose Content of Various Plant Materials and Their Suitability for Paper Production*. Indus. Corps Prod. 19(3), 245-254, 2004.
- [106] Akhtar, M.W., Kleis, S.J., *Boiling Flow Simulations on Adaptive Octree Grids*. Int. J. Multiphase Flow. 53, 88-99, 2013.
- [107] Welch, S.W., Wilson, J., *A Volume of Fluid Based Method for Fluid Flows with Phase Change*. J. Comp. Phys. 160(2), 662-682, 2000.
- [108] Hirt, C.W., Nichols, B.D., *Volume of Fluid (VOF) Method for the Dynamics of Free Boundaries*. J. Comp. Phys. 39(1), 201-225, 1981.
- [109] Asensio, M.C., Seyed-Yagoobi, J., *Simulation of Paper-Drying Systems with Incorporation of an Experimental Drum/Paper Thermal Contact*, J. Energy Resour. Technol. 115(4), 291-300, 1993.
- [110] Brackbill, J.U., Kothe, D.B., Zemach, C., *A Continuum Method for Modeling Surface Tension*. J. Comput. Phys, 100, 335-354, 1992.
- [111] Von Bahr, M., et al., *Dynamic Wetting of AKD-Sized Papers*. J. Pulp Paper Sci. 30, 74-81, 2004.
- [112] Karchevsky, A.L., Marchuk, I.V., Kabov, O.A. *Calculation of the Heat Flux Near the Liquid–Gas–Solid Contact Line*. Appl. Math. Mod. 40(2), 1029-1037, 2016.

- [113] Ajaev, V.S., Gatapova, E.Y., Kabov, O.A. *Rupture of Thin Liquid films on Structured Surfaces*. Phys. Rev. E, 84(4), 1-7, 2011.
- [114] Kline, S.J., *Describing Uncertainty in Single Sample Experiments*. Mech. Eng. 75, 3-8, 1953.
- [115] Montgomery, D.C., *Design and Analysis of Experiments*. John Wiley and Sons, 2017.
- [116] Motamedian, H.R., Halilovic, A.E., Kulachenko, A., *Mechanisms of Strength and Stiffness Improvement of Paper after PFI Refining with a Focus on the Effect of Fines*. Cellulose. 26(6), 4099-4124, 2019.
- [117] Hagglund, R., Gradin, P., Tarakameh, D., *Some Aspects on the Zero-Span Tensile Test*. Exp. Mech. 44, 365-374, 2004.
- [118] Batchelor, W.J., et al., *Effect of Test Conditions on Measured Loads and Displacements in Zero-Span Testing*. TAPPI J. 5, 3-8, 2006.
- [119] Andres, R.R., et al., *Acoustic Field Generated by an Innovative Airborne Power Ultrasonic System with Reflectors for Coherent Radiation*. Ultrasonics. 99, 1-13, 2019.
- [120] Pusonics S.L., Report on *Characterization of the Acoustic Field Generated by the Rectangular Plate Transducer under stationary Field Conditions*, 2022.
- [121] Pusonics S.L., Report on *Acoustic Distribution of the Rectangular Plate in the Near Field*, 2022.
- [122] Kowalski, S.J., Mierzwa, D., *US-Assisted Convective Drying of Biological Materials*. Dry. Tech. 33, 1601-1613, 2015.
- [123] Colucci, D.; et al. *On the Effect of Ultrasound-Assisted Atmospheric Freeze-Drying on the Antioxidant Properties of Eggplant*. Food Res. Int. 106, 580-588, 2018.
- [124] Mierzwa, D., Kowalski, S.J., *Ultrasound-Assisted Osmotic Dehydration and Convective Drying of Apples: Process Kinetics and Quality Issues*. Chem. Proc. Eng. 37, 383-391, 2016.
- [125] Asensio, M.C., *Transport Phenomena During Drying of Deformable, Hygroscopic Porous Media: Fundamentals and Applications*. Texas A&M University, 2000.

- [126] Bantle, M., Eikevik, T.M., *A Study of the Energy Efficiency of Convective Drying Systems Assisted by Ultrasound in the Production of Cliffish*. J. Cleaner Prod. 65, 217-223, 2014.
- [127] Lakehal, D., Meier, M., Fulgosi, M., *Interface Tracking Towards the Direct Simulation of Heat and Mass Transfer in Multiphase Flows*. Int. J. Heat Fluid Flow. 23(3), 242-257, 2002.
- [128] Eisenmenger, W., *Dynamic Properties of the Surface Tension of Water and Aqueous Solutions of Surface Active Agents with Standing Capillary Waves in the Frequency Range from 10 kc/s to 1.5 Mc/s*. Acta Acustica united with Acustica. 9(4), 327-340, 1959.
- [129] Lierke, E., Griesshammer, G., *The Formation of Metal Powders by Ultrasonic Atomization of Molten Metals*. Ultrasonics. 5(4), 224-228, 1967.
- [130] James, A., et al., *Vibration-Induced Drop Atomization and Bursting*. 476, 1-28, 2003.
- [131] Peskin, R.L., Raco, R.J., *Ultrasonic Atomization of Liquids*. 35(9), 1378-1381, 1963.
- [132] Edwards, W.S., Fauve, S., *Patterns and Quasi-Patterns in the Faraday Experiment*. J. Fluid Mech. 278, 123-148, 1994.
- [133] Teichert, J., et al., *Color Stability of Fermented Mare's Milk and a Fermented Beverage from Cow's Milk Adapted to Mare's Milk Composition*. Foods. 9, 1-11, 2020.
- [134] Jamil, M. F., et al., *Transesterification of Mixture of Castor Oil and Sunflower Oil in Milli Channel Reactor: FAME Yield and Flow Behavior*. Procedia Eng. 148, 378-384, 2016.
- [135] Bhatluri, K. K., et al., *Separation of Toxic Heavy Metals from its Aqueous Solution Using Environmentally Benign Vegetable Oil as Liquid Membrane*. RSC Advances. 5(107), 88331-88338, 2015.
- [136] Suzuki, T., Mitsuishi, A., *Numerical Study of Droplet Behavior on an Oscillating Plate Using OpenFOAM*. Mater. Sci. Eng. 920, 1-12, 2020.
- [137] Net Zero Coalition. *The United Nations*. <https://www.un.org/en/climatechange/net-zero-coalition#:~:text=Currently%2C%20the%20Earth%20is%20already,reach%20net%20zero%20by%202050>.

[138] Sources of Greenhouse Gas Emissions, <https://www.epa.gov/ghgemissions/sources-greenhouse-gas-emissions#colorbox-hidden>, 2021.

[139] Greenhouse Gas Equivalencies Calculator. *U.S. Environmental Protection Agency*. <https://www.epa.gov/energy/greenhouse-gas-equivalencies-calculator>, 2021.

[140] Inyang, U.E., Oboh, I.O., Etuk, B.R. *Kinetic Models for Drying Techniques-Food Materials*. *Adv. Chem. Eng. Sci.*, 8(02), 27-48, 2018.

Publications, Awards, and Affiliations

Scientific Journal Publications

1. **Z. Noori O'Connor**, J. Yagoobi, A. Gnanaskandan, *Fundamental Understanding of Airborne Ultrasonic Atomization – A Numerical Study*, To be submitted to Physics of Fluids Journal.
2. **Z. Noori O'Connor**, J. Yagoobi, A. Gnanaskandan, *Fundamental Understanding of Ultrasonic Atomization and Resultant Droplet Size – A Numerical Study*, To be submitted to Physics of Fluids Journal.
3. **Z. Noori O'Connor**, J. Yagoobi, *Airborne Power Ultrasound for Paper Drying: An Experimental Study*, Submitted to Drying Technology Journal.
4. **Z. Noori O'Connor**, J. Yagoobi, and B. Tilley, *Experimental Study of Paper Drying with Direct-Contact Ultrasound Mechanism*, Drying Technology Journal, 10.1080/07373937.2022.2150635, 2022.
5. **Z. Noori O'Connor**, J. Yagoobi, and B. S. Tilley, *Analysis of Removal of Water Trapped Inside a Single Cellulose Fiber*, To be submitted to Journal of Heat and Mass Transfer. Under internal review.
6. J. Rodriguez Ramirez, M. Farzad, **Z. Noori O'Connor**, J. Yagoobi, *Radial Jet Reattachment Impingement Drying of Corn Tortillas*, Submitted to Drying Technology Journal.
7. **Z. Noori**, J. Yagoobi, and B. Tilley, *Fundamental Understanding of Removal of Liquid Film Trapped Between Fibers in the Paper Drying Process: A Microscopic Approach*, TAPPI J. 19 (5), 245-258, 2020.
8. **Z. Noori**, M. Panjepour and M. Ahmadian, *Study of the Effect of Grain Size on the Melting Temperature of Al Nanocrystals by Molecular Dynamics Simulation*, Journal of Materials Research, 30, 1648-1660, 2015.

Technical Conference Papers and Presentations

1. **Z. Noori O'Connor**, J. Yagoobi, and B. Tilley, *Experimental Study of Drying of Paper with Ultrasound Mechanism*, 22nd International Drying Symposium, Worcester, MA, June 2022.
2. J. Rodriguez Ramirez, M. Farzad, **Z. Noori O'Connor**, J. Yagoobi, *Radial Jet Reattachment Impingement Drying of Corn Tortillas*, 22nd International Drying Symposium, Worcester, MA, June 2022.
3. M. Dardashti, **Z. Noori O'Connor**, M. Yang, J. Yagoobi, *Slurry Dehydration Using Ultrasound Mechanism*, 22nd International Drying Symposium, Worcester, MA, June 2022.
4. **Z. Noori O'Connor**, J. Yagoobi, and B. Tilley, *Visualization of Applications of Ultrasonic Drying for Moist Porous Paper*, Springer Album of Porous Media, 2021.
5. **Z. Noori**, J. Yagoobi, and B. Tilley, *Fundamental Understanding of Removal of Liquid Film Trapped Between Fibers in the Paper Drying Process: A Microscopic Approach*, TAPPICon, Indianapolis, Indiana, 2019.
6. **Z. Noori**, M. Panjepour, M. Ahmadian, and M. D. Emami, *Comparison of Fluid Flow Behavior in a Fixed Bed of Ceramic Foam Spheres with a Monolithic Ceramic Foam*, in proceedings of *International Porous and Powder Materials (PPM)*. Istanbul, Turkey, 2015.
7. **Z. Noori**, M. Panjepour and M. Ahmadian, *Study of the Effect of Grain Size on Melting Temperature and Latent Heat of Al Nanocrystals by Molecular Dynamics Simulation*, *The 1st International and the 6th Joint Conference of Iranian Metallurgical Engineering Society and Iranian Foundrymen's Society*, Tehran, Iran, 2012.

Awards

1. Best non-CARD project poster winner in Semi-Annual Meeting for the Center for Advanced Research in Drying (CARD), 2022.
2. 1st place winner and people's choice in the WPI Graduate Research Innovation Exchange (GRIE), 2020, 2021, and 2022.

3. 1st place winner and people's choice in the 11th and 13th Annual Sustainability Project Competitions at WPI, 2020 and 2021.
4. 1st place winner in the poster presentation session in Semi-Annual Meeting for the Center for Advanced Research in Drying (CARD), 2020.
5. Teaching assistant (TA) of the year award in Mechanical Engineering at WPI, 2019.

Affiliations

Center for Advanced Research in Drying (CARD)

American Society of Mechanical Engineers (ASME)

American Society of Gravitational and Space Research (ASGSR)

Technical Association of the Pulp and Paper Industry (TAPPI)

Society of Women in Mechanical and Materials Engineering at WPI (WMME)

This page is intentionally left blank